Nanomaterials for Light Management in Electro-Optical Devices

Guest Editors: Vo-Van Truong, Jai Singh, Sakae Tanemura, and Michael Hu

Nanomaterials for Light Management in Electro-Optical Devices

Nanomaterials for Light Management in Electro-Optical Devices

Guest Editors: Vo-Van Truong, Jai Singh, Sakae Tanemura, and Michael Hu

Editorial Board

Contents

Editorial

Nanomaterials for Light Management in Electro-Optical Devices

Vo-Van Truong,[1] Jai Singh,[2] Sakae Tanemura,[3] and Michael Hu[4]

[1] *Department of Physics, Concordia University, Montréal, QC, Canada H4B 1R6*
[2] *Faculty of Engineering, Health, Science and the Environment, Charles Darwin University, Darwin, NT 0810, Australia*
[3] *Japan Fine Ceramics Center, Nagoya 456-8587, Japan*
[4] *Energy and Transportation Science Division, Oak Ridge National Laboratory, Oak Ridge, TN 37831, USA*

Correspondence should be addressed to Vo-Van Truong, tvovan@alcor.concordia.ca

In the past decade, nanostructured materials and nanoparticles have emerged as the necessary ingredients for electrooptical applications and enhancement of device performance, in particular by making use of the light management aspects of the nanomaterials. The application areas that are being transformed profoundly include smart coating devices (e.g., electrochromic, photochromic, and thermochromic devices), solar energy, and sensing. Despite the large volume of work in the past on smart coating devices, and in particular on electrochromic devices and thermochromic fenestrations, for optical transmission or reflection control, applications remain limited because of slow response time and nonuniformity in the case of large surfaces. Recent works in the field indicate that nanostructured electrochromic coatings would be an integral part of the solution to the above problem. One aspect that can thus be focused on would be the fabrication and characterization of the nanostructured smart coating materials and their compatibility with other layers in the overall smart coating device. In the area of solar photovoltaics, nanomaterials have been used in designing light-trapping schemes for inorganic as well as organic solar cells. One particular category of solar cells that has attracted much interest is the plasmonic solar cells in which metallic nanoparticles are incorporated, helping in enhancing their energy conversion efficiency. Nanostructured solar cells would eventually develop into a "game changing" technology for making solar cells that are affordable and highly efficient, providing a sizeable alternative energy source for our ever-increasing energy needs. Sensors based on the optical properties of constituting nanostructures and nanoparticles also form a most interesting class of bio- and electrochemical

sensing devices. The possibility of synthetizing nanoparticles and structures of specifically desired sizes and shapes has indeed opened a whole new range of sensing applications. In parallel to the experimental development of nanomaterials for light management in devices, theoretical modeling and analysis have also accomplished much progress, and different methods for simulating the optical properties of nanoparticles and structures have been proposed. This special issue of the Journal of Nanomaterials is thus dedicated to articles dealing with nanostructured materials that can be used for light management purpose in different applications.

Silicon-rich oxide (SRO) is a dielectric material that contains Si nanoparticles and exhibits interesting physical characteristics for applications in optoelectronic devices. The work by Aceves-Mijares et al. examine, in detail the electro-, cathode-and photoluminescence properties of SRO and discuss the origin of light emission in this type of materials. SRO films, of high and medium silicon excess density, obtained by low-pressure chemical vapor deposition and annealed at $1,100°C$ have been studied. Results obtained by the authors have led to conclude that SRO emission properties are due to oxidation state nanoagglomerates rather than to nanocrystals, and the emission mechanism is similar to that in the donor-acceptor decay in semiconductors with a specific wide emission spectrum.

Two papers are devoted to nanostructured electrochromic thin films, a category of materials most suitable for controlling light transmission or absorption in electroptical devices, including smart window coatings. Dinh et al. have shown that by mixing nanostructured Ti and W oxides

films, one can obtain devices with considerable enhancement of electrochromic efficiency and electrochemical stability as compared to the conventional nonnanostructured films. As large-area mixed Ti and W oxides can be prepared by the simple doctor blade technique followed by an electrochemical process, this type of nanostructured electrochromic films can be considered a good candidate for smart window applications. In another paper, Djaoued et al. have presented their studies on the synthesis, characterization, and electrochromic applications of porous WO_3 thin films with different nanocrystalline phases. Asymmetric type electrochromic devices have been constructed using hexagonal, monoclinic, and orthorhombic porous WO_3 thin porous films, and their enhanced electrochromic functionality has been well demonstrated. The paper on smart materials by Chen et al. presents the synthesis of thermochromic W-doped VO_2 (monoclinic/rutile) nanopowders using a novel and simple solution-based process as opposed to other conventional techniques such as excimer laser-assisted metal organic deposition and magnetron sputtering. This simple process is based on the reaction of ammonium metavanadate (NH_4VO_3) and oxalic acid dihydrate ($C_2H_2O_4 \cdot 2H_2O$) followed by addition of appropriate ammonium tungstate ($N_5H_{37}W_6O_{24} \cdot H_2O$).

ZnO nanorods photoluminescence properties are reported by E. Sönmez and K. Meral. The authors have investigated the correlation of photoluminescence lifetime between ZnO nanorods and thiourea-doped ZnO nanorods and concluded that by making use of thiourea, the photoluminescence lifetime of ZnO nanorods can be enhanced significantly. The structural changes observed in thiourea-containing samples are reflected in thinner and longer ZnO nanorods as compared to those without thiourea. Xi et al. have synthesized single-crystal silicon oxynitride nanowires with high N concentrations on silicon substrate at $1200°C$ without any metal catalyst. This process has yielded ultrabright white nanowires that can be used as reflecting surfaces in bright white light-emitting-diodes for lighting applications. A mechanism for the growth of these typical nanowires is also proposed by these authors. Banerjee et al. in their paper have studied the photocatalytic degradation of organic dyes by sol gel-derived gallium-doped anatase titanium oxide. With these doped nanoparticles, almost 90% degradation efficiency can be achieved within 3 hrs of UV irradiation of organic dye samples. It is suggested that the cost-effective $TiO_2 : Ga$ nanoparticles can be used efficiently for light-assisted oxidation of toxic organic molecules.

A final contribution is made by S. Gauvin and M. Boudreau in the field of nonlinear multilayer microcavities. The authors have shown that even in the case of very weak pump-depletion conditions, an optical structure that allows multipass optical paths, such as high finesse multilayer microcavities, could lead to significant cumulative pump wave depletion. To account for these nonnegligible effects, the authors have developed a matrix formalism that can be applied to absorbing media and extended to include anisotropic layers and cascading effects.

Acknowledgments

Research Article

Harmonic Generation and Wave Mixing in Confinement Structures: An Account of Pump Depletion in Second-Order Nonlinear Multilayer Microcavities

Serge Gauvin and Maxime Boudreau

Groupe de Recherche sur les Couches Minces et la Photonique, Département de Physique et d'Astronomie, Université de Moncton, Moncton, NB, Canada E1A 3E9

Correspondence should be addressed to Serge Gauvin, serge.gauvin@umoncton.ca

In presence of weakly nonlinear media, it is tempting to neglect pump wave depletion when calculating the intensity of the various generated nonlinear components. However, even in the case of very weak pump wave depletion conditions, an optical structure that allows multipass optical paths, such as high finesse multilayer microcavities, could lead to significant cumulative pump wave depletion. In such conditions, neglecting pump depletion might lead to large computational errors. A matrix formalism devoted to such pump depletion in planar layered nonlinear structures without resort to the "bound" and "free" waves concept is described. A general approach that makes use of "intrinsic" and "extrinsic" waves concept is given, through a slight modification of the canonical propagation matrix. The theoretical results show that even in the case of very weak pump depletion conditions, the cumulative effect due to confinement actually leads to very significant effects. It turns out that taking into account the pump depletion is mandatory for numerous experimental conditions. This matrix formalism applies to absorbing media, and is extensible to include the case of anisotropic layers and cascading effects.

1. Introduction

From both classical electromagnetism and quantum electrodynamics point of view, there is a constantly growing interest with respect to nonlinear optics in confined structures [1–10]. In the last two decades, a large amount of theoretical and experimental efforts have been devoted to nonlinear processes in optical microcavities, including layered structures [11–22]. Notable attention was given to harmonic generation. Besides a better understanding of basic phenomena in highly confined media, interest is also linked to the possibility of conceiving new technological devices. Indeed, it is now well established that in highly confined structures many optical processes are strongly modified [23–29]. From the point of view of quantum electrodynamics, the modification of vacuum field fluctuations and the concomitant modulation of the density of states are responsible for such effects [30]. The resultant enhancement and inhibition for specific optical processes open doors toward new possibilities devoted to the manipulation of electromagnetic radiation. An important applications field is integrated optics and significant innovations are anticipated.

Because high-confinement structures imply many roundtrips of optical waves, even small pump depletion could cause a significant cumulative reduction in the pump wave amplitude. It is an important goal of the present paper to address this issue. Among other possible formal approaches, including purely numerical ones, here we focus on the transfer matrix method and show how a generalized version of the so-called "propagation matrix" leads to a convenient matrix formalism. Indeed, the transfer matrix method is widely used to calculate the optical properties of layered structures. This formalism automatically takes into account all multiple reflections for all waves components (pump and nonlinear waves) without explicit enumeration and cumbersome summations. Moreover, this formalism is
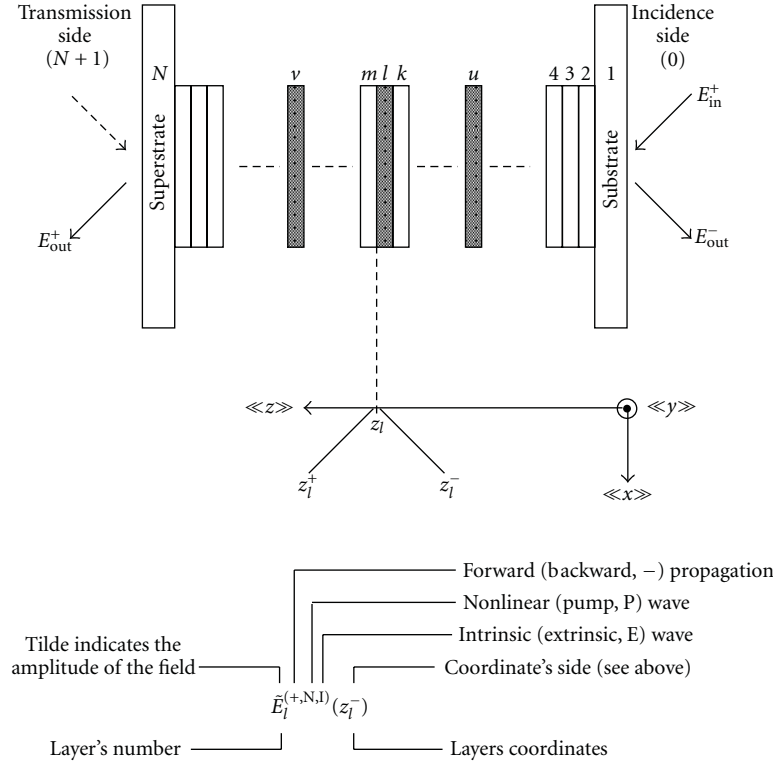
FIGURE 1: General planar multilayered structure and notation system example. Dark layers are assumed nonlinear.

well suited to computer calculations. This formalism could be especially useful in the context of multilayer microcavities. In brief, this paper describes an alternative approach and we believe that the picture and formalism linked to this formalism are both simple and allow further generalization.

2. System Description

Figure 1 shows a general planar multilayered structure made of N stratums (including the substrate and the superstrate). The layers are of infinite extension in the "x-y" plane. The incidence medium is labeled 0. The layer in concern is medium l (which should go over 0 to N in order to account for all nonlinear layers). The transmission medium is $N + 1$. It is assumed that both media 0 and $N + 1$ are semi-infinite and transparent. All layers are nonmagnetic ($\mu \equiv \mu_o$), can be nonlinear and anisotropic. However, they are homogeneous. For every layer, including the substrate and the superstrate, the coherence length of the incident radiation is assumed much larger than its optical thickness. The substrate and superstrate can thus be accounted by the matrices described below. If the substrate or the superstrate have an optical thickness much larger than the incident radiation coherence length and are made of linear material, one takes account of their presence through the reflectance of their respective interface with surrounding media. The intermediate context of layers thickness similar to the incident radiation coherence length needs specific approach. It is omitted here. As for any layer, when the substrate or the superstrate are absorbing,

one includes the exponential decrease absorption law (Beer-Lambert-Bouguer).

The incident radiation is a plane wave. Section 4 describes the formal details. In a few words, each layer l has a thickness s_l and a complex refractive index $\eta_l \equiv n_l - i\kappa_l$ (The layer is absorbing when κ_l is positive). This choice presumes that a forward traveling wave is described by an exponential phase factor of the form $(\omega t - \vec{k} \cdot \vec{r})$. Care must be practiced with various possible conventions [31]. The electric field of the light wave components is E. The input field, E_{in}^+, is associated to the incident (external) pump wave while the output fields, E_{out}^- and E_{out}^+, are linked to the nonlinear outgoing waves emerging from the structure. The outgoing components E_{out}^- and E_{out}^+ are propagating in the backward (incidence side) and forward (transmission side) direction respectively.

3. Formalism Overview

Our approach is based on a matrix formalism [32–35]. In brief, column vectors describe the fields everywhere along the "z" axis while square "transmission matrices" describes the system. Any field vectors pairs are linked through a square transmission matrix. In presence of isotropic media, the field vectors have two rows, and are linked through 2×2 matrices. In presence of anisotropic media, the field distribution within each layer can be expressed as a sum of four partial waves (eigenwaves) [34–46]. Then, one deals with four-row field vectors and 4×4 matrices. Fortunately,

in numerous practical applications we deal with anisotropic transparent layer having one axis normal to the layers' plane. Then, working with plane polarized pump waves, orienting properly its polarization plane, and restraining the incidence to the normal angle in case of biaxial material, the isotropic matrix formalism is suitable. Working with effective nonlinear coefficient is another possibility when dealing with anisotropic nonlinear media [47].

The point of view underlying the current formal approach can be summarized simply with the concept of "intrinsic" and "extrinsic" waves. This concept was already put forward with success [15] (the concept of "intrinsic" and "extrinsic" waves, equivalent of the one of "self" and "add" waves found in [15], were coined without knowledge of [15], during a study on microcavities in France Telecom's laboratories, in 1995). In brief, *a contrario* to the point of view based on the concept of "bound" and "free" waves [48–50], here there is no need for a source vector and, in addition, we use a modified "propagation matrix" (details specified in Section 5).

For the purpose of the present discussion, we are dealing with two semi-infinite media where the intrinsic wave does not suffer any reflection. From the intrinsic and extrinsic waves point of view, a nonlinear wave generated *within a bulk medium* is depicted as a *unique* wave propagating along with the pump wave and having amplitude that varies in space. Because this wave does not originate from outside the bulk medium nor depends on external factors such as the presence of interfaces, this wave is thus said to be "intrinsic". Consequently, in context of harmonic generation the nonlinear wave is not given by the superposition of constant amplitude "bound" and "free" waves from which interference governs the spatial amplitude modulation. As shown in Figure 2, an *intrinsic* nonlinear wave propagating in a medium, l, originates *from within* that medium. *A contrario*, an "extrinsic" wave propagating in a medium, l, originates from an interface or an external stratum. The most important feature of an extrinsic wave is that it travels in space with constant amplitude (except when linear absorption occurs).

Figure 2 also depicts the spatial evolution of the pump and nonlinear waves as they go deeper into a nonlinear medium. Both waves have variable amplitude. The (internal) pump field is the *one inside the nonlinear medium*, not the one incident on the medium l.

Our approach involves each nonlinear layer separately. For each such layer, the specific goal is to calculate the field amplitude of the corresponding intrinsic (nonlinear) and pump waves versus depth inside the medium, at every wavelength. From now on, this pair of solutions is the so-called "non-linear-layer solution." Once that solution is known for the layer l, the matrix formalism allows to easily relates the nonlinear fields inside the structure to its outside. Of course, the use of the Manley-Rowe relation is invaluable to compute pump depletion.

Wave mixing is also important in nonlinear optics. Here we wish to make distinction between mixing of two, or more, incident pump waves and mixing of generated nonlinear waves with pump wave or other nonlinear waves (cascading).
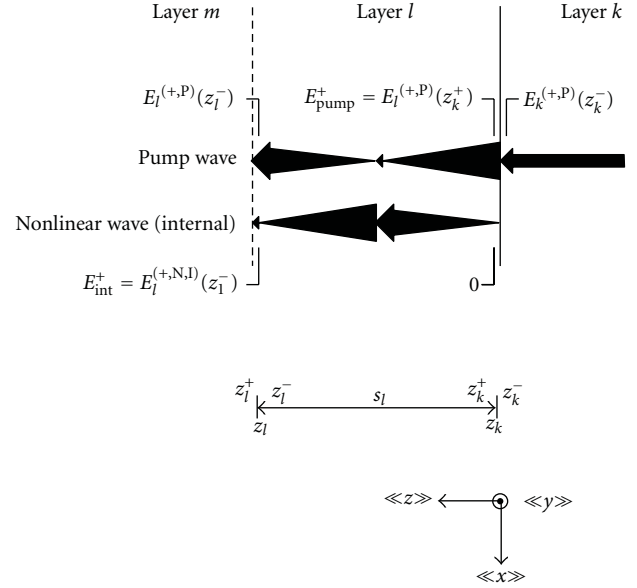
FIGURE 2: Variable-amplitude pump and nonlinear waves in semi-infinite media. The nonlinear wave defines the ≪internal≫ wave.

We refer to the former as "primary mixing" while the later is designated as "secondary mixing". In the context of primary wave mixing, the overall pump field in the layer l is given by the superposition of the incident pump waves. On the other hand, the intrinsic wave is alternatively one of the nonlinear components making the global "nonlinear layer solution". Thus, in case of two pump waves, ω_1 and ω_2, in a second-order nonlinear medium, one computes every component $\omega_1 + \omega_2$, $\omega_1 - \omega_2$, $2\omega_1$, and $2\omega_2$ separately. Even if only one of these nonlinear components is under concern, one has to compute all components if accurate pump depletion is required.

In presence of many nonlinear layers, when secondary mixing is neglected, the overall output is obtained by running l through all layers and summing all the outgoing nonlinear waves (including the phase) propagating in the transmission side. From now on, this is the so-called "process." Provided that secondary mixing entails negligible depletion, the matrix method presented below can account for cascading. Indeed the secondary mixing waves are simply seen as usual pump waves.

In presence of weak nonlinearity, it would be tempting to neglect pump depletion. However, in case of large number of nonlinear layers, the cumulative effect of even weak pump depletion in each layer could lead to large computational error. Thus, in order to take account of pump depletion that might occur in nonlinear layers, the pump field distribution within the structure is treated as a whole (self-consistency).

The linear and nonlinear properties of every layer are supposed known. This adds to material's axis orientations when anisotropy can't be neglected. It will soon

become obvious to the reader that the extension of our approach to anisotropic layers is straightforward, though more algebraically cumbersome. The difficulties are only computational, not conceptual. However, it adds very little to the comprehension of the current approach to keep track of every field components and advance with a complete formal treatment of N anisotropic layers. Because the isotropic and anisotropic formalisms are isomorphic, the generalization to the case of anisotropic layers is left as a forthcoming paper. Specific formalisms are better adapted to this extension than others [41–46]. Then, for the sake of simplicity the formalism put forward in this paper is devoted to isotropic layers. It provides the basic description of our formalism. Subsidiary parameters such as, inhomogeneity, interface roughness, coherence length, beam size, anisotropy and so forth are omitted. This enables us to focus on the basic ideas without the added algebraic complications.

In presence of isotropic layers only, an arbitrary pump wave has to be separated into two orthogonal eigenmodes ("s" and "p" polarization). The resultant, overall outgoing waves are calculated separately and combined at the end of the "process". Because of their more general structure, no such double treatment is required when anisotropic media matrices are in use.

4. Definitions, Conventions, and Notation System

For sake of simplicity, and in order to keep track of all phase shifts, the complex amplitude (phasor) notation is used to fully describe the electric field. Because it doesn't add any supplementary information, the use of complex conjugate when dealing with real quantities is redundant and not systematically shown in equations.

In order to avoid confusion, the formalism makes use of a subscripts-superscripts notation system, for both coordinates and fields. The superscripts are sometime bracketed to avoid mixup with mathematical exponents. As shown in Figure 1, the incident waves propagate along the "z" axis, forward from the right to the left. The superscripts "+" and "−" are used to indicate the propagation direction when applied to E. These superscripts are also applied to z with a slightly different meaning. A self-explained example is shown in Figure 1. It designates the amplitude ($\sim$) of the intrinsic (I), nonlinear (N), and electric field (E) of a wave located on the backward side ($-$) of the coordinate z_l (the interface between layers m and l) and propagating into layer l in the forward (+) direction.

For the purpose of easy reading of some important equations, we sometimes write the abbreviated form of selected specific fields. According to the notation system, the abbreviated forms for the incident pump wave field (E_{in}^+) and the generated outgoing waves (E_{out}^-, E_{out}^+) are defined by

$$E_{in}^+ \equiv E_0^{(+,P)}(z_0^-), \tag{1}$$

$$E_{out}^- \equiv E_0^{(-,N)}(z_0^-), \tag{2}$$

$$E_{out}^+ \equiv E_{N+1}^{(+,N)}(z_N^+). \tag{3}$$
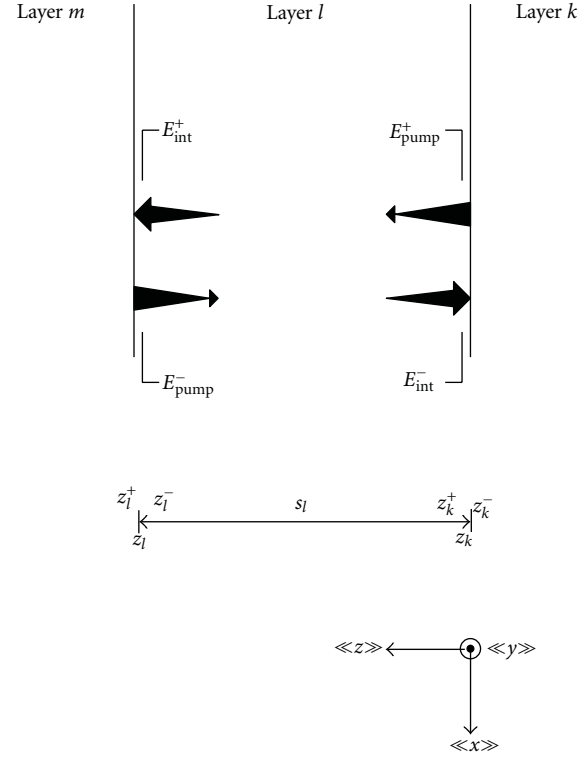
Figure 3: Definition of "intrinsic" and (internal) pump waves.

In (1), we keep the superscript + in order to distinguish from an ongoing pump wave eventually incident on the structure from the transmission side. Indeed, the picture described below remains valid. Nevertheless, here we set the negative input component to 0 ($E_{in}^- = 0$). We define the abbreviated forms for intrinsic (E_{int}^+ and E_{int}^-) and pump (E_{pump}^+ and E_{pump}^-) fields, shown in Figure 3, as follows

$$E_{int}^+ \equiv E_l^{(+,N,I)}(z_l^-), \tag{4}$$

$$E_{int}^- = E_l^{(-,N,I)}(z_k^+), \tag{5}$$

$$E_{pump}^+ = E_l^{(+,P)}(z_k^+), \tag{6}$$

$$E_{pump}^- = E_l^{(-,P)}(z_l^-). \tag{7}$$

Finally, our convention for isotropic media is that the forward traveling waves amplitude figures in the first row of the column field vectors.

5. Basic Matrices

In regard to the current formalism, four basic system matrices are required ("coupling," "continuity," "propagation," and "characteristic" matrix). Care must be practiced with various possible conventions [31] when writing matrices.

5.1. Coupling Matrix. On both sides of an interface, say interface l/k, the field vectors are related through a "coupling

matrix," $\widehat{C}_{lk}$, such that (incidence medium is labeled by the rightmost index)

$$\begin{bmatrix} E_l^+ \left(z_k^+ \right) \\ E_l^- \left(z_k^+ \right) \end{bmatrix} = \widehat{C}_{lk} \begin{bmatrix} E_k^+ \left(z_k^- \right) \\ E_k^- \left(z_k^- \right) \end{bmatrix}. \tag{8}$$

The form of the coupling matrix does not depend on the polarization type and is given by

$$\widehat{C}_{lk} \equiv \frac{1}{\tau_{kl}} \begin{bmatrix} 1 & \rho_{kl} \\ \rho_{kl} & 1 \end{bmatrix}. \tag{9}$$

However, the Fresnel coefficients ρ and τ (reflection and transmission, resp.) depend on the polarization type. Here, we adhere to the normal (Fresnel) convention [31]. We refer the reader to literature for their explicit expression.

5.2. Continuity Matrix.
On both sides of an interface, say interface l/k, the field vectors are also related through "continuity matrices" (This matrix is also known as "admittance matrix" and "dynamical matrix"), $\widehat{D}_l$ and $\widehat{D}_k$, such that

$$\widehat{D}_l \begin{bmatrix} E_l^+ \left(z_k^+ \right) \\ E_l^- \left(z_k^+ \right) \end{bmatrix} = \widehat{D}_k \begin{bmatrix} E_k^+ \left(z_k^- \right) \\ E_k^- \left(z_k^- \right) \end{bmatrix}. \tag{10}$$

These matrices originate from the tangential continuity condition for electric and magnetic fields at an interface (in absence of interfacial current density). They can be used as an alternative definition to the coupling matrix. Indeed, from (8) and (10), we conclude that

$$\widehat{C}_{lk} = \widehat{D}_l^{-1} \widehat{D}_k. \tag{11}$$

The continuity matrix depends on polarization. It is given by (Y is the admittance and θ the propagation angle)

$$\widehat{D}_l = \begin{bmatrix} 1 & 1 \\ -Y_l \cos(\theta_l) & Y_l \cos(\theta_l) \end{bmatrix} \tag{12}$$

for s type polarization, and by

$$\widehat{D}_l = \begin{bmatrix} \cos(\theta_l) & \cos(\theta_l) \\ -Y_l & Y_l \end{bmatrix} \tag{13}$$

for p type polarization.

5.3. Propagation Matrix.
On both intrinsic sides of a single layer, say layer l, the field vectors are related through a "propagation matrix" (we prefer "propagation matrix" to the denomination "phase matrix" because that matrix contains information on amplitude in addition to translational phase shift), $\widehat{P}_l$, such that

$$\begin{bmatrix} E_l^+ \left(z_l^- \right) \\ E_l^- \left(z_l^- \right) \end{bmatrix} = \widehat{P}_l \begin{bmatrix} E_l^+ \left(z_k^+ \right) \\ E_l^- \left(z_k^+ \right) \end{bmatrix}. \tag{14}$$

The propagation matrix does not depend on polarization and is given by

$$\widehat{P}_l = \begin{bmatrix} A_l^+ \exp(-i\varphi_l) & 0 \\ 0 & A_l^- \exp(+i\varphi_l) \end{bmatrix}. \tag{15}$$

This matrix also agrees with the convention that a forward traveling wave is described by an exponential phase factor of the form $(\omega t - \vec{k} \cdot \vec{r})$. The reader would notice that, the propagation matrix defined here has a slightly different form than usual. Indeed, we introduced the "nonlinear amplitude coefficients" A_l^+ and A_l^-. This allows accounting for the amplitude variation *other than linear absorption* (Amplification in case of lasing medium). Indeed, linear absorption is fully described by the complex phase φ_l. In context of linear optics the amplitude coefficients both reduce to 1. Formally, we define the amplitude coefficients for both *internal* (not the incident or external) *pump waves* as, using (6) as follows:

$$A_l^+ \equiv \frac{\widetilde{E}_l^+ \left(z_l^- \right)}{\widetilde{E}_l^+ \left(z_k^+ \right)} = \frac{\widetilde{E}_l^+ \left(z_l^- \right)}{\widetilde{E}_{\text{pump}}^+} = A_l^+ \left(\widetilde{E}_{\text{pump}}^+ \right) \tag{16}$$

and, using (7) as

$$A_l^- \equiv \frac{\widetilde{E}_l^- \left(z_l^- \right)}{\widetilde{E}_l^- \left(z_k^+ \right)} = \frac{\widetilde{E}_{\text{pump}}^-}{\widetilde{E}_l^- \left(z_k^+ \right)} = A_l^- \left(\widetilde{E}_{\text{pump}}^- \right). \tag{17}$$

In presence of depletion, the pump waves are such that $|A_l^+| < 1$ and $|A_l^-| > 1$. Most of the formal difficulties come from the nonlinear behavior of the optical process. Indeed, nonlinearity imposes that A_l^+ and A_l^- depend on the field amplitudes $\widetilde{E}_{\text{pump}}^+$ and $\widetilde{E}_{\text{pump}}^-$ respectively. We discuss the formal implications below. For the moment, we assume that the amplitude coefficients are known. As stated in Section 3, the most important feature of the *extrinsic* waves is that they are described by propagation matrices having amplitude coefficients A_l^+ and A_l^- set to 1.

5.4. Charateristic Matrix.
With the help of continuity and propagation matrices, one defines the "characteristic matrix" ("Characteristic matrices" are also known as "Abelès matrices") as

$$\widehat{M}_l \equiv \widehat{D}_l \widehat{P}_l \widehat{D}_l^{-1}. \tag{18}$$

The characteristic matrix contains all the necessary information about the layer l.

5.5. Transmission Matrix.
Writing an ordered product of coupling and propagation matrices, we can establish a connection anywhere along the z-axis between any field

vectors pairs, say the fields within the layers v and u as follows:

$$\begin{bmatrix} E_v^+ \left(z_{v-1}^+\right) \\ E_v^- \left(z_{v-1}^+\right) \end{bmatrix}$$

$$= \widehat{C}_{v(v-1)} \widehat{P}_{v-1} \widehat{C}_{(v-1)(v-2)} \widehat{P}_{v-2} \qquad (19)$$

$$\cdots \widehat{P}_{u+2} \widehat{C}_{(u+2)(u+1)} \widehat{P}_{(u+1)} \widehat{C}_{(u+1)u} \begin{bmatrix} E_u^+ \left(z_u^-\right) \\ E_u^- \left(z_u^-\right) \end{bmatrix}.$$

Even in presence of many nonlinear layers causing pump depletion, the formalism remains well founded if one uses the propagation matrices through (15). Introducing the characteristic matrices, we reduce the number of required matrices by a factor of two. Making use of (11), (18) and (19) we easily get

$$\begin{bmatrix} E_v^+ \left(z_{v-1}^+\right) \\ E_v^- \left(z_{v-1}^+\right) \end{bmatrix} = \widehat{D}_v^{-1} \widehat{M}_{v-1} \widehat{M}_{v-2} \cdots \widehat{M}_{U+2} \widehat{M}_{u+1} \widehat{D}_u \begin{bmatrix} E_u^+ \left(z_u^-\right) \\ E_u^- \left(z_u^-\right) \end{bmatrix}. \qquad (20)$$

This allows defining the system transmission matrix as

$$\widehat{T}_{vu} = \widehat{D}_v^{-1} \widehat{M}_{v-1} \widehat{M}_{v-2} \cdots \widehat{M}_{u-2} \widehat{M}_{u+1} \widehat{D}_u. \qquad (21)$$

Equation (20) then takes the abbreviated form

$$\begin{bmatrix} E_v^+ \left(z_{v-1}^+\right) \\ E_v^- \left(z_{v-1}^+\right) \end{bmatrix} = \widehat{T}_{vu} \begin{bmatrix} E_u^+ \left(z_u^-\right) \\ E_u^- \left(z_u^-\right) \end{bmatrix}. \qquad (22)$$

6. Pump and Nonlinear Waves in Layered Structures

In the act of a starting point we assume that the whole structure contains only one (isotropic) nonlinear layer, l. From (22) we connect the field of the nonlinear wave emerging from the structure in the transmission side to the layer l through

$$\begin{bmatrix} E_{N+1}^{(+,N)}\left(z_N^+\right) \\ 0 \end{bmatrix} = \widehat{T}_{(N+1)l}^{(N)} \begin{bmatrix} E_l^{(+,N,I)}\left(z_l^-\right) & + & E_l^{(+,N,E)}\left(z_l^-\right) \\ 0 & + & E_l^{(-,N,E)}\left(z_l^-\right) \end{bmatrix} \qquad (23)$$

or equivalently as

$$\begin{bmatrix} E_l^{(+,N,E)}\left(z_l^-\right) \\ E_l^{(-,N,E)}\left(z_l^-\right) \end{bmatrix} = \widehat{T}_{(N+1)l}^{-1(N)} \begin{bmatrix} E_{N+1}^{(+,N)}\left(z_N^+\right) \\ 0 \end{bmatrix} - \begin{bmatrix} E_l^{(+,N,I)}\left(z_l^-\right) \\ 0 \end{bmatrix}. \qquad (24)$$

On the other hand, we connect the field of the nonlinear wave emerging from the structure in the incidence side to the layer l as

$$\begin{bmatrix} E_l^{(+,N,E)}\left(z_k^+\right) \\ E_l^{(-,N,E)}\left(z_k^+\right) \end{bmatrix} = \widehat{T}_{l0}^{(N)} \begin{bmatrix} 0 \\ E_0^{(-,N)}\left(z_0^-\right) \end{bmatrix} - \begin{bmatrix} 0 \\ E_l^{(-,N,I)}\left(z_k^+\right) \end{bmatrix}. \qquad (25)$$

Equations (24) and (25) can now be connected via the propagation matrix $\widehat{P}_l^{(N,E)}$ such as

$$\begin{bmatrix} E_l^{(+,N,E)}\left(z_l^-\right) \\ E_l^{(-,N,E)}\left(z_l^-\right) \end{bmatrix} = \widehat{P}_l^{(N,E)} \begin{bmatrix} E_l^{(+,N,E)}\left(z_k^+\right) \\ E_l^{(-,N,E)}\left(z_k^+\right) \end{bmatrix}. \qquad (26)$$

In (26) we connect extrinsic waves. As stated above, the extrinsic waves are described by propagation matrices having amplitude coefficients A_l^+ and A_l^- set to 1 (superscript E is used as a reminder). This connection leads to the following:

$$\begin{bmatrix} E_{N+1}^{(+,N)}\left(z_N^+\right) \\ 0 \end{bmatrix} - \widehat{T}_{(N+1)0}^{(N)} \begin{bmatrix} 0 \\ E_0^{(-,N)}\left(z_0^-\right) \end{bmatrix}$$

$$= \widehat{T}_{(N+1)l}^{(N)} \begin{bmatrix} E_l^{(+,N,I)}\left(z_l^-\right) \\ 0 \end{bmatrix} - \widehat{T}_{(N+1)l}^{(N)} \widehat{P}_l^{(N,E)} \begin{bmatrix} 0 \\ E_l^{(-,N,I)}\left(z_k^+\right) \end{bmatrix}. \qquad (27)$$

Making use of (2), (3), (4), and (5), we abbreviate this equation for easier reading as

$$\begin{bmatrix} E_{out}^+ \\ 0 \end{bmatrix} - \widehat{T} \begin{bmatrix} 0 \\ E_{out}^- \end{bmatrix} = \widehat{T}_l \begin{bmatrix} E_{int}^+ \\ 0 \end{bmatrix} - \widehat{\Pi}_l \begin{bmatrix} 0 \\ E_{int}^- \end{bmatrix}, \qquad (28)$$

where

$$\widehat{T} \equiv \widehat{T}_{(N+1)0}^{(N)},$$

$$\widehat{T}_l \equiv \widehat{T}_{(N+1)l}^{(N)}, \qquad (29)$$

$$\widehat{\Pi}_l \equiv \widehat{T}_{(N+1)l}^{(N)} \widehat{P}_l^{(N,E)}.$$

Equation (28) set up an explicit link between the pump wave incident on the structure and the outgoing nonlinear components. Indeed, the field amplitudes $\widetilde{E}_{int}^+$ and $\widetilde{E}_{int}^-$ are determined from the "nonlinear-layer solution," and are known functions. From (28) we get (the matrix element indexes are bracketed to avoid confusion with layers' labels)

$$E_{out}^- = -\frac{T_{l[21]} E_{int}^+ - \Pi_{l[22]} E_{int}^-}{T_{[22]}},$$

$$E_{out}^+ = -\left(\frac{T_{[12]}}{T_{[22]}} T_{l[21]} - T_{l[11]}\right) E_{int}^+ \qquad (30)$$

$$+ \left(\frac{T_{[12]}}{T_{[22]}} \Pi_{l[22]} - \Pi_{l[12]}\right) E_{int}^-.$$

As illustrated in Figure 3, the process of calculating E_{int}^+ and E_{int}^- requires the amplitude of the pump waves E_{pump}^+ and E_{pump}^- given by (6) and (7) respectively. They are determined from (ρ is the amplitude reflection coefficient of the whole structure at pump wavelength)

$$\begin{bmatrix} E_{pump}^+ \\ E_l^{(-,P)}\left(z_k^+\right) \end{bmatrix} = \widehat{T}_{l0}^{(P)} \begin{bmatrix} 1 \\ \rho \end{bmatrix} E_{in}^+, \qquad (31)$$

$$\begin{bmatrix} E_l^{(+,P)}\left(z_l^-\right) \\ E_{pump}^- \end{bmatrix} = \widehat{P}_l^{(P)} \widehat{T}_{l0}^{(P)} \begin{bmatrix} 1 \\ \rho \end{bmatrix} E_{in}^+ = \widehat{\Pi}_l^{(P)} \begin{bmatrix} 1 \\ \rho \end{bmatrix} E_{in}^+. \qquad (32)$$

Here, ρ is given by

$$\rho \equiv \frac{\widetilde{E}_0^{(-,\mathrm{P})}}{\widetilde{E}_0^{(+,\mathrm{P})}} = -\frac{T_{[21]}^{(\mathrm{P})}}{T_{[22]}^{(\mathrm{P})}}, \qquad (33)$$

with $\widehat{T}^{(\mathrm{P})}$ now defined by

$$\widehat{T}^{(\mathrm{P})} \equiv \widehat{T}_{(N+1)0}^{(\mathrm{P})}. \qquad (34)$$

In presence of pump depletion, we make use of the generalized propagation matrix introduced in (15). The amplitude coefficients A_l^+ and A_l^- are determined from the "nonlinear layer solution" for l and are known. One understands that in presence of pump depletion, the amplitude coefficients A_l^+ and A_l^- cannot be set to 1. Unfortunately, from (6), (7), (15), (16), (17), (18), (31), and (32) one realizes that the fields E_{pump}^+ and E_{pump}^- are themselves required for their own determination. Indeed, the pump fields are required in the computation of $\widehat{P}_l^{(\mathrm{P})}$, and therefore also for the computation of ρ. This self-consistency requirement leads to two complex implicit equations for E_{pump}^+ and E_{pump}^-. More specifically, writing (31) and (32) in the following compact forms

$$\begin{bmatrix} E_{\mathrm{pump}}^+ \\ E_l^{(-,\mathrm{P})}\left(z_k^+\right) \end{bmatrix} = \begin{bmatrix} f_1 \\ f_2 \end{bmatrix} E_{\mathrm{in}}^+,$$
$$\begin{bmatrix} E_l^{(+,\mathrm{P})}\left(z_l^-\right) \\ E_{\mathrm{pump}}^- \end{bmatrix} = \begin{bmatrix} g_1 \\ g_2 \end{bmatrix} E_{\mathrm{in}}^+, \qquad (35)$$

and the implicit equations are (here pump depletion occurs only in one layer)

$$E_{\mathrm{pump}}^+ = f_1\left(E_{\mathrm{pump}}^+, E_{\mathrm{pump}}^-\right) E_{\mathrm{in}}^+,$$
$$E_{\mathrm{pump}}^- = g_2\left(E_{\mathrm{pump}}^+, E_{\mathrm{pump}}^-\right) E_{\mathrm{in}}^+. \qquad (36)$$

In (36) we explicitly introduced the fields as variable for clarity. From these equations, we now introduce the "deviation functions" $\Delta^+ \equiv \Delta_{\mathrm{re}}^+ + i\Delta_{\mathrm{im}}^+$ and $\Delta^- \equiv \Delta_{\mathrm{re}}^- + i\Delta_{\mathrm{im}}^-$ as

$$\Delta^+ \equiv f_1\left(E_{\mathrm{pump}}^+, E_{\mathrm{pump}}^-\right) E_{\mathrm{in}}^+ - E_{\mathrm{pump}}^+ = \Delta^+\left(E_{\mathrm{pump}}^+, E_{\mathrm{pump}}^-\right),$$
$$\Delta^- \equiv g_2\left(E_{\mathrm{pump}}^+, E_{\mathrm{pump}}^-\right) E_{\mathrm{in}}^+ - E_{\mathrm{pump}}^- = \Delta^-\left(E_{\mathrm{pump}}^+, E_{\mathrm{pump}}^-\right). \qquad (37)$$

In general, these functions do not have simple analytic representation. Finding analytic solution to this system could be difficult. However, (37) are easily computable once the amplitude coefficients A_l^+ and A_l^- are known. Because the pump fields are complex numbers, each deviation function depends on four parameters (in addition to E_{in}^+). From a geometrical point of view, the deviation functions describe two complex (Δ^+ and Δ^-), or evenly four real (Δ_{re}^+, Δ_{im}^+, Δ_{re}^- and Δ_{im}^-), hypersurfaces in a five dimensional space. The solution for the pump fields E_{pump}^+ and E_{pump}^- is clearly given at the crossing point of the hypersurfaces in the hyperplane $\Delta = 0$. This procedure is equivalent to solving

a system of four-variable nonlinear algebraic equations. It is also analogous to load-line analysis practiced in electronics when dealing with nonlinear electronic devices and searching for the operating (quiescent) point. Thus, one solves self-consistency approximately through numerical calculations. However, the accuracy level can be made arbitrary small. Developing algorithms that locate the crossing point is not a difficult task, especially if one puts forward the knowledge one has on the gradient of the hypersurfaces. The solution can be granted *a posteriori* by the application of conservation laws such as field continuity at all interfaces and/or energy balance accounting for linear and nonlinear waves (even in presence of absorption, if known). In case of many depleting layers, the approach described here still applies. One has to add four more dimensions to the hyperspace each time one includes a depleting layer. As an alternative, an iterative algorithm applied to the pump fields could also help. Finally, the above algorithms extend to the context of primary wave mixing. One adds four dimensions to the hyperspace for each pump wave. Nonetheless, it is not the purpose of this paper to further scrutinize the aspects of pump fields' self-consistency.

7. Testing the Formalism: Second Harmonic Generation

7.1. Structure Description. The cavity's thickness is defined by the thickness of the confined nonlinear layer. The microcavity involves two identical mirrors with one nonlinear layer imbedded in-between. Each mirror consists of $23 \times \lambda/4$ dielectric layers. The low index $\lambda/4$ layers are 205.4 nm thick SiO_2 ($n = 1,448$) and the high-index layers are 151.7 nm thick ZrO_2 ($n = 1,961$). The layers in contact with the nonlinear layer are both SiO_2. All dielectric layers are assumed transparent, isotropic and achromatic. The cavity's finesse is close to 400. The incoming pump wave amplitude is $2,0 \times 10^6$ V/m. This corresponds to a fairly small pump intensity of $5,31$ GW/m^2 (531 kW/cm^2, this intensity is approximately obtained with a $1\,\mu$J, 50 ps duration pulse focalized on a $200\,\mu$m diameter spot.). The nonlinear medium is presumed to be 2-methyl-4-nitroaniline (MNA), a highly nonlinear material [51, 52], known as a "yellow material". The only important nonlinear axis is along the cleavage plane. Fortunately, this axis is parallel to the layers' plane [53]. Working with linearly polarized pump wave having their plane aligned along the nonlinear axis, an isotropic medium formalism is adequate. The incidence angle is set normal. The nonlinear layer is assumed transparent, although chromatic dispersion is included [54]. The second order susceptibility is $\chi^{(2)} = 225$ pm/V [55]. Finally, the intensity is obtained from

$$I = \frac{1}{2Z}\left|\widetilde{E}\right|^2. \qquad (38)$$

7.2. Comparison of Conceptual Approaches. In order to test the current matrix formalism, we compare calculations, based on the intrinsic and extrinsic waves concept, with previous one [29], based on the concept of bound and free waves (Bethune's formalism [11]). Of course, because only the current formalism takes into account the pump
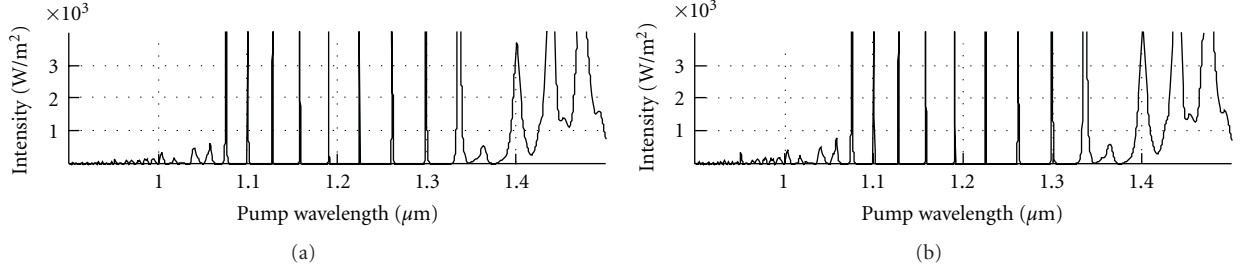
(a)

(b)

FIGURE 4: Calculation comparisons. (a) calculation based on "bound" and "free" waves concept (Bethune's formalism), (b) calculation based on "intrinsic" and "extrinsic" waves concept (present formalism).

TABLE 1: "Nonlinear layer solutions" (Equations number are below each one).

	Without pump depletion	With pump depletion
Non-phase matching	NMND $$\widetilde{E}(z) = 2\pi \frac{1}{n_\mathrm{p}\lambda_\mathrm{p}}\chi^{(2)}\widetilde{E}_\mathrm{P}^2(0)\frac{e^{-i\Delta kz}-1}{\Delta k}$$ $(*)$	NMWD $$\widetilde{E}(z) = \sqrt{\frac{n_\mathrm{p}}{n}}\widetilde{E}_\mathrm{P}(0)\tanh\left[2\pi\frac{1}{\sqrt{nn_\mathrm{p}}\lambda_\mathrm{p}}\chi^{(2)}\widetilde{E}_\mathrm{P}(0)\frac{e^{-i\Delta kz}-1}{\Delta k}\right]$$ $(**)$
Phase matching	PMND $$\widetilde{E}(z) = -i2\pi\frac{1}{n_\mathrm{p}\lambda_\mathrm{p}}\chi^{(2)}\widetilde{E}_\mathrm{P}^2(0)z$$ $(***)$	PMWD $$\widetilde{E}(z) = \widetilde{E}_\mathrm{P}(0)\tanh\left[-i2\pi\frac{1}{n_\mathrm{p}\lambda_\mathrm{p}}\chi^{(2)}\widetilde{E}_\mathrm{P}(0)z\right]$$ $(****)$

depletion, for the purpose of comparison we neglected pump depletion. In [29], our aim was to calculate the outgoing second harmonic generation (SHG) from a layered microcavity embedding only one second-order nonlinear layer. The calculations are performed for a "thick" microcavity, that is a "$30 \times \lambda/2$ microcavity" ($\lambda = 1,19\,\mu$m). Figure 4(a) shows calculation based on bound and free waves concept while Figure 4(b) shows calculation based on the current matrix formalism, founded on the concept of intrinsic and extrinsic nonlinear waves. The agreement appears very satisfying. Only minute differences (due to graphical resolution) can be seen. This comparison is an indication that both conceptual approaches are well founded.

Figure 4 does not show however that the intensity of modes is strongly wavelength dependent. Indeed, the intensity of the sharp peaks between 1,05 and 1,30 μm goes far beyond the graph limit of 4000 W/m^2. This modulation and "pseudomodes" very close to the edges of the mirror's bandgap below 1,1 μm and above 1,3 μm are discussed elsewhere [29].

7.3. Nonlinear Layer Solutions.

To determine the nonlinear-layer solutions, we solve the following one-dimensional nonlinear wave equation (here it is implicit that E applies to the nonlinear wave and v is its phase velocity):

$$\partial_z^2 E(z,t) - \frac{1}{v^2}\partial_t^2 E(z,t) = S(z,t). \tag{39}$$

This equation is readily obtained from basic electromagnetic theory [47]. We assume that the source of nonlinear component is only the second-order nonlinear susceptibility.

The nonlinear source function, $S(z,t)$, is then given by (the subscript stands for "pump")

$$S(z,t) = \varepsilon_o\mu_o\chi^{(2)}\widetilde{E}_\mathrm{P}^2(z)\partial_t^2\exp[i2(\omega_\mathrm{P}t - k_\mathrm{P}z)]. \tag{40}$$

As above, the permeability is set to 1. We search for solutions in the form of a modulated amplitude plane wave

$$E(z,t) = \widetilde{E}(z)\exp[i(\omega t - kz)] = \widetilde{E}(z)\exp[i(2\omega_\mathrm{P}t - kz)]. \tag{41}$$

The occurrence of phase mismatch is formally described through

$$\Delta k \equiv 2k_\mathrm{p} - k = -4\pi\frac{n - n_\mathrm{p}}{\lambda_\mathrm{p}}. \tag{42}$$

For convenience, we investigated four possibilities; (1) non-phase matching SHG without pump depletion (NMND), (2) nonphase matching SHG with pump depletion (NMWD), (3) phase matching SHG without pump depletion (PMND), (4) phase matching SHG with pump depletion (PMWD). The corresponding "nonlinear-layer solutions" are already known (can be found in any good book on nonlinear optics) and summarized in Table 1. They assume slowly varying amplitude approximation (the context of important amplitude variation is easier solved through numerical calculations.) and no absorption at pump and harmonic waves. Nonetheless, absorption at pump wavelength can be included in the calculation of pump fields E_pump^+ and E_pump^- given by (31) and (32), respectively.

In order to complete the pertaining "nonlinear-layer solution," the pump wave amplitude is found through the use
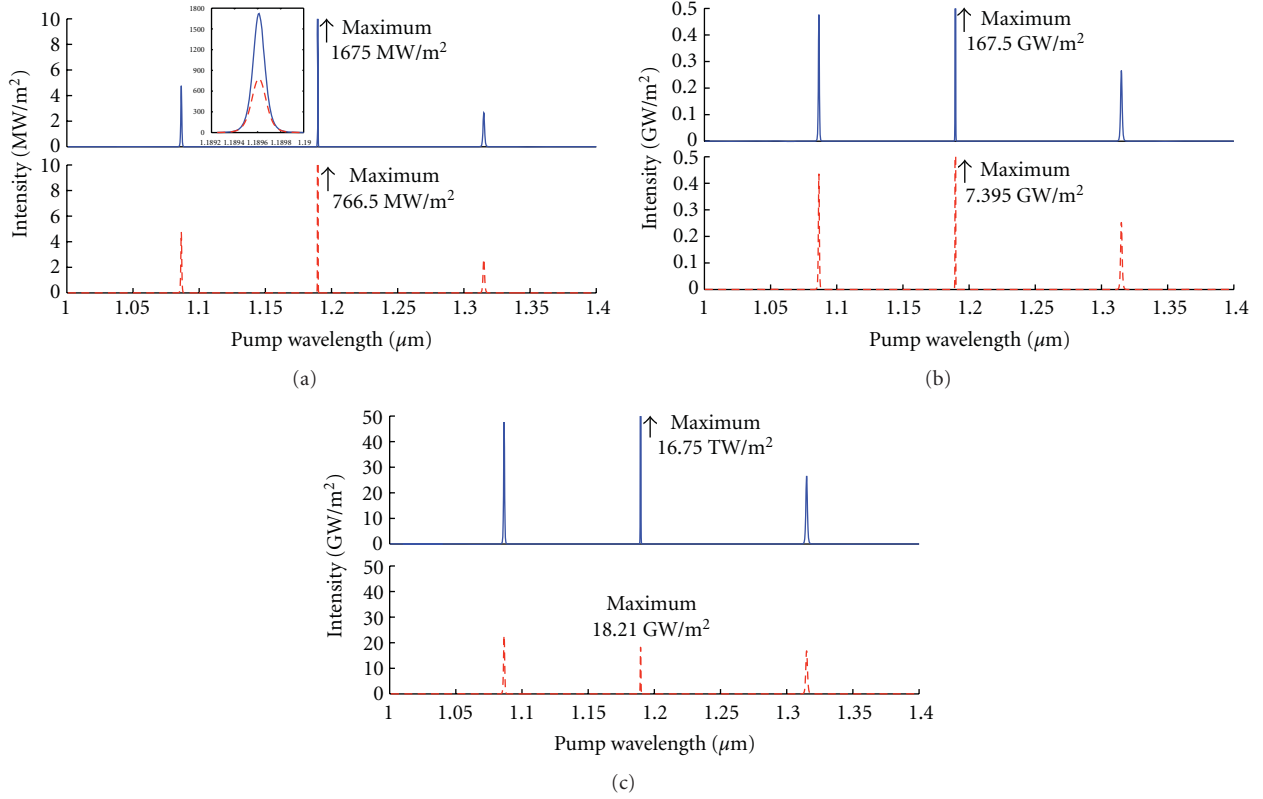
(a)

(b)

(c)

FIGURE 5: Effect of incident-pump-wave intensity on pump depletion, versus wavelength. Continuous (blue) curve: pump depletion neglected; dashed (red) curve: pump depletion taken into account. (a) "weak" incident-pump-wave intensity (5,31 GW/m² or 2,0 MV/m). The inset is a zoom-in on the central peak. (b) "Intermediate" incident-pump-wave intensity (53,1 GW/m²). (c) "Strong" incident-pump-wave intensity (531 GW/m²).

of Manley-Rowe relation expressed in the following form (by definition the phase of pump wave is set to 0)

$$\left| \tilde{E}_P(z) \right|^2 = \tilde{E}_P^2(0) - \frac{n}{n_P} \left| \tilde{E}(z) \right|^2. \qquad (43)$$

We note that from (43), (∗∗), and (∗∗∗∗) in Table 1 one sees the implicit dependence of the amplitude coefficients on the pump fields.

From (43) and (∗∗∗∗) in Table 1, one determines that pump wave suffers an amplitude decline of about 15% when

$$2\pi \frac{1}{n_P \lambda_P} \chi^{(2)} \tilde{E}_P(0) z \approx \frac{1}{2}. \qquad (44)$$

From (38), this imposes a limit on pump wave intensity given by

$$I_{\lim}(15\%) \approx \frac{1}{2Z_o} \left| \frac{1}{4\pi} \frac{n_P \lambda_P}{s_l} \frac{1}{\chi^{(2)}} \right|^2 = \frac{1}{32\pi Z_o} \left(\frac{n_P \lambda_P}{s_l} \frac{1}{\chi^{(2)}} \right)^2. \qquad (45)$$

For a 1 μm thick MNA pumped at $\lambda = 1\,\mu m$, this limit is about 1,64 PW/m² (164 GW/cm²). Through focusing, such value is easily achievable with typical ps-lasers.

8. Results and Discussion

With the aim to characterize the significance, or not, of pump depletion in nonlinear multilayer microcavities, we investigate the effects of three important parameters; (1) intensity of the incident (external) pump wave (Figure 5), (2) thickness of the nonlinear layer (Figure 6), and (3) nonlinear susceptibility of the nonlinear layer (Figure 7). For all figures, a continuous (blue) curve means "without pump depletion" while a dashed (red) curve means "with pump depletion."

In Figure 5, the calculations are performed in the cases of PMND and PMWD, for a "thin" microcavity, that is a "6 × λ/2 microcavity" ($\lambda = 1,19\,\mu m$). This thickness allows one mode in the center of the mirror's bandgap and two pseudomodes. In Figure 5 the intensity of the incident pump wave varies from 5,31 GW/m² (as previously) to 531 GW/m². The effect of pump depletion is clearly seen even at weak intensity and is dominant for the central mode, relatively to the pseudomodes. This is expected because the central mode suffers much more roundtrips than pseudomodes. Also anticipated and in agreement with the results from the undepleted case, an increase in incoming pump wave intensity by one order of magnitude increases the outgoing harmonic wave by two orders of magnitude. Also expected and shown in Figures 5(b) and 5(c), neglecting the pump depletion might lead to such a large computational error that
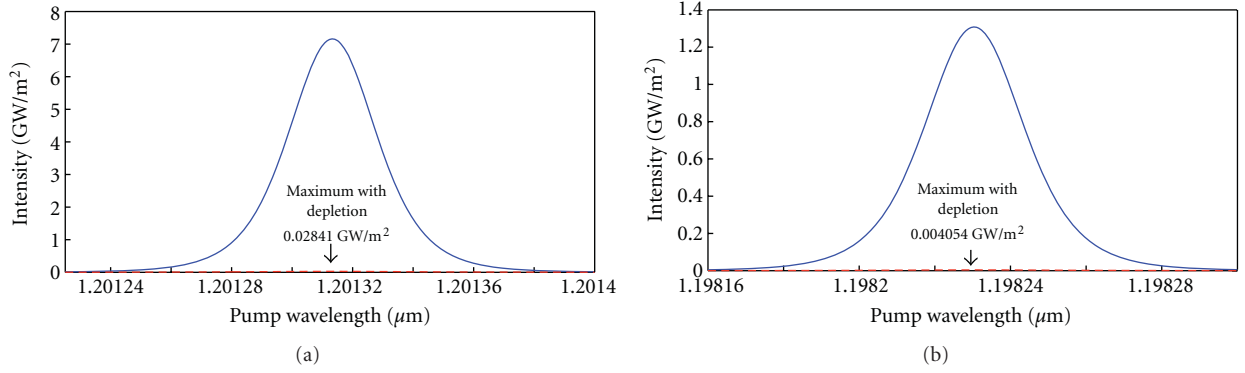
(a)

(b)

FIGURE 6: Effect of high nonlinear layer's thickness on pump depletion, versus wavelength. Continuous (blue) curve: pump depletion neglected, dashed (red) curve: pump depletion taken into account. (a) $s_l = 10\,\mu m$ or $\approx 11 l_{\mathrm{coh}}$. (b) $s_l = 11\,\mu m$ or $\approx 12 l_{\mathrm{coh}}$.

(a)

(b)
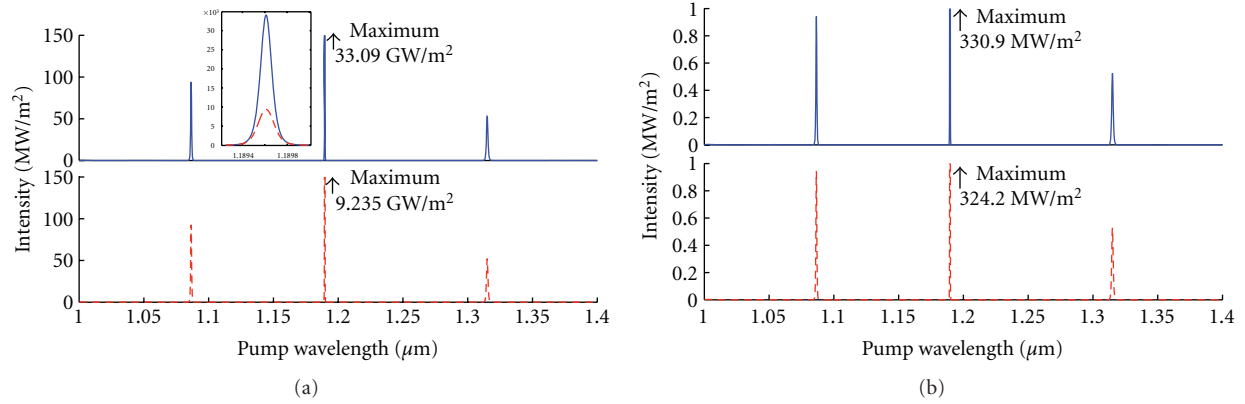
FIGURE 7: Effect of high nonlinear susceptibility on pump depletion versus wavelength. Continuous (blue) curve: pump depletion neglected, dashed (red) curve: pump depletion taken into account. (a) $\chi^{(2)} = 100$ pm/V. (b) $\chi^{(2)} = 10$ pm/V.

the outgoing harmonic intensity can be calculated having a higher value than the incoming pump wave intensity, which is not the case when taking into account the pump depletion. Finally, it worth noting that even the "strong" incident pump wave intensity (531 GW/m^2) is far from the strongest possible intensity.

In Figure 6, the calculations are performed in the cases of NMND and NMWD, at the "intermediate" incident pump wave intensity (53,1 GW/m^2). In Figure 6 the thickness of the nonlinear layer varies from $10\,\mu m$ to $11\,\mu m$. The $10\,\mu m$ thickness corresponds very closely to an odd number, 11, of nonlinear coherence lengths (in this work, we adopt the definition of the nonlinear coherence length, l_{coh}, as the distance between a minimum and a maximum in the spatial profile of SHG intensity. Formally, here, $l_{\mathrm{coh}} = \pi/|\Delta k|$. Some authors define the nonlinear coherence length as twice this value), so that SHG is maximized. *A contrario*, The $11\,\mu m$ thickness corresponds very closely to an even number, 12, of coherence lengths, so that SHG is minimized. As expected, the layer having an odd number of coherence lengths in thickness yield a greater SHG wave than for an even number of coherence lengths.

In Figure 7, the calculations are performed in the cases of PMND and PMWD, for a "thin" microcavity, that is a "$6 \times \lambda/2$ microcavity" ($\lambda = 1, 19\,\mu m$), at the "intermediate" incident pump wave intensity (53,1 GW/m^2). In Figure 7 the nonlinear susceptibility varies from $\chi^{(2)} = 100$ pm/V to $\chi^{(2)} = 10$ pm/V. As expected from the undepleted case, a decrease in nonlinearity by one order of magnitude decreases the resulting outgoing harmonic wave by two orders of magnitude. From the numerical values found in Figure 7, neglecting the pump depletion for the current structure (a typical multilayered microcavity embedding a nonlinear medium the order of 100 pm/V) when submitted to a moderate incident pump wave intensity (~ 50 GW/m^2), causes an inaccuracy as large as 350% in the intensity of the outgoing harmonic wave. This error is reduced to a mere 2% in presence of a moderately nonlinear medium (~ 10 pm/V). We expect a negligible error in case of a weakly nonlinear medium (~ 1 pm/V). Of course, this is not a general rule and various structures embedding arbitrary nonlinear medium and submitted to variable incident pump wave intensity should be covered with proper calculation.

9. Summary, Conclusions, and Perspectives

In summary, in presence of optically confining structures embedding nonlinear medium, even submitted to a low incident pump wave intensity, neglecting the pump depletion could lead to large errors in the computation of the intensity of the outgoing harmonic waves. This could have important consequences when light control and management in stratified nanostructures is involved. The matrix formalism described in this paper appears very suitable to this task and could be helpful in numerous interesting situations where the simulation of the optical properties on nonlinear-layered nanostructures is required. The complete formalism presented here is easily implemented on a computer in few hours.

The approach given in this paper is a step forward; a very general formalism devoted to the theory of nonlinear processes in layered structure. Especially when multiple layer (cumulative) pump depletion might occur. It would also be of interest to study different structures incorporating some nonlinear layers. The effect of various parameters such as their thickness and/or separation would strongly affect the emerging nonlinear waves. A forthcoming next step could be the extension of this approach to include subsidiary parameters neglected above such as, anisotropy, inhomogeneity, and strongly depleting secondary wave mixing.

Acknowledgment

References

[1] H. Yokoyama and K. Ujihara, Eds., *Spontaneous Emission and Laser Oscillation Microcavities*, CRC Press, 1995.

[2] R. Chang and A. Campillo, Eds., *Optical Processes in Microcavities*, World Scientific, 1996.

[3] K. Vahala, Ed., *Optical Microcavities*, World Scientific, 2004.

[4] S. Dutra, *Cavity Quantum Electrodynamics: The Strange Theory of Light in a Box*, Wiley, 2005.

[5] S. Haroche and J. M. Raimond, *Exploring the Quantum: Atoms, Cavities, and Photons*, Oxford University Press, 2006.

[6] A. Kavokin, J. Baumberg, G. Malpuech, and F. Laussy, *Microcavities*, Oxford University Press, 2007.

[7] B. Deveaud, Ed., *The Physics of Semiconductor Microcavities*, Wiley-VCH, 2007.

[8] J. Heebner, R. Grover, and T. Ibrahim, *Optical Microresonators: Theory, Fabrication and Applications*, Springer, 2008.

[9] A. Matsko, Ed., *Practical Applications of Microresonators in Optics and Photonics*, CRC Press, 2009.

[10] K. Ujihara, *Output Coupling in Optical Cavities and Lasers*, Wiley-VCH, 2010.

[11] D. S. Bethune, "Optical harmonic generation and mixing in multilayer media: analysis using optical transfer matrix techniques," *Journal of the Optical Society of America B*, vol. 6, pp. 910–916, 1989.

[12] D. S. Bethune, "Optical harmonic generation and mixing in multilayer media: extension of optical transfer matrix approach to include anisotropic materials," *Journal of the Optical Society of America B*, vol. 8, pp. 367–373, 1991.

[13] S. Bauer, "Second-harmonic generation of light in ferroelectric polymer films with a spatially nonuniform distribution of polarization," *IEEE Transactions on Electrical Insulation*, vol. 27, no. 4, pp. 849–855, 1992.

[14] N. C. Frateschi, P. D. Dapkus, S. S. Ou, J. J. Yang, and M. Jansen, "Analysis of nonplanar wave propagation through multilayer bragg reflectors for folded cavity and vertical cavity surface emitting laser structures," *IEEE Journal of Quantum Electronics*, vol. 31, no. 4, pp. 627–635, 1995.

[15] N. Hashizume, M. Ohashi, T. Kondo, and R. Ito, "Optical harmonic generation in multilayered structures: a comprehensive analysis," *Journal of the Optical Society of America B*, vol. 12, pp. 1894–1904, 1995.

[16] E. Rosencher, B. Vinter, and V. Berger, "Second-harmonic generation in nonbirefringent semiconductor optical microcavities," *Journal of Applied Physics*, vol. 78, no. 10, pp. 6042–6045, 1995.

[17] R. J. Gehr, G. L. Fischer, R. W. Boyd, and J. E. Sipe, "Nonlinear optical response of layered composite materials," *Physical Review A*, vol. 53, no. 4, pp. 2792–2798, 1996.

[18] C. Pedersen and T. Skettrup, "Laser modes and threshold conditions in N-mirror resonators," *Journal of the Optical Society of America B*, vol. 13, no. 5, pp. 926–937, 1996.

[19] M. Auslender and S. Hava, "Scattering-matrix propagation algorithm in full-vectorial optics of multilayer grating structures," *Optics Letters*, vol. 21, no. 21, pp. 1765–1767, 1996.

[20] L. Caleo, C. Sibilia, P. Masciulli, and M. Bertolotti, "Nonlinear-optical filters based on the cascading second-order effect," *Journal of the Optical Society of America B*, vol. 14, no. 9, pp. 2315–2324, 1997.

[21] S. Enoch and H. Akhouayri, "Second-harmonic generation in multilayered devices: theoretical tools," *Journal of the Optical Society of America B*, vol. 15, no. 3, pp. 1030–1041, 1998.

[22] S. V. Fedorov, M. A. Kaliteevskii, N. V. Lukovskaya, and V. V. Nikolaev, "Transfer matrix method for media with quadratic optical nonlinearity," *Technical Physics*, vol. 44, no. 4, pp. 456–457, 1999.

[23] F. De Martini, "Vacuum confinement effects on molecular dynamics in a microscopic cavity," *Physica Scripta*, vol. 21, pp. 58–64, 1988.

[24] S. Haroche and D. Kleppner, "Cavity quantum electrodynamics," *Physics Today*, vol. 42, no. 1, pp. 24–30, 1989.

[25] G. Björk, S. MacHida, Y. Yamamoto, and K. Igeta, "Modification of spontaneous emission rate in planar dielectric microcavity structures," *Physical Review A*, vol. 44, no. 1, pp. 669–681, 1991.

[26] H. Yokoyama, K. Nishi, T. Anan et al., "Controlling spontaneous emission and threshold-less laser oscillation with optical microcavities," *Optical and Quantum Electronics*, vol. 24, no. 2, pp. S245–S272, 1992.

[27] G. Rempe, "Atoms in an optical cavity: quantum electrodynamics in confined space," *Contemporary Physics*, vol. 34, pp. 119–129, 1993.

[28] S. W. Koch, F. Jahnke, and W. W. Chow, "Physics of semiconductor microcavity lasers," *Semiconductor Science and Technology*, vol. 10, no. 6, pp. 739–751, 1995.

[29] S. Gauvin and J. Zyss, "Optical parametric processes in crystalline molecular layered confinement structures: Second harmonic generation in microcavities," in *Applications of Photonic Technology 2*, G. A. Lampropoulos and R. A. Lessard, Eds., pp. 41–49, Plenum Press, 1997.

[30] S. Gauvin and C. Walker, "Strong intensification of parametric fluorescence due to the confinement of vacuum field fluctuations inside microcavities: formalism without resort to the concept of density of states," *Nonlinear Optics and Quantum Optics*, vol. 43, pp. 303–317, 2012.

[31] R. T. Holm, "Convention confusions," in *Handbook of Optical Constants of Solids II*, E. D. Palik, Ed., p. 39, Academic Press, 1991.

[32] O. S. Heavens, *Optical Properties of Thin Films*, Dover, 1965.

[33] Z. Knittl, *Optics of Thin Films*, Wiley, 1976.

[34] P. Yeh, *Optical Waves in Layered Media*, Wiley, 1988.

[35] A. Sh Furman and A. V. Tikhonravov, *Basics of Optics of Multilayer Systems*, Frontières, 1992.

[36] S. Teitler and B. W. Henvis, "Refraction in stratified, anisotropic media," *Journal of the Optical Society of America*, vol. 60, pp. 830–834, 1970.

[37] D. W. Berreman, "Optics in stratified and anisotropic media: 4×4-matrix formulation," *Journal of the Optical Society of America A*, vol. 62, pp. 502–510, 1972.

[38] M. O. Vassell, "Structure of optical guided modes in planar multilayers of optically anisotropic materials," *Journal of the Optical Society of America*, vol. 64, no. 2, pp. 166–173, 1974.

[39] D. J. De Smet, "Generalized ellipsometry and the 4×4 matrix formalism," *Surface Science*, vol. 56, pp. 293–306, 1976.

[40] R. M. A. Azzam and N. M. Bashara, *Ellipsometry and Polarized Light*, North-Holland, 1977.

[41] P. Yeh, "Electromagnetic propagation in birefringent layered media," *Journal of the Optical Society of America*, vol. 69, no. 5, pp. 742–756, 1979.

[42] P. J. Lin-Chung and S. Teitler, "4×4 matrix formalisms for optics in stratified anisotropic media," *Journal of the Optical Society of America A*, vol. 1, no. 7, pp. 703–705, 1984.

[43] R. S. Weis and T. K. Gaylord, "Electromagnetic transmission and reflection characteristics of anisotropic multilayered structures," *Journal of the Optical Society of America A*, vol. 4, pp. 1720–1740, 1987.

[44] K. Eidner, "Light propagation in stratified anisotropic media: orthogonality and symetry properties of the 4×4 matrix formalisms," *Journal of the Optical Society of America A*, vol. 6, pp. 1657–1660, 1989.

[45] M. Schubert, "Polarization-dependent optical parameters of arbitrarily anisotropic homogeneous layered systems," *Physical Review B*, vol. 53, no. 8, pp. 4265–4274, 1996.

[46] I. J. Hodgkinson and Q. H. Wu, *Birefringent Thin Films and Polarizing Elements*, World Scientific, 1997.

[47] B. E. A. Saleh and M. C. Teich, *Fundamentals of Photonics*, Wiley, 2nd edition, 2007.

[48] J. A. Armstrong, N. Bloembergen, J. Ducuing, and P. S. Pershan, "Interactions between light waves in a nonlinear dielectric," *Physical Review*, vol. 127, no. 6, pp. 1918–1939, 1962.

[49] N. Bloembergen and P. S. Pershan, "Light waves at the boundary of nonlinear media," *Physical Review*, vol. 128, no. 2, pp. 606–622, 1962.

[50] D. A. Kleinman, "Theory of second harmonic generation of light," *Physical Review*, vol. 128, no. 4, pp. 1761–1775, 1962.

[51] B. F. Levine, C. G. Bethea, C. D. Thurmond, R. T. Lynch, and J. L. Bernstein, "An organic crystal with an exceptionally large optical second-harmonic coefficient: 2-methyl-4-nitroaniline," *Journal of Applied Physics*, vol. 50, no. 4, pp. 2523–2527, 1979.

[52] G. F. Lipscomb, A. F. Garito, and R. S. Narang, "An exceptionally large linear electro-optic effect in the orgranic solid MNA," *Journal of Chemical Physics*, vol. 75, no. 3, pp. 1509–1516, 1981.

[53] S. Gauvin and J. Zyss, "Growth of organic crystalline thin films, their optical characterization and application to nonlinear optics," *Journal of Crystal Growth*, vol. 166, no. 1–4, pp. 507–527, 1996.

[54] R. Morita, N. Ogasawara, S. Umegaki, and R. Ito, "Refractive indices of 2-methyl-4-nitroaniline (MNA)," *Japanese Journal of Applied Physics, Part 2*, vol. 26, no. 10, pp. L1711–L1713, 1987.

[55] R. Morita, T. Kondo, Y. Kaneda et al., "Dispersion of second-order nonlinear optical coefficient d_{11} of 2-methyl-4-nitroaniline (MNA)," *Japanese Journal of Applied Physics, Part 2*, vol. 27, no. 6, pp. L1131–L1133, 1988.

Research Article

Electrochromic Devices Based on Porous Tungsten Oxide Thin Films

Y. Djaoued,[1] S. Balaji,[1] and R. Brüning[2]

[1] *Laboratoire de Recherche en Matériaux et Micro-Spectroscopies Raman et FTIR, Université de Moncton—Campus de Shippagan, 218 Boulevard J.-D. Gauthier, Shippagan, NB, Canada E8S 1P6*
[2] *Physics Department, Mount Allison University, 67 York Street, Sackville, NB, Canada E4L 1E6*

Correspondence should be addressed to Y. Djaoued, yahia.djaoued@umoncton.ca

Recent developments in the synthesis of transition metal oxides in the form of porous thin films have opened up opportunities in the construction of electrochromic devices with enhanced properties. In this paper, synthesis, characterization and electrochromic applications of porous WO_3 thin films with different nanocrystalline phases, such as hexagonal, monoclinic, and orthorhombic, are presented. Asymmetric electrochromic devices have been constructed based on these porous WO_3 thin films. XRD measurements of the intercalation/deintercalation of Li^+ into/from the WO_3 layer of the device as a function of applied coloration/bleaching voltages show systematic changes in the lattice parameters associated with structural phase transitions in Li_xWO_3. Micro-Raman studies show systematic crystalline phase changes in the spectra of WO_3 layers during Li^+ ion intercalation and deintercalation, which agree with the XRD data. These devices exhibit interesting optical modulation (up to ~70%) due to intercalation/deintercalation of Li ions into/from the WO_3 layer of the devices as a function of applied coloration/bleaching voltages. The obtained optical modulation of the electrochromic devices indicates that, they are suitable for applications in electrochromic smart windows.

1. Introduction

Tungsten oxide (WO_3) has been one of the most widely studied materials due to its multifunctional properties that have wide spectrum of applications in electrochromic devices, catalysers, gas sensors, optical switching devices, and so forth [1–3]. Over the past three decades, intensive research has been carried out towards improving WO_3-based electrochromic (EC) devices due to their important energy saving properties [4–7]. A typical asymmetric EC device consists of an ion conducting (IC) layer, which also acts as a counter electrode and a WO_3 electrochromic layer as the working cathode, sandwiched between two transparent conductive electrodes (TEs) [8, 9]. When a low voltage (1–3 V) is applied across the TEs, Li^+ ions from the counter electrode and electrons (e^-) from the TE move to the EC WO_3 layer. This double injection results in the formation of colored Li_xWO_3 bronzes, with a controllable degree of coloration as a function of x (Li ion concentration). When the applied voltages are reversed, the Li^+ ions deintercalate,

leading to a bleached state. The EC phenomenon, with xe^- and Li^+ ions inserted into (ejected out of) the system, can be represented as:

$$\underset{\text{clear}}{WO_3} + xLi^+ + xe^- \longleftrightarrow \underset{\text{dark blue}}{Li_xWO_3} \tag{1}$$

The performance of an EC device depends on the crystallinity, crystallite size, porosity, and thickness of the electrochromically active layer [10–14]. As far as the preparation of individual layers in an EC device is concerned, PVD techniques (thermal evaporation, sputtering, pulsed laser deposition) and mild chemical approaches such as sol-gel processes have been used [10–15]. Among these, the sol-gel technique is attractive. The sol-gel process allows a detailed control of the film texture and structure, leading to tailored electrochromic properties. Mesoporous WO_3 films prepared by a sol-gel method with block copolymer templates have been investigated by Cheng et al. and by Djaoued et al. [11, 14]. Macroporous WO_3 films were also synthesized via

sol-gel processing using polyethylene-glycol as a templating agent [12]. Mesoporous materials, due to their higher surface area, exhibit better kinetics for coloration and bleaching in comparison with standard sol-gel-derived WO$_3$ thin films. On the other hand, macroporous WO$_3$, which may have a wider range of applications as an ion hosting material, has displayed coloration efficiency values higher than those previously reported in the literature [12]. The motivation for synthesizing such porous materials emerges from the increased diffusion constant of intercalating ions by two orders of magnitude in porous EC-layer-based devices. Templating agents such as polyethyleneglycol (PEG), pluronic (P123), or organically modified silane (ORMOSIL) increase the porosity of the electrochromic layer [8, 9]. In addition to that ORMOSIL has certain other advantages upon annealing, as the silane in the ORMOSIL provides a silica network which helps to prepare crack-free WO$_3$ films. Crystalline phases of WO$_3$ occur primarily in three forms: distorted cubic ReO$_3$ structures, hexagonal, and pyrochlore. The distorted cubic ReO$_3$ structure manifests itself, in monoclinic (Pc), triclinic (P1), monoclinic (P21/n), orthorhombic (Pmnb), and tetragonal (P4/nmm) phases at various temperatures ranging from -263 to $900°C$, in increasing order of symmetry. Usually electrochromic studies have been performed on hexagonal (h), pyrochlore, and monoclinic (m) phases as they are naturally stable or metastable at room temperature [4, 8, 9, 16, 17]. Another factor that influences the performance of the electrochromic devices is the nanostructures of WO$_3$. A detailed study of electrochromic properties of nanostructured tungsten oxide with room temperature stable structure of m-WO$_3$, metastable structure of h-WO$_3$, and titania-stabilized o-WO$_3$ (higher temperature phase) has not been published until recently. Another interesting aspect is the phase changes that are associated with the electrochromic effect in crystalline WO$_3$. Intercalation of Li into ReO$_3$ type tungsten oxides transforms lower symmetry phases to the higher symmetry phases. This phase change has been studied by Raman spectroscopy or by XRD by many researchers [16–19].

When both Raman spectroscopy and XRD techniques are employed simultaneously, a detailed study of the intermediate structural changes in the Li$_x$WO$_3$ can be performed. These methods are practical for the device characterization as they can be performed nondestructively, they can probe the structural changes occurring in the EC layer and provide an estimate of the quantity of intercalated ions.

In this paper, we present a sol-gel methodology based on tungstic acid in the presence of ORMOSIL as a templating agent to prepare films of nanostructured hexagonal-WO$_3$, nanostructured monoclinic-WO$_3$, and titania-stabilized orthorhombic WO$_3$ with mesomacroporous features. These phases have been stabilized as thin films and used as an active electrochromic layers for the construction of asymmetric electrochromic devices. A detailed micro-Raman spectroscopic structural characterization of Li ions intercalation/deintercalation into the WO$_3$ layer of the operating EC devices as a function of applied coloration/bleaching voltages has been performed. Results of the XRD characterization of the structural changes occurring during the

intercalation/deintercalation of Li ions into the WO$_3$ layers of the operating EC device as a function of applied voltages are described. The optical transmittance data obtained in conjunction with the Raman and the XRD studies are presented to demonstrate the applicability of these materials for energy saving electrochromic smart windows.

2. Experimental Details

In order to obtain porous WO$_3$ films with sufficient thickness, hybrid organically modified silicates (ORMOSIL) was used as a template precursor. It was prepared by an acylation reaction between poly(propylene glycol) bis(2-aminopropyl ether) (2-APPG) with isocyanatopropyltriethoxysilane (ICS) in tetrahydrofuran (THF) in the volume ratio 1 : 0.1 : 1 [6, 8, 20].

2.1. Synthesis of h-WO$_3$ and m-WO$_3$. The sol-gel coating solutions used for the preparation of h-WO$_3$ and m-WO$_3$ films were synthesized according to the following procedures. WO$_3$ sols were prepared by dissolving tungsten powder (99.9%) in 35% hydrogen peroxide. The mixture was left to stir at room temperature for 8 hours. After the addition of a small amount of ethanol (EtOH), the sol was refluxed for 4 hours at a temperature of 80°C. Finally, 1.5 g of the hybrid ORMOSIL dissolved in EtOH was added dropwise into the WO$_3$ sol and stirred for one hour. The final sol was used for the WO$_3$ film coating. The WO$_3$ films were deposited by dip coating onto SiO$_2$-coated glass or indium tin oxide (ITO) coated-glass substrates with a surface resistivity of 5–15 Ω/sq, at a controlled speed of 4 mm/s. After drying at 60°C, the films were annealed at 400 and 500°C and were held at the peak temperature for one hour and then cooled to room temperature which resulted in h-WO$_3$ and m-WO$_3$, respectively.

2.2. Synthesis of o-WO$_3$. It has been a challenge to stabilize the higher symmetric phases of WO$_3$ such as orthorhombic (o), tetragonal (t), and cubic (c) at room temperature, since ReO$_3$-type WO$_3$ reverts to m-WO$_3$, due to a second-order Jahn-teller distortion, irrespective of thermal treatment [21]. A two-stage process was adopted to prepare o-WO$_3$ thin films on ITO-coated glass substrates. The first stage involves the dip coating of a tungsten oxide film using the above described tungstic acid sol in the presence of ORMOSIL as a templating agent, followed by an annealing at 600°C for one hour, resulting in the formation of a porous WO$_3$ thin film. In the second stage, the porous WO$_3$ film was dip coated with a titanium-alkoxide-based ethanol solution containing ORMOSIL, followed by another annealing at 600°C to prepare TiO$_2$-stabilized o-WO$_3$ film.

2.3. Fabrication of EC Devices. We prepared several electrochromic devices with the configuration:

$$\text{ITO-coated-glass-1/WO}_3\text{/ICL/ITO-coated-glass-2,} \quad (2)$$

where ITO-coated-glass-1 and ITO-coated-glass-2 are the two transparent electrodes (TEs) used to apply the electric
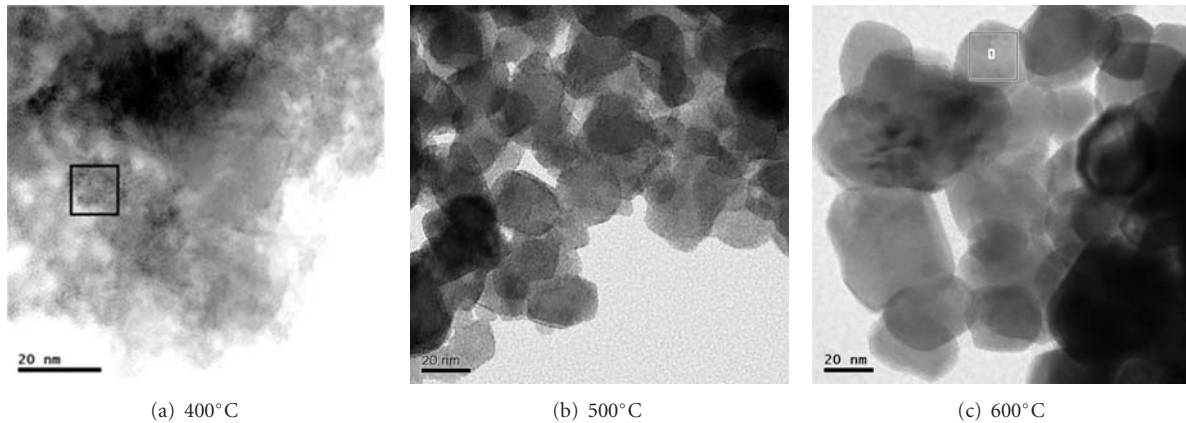
(a) 400°C   (b) 500°C   (c) 600°C

FIGURE 1: Transmission electron micrographs of tungsten oxide films prepared at 400 (grain size ~10 nm), 500 (grain size ~19 nm), and 600°C (grain size ~25 nm).

field, WO_3 is the electrochromic layer and ICL is the ion conducting and electronically insulating layer. The ICL is applied on top of the WO_3 layer and the ITO-coated-glass-2 is gently pressed against this coating to ensure a uniform distribution of the ICL. After making the electrical connections, the EC device is ready for testing. The area of the EC devices was $5 \times 2.5 \, cm^2$.

2.4. Structural and Optical Characterization

2.4.1. Transmission Electron Microscopy. A WO_3 layer was deposited onto a SiO_2-coated glass substrate and annealed in air at 400, 500, or 600°C for one hour. TEM of the WO_3 layers was performed on a small amount of film scrapped off the SiO_2-coated glass substrate and placed into a glass vial. The sample was imaged using a 2011 JEOL STEM at 200 keV. Images were captured on a $4 \, k \times 4 \, k$ multiscan CCD camera using Digital Micrograph from Gatan.

2.4.2. Raman Spectroscopy. Raman spectra were recorded at room temperature with a Jobin-Yvon Labram HR micro-analytical spectrometer equipped with a motorized xy stage and autofocus. The spectra were generated with 17 mW, 632.8 nm He-Ne laser excitation and dispersed with the 1800 grooves/mm grating across the 0.8 m length of the spectrograph. The laser power was 4 mW at the sample surface. The spectral resolution is estimated to be less than $0.5 \, cm^{-1}$ for a slit width of $150 \, \mu m$ and a confocal hole of $300 \, \mu m$.

2.4.3. X-Ray Diffraction (XRD). XRD measurements were carried out in reflection with a custom built theta-theta diffractometer equipped with pyrolytic graphite monochromator and analyzer crystals. Cu K-α radiation ($\lambda = 0.154178$ nm) was used for the measurements, and the data are shown as a function of the modulus of the scattering vector $q = 4\pi\lambda^{-1} \sin\theta$, where 2θ is the scattering angle. Air scattering was avoided by evacuating the sample space. We determine the lattice constants for different sample states by fitting the diffraction patterns. Each spectrum is fitted to a series of Gaussian peaks superimposed on an overall quadratic background. These fits, shown as lines in the figure, match the data points closely. The peak width, assumed to be the same for all reflections, and the intensities of the individual peaks are treated as fitting parameters. We correct the peak width for the instrument resolution and use it to estimate the crystallite size using the Scherrer method, assuming that for example, crystallite-to-crystallite variations of the lattice parameter do not contribute to the peak widths.

2.4.4. UV-VIS Spectrophotometery. The optical transmittance spectra of the EC devices in their colored/bleached states were recorded at normal incidence with a Biochrom Ultrospec 2000 UV-visible spectrophotometer.

3. Results and Discussion

3.1. Microstructure of the EC Layer Prepared at Different Temperatures. TEM of the WO_3 layers was performed on a small amount of film scraped off the SiO_2-coated glass substrate. Figure 1(a) shows the TEM image of the nanocrystalline WO_3 annealed at 400°C. The nanocrystalline nature is evident from the dimension of domain which is showing crystalline lattice. The interplanar distances obtained by inverse Fast Fourier transforms (FFTs) of lattice spacing shown in the region indicated by the box were found to be 0.72 and 0.79 nm, respectively. These lattice spacings correspond to those of hexagonal WO_3 (h-WO_3) which are $a = 0.7298(2)$ nm, $c = 0.7798(3)$ nm. Figure 1(b) shows the TEM image for the film annealed at 500°C. The average crystallite size was found to be 19.3 nm. The lattice spacings were determined by the FFT of the lattice fringes at two different points on the WO_3 crystallites (not shown here) and are found to be 0.3658 and 0.3625 nm, again matching m-WO_3. Figure 1(b) also shows the mesoporous structure of the walls separating the macropores in the WO_3 films. Figure 1(c) shows the TEM image of the similarly prepared
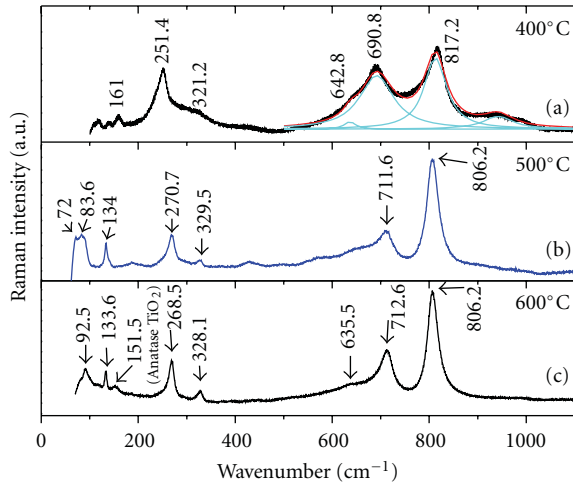
Figure 2: Micro-Raman spectra of tungsten oxide thin films prepared at 400, 500, 600°C indicating the formation of h-WO$_3$, m-WO$_3$, and o-WO$_3$.
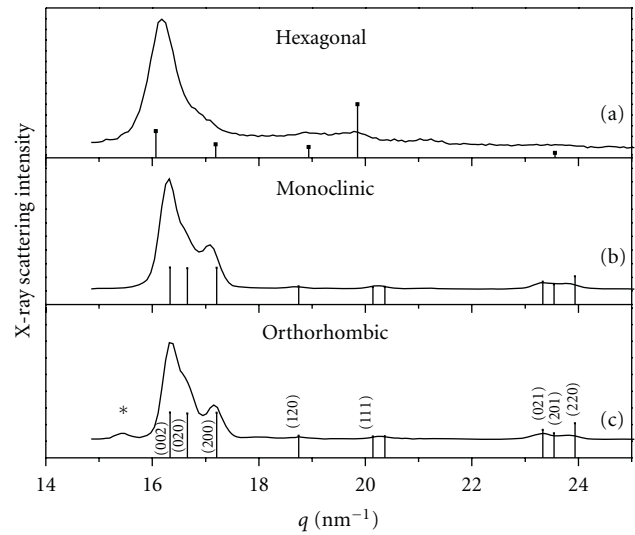

Figure 3: XRD patterns of tungsten oxide thin films prepared at 400, 500, 600°C indicating the formation of h-WO$_3$, m-WO$_3$, and o-WO$_3$. The peak at 15.5 nm^{-1}, indicated by *, is emerging from the ITO layer (c).

sample. From the TEM image, it can be observed that the film is composed of WO$_3$ nanocrystallites of an average size ~25 nm. The value of the interplanar distance is 0.3683 nm, which is the lattice parameter c of m-WO$_3$.

3.2. Crystalline Phases of the EC Layers Prepared at 400, 500, and 600°C.

Raman spectra of the WO$_3$ film heat treated at 400 and 500°C are shown in Figures 2(a) and 2(b). For the films heat treated at 400°C, the bands below 200 cm^{-1} can be ascribed to lattice vibrations. The band observed at 251.4 cm^{-1} is assigned to δ(O-W-O) deformation vibrations, while the bands at 690.8 and 817.2 cm^{-1} are due to ν(O-W-O) stretching vibrations. These bands are characteristic features of h-WO$_3$. The Raman peak positions of our h-WO$_3$ films match those reported for h-WO$_3$ powder by Daniel et al. [21]. The bands at 817.2 and 690.8 cm^{-1} are broadened due to the nanocrystalline nature of the h-WO$_3$ films. Figure 2(b) shows the Raman spectrum of the films prepared at 500°C. The m-WO$_3$ features are observed from the Raman peaks at 134.0 cm^{-1} (lattice mode), 270.7 cm^{-1} δ(O-W-O), and ν(O-W-O) modes at 711.6 and 806.2 cm^{-1}.

The Raman spectrum (Figure 2(c)) of the WO$_3$-TiO$_2$ composite film heat treated at 600°C shows peaks at 806.2, 712.6 cm^{-1} (ν(O-W-O)), 328.1, 268.5 cm^{-1} (δ(O-W-O)), 133.6, 92.5 cm^{-1} (lattice modes) and a low intensity peak at 151.5 cm^{-1}. It is well known that the peak positions corresponding to the stretching vibrations of O-W-O bonds are the same for the triclinic, monoclinic, and orthorhombic phases of WO$_3$, whereas their lattice vibrations in the range 70–100 cm^{-1} show a difference in the Raman spectra [17, 22]. This is primarily due to the fact that the lattice vibrational bands arise from the $(W_2O_2)_n$ chains of WO$_3$. As the low temperature phases of WO$_3$ are less symmetric than the high-temperature phases, the lattice vibrations between 70 and 100 cm^{-1} in Figure 2(b) exhibit more Raman bands for the monoclinic phase (83.6, and 72.0 cm^{-1}) and only one mode at 92.5 cm^{-1} for the orthorhombic phase (Figure 2(c)).

Pecquenard et al. have shown that o-WO$_3$ can be crystallized at temperatures between 600 and 800°C using titanium oxide as structure stabilizer [22]. They reported the lattice vibrational mode of o-WO$_3$ at 91 cm^{-1}, which is similar to our result for the WO$_3$-TiO$_2$ composite film annealed at 600°C.

Figure 3(a) shows the X-ray scattering of the WO$_3$ layer, deposited on the ITO glass substrate and annealed at 400°C for one hour corresponds to hexagonal WO$_3$, for which the JCPDS card 85–2460 diffraction pattern is shown by the vertical bars [23]. By fitting the diffraction pattern, we find the lattice constants of the hexagonal phase to be $a = 0.7379 \pm 0.0008$ and $c = 0.7756 \pm 0.0002$ nm.

Figure 3(b) shows the diffraction pattern of the WO$_3$ film heat treated at 500°C. It matches with the JCPDS card 43–1035 diffraction pattern of pure m-WO$_3$ (vertical bars). The lattice parameters obtained from the fitting of the diffraction pattern are $a = 0.7351 \pm 0.0002$, $b = 0.75396 \pm 0.0005$, $c = 0.7712 \pm 0.0002$ nm, with $\beta = 90.3°$. Although the peaks are similar in Figures 3(b) and 3(c), the lattice parameters obtained from the fitting for the sample annealed at 600°C are $a = 0.7351 \pm 0.0019$, $b = 0.7566 \pm 0.0019$, and $c = 0.7724 \pm 0.0021$ nm, with $\beta = 90°$ indicating that the WO$_3$ is in the orthorhombic phase.

3.3. Construction of Asymmetric Electrochromic Devices Based on h-WO$_3$, m-WO$_3$, and o-WO$_3$ Layers.

In this section we describe the construction of asymmetric EC devices by using the thus synthesised h-WO$_3$, m-WO$_3$, and o-WO$_3$ thin films as the active electrochromic layer. The asymmetric EC device consists of an ion conductor layer, which also acts as a counter electrode and a WO$_3$ EC layer as the working cathode. These are sandwiched between two transparent conductive electrodes. As a low voltage is applied across the
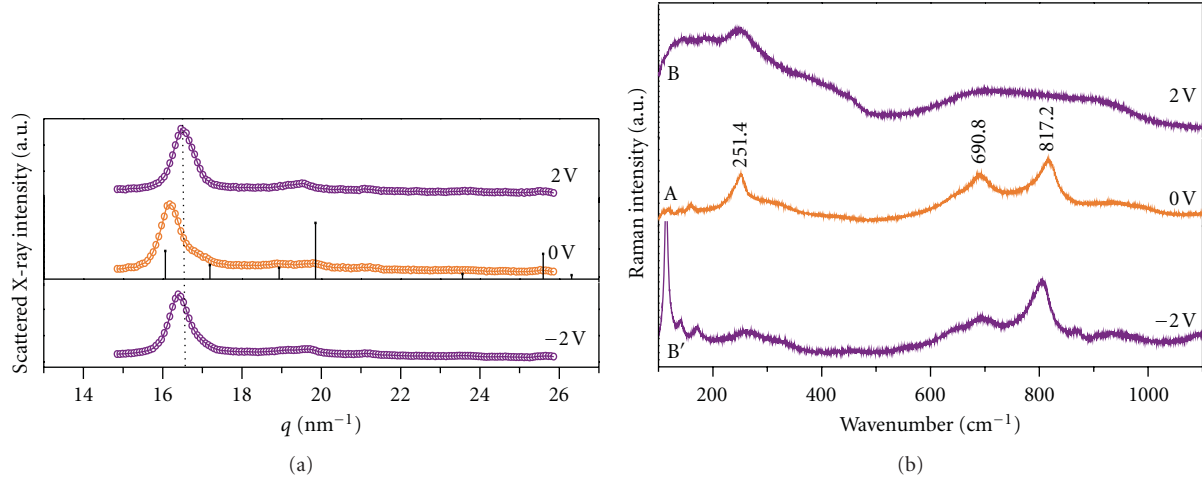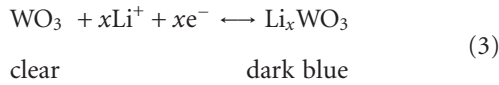
FIGURE 4: Electrochromic structural changes in the EC device constructed using h-WO$_3$ layer.

transparent conductors (1–3 V), ions move from the counter electrode and electrons from the transparent electrode to the EC layer to trigger a color change. The EC phenomenon occurring with such double injection can be represented as:

$$WO_3 + xLi^+ + xe^- \longleftrightarrow Li_xWO_3$$

$$\text{clear} \qquad\qquad\qquad \text{dark blue}$$ (3)

where x electrons (e^-) and lithium ions (Li^+) are inserted into or ejected from the system. Reversing the voltage restores the device to its previous clear (bleached) optical state. The ion conducting layer is a gel which is prepared by mixing lithium iodide (LiI) and iodine (I$_2$) in an ethanol solution with ORMOSIL. A network of silanes, present in ORMOSIL, acts as the ion storage layer. This ion conducting layer supplies Li$^+$ ions to the EC layer under proper biasing. This layer is applied on top of the WO$_3$ layer and another ITO-coated glass substrate is gently pressed against the ICL gel. The transparent conductive electrode (ITO layer) is 190 ± 40 nm thick. The thickness of the WO$_3$ layer used in the EC device was of 842 ± 50 nm. The 12 ± 1 μm thick ICL is sandwiched between the WO$_3$ layer and a second ITO coated-glass slide. Then the device is connected to the leads, and it is ready for the testing.

3.4. Electrochromic Structural Studies during Intercalation (Deintercalation) of Li$^+$ Ions into (Ejected out of) the h-WO$_3$ Layer of the EC Device. Figure 4 shows the XRD pattern (a) and the Raman spectrum (b) of the EC device constructed by using the h-WO$_3$ layer as an active working layer, in its colored and bleached states for applied potentials of 0.0 and ±2.0 V. Inserting and extracting lithium at ±2.0 V shift the diffraction peak positions as seen in the figure. The lattice parameters of the WO$_3$ EC layer at 0 V are a = 0.7379 ± 0.0008 and c = 0.7756 ± 0.0002 nm. We note that the lattice parameter c decreases to 0.76152 ± 0.0003 during the sequence of measurements. The observed variations in the lattice parameters of h-WO$_3$ EC layer upon lithiation are compared in the Table 1. The lattice parameter a remains

initially the same, indicating that the unit cell volume decreases as the device ages during cycling. With an applied voltage of ±2.0 V, we observe that the lattice constant c is significantly lower for the Li-intercalated state (positive voltage) and that c increases as the lithium ions are extracted. The crystallite size remains generally close to 10 nm, with a possible slight increase during the measurement sequence.

Raman spectra show strong changes in the stretching bands. Figure 4(b)A shows the Raman spectrum of the pure h-WO$_3$ layer. The bands located at 251.4 cm^{-1}, due to δ(O-W-O), and at 690.8 and 817.2 cm^{-1} due to the ν(O-W-O), are the characteristic Raman modes of the h-WO$_3$. By applying a potential of 2.0 V across the device, Li ions are intercalated from ICL into the h-WO$_3$ layer. Figure 4(b)B shows the Raman spectrum of the EC device in its colored state after applying a voltage of 2.0 V. It can be seen that upon Li intercalation at this potential, the modes due to the ν(O-W-O) stretching vibrations disappear. Correspondingly, by reversing the potential (−2.0 V), the device reverts to its previous bleached state by deintercalating Li (Figure 4(b)B′), clearly demonstrating the structural reversibility of the active layer of the EC device.

A striking difference in the Raman spectra of h-Li$_x$WO$_3$ is the vanishing of bands at the applied coloration potentials of 2.0 V, although XRD pattern showed no structural transition. In order to understand the vanishing of the stretching ν(O-W-O) modes in the Raman spectra (Figure 4(b)B), while the EC active layer remains (h-Li$_x$WO$_3$) we consider the Li$^+$ occupancy for the applied potential of 2.0 V. In this scenario, Li ions inside the hexagonal windows (HW) start moving towards the four coordinated square window (SW) in order to accommodate the additional Li ions [9]. Hibino et al. have suggested that the location of Li ion near the SW is governed by the Li-Li ionic distances and the distance between the SW [24]. As there is no shielding for the Li ions and the Li-Li ionic distance is more than 5.5 Å, Li ions can only occupy alternate sites close to SW. This leads to ordering of Li ions inside the h-WO$_3$. Hibino et al. have mentioned that for Li/W ratios >0.4, the SWs of the h-WO$_3$

TABLE 1: The lattice parameters of WO$_3$ EC layer prepared at 400, 500, and 600°C and the lattice parameters after lithiating the sample at +2.0 V.

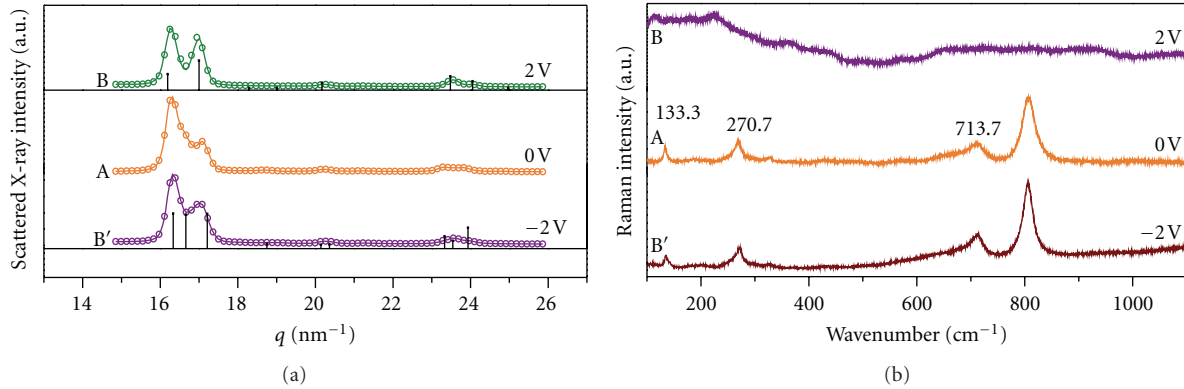| S. No.	Sample name	Coloration voltage	Lattice parameter nm			Angle
			a	b	c	β
1	400°C (Hexagonal)	0 V	0.7379 ± 0.0008	—	0.7756 ± 0.0002	—
		+2 V	0.74118 ± 0.0012		0.76152 ± 0.0003	
2	500°C (Monoclinic)	0 V	0.7351 ± 0.0002	0.7540 ± 0.0005	0.7712 ± 0.00019	90.3 ± 0.6
		+2 V	0.7397 ± 0.0015	0.7418 ± 0.002	0.7717 ± 0.0002	89.6 ± 10.1
3	600°C (Orthorhombic)	0 V	0.7351 ± 0.0019	0.7566 ± 0.0019	0.7724 ± 0.0021	90.0
		+2 V	0.7445 ± 0.0023	0.7469 ± 0.0058	0.7624 ± 0.0055	90.0

FIGURE 5: Electrochromic structural changes in the EC device constructed using m-WO$_3$ layer.

structure start to be occupied. In our case this happens when a coloration voltage of 2.0 V is applied to the EC device [24]. h-WO$_3$ is constituted by WO$_6$ octahedrons. The ab plane in WO$_6$ is already nearly symmetric. When Li is inserted into the square windows, the axial oxygen is also symmetrized, which results in isostructural WO$_6$ octahedra as in the cubic-ReO$_3$ structure. For this type of structure vibrations are not Raman active. Hence Raman modes vanish for the Li ion intercalation at a coloration potential of 2.0. A detailed account on the structural transformation of h-Li$_x$WO$_3$ is presented elsewhere [9].

3.5. Electrochromic Structural Studies during Intercalation (Deintercalation) of Li$^+$ Ions into (Ejected out of) the m-WO$_3$ Layer of the EC Device. Figure 5 shows the XRD pattern (a) and the Raman spectra (b) of the EC device constructed by using the m-WO$_3$ layer as an active working layer, in its colored and bleached states for applied potentials of 0.0 and ±2.0 V. The X-ray scattering of the Li$_x$WO$_3$ layer of the EC device based on the m-WO$_3$ layer is shown in Figure 5(a) as a function of the applied voltage. The diffraction pattern of the pure m-WO$_3$ layer, for which the JCPDS card 43–1035 diffraction pattern is represented by the vertical bars, is shown in Figure 5(a)B′. We determine the lattice constants *a, b,* and *c* and the angle β of the monoclinic phase for different sample states by fitting the diffraction patterns shown in Figure 5(a). The XRD pattern of the pure m-WO$_3$ layer has the lattice parameter $a = 0.7351 \pm 0.0002$,

$b = 0.75396 \pm 0.0005$, $c = 0.7712 \pm 0.0002$ nm, with $\beta = 90.3°$. As the coloration voltages were applied, the XRD peaks change in the position and in the intensities indicating a structural transition associated with intercalation of Li. When a coloration potential of 2.0 V is applied, the *a* and *b* lattice parameters converge to a value of 0.7412 nm, while *c* parameter is 0.77165 nm. The XRD pattern of the Li$_x$WO$_3$ after Li intercalation resembles that of the tetragonal WO$_3$ crystalline phase (JCPDS 89–1287). The phase transition from m-WO$_3$ to tetragonal Li$_x$WO$_3$ (t-Li$_x$WO$_3$) is obtained. It should be noted that, when the Li ions are deintercalated by applying reverse potential, the crystalline structure of m-WO$_3$ layer reverts back to the initial monoclinic lattice as shown in Figure 5(a)(B′). The observed variations in the lattice parameters of m-WO$_3$ EC layer upon lithiation are compared in the Table 1.

Figure 5(b) A shows the Raman spectrum of the pure m-WO$_3$ layer. The Raman peaks at 713.7 and 806.2 cm^{-1}, attributed to ν(O-W-O) modes of m-WO$_3$, were followed during the EC coloration and bleaching at ±2.0 V. Figure 5(b)B shows the Raman spectrum of the m-WO$_3$ layer, coloured at 2.0 V. The Raman modes due to ν(O-W-O) vanish completely. It has been observed from our previous work on XRD of Li$_x$WO$_3$ layer that for the applied coloration potential of 1.0 V, the lattice parameter *c* decreases from 0.77418 ± 0.0002 nm to 0.7717 ± 0.00015 nm. At the same time, the lattice parameters *a* (= 0.7397 ± 0.00145 nm) and *b* (= 0.7418 ± 0.0021 nm) converge to a same value within the
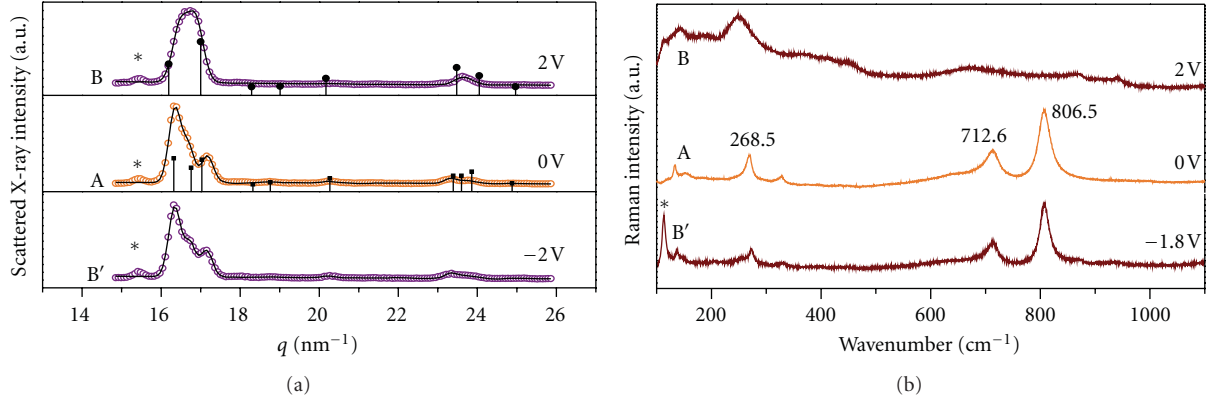
FIGURE 6: Electrochromic structural changes in the EC device constructed using o-WO$_3$ layer.

experimental error. This tendency of c to converge towards a and b indicates that the system is moving towards a cubic phase as the amount of intercalated Li is increased. The vanishing of the Raman mode is also attributed to this trend of Li$_x$WO$_3$ system to move towards cubic phase. It has been reported that the cubic Li$_x$WO$_3$ phase was obtained for $x > 0.5$ [5, 16]. In our case, Li intercalation into WO$_3$ at 2.0 V is not sufficient to reach cubic phase, whereas a higher symmetric state than that of the tetragonal phase is clearly observed. This indicates that for the applied potential of 2.0 V the amount of Li that has intercalated into m-WO$_3$ is between 0.23 and 0.5. The complete vanishing of ν(O-W-O) Raman modes observed at a coloration potential of +2.0 V is attributed to a phase transition to a higher symmetric state than that of t-Li$_x$WO$_3$. Also, it is possible that atomic displacement within the unit cell could take place with the same lattice parameters, as Raman spectroscopy is sensitive even to a small change in the lattice parameters. Figure 5(b)B′ shows the Raman spectrum of the m-WO$_3$ layer of the EC device after the deintercalation of Li at −2.0 V. The recorded Raman spectra exhibit the spectral features of the initial pure m-WO$_3$ layer (Figure 5(b)A). This demonstrates the structural EC reversibility of the system.

3.6. Electrochromic Structural Studies during Intercalation (Deintercalation) of Li$^+$ Ions into (out of) the o-WO$_3$ Layer of an EC Device.

Figure 6(a) shows the X-ray scattering of the Li$^+$ intercalated/deintercalated o-WO$_3$ layer in a working EC device for applied potentials of ±2.0 V. The differences in the positions and intensity of the diffraction lines observed in Figure 6(a) show the structural changes associated with Li ion intercalation/deintercalation. The XRD pattern of Li ion deintercalated state is similar to that of the o-WO$_3$ state at 0 V. The lattice parameters of the o-WO$_3$ layer calculated from the fitting of the XRD patterns are $a = 0.7351 \pm 0.0019$, $b = 0.7566 \pm 0.0019$, and $c = 0.7724 \pm 0.0021$ nm, with $\beta = 90°$. Upon applying a coloration potential of 2.0 V, a transition to the t-Li$_x$WO$_3$ phase is obtained. At this potential, the lattice parameters a and b attain about the same value ($a = 0.7445 \pm 0.0023$, $b = 0.7469 \pm 0.0058$ nm), whereas c is reduced to 0.7624 ± 0.0055 nm. The observed variations in the lattice parameters of titania stabilized

o-WO$_3$ EC layer, upon lithiation, are compared in the Table 1. This observed structural change is consistent with the well-established Li-induced phase transitions of low- to high-symmetric phases in ReO$_3$-type tungsten oxides [16, 17, 19]. Upon lithium intercalation, the low-symmetry phases of WO$_3$, such as triclinic and monoclinic, transform to higher symmetry structures such as tetragonal and cubic [16, 17, 19]. In this work, upon lithium ion intercalation, we have observed the phase transition from o-WO$_3$ to t-Li$_x$WO$_3$, the next higher symmetric phase. In this tetragonal phase the "ab" plane of the WO$_6$ octahedron is symmetric, a transformation induced by Li ion intercalation at 2.0 V. At this potential, the Li ion concentration is 0.226 and a complete phase transformation to the t-Li$_x$WO$_3$ is achieved. These values of Li ion concentrations for the observed phases are consistent with the values reported by other authors [16, 19]. The phase transition as a function of the applied potential occurs gradually from o-WO$_3$ to t-Li$_x$WO$_3$ with a tendency for a phase transition towards a cubic Li$_x$WO$_3$, as the concentration of the inserted Li ions increases from 0.090 to 0.226.

Figure 6(b) shows the Raman spectra of the o-WO$_3$ layer in a working EC device as a function of applied voltage. When a coloration potential of 2.0 V is applied, all the O-W-O stretching modes vanish (Figure 6(b)B), as expected for the more symmetric phases. The XRD analysis shows that the phase transition occurs gradually, and it is impossible to clearly identify the phase of the Li$_x$WO$_3$; since the lattice parameters are changing continuously as a function of applied potential or in other words, as a function of the amount of intercalated Li ions. The Raman spectrum in Figure 6(b)B shows no O-W-O stretching modes due to the fact that the structure of the o-WO$_3$ layer is gradually becoming more symmetric. In a previous work, we have shown that for higher voltages such as 3.0 V, the Li$_x$WO$_3$ attains a cubic phase when starting from the m-WO$_3$ phase and that all the Raman modes vanished [5]. Figure 6(b)B′ show that the o-WO$_3$ crystalline structure is recovered, when the coloring voltage is reversed (−2.0 V), demonstrating the reversibility of the device. The detailed report on the performance of the o-WO$_3$ layer as EC active layer is presented in our previous paper [25].
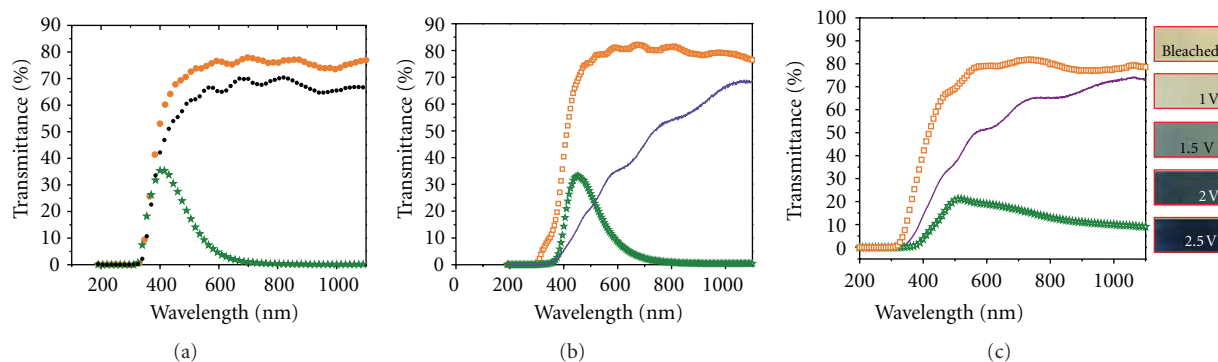
(a)   (b)   (c)

FIGURE 7: Transmission spectra of the EC devices constructed using h-WO$_3$, m-WO$_3$, and o-WO$_3$ in the as prepared state, at coloration potential of 2.5 V and at bleaching potential of -1.0 V. The photos show the visible coloration to the naked eye when the EC devices are colored at various coloration potential. The photos represent typically the EC device based on m-WO$_3$.

3.7. Optical Studies of the Electrochromic Devices Based on the h-WO$_3$, m-WO$_3$, and o-WO$_3$ Layers. The optical transmittance of the EC device constructed by using the h-WO$_3$, layer in its colored and bleached states for an applied coloration potential of 2.5 V and at bleaching potential of -1.0 V is shown in Figure 7(a). The recorded transmission spectra of the device in the bleached state for potentials at -2.5 V are indistinguishable from the spectrum of the device bleached at -1.0 V (hence not shown), clearly demonstrating the reversibility of the device. In the bleached state, the transmittance of the device at a wavelength 1100 nm was 76.9%. At +2.5 V the transmittance is reduced 0.1%. When the coloration potentials of +2.5 V are applied, the maximum transmittance is observed at 403.5 nm, and the transmittance FWHM is 147.0 nm. The optical modulation of ~76% above 800 nm obtained here is exceptionally high for EC devices [26]. Figure 7(b) shows the optical transmittance spectra of a m-WO$_3$-(prepared at 500°C) based EC device in bleached state (-1.0 V) and coloured at +2.5 V. In the bleached state, the transmittance of the device at 1100 nm was 76.4%. At the coloration potential of +2.5 V the transmittance was reduced to 0.0%. The device exhibits an optical modulation of 76.1%. Figure 7(c) shows the transmission spectra of the o-WO$_3$, based EC device in its colored and bleached states. In the bleached state the transmittance at a wavelength of 1100 nm was 78.5%. At a coloration potential of +2.5 V the corresponding transmittance is reduced to 9.1%. The actual digital photograph images of the device in the bleached and colored states for the device prepared using m-WO$_3$ (i.e, EC layer prepared at 500°C) are also presented in Figure 7. The optical modulation of about ~70% or more obtained in the EC devices constructed in this work is highly desirable for practical applications in electrochromic smart windows. Further, the transmittance of the mesomacroporous WO$_3$ layer (solid line) is lower than the bleached transmission spectrum of the device, which is attributed to the volume scattering in the film due to the microstructure [27].

4. Summary

Various mesomacroporous, crack-free, nanocristalline (NC) WO$_3$ thin films up to ~850 nm thick were prepared using tungstic acid as a precursor and ORMOSIL as a templating agent. Pure h-WO$_3$ NC films with crystallite size of ~10 nm were obtained after calcination at 400°C. Pure m-WO$_3$ films with crystallite size of ~16 nm were synthesized after annealing at 500°C. o-WO$_3$ thin films, stabilized by NC anatase TiO$_2$, are obtained by a sol-gel-based two-stage dip coating method and subsequent annealing at 600°C. Thus prepared WO$_3$ films on ITO coated glass substrate were used as the active EC layer for the construction of various asymmetric EC devices. Coloration and bleaching of the EC devices were achieved by intercalating and deintercalating Li into the WO$_3$ layers at coloration potential of 2.5 V and at bleaching potential of -1.0 V. The EC devices based on h-WO$_3$, m-WO$_3$, and o-WO$_3$ as EC active layers exhibit an exceptionally high optical modulation of 70% and qualify the device for EC smart window applications.

References

[1] E. Rossinyol, A. Prim, E. Pellicer et al., "Synthesis and characterization of chromium-doped mesoporous tungsten oxide for gas-sensing applications," *Advanced Functional Materials*, vol. 17, no. 11, pp. 1801–1806, 2007.

[2] T. He and J. Yao, "Photochromic materials based on tungsten oxide," *Journal of Materials Chemistry*, vol. 17, no. 43, pp. 4547–4557, 2007.

[3] C. G. Granqvist, "Out of a niche," *Nature Materials*, vol. 5, no. 2, pp. 89–90, 2006.

[4] S. K. Deb, "Opportunities and challenges in science and technology of WO$_3$ for electrochromic and related applications," *Solar Energy Materials and Solar Cells*, vol. 92, no. 2, pp. 245–258, 2008.

[5] C. G. Granqvist, "Electrochromic tungsten oxide films: review of progress 1993–1998," *Solar Energy Materials and Solar Cells*, vol. 60, no. 3, pp. 201–262, 2000.

[6] E. Stathatos, P. Lianos, U. Lavrencic-Stangar, and B. Orel, "A high-performance solid-state dye-sensitized photoelectrochemical cell employing a nanocomposite gel electrolyte made by the sol-gel route," *Advanced Materials*, vol. 14, no. 5, pp. 354–357, 2002.

[7] P. R. Somani and S. Radhakrishnan, "Electrochromic materials and devices: present and future," *Materials Chemistry and Physics*, vol. 77, no. 1, pp. 117–133, 2003.

[8] S. Balaji, A.-S. Albert, Y. Djaoued, and R. Brüning, "Micro-Raman spectroscopic characterization of a tunable electrochromic device for application in smart windows," *Journal of Raman Spectroscopy*, vol. 40, no. 1, pp. 92–100, 2009.

[9] S. Balaji, Y. Djaoued, A.-S. Albert, R. Z. Ferguson, and R. Brüning, "Hexagonal tungsten oxide based electrochromic devices: spectroscopic evidence for the Li ion occupancy of four-coordinated square windows," *Chemistry of Materials*, vol. 21, no. 7, pp. 1381–1389, 2009.

[10] S.-H. Baeck, K. S. Choi, T. F. Jaramillo, G. D. Stucky, and E. W. McFarland, "Enhancement of photocatalytic and electrochromic properties of electrochemically fabricated mesoporous WO_3 thin films," *Advanced Materials*, vol. 15, no. 15, pp. 1269–1273, 2003.

[11] W. Cheng, E. Baudrin, B. Dunn, and J. I. Zink, "Synthesis and electrochromic properties of mesoporous tungsten oxide," *Journal of Materials Chemistry*, vol. 11, no. 1, pp. 92–97, 2001.

[12] Y. Djaoued, P. V. Ashrit, S. Badilescu, and R. Brüning, "Synthesis and characterization of macroporous tungsten oxide films for electrochromic application," *Journal of Sol-Gel Science and Technology*, vol. 28, no. 2, pp. 235–244, 2003.

[13] C. Santato, M. Odziemkowski, M. Ulmann, and J. Augustynski, "Crystallographically oriented mesoporous WO_3 films: synthesis, characterization, and applications," *Journal of the American Chemical Society*, vol. 123, no. 43, pp. 10639–10649, 2001.

[14] Y. Djaoued, S. Priya, and S. Balaji, "Low temperature synthesis of nanocrystalline WO_3 films by sol-gel process," *Journal of Non-Crystalline Solids*, vol. 354, no. 2–9, pp. 673–679, 2008.

[15] C. G. Granqvist, *Handbook of Inorganic Electrochromic Materials*, Elsevier, New York, NY, USA, 1995.

[16] Q. Zhong, J. R. Dahn, and K. Colbow, "Lithium intercalation into WO_3 and the phase diagram of Li_xWO_3," *Physical Review B*, vol. 46, no. 4, pp. 2554–2560, 1992.

[17] A. Kuzmin, J. Purans, E. Cazzanelli, C. Vinegoni, and G. Mariotto, "X-ray diffraction, extended x-ray absorption fine structure and Raman spectroscopy studies of WO_3 powders and $(1-x)WO3-y \cdot xReO2$ mixtures," *Journal of Applied Physics*, vol. 84, no. 10, pp. 5515–5524, 1998.

[18] O. Pyper, A. Kaschner, and C. Thomsen, "In situ Raman spectroscopy of the electrochemical reduction of WO_3 thin films in various electrolytes," *Solar Energy Materials and Solar Cells*, vol. 71, no. 4, pp. 511–522, 2002.

[19] E. Cazzanelli, C. Vinegoni, G. Mariotto, A. Kuzmin, and J. Purans, "Low-temperature polymorphism in tungsten trioxide powders and its dependence on mechanical treatments," *Journal of Solid State Chemistry*, vol. 143, no. 1, pp. 24–32, 1999.

[20] T. Kudo, "A new heteropolyacid with carbon as a heteroatom in a Keggin-like structure," *Nature*, vol. 312, no. 5994, pp. 537–538, 1984.

[21] M. F. Daniel, B. Desbat, J. C. Lassegues, B. Gerand, and M. Figlarz, "Infrared and Raman study of WO_3 tungsten trioxides and WO_3, xH_2O tungsten trioxide tydrates," *Journal of Solid State Chemistry*, vol. 67, no. 2, pp. 235–247, 1987.

[22] B. Pecquenard, H. Lecacheux, J. Livage, and C. Julien, "Orthorhombic WO_3 formed via a Ti-stabilized $WO_3 \cdot 1/3H_2O$ phase," *Journal of Solid State Chemistry*, vol. 135, no. 1, pp. 159–168, 1998.

[23] *Powder Diffraction Files Inorganic and Organic (Card No: 85-2460 (Hexagonal-WO3)*, JCPDS-International Centre for Diffraction Data, PDF2 Data Base, Swarthmore, Pa, USA, 1996.

[24] M. Hibino, W. Han, and T. Kudo, "Electrochemical lithium intercalation into a hexagonal WO_3 framework and its structural change," *Solid State Ionics*, vol. 135, no. 1–4, pp. 61–69, 2000.

[25] S. Balaji, Y. Djaoued, A. S. Albert, R. Brüning, N. Beaudoin, and J. Robichaud, "Porous orthorhombic tungsten oxide thin films: synthesis, characterization, and application in electrochromic and photochromic devices," *Journal of Materials Chemistry*, vol. 21, no. 11, pp. 3940–3948, 2011.

[26] C. G. Granqvist, E. Avendaño, and A. Azens, "Electrochromic coatings and devices: survey of some recent advances," *Thin Solid Films*, vol. 442, no. 1-2, pp. 201–211, 2003.

[27] C. Amra, "From light scattering to the microstructure of thin-film multilayers," *Applied Optics*, vol. 32, no. 28, pp. 5481–5491, 1993.

Research Article

On the Origin of Light Emission in Silicon Rich Oxide Obtained by Low-Pressure Chemical Vapor Deposition

M. Aceves-Mijares,[1] A. A. González-Fernández,[2] R. López-Estopier,[3] A. Luna-López,[4] D. Berman-Mendoza,[5] A. Morales,[6] C. Falcony,[7] C. Domínguez,[2] and R. Murphy-Arteaga[1]

[1] *Department of Electronics, INAOE, 72840 Puebla, Mexico*

[2] *Department of Micro and Nanosystems, IMB-CNM (CSIC), 08193 Barcelona, Spain*

[3] *Department of Applied Physics and Electromagnetism, University of Valencia, 46100 Burjassot, Spain*

[4] *Research Center for Semiconductor Devices, Autonomous University of Puebla, 72570 Puebla, Mexico*

[5] *Departamento de Investigación en Física, Universidad de Sonora, 83000 Hermosillo, SON, Mexico*

[6] *Centro de Investigación en Materiales Avanzados S.C., Unidad Monterrey-PIIT, 66600 Apodaca, NL, Mexico*

[7] *Department of Physics, CINVESTAV-IPN, 07360 Mexico City, DF, Mexico*

Correspondence should be addressed to M. Aceves-Mijares, maceves@inaoep.mx

Silicon Rich Oxide (SRO) has been considered as a material to overcome the drawbacks of silicon to achieve optical functions. Various techniques can be used to produce it, including Low-Pressure Chemical Vapor Deposition (LPCVD). In this paper, a brief description of the studies carried out and discussions of the results obtained on electro-, cathode-, and photoluminescence properties of SRO prepared by LPCVD and annealed at 1,100°C are presented. The experimental results lead us to accept that SRO emission properties are due to oxidation state nanoagglomerates rather than to nanocrystals. The emission mechanism is similar to Donor-Acceptor decay in semiconductors, and a wide emission spectrum, from 450 to 850 nm, has been observed. The results show that emission is a function of both silicon excess in the film and excitation energy. As a result different color emissions can be obtained by selecting the suitable excitation energy.

1. Introduction

Silicon Rich Oxide (SRO) is a multiphase material composed of elemental Si, SiO_2, and SiO_x, with x between 0 and 2. DiMaria and coworkers distinguished between low and high density of elemental silicon (or silicon excess); films with low silicon excess were named "off stoichiometric oxide" [1]. Also, they did not find nanocrystals (nCs) in SRO annealed at 1,000°C with a 5-6 % silicon excess.

SRO can be obtained in different ways. However, (chemical vapor deposition) CVD and Si implantation into silicon oxide are the most common techniques. (Low-Pressure CVD) LPCVD is a simple method that easily allows varying the silicon excess [2]. In this technique, the flux ratio of reactive gases, Ro, is used to determine the silicon excess. Silane (SiH_4) and nitrous oxide (N_2O) are commonly used:

$$Ro = \frac{N_2O}{SiH_4}. \tag{1}$$

It is known that Ro = 3 produces an excess of silicon of 17%, and Ro > 100 is used to obtain stoichiometric silicon dioxide [2]. In the case of SRO fabricated by silicon implantation, silicon excess is related to the implantation dose.

SRO has been a matter of intense research due to its optical properties. SRO is totally compatible with MOS technology, and it has thus been used to overcome the limitations of silicon as an indirect material. DiMaria et al. observed emission of light by SRO for the first time [1], and researchers have been finding practical applications

for its properties ever since. Nevertheless, the number of applications is still reduced since the emission mechanisms are not completely understood. Nowadays, however, most of the authors accept that quantum effects in nanocrystals, and defects in the SiO_x matrix, are responsible for the emission of light [3].

Silicon nanocrystals have been commonly observed in high silicon excess SRO, higher than 10%. However, in LPCVD SRO, the highest light emission has been observed in films with silicon excess in the order of 5%, in which nanocrystals have not been observed [1, 4, 5]. Therefore, in low silicon excess the emission characteristics can be related to silicon, or silicon oxidation states, specifically to amorphous nanoagglomerates (Si nanopoints). Therefore, for low silicon excess SRO the dominant mechanism is not quantum confinement.

In this paper a review of our work on the different structural characteristics of SRO obtained by LPCVD is presented. Next, using experimental results of photo-, cathode-, and electroluminescence, a discussion of SRO emission mechanisms is presented. Finally, Donor-Acceptor decay is proposed to explain the emission mechanisms of the three excitation methods.

2. Experimental

All samples were obtained by LPCVD; the ratios Ro of reactive gases were 10, 20, and 30 (SRO10, SRO20, and SRO30), corresponding to approximately 12, 7, and 5% of silicon excess, respectively. A hot wall chamber was used, and the temperature was approximately 700°C. After deposition, the samples were annealed at 1,100°C in nitrogen gas for 180 minutes; however some samples underwent shorter annealing times; for these cases the annealing time will be indicated. In the following sections, references to our previous work are cited, and we suggest to the interested reader to refer to them to obtain more general details on experimental settings.

3. Results and Discussion

3.1. Silicon Excess. SRO silicon excess was measured by (X-Ray Photoelectron Spectroscopy) XPS and (Rutherford Backscattering Spectroscopy) RBS. Both techniques are used to determine the elemental composition of films. For more details on the characterization techniques, you can see, for example, [6]. With the RBS technique, Si can normally be detected up to 0.001%, whereas with XPS only to 0.1%. XPS can also be used to determine the Si oxidation states. Table 1 shows the compositional results of the SRO10, SRO20, and SRO30 samples (SRO with Ro = 10, 20, and 30, resp.). Note that only two samples were measured by RBS.

The microstructure of SRO films was studied analyzing the Si2p spectra, according to the Random Bonding Model [7]. The Si2p XPS peaks were decomposed considering the five possible oxidation states for silicon: Si, Si_2O, SiO, Si_2O_3, and SiO_2. Each oxidation state was fitted using Gaussian distributions, and the energy positions of the different peaks

were centered with those previously reported in the literature at ~99.8, 100.5, 101.5, 102.5 and 103.5 eV [8, 9]. The full widths at half maximum (FWHM) were allowed to vary within a small range [10, 11]. The relative concentration of each oxidation state was determined and is presented in Table 2 [12, 13].

Dong et al. [2], using electron microprobe analysis, determined the silicon excess in as-deposited atmospheric pressure CVD SRO films. The reactant gases were SiH_4 and N_2O, the same ones used in this study. For Ro ratios varying between 3 and 100, they found a silicon variation between 45 and 33%, respectively, which is 12 to 0 at.% Si excess. Based on the Dong results, it is accepted [4] that for APCVD and LPCVD (atmospheric and low pressure CVD, resp.) SRO films with Ro = 10, 20, and 30 correspond to silicon excesses of approximately 12, 7, and 5%.

The silicon excess results shown in Table 1 agree with those obtained by Dong. Hence, for the SRO films obtained by LPCVD with N_2O and SiH_4 as reactant gases, silicon excesses can be taken as 12, 7, and 5 at.% for Ro = 10, 20, and 30, respectively. Additionally, comparable optical and morphological properties were observed for SRO with silicon excess in a specific range. So, a high silicon excess range can be defined for Ro < 10, or silicon excess higher than 10 %. The medium silicon excess range is defined for Ro between 15 and 35, or silicon excess between 9 and 3 at.%. Finally, the low silicon excess range, for Ro > 40, or silicon excess between 2 and stoichiometric oxide, is defined. Then, the high range of silicon excess is distinguished by SRO films that show a high density of large nanocrystals, high electronic current and low light emission. On the other hand, the medium silicon excess range has a very low density, or none, of small nanocrystals and intense light emission. At the other extreme, low silicon excess SRO behaves as a stoichiometric oxide.

3.2. Nanocrystal Structure

3.2.1. X-ray Diffraction. (XRD) is mainly used to determine the crystal structure of solids, powders, and colloidal solutions. In our studies, XRD was used to determine if nanocrystals were embedded in the different SRO layers. Figure 1 shows the X-ray diffraction peaks for SRO films with different silicon excesses. For a high silicon excess, 12%, the nanocrystalline evidence is clear, whereas for a silicon excess of about 7% small peaks are still observed. However, for a silicon excess less than 6%, no crystalline evidence was observed [14].

In [15], an XRD study of films with medium to high silicon excesses obtained by (Plasma Enhanced CVD) PECVD and annealed at high temperature showed that as silicon increases, silicon nanocrystal density and size increase. However, for the smaller percentage of silicon in the film higher temperatures and longer times are needed to detect silicon crystals. This agrees well with our XRD observations, as shown in Figure 1. For SRO10, high Si excess range, the (220), and specially (111) crystalline orientations are clearly observed. As the silicon excess is reduced from SRO10 to

TABLE 1: Compositional results of SRO annealed at 1,100°C (TT) and as-deposited.

Ro	TT 1100°C	XPS Si excess at.%	XPS $x = O/Si$	RBS Si excess at.%	RBS $x = O/Si$	AFM Roughness (nm)
30	No	4.54	1.61	5	1.605	8
30	Yes	4.21	1.63	NA	NA	5
20	No	5.38	1.54	7	1.475	10
20	Yes	5.09	1.54	NA	NA	6
10	No	13.50	1.09	NA	NA	17
10	Yes	14.50	1.01	NA	NA	24

TABLE 2: Concentration of oxidation states for the SRO samples according to the random bonding model.

Oxidation state	Ro = 30	R = 20	R = 10
SiO_2%	47.35	42.89	45.86
Si_2O_3%	23.04	29.39	19.42
SiO %	19.57	18.23	13.02
Si_2O %	7.94	6.65	10.53
Elemental Si %	2.10	2.84	11.18
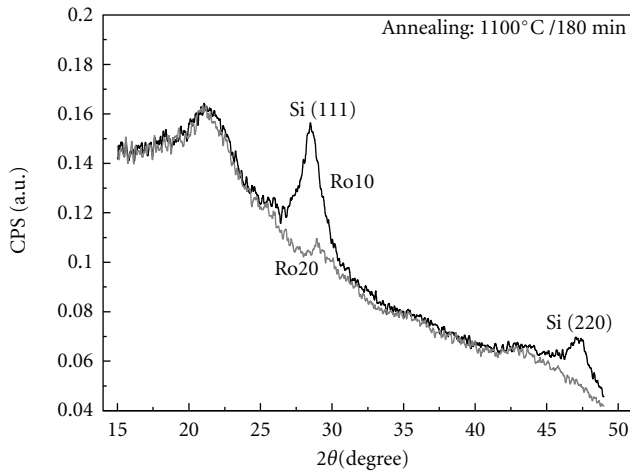
FIGURE 1: XRD results for SRO film with different silicon excesses; high silicon excess, 12%, clearly shows a crystalline phase. As the silicon excess is reduced, nano-crystal density is reduced until it disappears.

SRO20, the SiO_2 phase does not change, and the Si crystalline phase is scarcely observed. As the Si is further reduced, no evidence of any crystalline structure was detected.

3.2.2. Transmission Electron Microscopy. (TEM) observations were also performed for SRO with Ro = 10, 20, and 30, and the images were used to corroborate the presence of nano-crystals in the SRO films. At relatively low amplification, the absorption of electrons in the material is enough to produce an image. However, at higher magnifications, phase contrast is required for (high resolution TEM) HRTEM, and small non-crystalline particles are not easily observed [16].

Figure 2 shows a TEM image and a diffraction pattern of an SRO film with a silicon excess of 12%; silicon nanocrystals are clearly observed [17, 18]. The nanocrystal sizes are between 2 and 10 nm, the average size is around 5 nm, and their density is around 1.0×10^{12} cm^{-2}. However, for low silicon excesses, less than 6%, no nanocrystals were observed using high-resolution TEM. Nevertheless, using EFTEM, silicon agglomerates were observed for a 7% silicon excess, whereas for a 5% silicon excess not even these agglomerates were observed even though a silicon excess was corroborated by XPS.

Iacona et al. [19] have also done EFTEM studies on high silicon excess SRO obtained by PECVD. Their results show that after annealing a phase separation is observed, and crystals develop from amorphous homogeneous SiO_x. Similar to our results for the high Si excess films, large nanocrystals are observed after thermal annealing; in the upper limit of the medium excess range some small nanocrystal are still observed, but as the silicon excess is reduced it is not possible to detect nanocrystals at all [18].

3.2.3. Atomic Force Microscopy. (AFM) surface images of SRO films were obtained for all the samples studied; the typical roughness is shown in Table 1. Figures 3 and 4 show the AFM images and height profiles of SRO10 and SRO30. They look granular, and the grain size increases as the Ro is reduced, which indicates that the roughness should be proportional to the presence of silicon nanocrystals, as demonstrated by XRD and TEM. The roughness increases for the high Si excess films after annealing. For low silicon excesses, however, the roughness is reduced after thermal annealing [13]. This is an indication that after annealing, nanocrystals grow in high silicon excesses, while in the medium excess range formation of Si–O compounds takes place.

3.3. Molecular Analysis

3.3.1. Fourier Transform Infrared Spectroscopy. (FTIR) gives information of the molecular absorption; therefore it allows the study of the fundamental vibrations and associated rotational-vibrational structure. SRO films show characteristic infrared absorption peaks associated with the Si–O–Si bonds in SiO_2 [12, 20, 21]. The FTIR absorbance spectra of SRO samples are pictured in Figure 5 and were identified as (1) Si–O rocking at ~450 cm^{-1}, (2) Si–O bending at
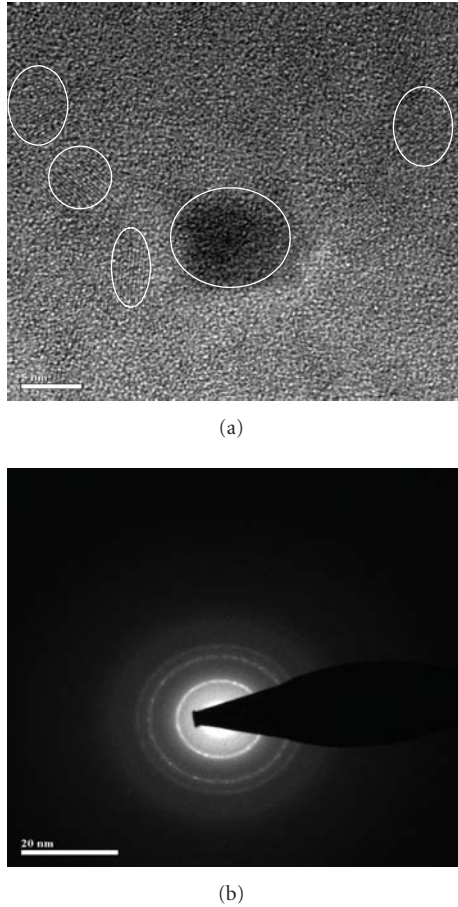
(a)

(b)

Figure 2: TEM images (a) and diffraction pattern (b) of a selected area of the annealed SRO film with a 12% silicon excess. Silicon nanocrystals are clearly observed.

~808 cm^{-1}, (5) Si–O symmetric stretching vibration from 1055 to 1082 cm^{-1} and (7) Si–O asymmetric stretching at ~1170 cm^{-1}. In addition, (3) Si–H bending at ~883 cm^{-1}, (4) Si–N stretching at ~984 cm^{-1}, and (7) Si–H stretching at ~2258 cm^{-1} bonds were also found in SRO samples [22, 23]. The inset in Figure 5 shows Si–N and Si–H bonding before and after annealing.

The as-deposited samples exhibit a characteristic IR absorption due to the stretching vibration of the Si–O–Si bonds around 1060–1055 cm^{-1}; the absorbance and frequency of stretching vibration peaks decrease as Ro decreases. Figure 6 shows the behavior of the Si–O stretching peak frequency for samples with different silicon excesses. The frequency is lower than that for an SiO$_2$ film (1080 cm^{-1}) and that of an amorphous a-SiO$_2$ film (1074 cm^{-1}) because Si atoms replace O atoms [21]. This result is related to the off-stoichiometry of SRO, which causes a decrease in the stretching frequency of Si–O as the x in SiO$_x$ decreases (silicon excess increases). For all samples, the stretching frequency increases after annealing for all silicon excesses, as also shown in Figure 6. This result suggests a phase separation during the thermal annealing and an increase of oxidized compounds from the oxide phase.
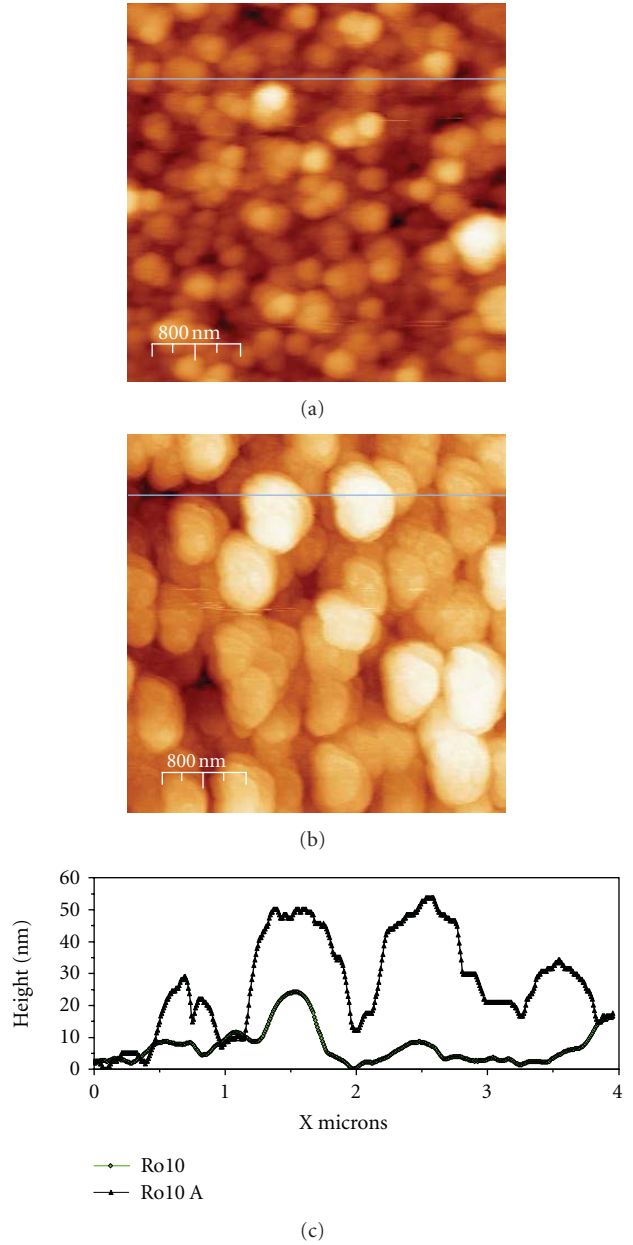

(a)

(b)

(c)

Figure 3: AFM images of SRO10 (a) as-deposited and (b) after annealing at 1,100°C for 180 minutes (Ro10 A), and (c) comparison of profiles along the lines in the images.

It has been reported that SRO films deposited with a mixture of N$_2$O and SiH$_4$ display absorption bands associated with Si–H (660, 880, and 2250 cm^{-1}), Si–N (870–1030 cm^{-1}), Si–OH (940, 3660 cm^{-1}), and N–H (1150, 1180, and 3380 cm^{-1}) in addition to the three characteristic bands related to the Si–O–Si bonding arrangement [21, 24]. The presence of some nitrogen and hydrogen characteristic peaks has been also observed in the IR spectra of our films. Si–H bending and stretching were observed only in as-deposited samples; these peaks disappear after annealing due to the high-temperature treatment. Si–N stretching was also found in both as-deposited and annealed samples.
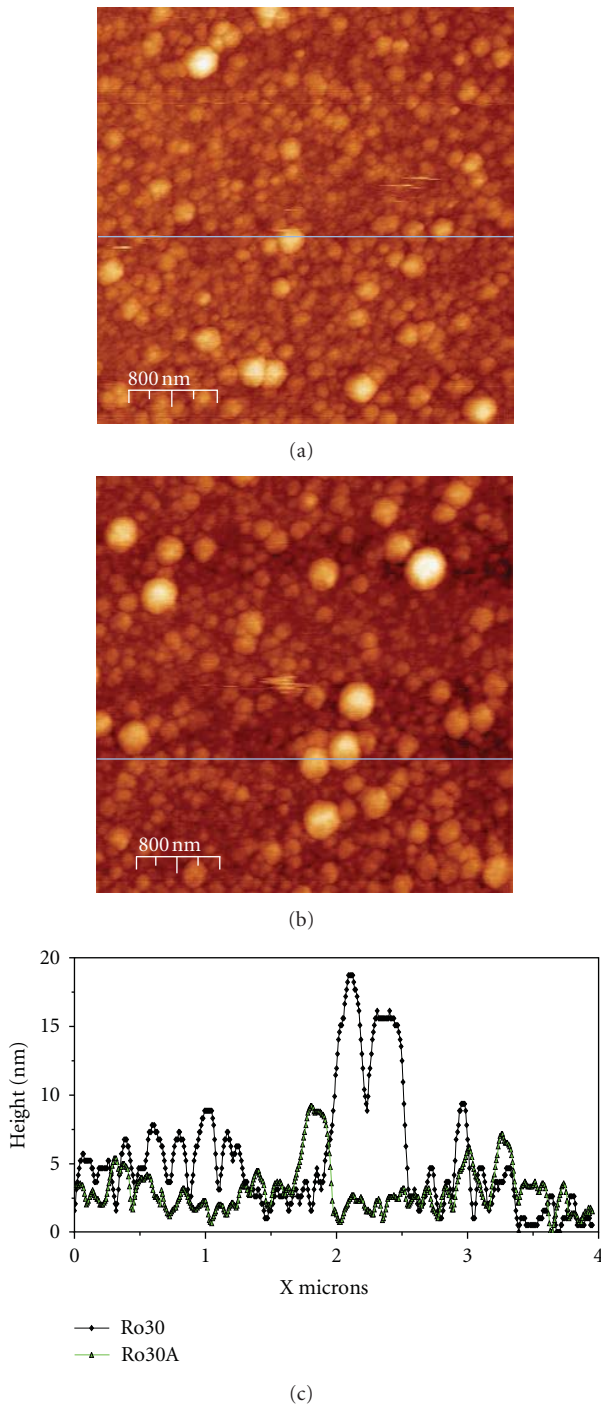
FIGURE 4: AFM images of SRO30 (a) as-deposited and (b) after annealing (Ro30 A) at 1,100°C for 180 minutes, and (c) comparison of profiles along the lines in the images.
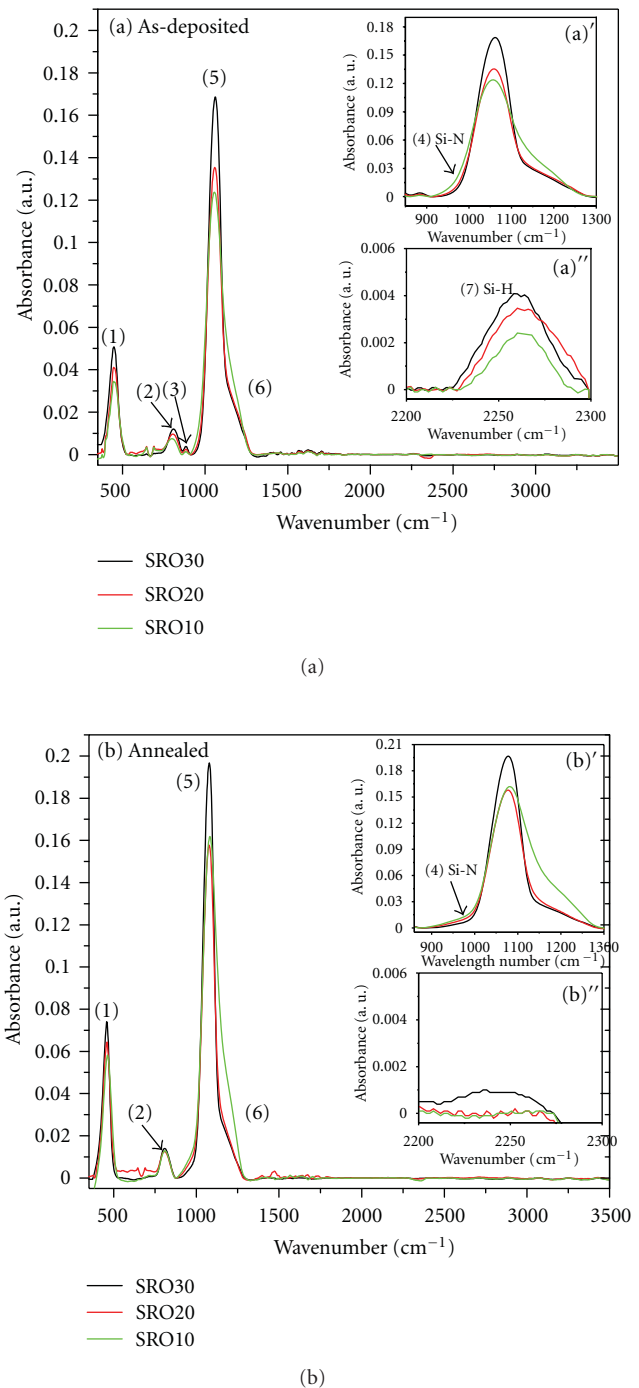

FIGURE 5: FTIR absorption spectra of SRO films (a) before and (b) after thermal annealing. The inset shows Si–N and Si–H bonding in the 850–1300 cm^{-1} and 2200–2300 cm^{-1} ranges, respectively.

Having analyzed the LPCVD-SRO in the three ranges of silicon excess, there is enough evidence to suppose that annealing at 1,100°C produces a phase separation of elemental silicon, SiO_x, and SiO_2. Depending on the silicon excess, the amount of each phase increases notoriously, as can be seen in Table 2. It is clear that in the high range the quantity of elemental silicon is the highest, 11% for SRO10

and only 2% for SRO30. However, SiO_x is as high as 54% for medium silicon excesses and only 40% for SRO10. The percentage of SiO_2 is similar for the high and medium ranges.

It is clear then that two competitive morphological mechanisms take place during annealing; one is the formation of silicon agglomerates, and the other is the formation of silicon and oxygen compounds. If silicon excess is high enough, the
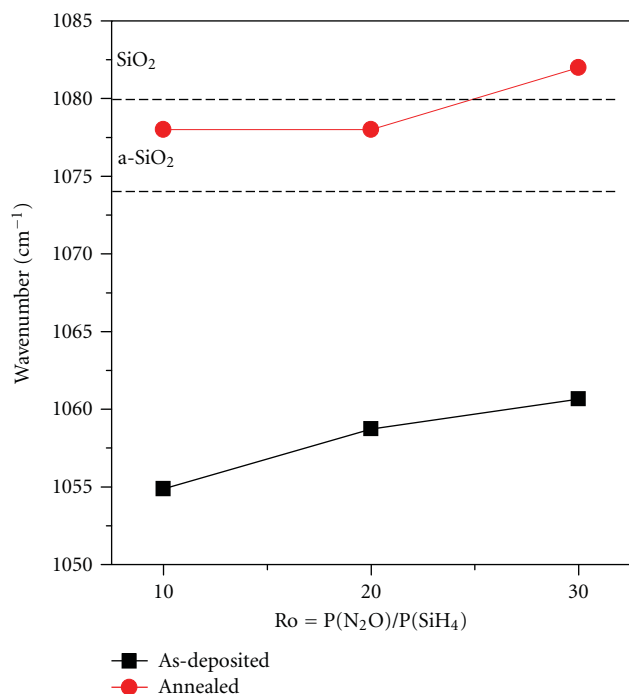
FIGURE 6: Si–O stretching frequency positions for different Ro, for SRO films before and after annealing at 1,100°C for 180 minutes.

silicon agglomerates will morph into nanocrystals. As Si is decreased, however, silicon oxidation states will dominate due to the larger separation between elemental silicon. As silicon excess increases, the SRO will tend towards a polysilicon layer; conversely, as silicon is reduced, the SRO film will move towards a stoichiometric SiO_2. In between these extremes, agglomeration of silicon shifts towards the agglomeration of Si-oxygen compounds as the silicon excess moves from high to low silicon excesses.

3.4. Luminescence.

The low-temperature emission of light from electronically or vibrational excited species is known as luminescence [25]. Depending on the excitation, it receives different names; for instance, when the excitation energy is due to photons, the emission mechanism is called photoluminescence. When emission is produced by an electric current passing through the sample, Electroluminescence, EL, is obtained. Cathode-luminescence, CL, is produced when an electron beam is accelerated and implanted into the sample. Thermoluminescence, TL, arises when electrons trapped in a sample are released by heat and then recombine emitting light [26]. SRO obtained by LPCVD and annealed at 1,100°C has shown PL, CL, EL, and TL [27].

Luminescence from samples can deliver significant information regarding the structure of a material; in the case of SRO, luminescence studies are particularly important, given the fact that these films are specifically seen as a light-emitting material. As mentioned previously, the first ones to observe luminescence in LPCVD SRO were DiMaria et al., but since then, Canham observed PL from porous silicon in 1990. The photoemissive properties of this material, along

with those of others based in nanostructurated Si such as SRO, have been extensively studied since. Despite these efforts, no clear consensus has been reached regarding the origin of luminescence, but recently, it has been generally accepted that it is due to a combination of quantum phenomena and defect-related emission [1, 28–30]. Electro- and cathode-luminescence studies are more complex than PL, because carriers are injected to the material; therefore luminescence can be either due to relaxation of higher-energy carriers through radiative centers or due to the recombination of excitons formed by impact ionization by the injected carriers [31, 32].

3.4.1. Photoluminescence (PL). spectra are obtained stimulating the samples with light in order to transfer energy to carriers that will later relax and radiatively recombine. The simple model proposes that recombination centers are distributed in the photoluminescent material, and these centers increase the probability of radiative recombination. The energetic distribution of such centers can be extracted when analyzing the emission spectra. The stimulation energy can also be varied in order to identify the absorption centers.

In this report, photoluminescence (PL) emission spectra were obtained pumping the samples with UV radiation with a wavelength of between 250 and 360 nanometers, measured between 400 and 900 nm. Absorption (or excitation) spectra were also obtained, stimulating the samples with light ranging from 200 to 400 nm and detecting the emission at a given wavelength. Figure 7 shows the emission spectra and Figure 8 shows the absorption spectra with the detector at 750 nm for SRO10, 20, and 30. Neither aged samples nor samples deposited at different times produce significant emission variations. In the as-deposited samples, there is practically no emission; only the SRO30 samples indicate a small emission in the range of 450 nm. Therefore, the discussion will be centered on the samples annealed at 1,100°C for 180 minutes, and the small peak at 450 nm will be discussed later.

The highest emission is obtained from SRO30 samples; as demonstrated in the morphological details, these samples do not show evidence of nanocrystals, and rather they contain Si–O compounds. Hence, the emission can be attributed to the oxidation states or defects. It is possible that during annealing, the defects agglomerate forming emission centers; for example, emissions at 460 nm, 520 nm, and 650 nm have been related to oxygen deficiency-related centers (ODCs) or oxygen vacancies [12, 33]. Besides, it has also been demonstrated that the electronic characteristics in SRO are due to traps [34, 35]. Then, in the medium range of silicon excess, the photoexcited electrons will jump to the traps leaving a positive mirror charge behind, and the Coulombic attraction promotes the decay of electrons producing emission. Naturally, there should be an optimum silicon excess density that produces the maximum emission, and according to our studies, this is around 5% silicon atomic excess. On the other hand, as the silicon excess increases, more nanocrystals grow, and less traps are obtained. As a result, the emission is reduced and the conductivity increases. In the high excess Si range the conduction is by tunneling through nanocrystals
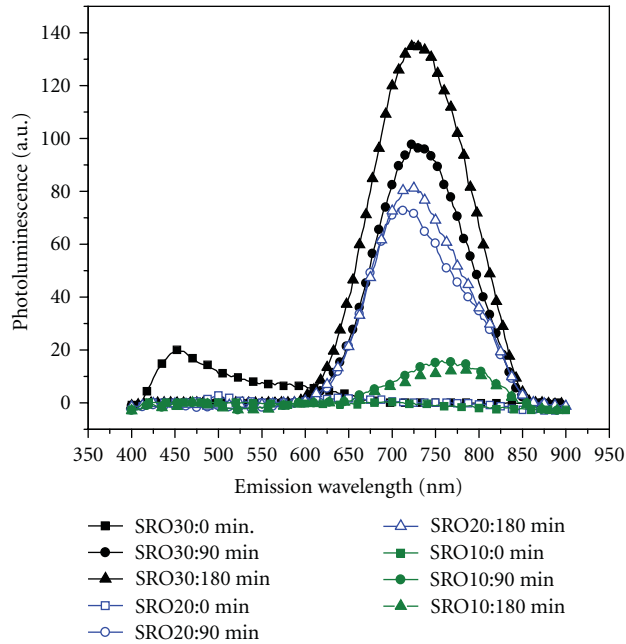
FIGURE 7: Photoluminescence for SRO10, 20, and 30 before and after annealing at 1,100°C for the time shown in the legend, for an excitation wavelength of 270 nm. No significant peak shifts are observed with time or with silicon excess.

FIGURE 8: Excitation wavelength with the detector centered at 750 nm for SRO10, 20, and 30 annealed at 1,100°C for 180 minutes.

[36]. In the nanocrystals the electrons will move in the conduction band, or they will nonradiatively recombine. Consequently, in the high range of silicon excess, most of the excited electrons will move, or decay without radiating, through the abundant nanocrystals, and only a few of them will find the rather scarce traps. Consequently, low emission is expected. In [37] the authors also propose that even for very small Si crystallites the bandgap remains indirect.

Figure 8 displays the wide excitation spectra for SRO10, 20, and 30. It does not exhibit the expected absorption peaks and the blue shift of an excitonic absorption. The observation of nonexcitonic absorption spectra for Si nanocrystals has been also reported by other authors [38].

Furthermore, from Figure 7 it is clear that as the Ro varies from 10 to 30, the SRO emission bands do not shift significantly to higher energies, as the size of the nanocrystals is reduced, notwithstanding the considerable size variation of the Si nanoagglomerates, crystalline, or not. However, in reports where emission is attributed to Si nanocrystals, wavelength shifts of hundreds of nanometers for smaller differences in the nanocrystal size have been experimentally corroborated [37, 39]. Additionally, a shift toward the blue side of the spectrum caused by different excitation energies has been reported. For example, in the study of nanocrystal PL emission in colloidal suspensions, green emission that shifts toward higher energies was observed when the incident photon energy was increased [40], but the authors mention that the Wolking model cannot be used to explain their results [41]. Wolking proposes that, in the emission of porous silicon, carriers are trapped in silicon oxide bonds, which
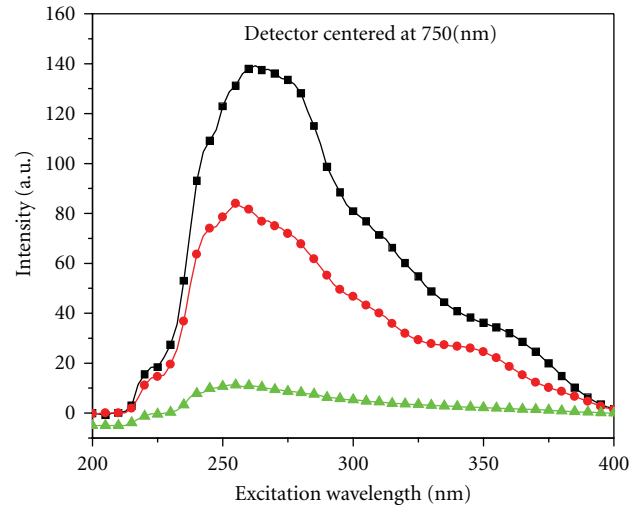
explains the 2.1 eV limit energy in nanocrystals smaller than 3 nm.

3.4.2. Electroluminescence (EL). increases the energy of emission since electrons are injected into the conduction band and holes into the valence band, allowing band edge emissions. Therefore, electro-luminescence can be due to relaxation of higher-energy carriers through radiative centers [42].

Electro-luminescence was tested in devices having a MOS-like structure, using polysilicon as the gate electrode (Light-Emitting Capacitor, LEC). Polysilicon is transparent enough in the emission range of SRO [43]. EL in SRO obtained by LPCVD and annealed at 1,100°C requires a high applied electric field and high currents, and thus these devices work close to the electrical damage point. Only devices that show high photoemission show electroemission; therefore, only devices with a medium silicon excess are suitable for EL. Figure 9 shows the EL emission spectrum of a capacitor with SRO30 as a function of applied voltage. Two peaks are very well defined; one centered at around 450 nm (blue emission), and the other around 700 nm (red emission). The peak intensity varies with the applied voltage; one shows a higher increment than the other, and a slight shift toward higher energies is observed. The spectrum of the one around 700 nm is similar to the one obtained with PL.

Figure 10 shows the percentage of intensity of each peak to the total emission. Total emission was obtained simply by adding the peak intensity of the red and blue peaks in arbitrary units. From the figure it is clear that the percentage of red emission is reduced as the electric field increases, and the percentage of blue emission increases with voltage. That is, as the applied energy increases, the part of the emission corresponding to the blue range is practically the
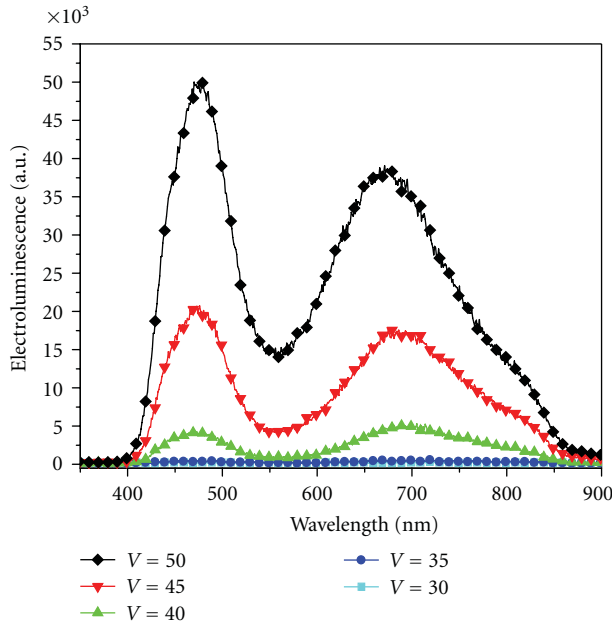
FIGURE 9: Electroluminescence versus wavelength as a function of applied voltage of a MOS-like structure with SRO30 and polysilicon as the gate electrode. As can be seen, two emission ranges are well defined. The intensity peaks vary with the applied voltage (V).
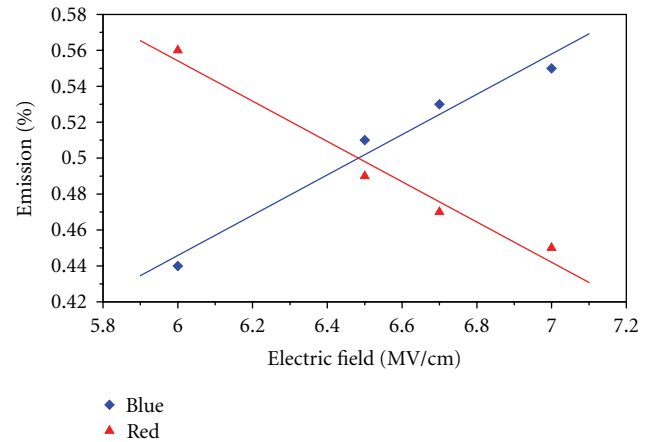

FIGURE 10: Percent of the total intensity emission of the blue and red peaks of Figure 9; the red emission tends towards 0 as the electric field increases and the blue emission tends to be the only one at high electric fields. The total emission was obtained adding the two peak intensities in Figure 9.

total emission (100%), and the red part is reduced towards 0%. This is corroborated when a very high energy is used, for example, in cathode-luminescence. The systematic variation of the spectra with energy indicates that the double emission is not due to the presence of singlets and triplets.

When electrons are injected into the SRO in the LEC, the charge is distributed among the cluster of defects, or Si–O compounds, which act as shallow and deep traps that behave as emission centers of low and high energy (red and blue), respectively. As it is known, the mobility of electrons in the SRO is very high compared with that of holes; it is then likely that the emission is due to electrons decaying into positive traps. The emission mechanism of an LEC is quite similar to that observed in organic light emitting diodes which also have a high distribution of traps [44].

In the medium silicon excess range especially, when electrons are injected from one electrode into the SRO by an electrical potential difference, they move through the film to the other electrode, and, as known [35], a fraction of them will be trapped. As the current increases, trapped electrons will block the conduction paths. Trapped electrons accumulate and consequently decay towards empty positive traps, in a similar fashion as the donor-acceptor pair decays in semiconductors [45]. The higher the applied voltage, the higher the energy driving the electrons is, and then the deep traps are reached, and more energetic photons are emitted.

From the morphological point of view in the medium Si excess films, the agglomerates of defects are constituted by compounds, which require different, higher or lower, energy to be excited. Then, at low electric fields, or using UV radiation, most of electrons will be trapped at lower energies,

producing emission mainly in the red side of the spectrum, as shown in Figure 9. As the applied energy is increased, more energetic compounds will be excited, or electrons are trapped in more energetic states, and when they relax, the blue emission becomes dominant.

Clearly, to obtain electroluminescence in LECs made of SRO obtained by LPCVD and annealed at 1,100°C three conditions have to be met: the density of Si–O compounds has to be high, the energy applied to the LEC has to be high enough to reach the different energetic states, and there must be a high injection of carriers from one electrode to produce agglomeration of electrons in the conduction trajectories in the film.

Cathode-Luminescence. (CL) is obtained when light is produced using a beam of high-energy electrons. CL is a technique that normally leads to emission by all of the mechanisms present in the material, and then CL, PL, and EL can be compared to complement the information in order to have more details of the emission properties of luminescent materials [46].

Cathode-luminescence spectra were obtained under different bombardment conditions. Figures 11 and 12 show the cathode-luminescence spectra of SRO10, 20, and 30 before and after annealing at 1,100°C for 180 minutes. As can be observed, the CL spectra of the as-deposited samples are similar to those of PL, and only emission at around 450 nm is observed for SRO30 films. From CL and PL results it can be inferred that no other but blue emission centers are present in the as-deposited samples. Because there are not any more centers, no competition takes place, and even when UV radiation impinges on the samples, blue emission is obtained. When the silicon excess shifts towards higher-density ranges, the amount of blue centers is reduced and emission is quenched.
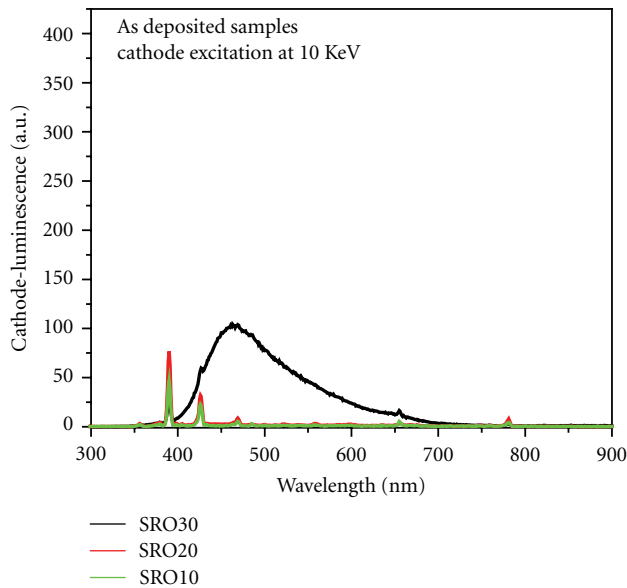
FIGURE 11: Cathode-luminescence spectrum for SRO10, 20, and 30 as-deposited films.

FIGURE 12: Cathode-luminescence for SRO10, 20, and 30 after annealing at 1,100°C for 180 minutes.

On the other hand, after annealing, more blue and red centers are produced, and emission in the red side increases. For PL of SRO30 and 20 the photoelectrons will only reach red centers, and red emission becomes dominant. However, more energetic cathode-electrons will reach both blue and red centers, causing emission of both colors, with blue dominating.

As already mentioned, the annealing produces a phase separation that agglomerates Si–O compounds and its density increases until an optimum is reached, corresponding to the medium density silicon excess films. This is particularly clear in Figure 12; in SRO10 low CL emission in red and blue is obtained, showing a slightly higher peak in the red side than in the blue, which means that red and blue density centers are comparable. As Ro increases towards SRO20, the emission in the blue side clearly shows a higher increase than red emission, indicating that the quantity of blue centers was increased at a higher rate than the red centers. Since the density of blue centers is not very high, the cathode electrons are shared between both the blue and red centers, producing both emissions. When SRO30 was excited with high-energy electrons, the blue emission became completely dominant. As a consequence of the higher density of blue centers that appears after annealing, the blue centers collect more of the high-energy electrons and only a few reach to the red centers.

Since different equipment and arbitrary units are used, it is not possible to compare the CL and PL emissions directly, but this could be a method to determine the density of emission centers. On the other hand, due to the fact that no UV emission was observed in CL, in spite of the very high energy used, it is evident that no UV centers are produced in the SRO films.

Figure 13 compares the most representative PL, CL, and EL normalized spectra. A blue shift clearly occurs as the excitation energy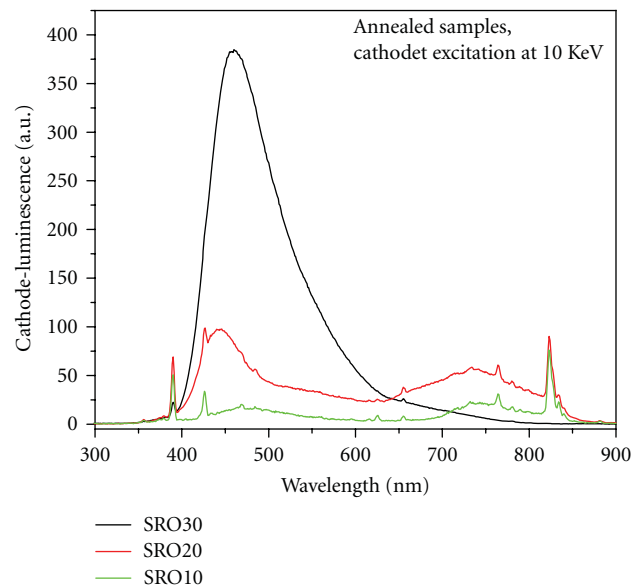 increases, and emission centers of a wide color spectra (from 450 to 850 nm) are observed in the SRO films obtained by LPCVD and annealed at 1,100°C. Therefore, 450 to 850 nm emission centers evolve with the annealing. As implied in Figure 12, for SRO30, the density of blue centers is the highest. Then, as can be observed from CL, PL, and EL, the as-deposited SRO30 film already presents blue emission centers, and after annealing many other centers evolve specially in the medium Si excess range; that is, the density of blue centers increases, followed by the density of red centers. However, the density of green centers of around 550 nm is the smallest one.

From Figure 13, it is also clear that when the energy increases, high-energy emission centers are reached; however the density of such centers limits the emission. Then, CL for SRO30 emits basically in the blue region because the blue center density is the highest. As the silicon excess increases, the density of blue centers is reduced and blue and red emissions compete, as in the case of CL in SRO20. Correspondingly for EL, red and blue emissions compete as a function of applied energy. At low voltages, low peaks of similar intensity of both colors are observed; however when the voltage is increased, a clear blue shift is observed and the blue emission increases more than the red one. PL, on the other hand, is pumped with relatively low-energy photons, producing low-energy photoelectrons that cannot reach the high-energy blue centers, and emitting only in the red part of the spectrum. Then, blue-to-red emission of different intensities can be observed for the medium silicon excess range.

In the high-density range, as for the SRO10 films, the emission centers barely develop. Consequently, for this range almost no emission is observed. Therefore, the light emission in SRO annealed at 1,100°C will be a function of the excitation energy and silicon excess. Therefore, a specific color emission can be selected as a function of the applied voltage exploiting EL.
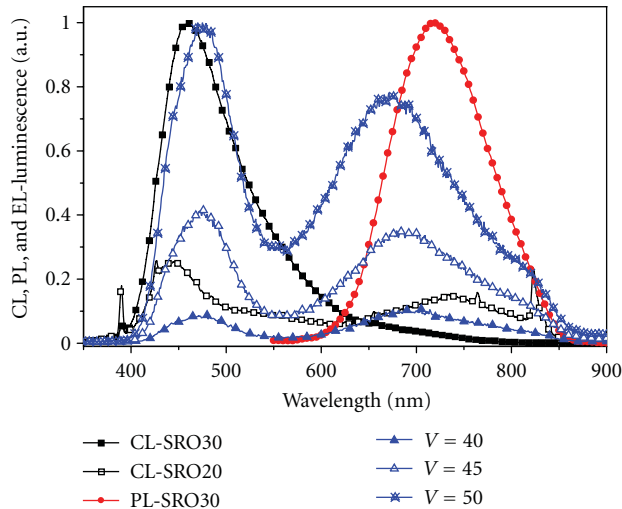
FIGURE 13: Normalized electro-, cathode- and photoluminescence of SRO with more representative silicon excesses. CL is shown for SRO20 and 30, PL and EL is shown for SRO30, and EL is shown for three different voltages.

4. Conclusions

Structural and emission properties of SRO films, of high and medium silicon excess density, obtained by LPCVD and annealed at 1,100°C were studied. Three ranges of silicon excess were defined, in which the SRO shows similar characteristics. After annealing, the high-density range is characterized by the agglomeration and crystallization of elemental silicon, so its characteristics are dominated by nanocrystals, with more conductive paths and lower light emission. Medium Si density is characterized by a high number of Si–O compounds that act as emission centers, and then light emission is easily stimulated. Additionally, the SRO emission spectrum is wide, in the range from 450 to 850 nm. The emission depends on excitation energy and on the density of Si compounds (or silicon excess). The highest emission was obtained for SRO with a silicon excess around 5 at.%. The excitation with low-energy UV radiation only produces photoemission in the red side of the spectrum; when the energy is increased by an electric field (electroluminescence) or a beam of high-energy electrons (cathodeluminescence), emission in the whole range is presented. As the excitation energy increases, the emission shifts towards the blue side of the spectrum. Then, the emission wavelength can be selected as a function of applied energy, but presenting a minimum around 550 nm.

Acknowledgments

References

[1] D. J. DiMaria, D. W. Dong, C. Falcony et al., "Charge transport and trapping phenomena in off-stoichiometric silicon dioxide films," *Journal of Applied Physics*, vol. 54, no. 10, pp. 5801–5827, 1983.

[2] D. Dong, E. A. Irene, and D. R. Young, "Preparation and some properties of chemically vapor-deposited Si-rich SiO and SigN, films," *Journal of the Electrochemical Society*, vol. 125, no. 5, pp. 819–823, 1978.

[3] X. X. Wang, J. G. Zhang, L. Ding et al., "Origin and evolution of photoluminescence from Si nanocrystals embedded in a SiO₂ matrix," *Physical Review B*, vol. 72, no. 19, Article ID 195313, 6 pages, 2005.

[4] D. J. DiMaria, J. R. Kirtley, E. J. Pakulis et al., "Electroluminescence studies in silicon dioxide films containing tiny silicon islands," *Journal of Applied Physics*, vol. 56, no. 2, pp. 401–416, 1984.

[5] A. Morales, J. Barreto, C. Domínguez, M. Riera, M. Aceves, and J. Carrillo, "Comparative study between silicon-rich oxide films obtained by LPCVD and PECVD," *Physica E*, vol. 38, no. 1-2, pp. 54–58, 2007.

[6] C. P. Poole Jr. and F. J. Owens, *Introduction to Nanotechnology*, Wiley-Interscience, New York, NY, USA, 2003.

[7] H. R. Philipp, "Optical and bonding model for non-crystalline SiOₓ and SiOₓNᵧ materials," *Journal of Non-Crystalline Solids*, vol. 8–10, no. C, pp. 627–632, 1972.

[8] R. Alfonsetti, L. Lozzi, M. Passacantando, P. Picozzi, and S. Santucci, "XPS studies on SiOx thin films," *Applied Surface Science*, vol. 70-71, no. 1, pp. 222–225, 1993.

[9] D. Q. Yang, J. N. Gillet, M. Meunier, and E. Sacher, "Room temperature oxidation kinetics of Si nanoparticles in air, determined by x-ray photoelectron spectroscopy," *Journal of Applied Physics*, vol. 97, no. 2, Article ID 024303, 6 pages, 2005.

[10] E. Dehan, P. Temple-Boyer, R. Henda, J. J. Pedroviejo, and E. Scheid, "Optical and structural properties of SiOₓ and SiNₓ materials," *Thin Solid Films*, vol. 266, no. 1, pp. 14–19, 1995.

[11] Y. Liu, T. P. Chen, Y. Q. Fu et al., "A study on Si nanocrystal formation in Si-implanted SiO₂ films by x-ray photoelectron spectroscopy," *Journal of Physics D*, vol. 36, no. 19, pp. L97–L100, 2003.

[12] R. López-Estopier, M. Aceves-Mijares, and C. Falcony, "Cathodo- and photo- luminescence of silicon rich oxide films obtained by LPCVD," in *Cathodoluminescence*, N. Yamamoto, Ed., p. 324, InTech, 2012.

[13] J. A. Luna-López, M. Aceves-Mijares, O. Malik et al., "Compositional and structural characterization of silicon nanoparticles embedded in silicon rich oxide," *Revista Mexicana de Fisica*, vol. 53, no. 7, pp. 293–298, 2007.

[14] Z. Yu, M. Aceves-Mijares, and M. A. I. Cabrera, "Single electron charging and transport in silicon rich oxide," *Nanotechnology*, vol. 17, no. 15, article 059, pp. 3962–3967, 2006.

[15] D. Comedi, O. H. Y. Zalloum, E. A. Irving et al., "X-ray-diffraction study of crystalline Si nanocluster formation in annealed silicon-rich silicon oxides," *Journal of Applied Physics*, vol. 99, no. 2, Article ID 023518, 8 pages, 2006.

[16] X. Zhu, J. Zhu, A. Li, Z. Liu, and N. Ming, "Challenges in atomic-scale characterization of high-k dielectrics and metal gate electrodes for advanced CMOS gate stacks," *Journal of Materials Science and Technology*, vol. 25, no. 3, pp. 289–313, 2009.

[17] Z. Yu, M. Aceves, J. Carrillo, and R. López-Estopier, "Charge trapping and carrier transport mechanism in silicon-rich

silicon oxynitride," *Thin Solid Films*, vol. 515, no. 4, pp. 2366–2372, 2006.

[18] A. Morales-Sánchez, J. Barreto, C. Domínguez-Horna, M. Aceves-Mijares, and J. A. Luna-López, "Optical characterization of silicon rich oxide films," *Sensors and Actuators, A*, vol. 142, no. 1, pp. 12–18, 2008.

[19] F. Iacona, C. Bongiorno, C. Spinella, S. Boninelli, and F. Priolo, "Formation and evolution of luminescent Si nanoclusters produced by thermal annealing of SiOx films," *Journal of Applied Physics*, vol. 95, no. 7, pp. 3723–3732, 2004.

[20] F. Ay and A. Aydinli, "Comparative investigation of hydrogen bonding in silicon based PECVD grown dielectrics for optical waveguides," *Optical Materials*, vol. 26, no. 1, pp. 33–46, 2004.

[21] P. G. Pai, S. S. Chao, Y. Takagi, and G. Lucovsky, "Infrared spectroscopic study of SiOx films produced by plasma enhanced chemical vapor deposition," *Journal of Vacuum Science & Technology A*, vol. 4, no. 3, pp. 689–694, 1986.

[22] N. Daldosso, G. Das, S. Larcheri et al., "Silicon nanocrystal formation in annealed silicon-rich silicon oxide films prepared by plasma enhanced chemical vapor deposition," *Journal of Applied Physics*, vol. 101, no. 11, Article ID 113510, 7 pages, 2007.

[23] F. Iacona, G. Franzò, and C. Spinella, "Correlation between luminescence and structural properties of Si nanocrystals," *Journal of Applied Physics*, vol. 87, no. 3, pp. 1295–1303, 2000.

[24] E. Fazio, E. Barletta, F. Barreca, F. Neri, and S. Trusso, "Investigation of a nanocrystalline silicon phase embedded in SiO_x xthin films grown by pulsed laser deposition," *Journal of Vacuum Science and Technology B*, vol. 23, no. 2, pp. 519–524, 2005.

[25] B. Valeur and M. N. Berberan-Santos, "A brief history of fluorescence and phosphorescence before the emergence of quantum theory," *Journal of Chemical Education*, vol. 88, no. 6, pp. 731–738, 2011.

[26] N. Meriç, M. A. Atlihan, M. Koşal, Ü. R. Yüce, and A. Cinaroglu, "Infrared stimulated luminescence and thermoluminescence dating of archaeological samples from Turkey," *Geochronometria*, vol. 34, no. 1, pp. 25–31, 2009.

[27] T. M. Piters, M. Aceves-Mijares, D. Berman-Mendoza, L. R. Berriel-Valdos, and J. A. Luna-López, "Dose dependent shift of the TL glow peak in a silicon rich oxide (SRO) film," *Revista Mexicana De Física S*, vol. 57, no. 2, pp. 26–29, 2011.

[28] L. T. Canham, "Silicon quantum wire array fabrication by electrochemical and chemical dissolution of wafers," *Applied Physics Letters*, vol. 57, no. 10, pp. 1046–1048, 1990.

[29] M. Ray, S. M. Hossain, R. F. Klie, K. Banerjee, and S. Ghosh, "Free standing luminescent silicon quantum dots: evidence of quantum confinement and defect related transitions," *Nanotechnology*, vol. 21, no. 50, Article ID 505602, 2010.

[30] M. N. Islam and S. Kumar, "Influence of surface states on the photoluminescence from silicon nanostructures," *Journal of Applied Physics*, vol. 93, no. 3, pp. 1753–1759, 2003.

[31] G. Franzò, A. Irrera, E. C. Moreira et al., "Electroluminescence of silicon nanocrystals in MOS structures," *Applied Physics A*, vol. 74, no. 1, pp. 1–5, 2002.

[32] A. Irrera, D. Pacifici, M. Miritello et al., "Excitation and de-excitation properties of silicon quantum dots under electrical pumping," *Applied Physics Letters*, vol. 81, no. 10, pp. 1866–1868, 2002.

[33] M. Cervera, M. J. Hernández, P. Rodríguez et al., "Blue-cathodoluminescent layers synthesis by high-dose N^+, C^+ and B^+ SiO_2 implantation," *Journal of Luminescence*, vol. 117, no. 1, pp. 95–100, 2006.

[34] A. Kalnitsky, J. P. Ellul, E. H. Poindexter, P. J. Caplan, R. A. Lux, and A. R. Boothroyd, "Rechargeable E' centers in silicon-implanted SiO_2 films," *Journal of Applied Physics*, vol. 67, no. 12, pp. 7359–7367, 1990.

[35] M. Aceves, C. Falcony, A. Reynoso-Hernandez, W. Calleja, and A. Torres, "The conduction properties of the silicon/off-stoichiometry-SiO_2 diode," *Solid-State Electronics*, vol. 39, no. 5, pp. 637–644, 1996.

[36] Z. Yu, M. Aceves, F. Wang, J. Carrillo, R. Kiebach, and K. Monfil, "Room temperature quantum tunneling and Coulomb blockade in silicon-rich oxide," *Physica E*, vol. 41, no. 2, pp. 264–268, 2008.

[37] J. Heitmann, F. Müller, M. Zacharias, and U. Gösele, "Silicon nanocrystals: size matters," *Advanced Materials*, vol. 17, no. 7, pp. 795–803, 2005.

[38] J. Zhong Zhang, *Optical Properties and Spectroscopy of Nanomaterials*, chapter 5, Scientific, Norwood, NJ, USA, 2009.

[39] M. H. Nayfeh, S. Rao, O. M. Nayfeh, A. Smith, and J. Therrien, "UV photodetectors with thin-film Si nanoparticle active medium," *IEEE Transactions on Nanotechnology*, vol. 4, no. 6, pp. 660–668, 2005.

[40] J. Valenta, P. Janda, K. Dohnalová, D. Nižňansky, F. Vácha, and J. Linnros, "Colloidal suspensions of silicon nanocrystals: from single nanocrystals to photonic structures," *Optical Materials*, vol. 27, no. 5, pp. 1046–1049, 2005.

[41] M. V. Wolkin, J. Jorne, P. M. Fauchet, G. Allan, and C. Delerue, "Electronic states and luminescence in porous silicon quantum dots: the role of oxygen," *Physical Review Letters*, vol. 82, no. 1, pp. 197–200, 1999.

[42] A. Morales-Sánchez, J. Barreto, C. Domínguez, M. Aceves, and J. A. Luna-López, "The mechanism of electrical annihilation of conductive paths and charge trapping in silicon-rich oxides," *Nanotechnology*, vol. 20, no. 4, Article ID 045201, 2009.

[43] A. A. G. Fernández, M. A. Mijares, A. M. Sánchez, and K. M. Leyva, "Intense whole area electroluminescence from low pressure chemical vapor deposition-silicon-rich oxide based light emitting capacitors," *Journal of Applied Physics*, vol. 108, no. 4, Article ID 043105, 2010.

[44] H. S. Nalwa and L. S. Rohwer, Eds., *Handbook of Luminescence, Display Materials, and Devices, Volume 1 Organic Light-Emitting Diodes*, American Scientific, Valencia, Calif, USA, 2003.

[45] R. López-Estopier, M. Aceves-Mijares, Z. Yu, and C. Falcony, "Determination of the energy states of the donor acceptor decay emission in silicon rich oxide prepared by low-pressure chemical vapor deposition," *Journal of Vacuum Science and Technology B*, vol. 29, no. 2, Article ID 021017, 5 pages, 2011.

[46] B. G. Yacobi and D. B. Holt, *Cathodoluminescence Microscopy of Inorganic Solids*, Plenum Press, New York, NY, USA, 1990.

Research Article

Synthesis of Thermochromic W-Doped VO$_2$ (M/R) Nanopowders by a Simple Solution-Based Process

Lihua Chen,[1, 2] Chunming Huang,[1] Gang Xu,[1] Lei Miao,[1] Jifu Shi,[1] Jianhua Zhou,[1] and Xiudi Xiao[1]

[1] *Key Laboratory of Renewable Energy and Gas Hydrate, Guangzhou Institute of Energy Conversion, CAS, Guangzhou 510640, China*
[2] *Graduate University of CAS, Beijing 100080, China*

Correspondence should be addressed to Gang Xu, xugang@ms.giec.ac.cn

Thermochromic W-doped VO$_2$ nanopowders were prepared by a novel and simple solution-based method and characterized by a variety of techniques. We mainly investigated the effect of tungsten dopant on the structural properties and phase transition of V$_{1-x}$W$_x$O$_2$. The as-obtained nanopowders with tungsten content of ≤ 2.5 at% can be readily indexed as monoclinic VO$_2$ (M) while that of 3 at% assigned into the rutile VO$_2$ (R). The valence state of tungsten in the nanopowders is +6. TEM and XRD results show that the substitution of W atom for V in VO$_2$ results in a decrease of the d space of the (011) plane. The phase transition temperature is determined by differential scanning calorimetry (DSC). It is found, for the first time, that the reduction of transition temperature reaches to 17 K per 1 at% of W doping with the tungsten extents of ≤ 1 at%, but only 9.5 K per 1 at% with the tungsten extents of >1 at%. The reason of this arises from the difficulty of the formation of V^{3+}-W^{4+} and V^{3+}-W^{6+} pairs by the increasing of W ions doping in the V$_{1-x}$W$_x$O$_2$ system.

1. Introduction

Vanadium oxides have nearly 15–20 stable phases, meanwhile metalinsulator transition (MIT) has been reported in at least 8 vanadium oxide compounds (V$_2$O$_3$, VO$_2$, V$_3$O$_5$, V$_4$O$_7$, V$_5$O$_9$, V$_6$O$_{11}$, V$_2$O$_5$, V$_6$O$_{13}$, etc.) at temperatures ranging from -147°C to 68°C [1–3], in which VO$_2$ materials show the fully reversible phase transition between monoclinic VO$_2$ (M) and tetragonal rutile phase VO$_2$ (R) fascinatingly around 68°C. As a result, the resistance has a sharp change of 4–5 orders of magnitude, and the optical transmission alters correspondingly. Below the critical temperature (T_c), VO$_2$ is in the semiconductive state, in which the energy gap is around 0.6 eV [4], permitting high infrared (IR) transmission. Above T_c, VO$_2$ is in the metallic state, in which overlap between the Fermi level and the V$_{3d}$ band eliminates the aforementioned band gap, causing vanadium dioxide to be highly reflecting or opaque in the near-infrared (NIR) region [5–8]. Furthermore, the phase transition temperature can be adjusted to near room temperature by doping, which is realized by the incorporation of metal ions into the VO$_2$ lattice [3]. Tungsten, molybdenum, chromium, titanium, fluorine, and niobium, and so forth are frequently used for this purpose because they produce relatively larger T_c shifts with less dopant concentrations. It has been found that tungsten might be the most effective element [9–14]. Therefore, with such properties, VO$_2$ materials can be considered as a promising candidate for a variety of potential applications such as energy-efficient window coatings [8], thermal sensors [15], cathode materials for reversible lithium batteries [16], electrical and infrared light switching device [17, 18].

So far, as an intelligent window material, the study of W-doped VO$_2$ mainly focused on thin films and nanoparticles. It has been prepared by a variety of methods involving excimer-laser-assisted metal organic deposition (ELAMOD) [19], magnetron sputtering [20], chemical vapor deposition (CVD) [21], pulsed laser deposition (PLD) [22], and vacuum evaporation [23]. However, all of these methods are not suitable for putting into practice because of complex control parameters, unstable technology, and the necessity of special and expensive equipment [24]. Chemical solution deposition

(a)

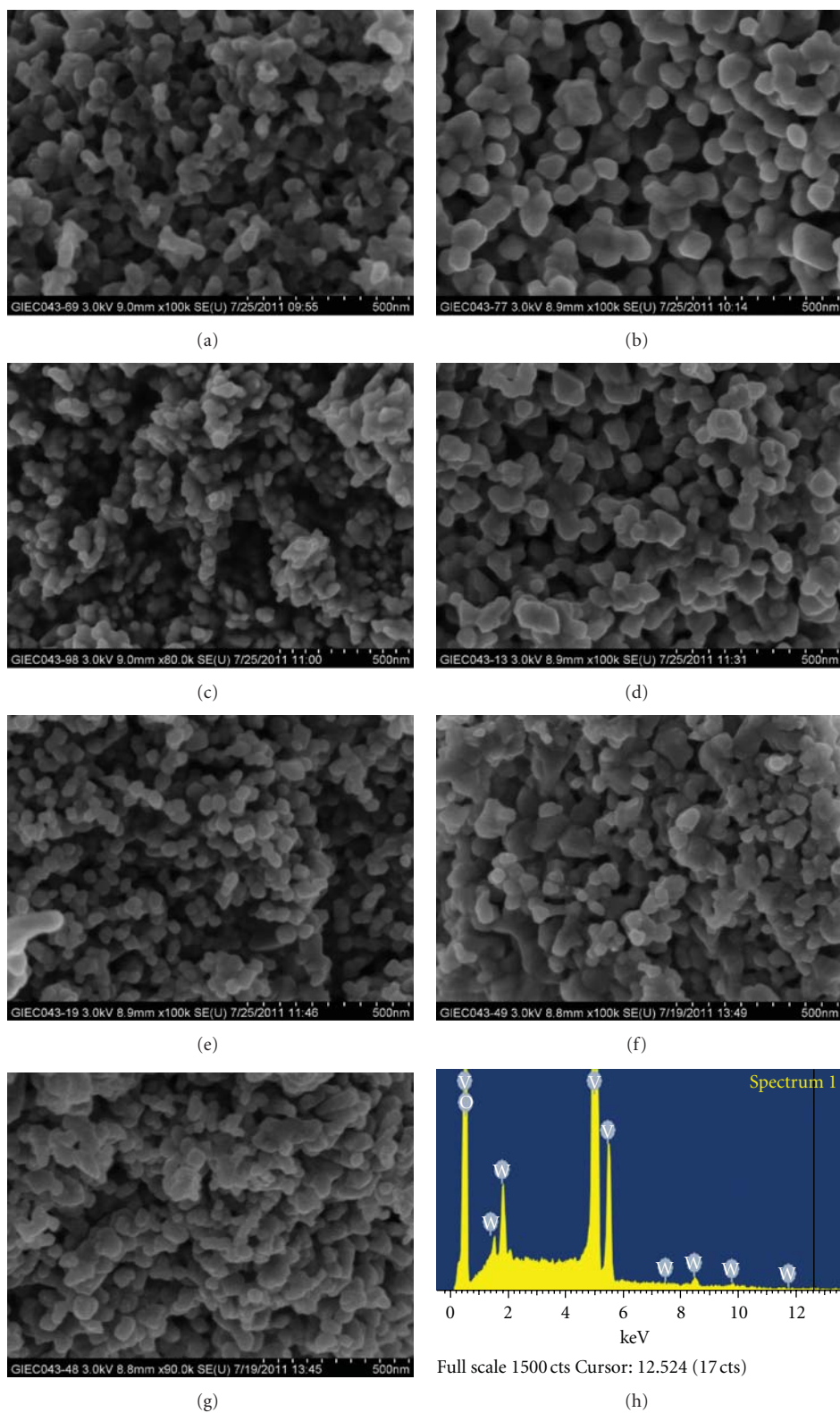
(b)

(c)

(d)

(e)

(f)

(g)

(h)

FIGURE 1: SEM images of vanadium dioxide nanopowders with different W-doped concentration from 0 to 3 atom% (at the intervals of 0.5) (a–g). EDS pattern for 2 at% W-doped VO_2 (h).
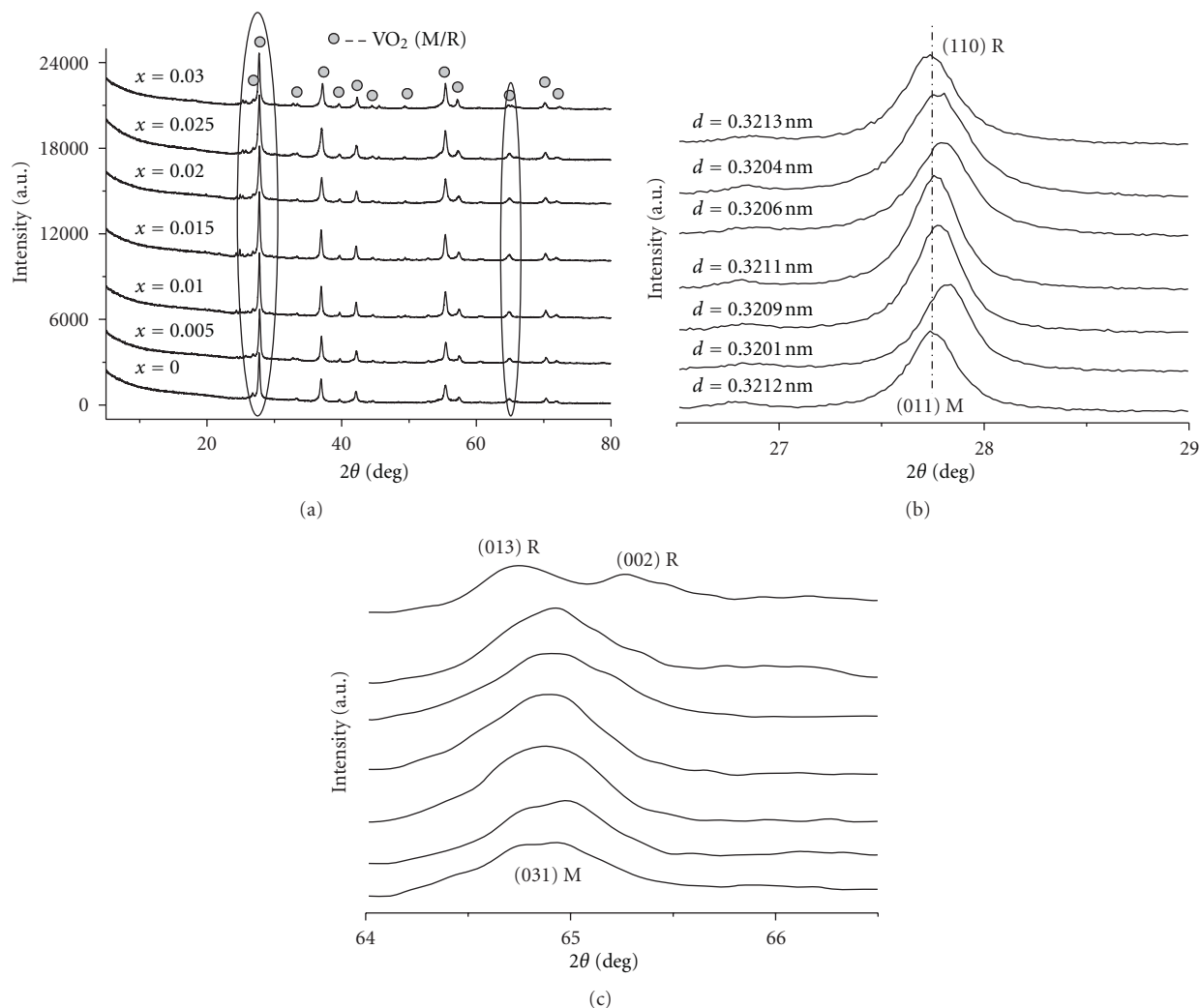
(a)

(b)

(c)

FIGURE 2: XRD patterns of $V_{1-x}W_xO_2$ nanopowders annealing at 500°C for 8 h with molar ratio of 2 : 3 (a) adding different extents of tungsten doping. A magnified version of the XRD data depicted in (b) in the 26.5° $\leq 2\theta \leq$ 29° range and in (c) in the 64° $\leq 2\theta \leq$ 66° range.

seems to be an alternative solution to the above problems due to its low cost and the option of metal doping. But this method usually requires specific raw materials or pretreatments which limit their practical applications [6]. Up to now, other modified methods for synthesis of M- or R-phase vanadium dioxide have been presented such as hydrothermal processes [25] and reduction-hydrolysis methods [26]. Nevertheless, long reaction time (12 h to several days) is often needed, or virulent precursor such as V_2O_5 is always required. Thus, more simple method for preparing vanadium dioxide with MIT property needs to be developed to promote its practical applications.

In this paper, we report a simple solution-based process to prepare pure VO_2 and W-doped VO_2 nanopowders with cheap and nontoxic vanadium (V) precursors and short reaction times. The characterization of the obtained nanopowders is studied through a variety of techniques. Furthermore, doping with tungsten could adjust the phase transition temperature remarkably, and thus put the thermochromic application into practice.

2. Experimental Section

2.1. Preparation of $V_{1-x}W_xO_2$ Nanopowders. First, a 0.5 g portion of ammonium metavanadate powders (NH_4VO_3, 99%, Tianjin Fuchen Chemical Reagents Factory) and appropriate amount of ammonium tungstate ($N_5H_{37}W_6O_{24}\cdot H_2O$, 85–90%, Sinopharm Chemical Reagent Co, Ltd.) with different W/V atom ratios were dissolved in 50 mL deionized water, respectively. Then oxalic acid dihydrate ($C_2H_2O_4\cdot 2H_2O$, 99.5%, Guangzhou Chemical Reagent Factory) was added to the above solution, where the molar ratio of NH_4VO_3 and $C_2H_2O_4\cdot 2H_2O$ was kept at 2 : 3. The mixture was stirred continuously for 30 min to form a sky blue clear solution, which indicated that the valence of vanadium in the solution was V^{4+}. As is known, the solution of V^{5+} is yellow, V^{4+} is blue, and that of V^{3+} is green, respectively. Then the above solution was dried below 100°C. Finally, W-doped VO_2 products, denoting as $V_{1-x}W_xO_2$ (x was appointed a delegate to the atomic ratio of W/V in the reactive precursors, $0 \leq x \leq 0.03$, at intervals of 0.005), were obtained after
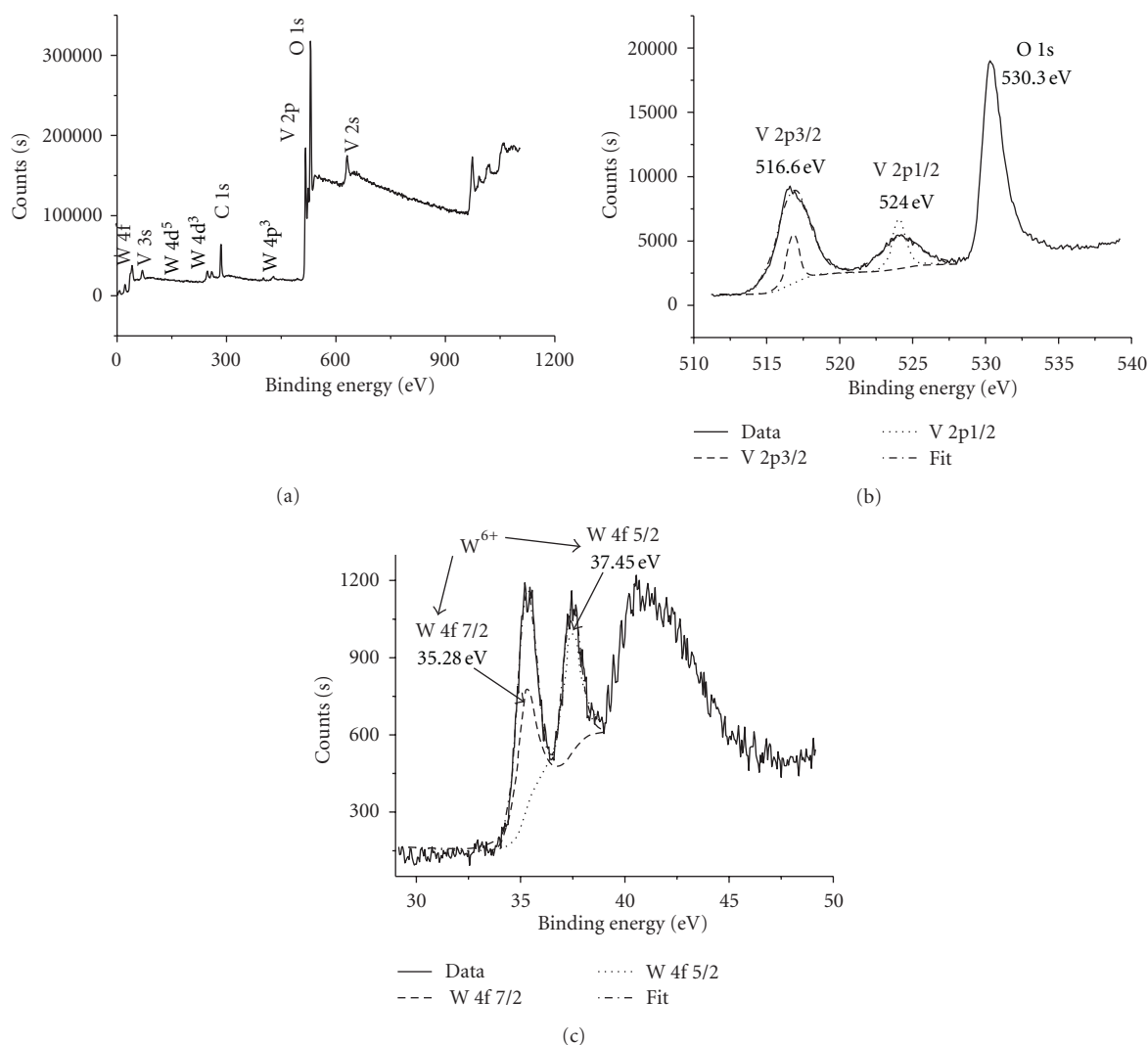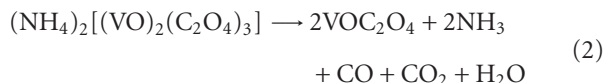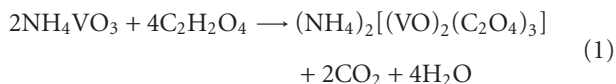
(a)

(b)

(c)

FIGURE 3: (a) XPS survey spectrum of 2 atom% W-doped VO_2. (b) V_{2p} peaks of the sample. (c) W_{4f} peaks of the sample.

annealing the collected powders at 500°C for 8 hours in nitrogen atmosphere. The possible reactions in the solution and the decomposition of the intermediate are listed as follows [27, 28]:

$$2NH_4VO_3 + 4C_2H_2O_4 \longrightarrow (NH_4)_2[(VO)_2(C_2O_4)_3] \\ + 2CO_2 + 4H_2O \tag{1}$$

$$(NH_4)_2[(VO)_2(C_2O_4)_3] \longrightarrow 2VOC_2O_4 + 2NH_3 \\ + CO + CO_2 + H_2O \tag{2}$$

$$VOC_2O_4 \longrightarrow VO_2 + CO + CO_2. \tag{3}$$

2.2. Characterization. Powder X-ray diffraction (XRD, PAN-alytical B.V., X′Pert Pro MPS PW3040/60) patterns of the samples were recorded in the scanning range of 5–80° at room temperature of 25°C. The morphologies, dimensions, elemental composition, and crystallinity of the nanopowders were examined by scanning electron

microscopy (SEM, Hitachi, S-4800), energy dispersive X-ray spectroscopy (EDS) attached to the SEM, transmission electron microscopy (TEM), and high-resolution TEM (JEOL, JEM-2010HR), respectively. Samples for TEM observation were prepared by dispersing in ethanol. Differential scanning calorimetry (DSC, Netzsch-Bruker, STA449F3Jupiter-TENSOR27) experiments were performed using a DuPont differential thermal analyzer under atmosphere flow in the range of 25–120°C with a heating rate of $5\,K\,min^{-1}$, and in the measure procedure heating process alternates with cooling process. The valance state of the as-obtained $V_{1-x}W_xO_2$ nanopowders was characterized by means of X-ray photoelectron spectroscopy (XPS, Thermo-V-G Scientific, ESCALAB250).

3. Results and Discussion

The morphology of the undoped and W-doped VO_2 nanopowders is characterized by SEM as shown in Figure 1. It is observed in Figures 1(a) to 1(g) that the tungsten dopant
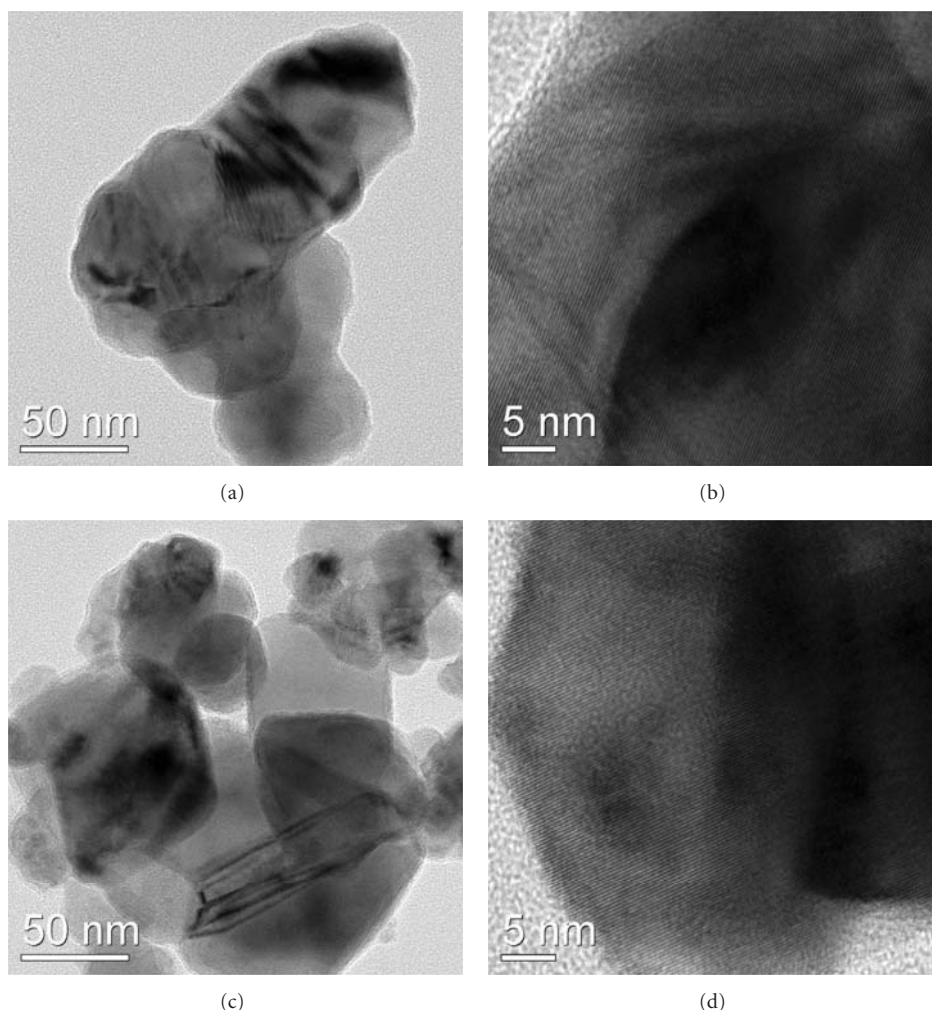
(a)

(b)

(c)

(d)

FIGURE 4: TEM and HRTEM images for the as-obtained undoped VO_2 (a; b) and $V_{0.98}W_{0.02}O_2$ (c; d) nanopowders.

concentration almost has no effect on the morphology of the nanoparticles, and the particle sizes are about 20–60 nm. The experimental results also indicate that particles will be congregated with the increase of annealing time. Especially, the particles with 2 at% W-doped are relatively uniform, and the size is about 25 nm, which is in favor of the practice application on thermochromic window coatings. As is known, small and uniform particles are relatively easy to disperse in solvent and obtain homogeneous coating. Therefore, the 2 at% W-doped sample is investigated in detail in the following experiments. EDS analysis results further confirm the existence of V, W, and O elements. The representative peaks of V and O elements appear in all of the obtained samples, and the representative peaks of W element also appear in each of W-doped products, which confirm a successful doping of W into VO_2. Here we just give the EDS pattern of 2 at% W-doped sample (Figure 1(h)) as a representative example.

The XRD patterns of W-doped VO_2 nanopowders with various tungsten contents are recorded in Figure 2(a). The magnified versions of the XRD data in the range of $26.5° \leq 2\theta \leq 29°$ and $64° \leq 2\theta \leq 66°$ are depicted in Figure 2(b)

and Figure 2(c), respectively. It is found that the as-obtained samples with the tungsten extents of ≤ 2.5 at% can be readily indexed as monoclinic VO_2 (M) (JCPDS card number 79-1655), while that of 3 at% assigned into the rutile VO_2 (R) (JCPDS card number 43-1051). For the sample doped 3 at% tungsten, the peak in $26.5° \leq 2\theta \leq 29°$ shifts left than the others figuring out the change of VO_2 (M) (011) to VO_2 (R) (110) in Figure 2(b), and meanwhile the VO_2 (M) (310) peak splits into the VO_2 (R) (013) and (002) in $64° \leq 2\theta \leq 66°$ (Figure 2(c)). The above two phenomena together indicate the occurrence of the diagnostic feature for the structural phase transition from monoclinic to tetragonal VO_2 phase, which are in good agreement with previous reports [7, 29]. Therefore, the changes in peak positions of as-obtained samples indicate that an appropriate amount of tungsten doping can promote the phase transition [30].

In Figure 3, XPS analysis of the as-obtained nanopowders with 2 at% W-doped is performed to understand in detail the valance state. The spectra indicate that there are four elements: oxygen, vanadium, carbon, and tungsten with binding energy peaks corresponding to C1s, O1s, V2s, V2p, V3s, W4f, W4d, and W4p in W-doped VO_2 nanopowders
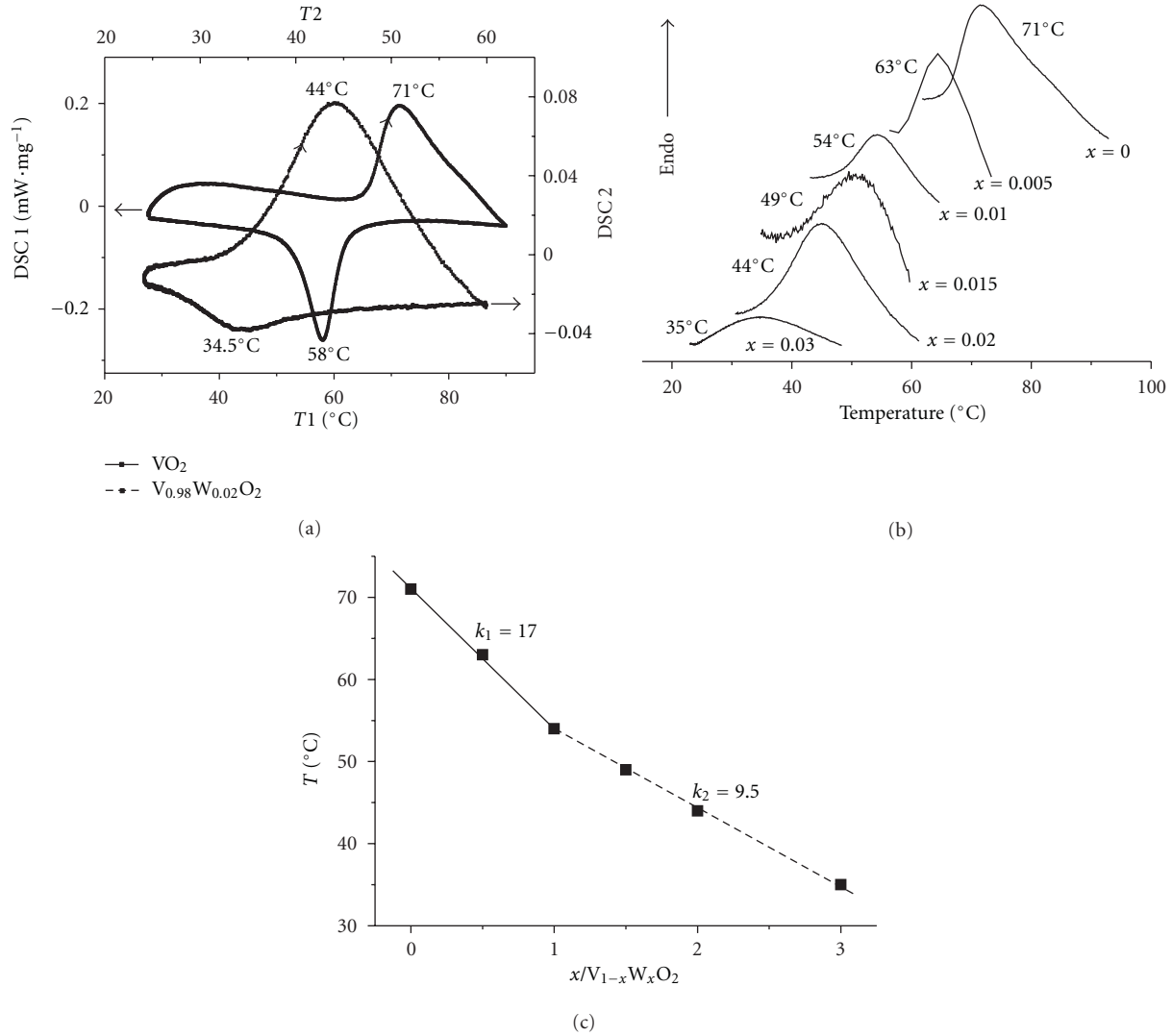
(a)

(b)

(c)

FIGURE 5: DSC curves of undoped VO_2 and 2 atom% W-doped VO_2 nanopowders during the heating and cooling cycles (a). The curves of as-obtained samples ($V_{1-x}W_xO_2$, $x = 0$–0.03, at intervals of 0.005) upon heating process (b). Effect of tungsten-doped vanadium dioxide concentration on the phase transition temperature upon heating process (c).

(Figure 3(a)). The forms of carbon are possibly from surface contamination [5, 9, 30]. The data reveals that the peak at 530.3 eV is associated with O1s [26]. The peaks located at 516.6 eV (reported values: 515.7–516.6 eV [5, 6, 9, 26, 30, 31]) and 524.0 eV (reported values: 522.6–524.0 eV [5, 6, 9, 26, 29, 30]) correspond to $V_{2p3/2}$ and $V_{2p1/2}$ (Figure 3(b)), respectively, and the binding energy of $V_{2p3/2}$ increases slightly after W doping [30]. The W_{4f} peaks follow with binding energies of $W_{4f7/2}$ and $W_{4f5/2}$ at 35.28 eV and 37.45 eV, respectively. According to the standard binding energy, tungsten atoms in these nanopowders exist as W^{6+} (Figure 3(c)) [9]. N-type semiconductor could form as W^{6+} ions replace V^{4+} ions.

TEM images of the undoped VO_2 and 2 at% W-doped VO_2 nanopowders are shown in Figures 4(a) and 4(c). The morphologies and sizes of the as-obtained samples are consistent with those of SEM images in Figures 1(a) and 1(e). Figures 4(b) and 4(d) show the lattice-resolved HRTEM images. The fringe spacing is 0.321 nm for undoped VO_2 (Figure 4(b)) sample, which is consistent with the d space of the (011) plane of monoclinic VO_2 (M) phase [32, 33], and the fringe spacing reduces to 0.314 nm (Figure 4(d)) for the sample of 2 at% W-doped VO_2. This decreased tendency of the fringe spacing with W doping is consistent with the calculated results by Scherrer formula. As the radius of W^{6+} ion (60 pm [34]) is smaller than that of the V^{4+} ion about 63 pm. The interstitial W^{6+} ions will cause the atoms to have larger interatomic spacings, and the interatomic spacings will be reduced in the case of substitutional defects with W^{6+} ions. The TEM results suggest that the substitution of W^{6+} ions for V^{4+} plays a dominant role in this work, which results in the reduction of d_{011} spacing. As the tungsten dopant concentration is 2 at%, the (011) peak of monoclinic VO_2 (M) shifts from 27.74° (undoped VO_2) to 27.79°, indicating the decrease of the crystal lattice spacing according to the Bragg equation ($2d\sin\theta = \lambda$; $\lambda_{Cu} = 0.154$ nm) [29, 35, 36].

As regards the rule of substitution or interstitial of W^{6+} ions for V^{4+} is unknown, and it needs further research.

When the phase transition of VO_2 occurs, it exhibits a noticeable endothermal or exothermal profile in the DSC curve. Figure 5(a) shows the typical DSC curves of undoped and 2 at% W-doped VO_2 nanopowders. With 2 at% W-doped sample, Mott phase transition arises at around 44°C and 34.5°C for the heating and cooling cycles, compared to 71°C and 58°C for the undoped VO_2, respectively. The phase transition can be modified under the different factors such as defect density or lattice change [3, 29]. The appearance of endothermal and exothermal peaks during the heating and cooling process confirms the first-order transition between monoclinic VO_2 (M) and tetragonal rutile VO_2 (R) [7]. To be vital for the practical thermochromic effect applications, the phase transition temperature of W-doped must be approaching to room temperature. In this case, the phase transition temperature could be reduced to 35°C with 3 at% W-doped in Figure 5(b).

A nonlinear decrease of the phase transition temperature with increasing percent of tungsten atom incorporation is observed upon heating process (Figure 5(c)). And the nonlinear decrease can be described by two linear fits. The reduction of transition temperature is estimated to be about 17 K per 1 at% of W doping with the tungsten extents of ≤ 1 at%, but only 9.5 K per 1 at% with the tungsten extents of >1 at%. With tungsten ion doping into VO_2, the reaction takes place as follows: $2V^{4+} + W^{4+} \rightarrow 2V^{3+} + W^{6+}$, which results in the formation of V^{3+}-V^{4+} and V^{3+}-W^{6+} pairs [35]. Then the transition temperature will be reduced due to the loss of direct bonding between V ions, which is resulted from the forming of the pairs. We can now assume that the change of transition temperature is determined by the difficulty of initial formation of V^{3+}-V^{4+} and V^{3+}-W^{6+} pairs. At the beginning, the pairs form easily with lower tungsten dopant concentration, so the transition temperature could remarkably change. By following the increase of W ions, it becomes relatively difficult to form the V^{3+}-V^{4+} and V^{3+}-W^{6+} pairs right away, resulting in a more gradual change in the transition temperature.

4. Conclusions

Well-crystallized nanopowders of W-doped VO_2 (M/R) were successfully synthesized by a simple solution-based process through the reaction of ammonium metavanadate (NH_4VO_3) and oxalic acid dihydrate ($C_2H_2O_4 \cdot 2H_2O$) followed by adding to appropriate ammonium tungstate ($N_5H_{37}W_6O_{24} \cdot H_2O$). It is shown that tungsten dopant concentration almost has no effect on the morphology of the nanoparticles and the granular particles are about 20–60 nm. As-obtained nanopowders with the tungsten extents of ≤ 2.5 at% can be readily indexed as monoclinic VO_2 (M), while that of 3 at% assigned into the rutile VO_2 (R). Substitutional W^{6+} ions could reduce the interatomic spacings, which results in the decrease of the d space of the (011) plane in monoclinic VO_2 (M) phase. Moreover, we found that the difficulty level in initial formation of

V^{3+}-V^{4+} and V^{3+}-W^{6+} pairs determines the rate of change of the critical temperature. The reduction of transition temperature is estimated to be about 17 K per 1 at% of W doping with the tungsten extents of ≤ 1 at%, only about 9.5 K per 1 at% with the tungsten extents of >1 at%. With 3 at% W-doped VO_2, the phase transition temperature can be reduced to 35°C. In short, this paper provides a simple solution-based method to prepare W-doped VO_2 nanopowders with good thermochromic properties showing the transition temperature required to building glazing, which is in favor of promoting the practical applications of smart window.

Acknowledgments

References

[1] F. J. Morin, "Oxides which show a metal-to-insulator transition at the neel temperature," *Physical Review Letters*, vol. 3, no. 1, pp. 34–36, 1959.

[2] D. P. Partlow, S. R. Gurkovich, K. C. Radford, and L. J. Denes, "Switchable vanadium oxide films by a sol-gel process," *Journal of Applied Physics*, vol. 70, no. 1, pp. 443–452, 1991.

[3] Z. F. Peng, Y. Wang, Y. Y. Du, D. Lu, and D. Z. Sun, "Phase transition and IR properties of tungsten-doped vanadium dioxide nanopowders," *Journal of Alloys and Compounds*, vol. 480, no. 2, pp. 537–540, 2009.

[4] G. H. Liu, X. Y. Deng, and R. Wen, "Electronic and optical properties of monoclinic and rutile vanadium dioxide," *Journal of Materials Science*, vol. 45, no. 12, pp. 3270–3275, 2010.

[5] J. Zhang, Eerdemutu, C. X. Yang et al., "Size- and shape-controlled synthesis of monodisperse vanadium dioxide nanocrystals," *Journal of Nanoscience and Nanotechnology*, vol. 10, no. 3, pp. 2092–2098, 2010.

[6] Z. T. Zhang, Y. F. Gao, Z. Chen et al., "Thermochromic VO_2 thin films: solution-based processing, improved optical properties, and lowered phase transformation temperature," *Langmuir*, vol. 26, no. 13, pp. 10738–10744, 2010.

[7] C. Z. Wu, X. D. Zhang, J. Dai et al., "Direct hydrothermal synthesis of monoclinic VO_2(M) single-domain nanorods on large scale displaying magnetocaloric effect," *Journal of Materials Chemistry*, vol. 21, no. 12, pp. 4509–4517, 2011.

[8] G. Xu, C. M. Huang, P. Jin, M. Tazawa, and D. M. Chen, "Nano-Ag on vanadium dioxide. I. Localized spectrum tailoring," *Journal of Applied Physics*, vol. 104, no. 5, Article ID 053101, 6 pages, 2008.

[9] J. W. Ye, L. Zhou, F. J. Liu et al., "Preparation, characterization and properties of thermochromic tungsten-doped vanadium dioxide by thermal reduction and annealing," *Journal of Alloys and Compounds*, vol. 504, no. 2, pp. 503–507, 2010.

[10] J. Z. Yan, Y. Zhang, W. X. Huang, and M. J. Tu, "Effect of Mo-W Co-doping on semiconductor-metal phase transition temperature of vanadium dioxide film," *Thin Solid Films*, vol. 516, no. 23, pp. 8554–8558, 2008.

[11] C. Batista, V. Teixeira, and R. M. Ribeiro, "Synthesis and characterization of $V_{1-x}Mo_xO_2$ thermochromic coatings with

reduced transition temperatures," *Journal of Nanoscience and Nanotechnology*, vol. 10, no. 2, pp. 1393–1397, 2010.

[12] W. Burkhardt, T. Christmann, S. Franke et al., "Tungsten and fluorine co-doping of VO₂ films," *Thin Solid Films*, vol. 402, no. 1-2, pp. 226–231, 2002.

[13] I. Takahashi, M. Hibino, and T. Kudo, "Thermochromic properties of double-doped VO₂ thin films prepared by a wet coating method using polyvanadate-based sols containing W and Mo or W and Ti," *Japanese Journal of Applied Physics*, vol. 40, no. 3, pp. 1391–1395, 2001.

[14] C. Marini, E. Arcangeletti, D. D. Castro et al., "Optical properties of $V_{1-x}Cr_xO_2$ compounds under high pressure," *Physical Review B*, vol. 77, no. 23, Article ID 235111, 9 pages, 2008.

[15] C. Sella, M. Maaza, O. Nemraoui, J. Lafait, N. Renard, and Y. Sampeur, "Preparation, characterization and properties of sputtered electrochromic and thermochromic devices," *Surface and Coatings Technology*, vol. 98, no. 1–3, pp. 1477–1482, 1998.

[16] J. Ni, W. T. Jiang, K. Yu, Y. F. Gao, and Z. Q. Zhu, "Hydrothermal synthesis of VO₂ (B) nanostructures and application in aqueous Li-ion battery," *Electrochim Acta*, vol. 56, no. 5, pp. 2122–2126, 2011.

[17] C. H. Chen, R. F. Wang, L. Shang, and C. F. Guo, "Gate-field-induced phase transitions in VO₂: monoclinic metal phase separation and switchable infrared reflections," *Applied Physics Letters*, vol. 93, no. 17, Article ID 171101, 3 pages, 2008.

[18] B. Viswanath, C. Ko, and S. Ramanathan, "Thermoelastic switching with controlled actuation in VO₂ thin films," *Scripta Materialia*, vol. 64, no. 6, pp. 490–493, 2011.

[19] M. Nishikawa, T. Nakajima, T. Kumagai, T. Okutani, and T. Tsuchiya, "Ti-doped VO₂ films grown on glass substrates by excimer-laser-assisted metal organic deposition process," *Japanese Journal of Applied Physics*, vol. 50, no. 1, pp. 01BE04–01BE04-5, 2011.

[20] G. Gopalakrishnan and S. Ramanathan, "Compositional and metal-insulator transition characteristics of sputtered vanadium oxide thin films on yttria-stabilized zirconia," *Journal of Materials Science*, vol. 46, no. 17, pp. 5768–5774, 2011.

[21] R. Binions, G. Hyett, C. Piccirillo, and I. P. Parkin, "Doped and un-doped vanadium dioxide thin films prepared by atmospheric pressure chemical vapour deposition from vanadyl acetylacetonate and tungsten hexachloride: the effects of thickness and crystallographic orientation on thermochromic properties," *Journal of Materials Chemistry*, vol. 17, no. 44, pp. 4652–4660, 2007.

[22] R. T. R. Kumar, B. Karunagaran, D. Mangalaraj, S. K. Narayandass, P. Manoravi, and M. Joseph, "Characteristics of amorphous VO₂ thin films prepared by pulsed laser deposition," *Journal of Materials Science*, vol. 39, no. 8, pp. 2869–2871, 2004.

[23] F. C. Case, "Modifications in the phase transition properties of predeposited VO₂ films," *Journal of Vacuum Science & Technology A*, vol. 2, no. 4, p. 1509, 1984.

[24] Z. F. Peng, W. Jiang, and H. Liu, "Synthesis and electrical properties of tungsten-doped vanadium dioxide nanopowders by thermolysis," *The Journal of Physical Chemistry C*, vol. 111, no. 3, pp. 1119–1122, 2007.

[25] J. Li, C. Y. Liu, and L. J. Mao, "The character of W-doped one-dimensional VO₂ (M)," *Journal of Solid State Chemistry*, vol. 182, no. 10, pp. 2835–2839, 2009.

[26] C. L. Xu, L. Ma, X. Liu, W. Y. Qiu, and Z. X. Su, "A novel reduction–hydrolysis method of preparing VO₂ nanopowders," *Materials Research Bulletin*, vol. 39, no. 7-8, pp. 881–886, 2004.

[27] D. N. Sathyanarayana and C. C. Patel, "Studies of ammonium dioxovanadium(V) bisoxalate dihydrate," *Bulletin of the Chemical Society of Japan*, vol. 37, no. 12, pp. 1736–1740, 1964.

[28] D. N. Sathyanarayana and C. C. Patel, "Studies on oxovanadium (IV) oxalate hydrates," *Journal of Inorganic and Nuclear Chemistry*, vol. 27, no. 2, pp. 297–302, 1965.

[29] L. Whittaker, T. L. Wu, C. J. Patridge, G. Sambandamurthy, and S. Banerjee, "Distinctive finite size effects on the phase diagram and metal-insulator transitions of tungsten-doped vanadium(iv) oxide," *Journal of Materials Chemistry*, vol. 21, no. 15, pp. 5580–5592, 2011.

[30] C. X. Cao, Y. F. Gao, and H. J. Luo, "Pure single-crystal rutile vanadium dioxide powders: synthesis, mechanism and phase-transformation property," *Journal of Physical Chemistry C*, vol. 112, no. 48, pp. 18810–18814, 2008.

[31] N. Alov, D. Kutsko, I. Spirovová, and Z. Bastl, "XPS study of vanadium surface oxidation by oxygen ion bombardment," *Surface Science*, vol. 600, no. 8, pp. 1628–1631, 2006.

[32] L. Whittaker, C. Jaye, Z. G. Fu, D. A. Fischer, and S. Banerjee, "Depressed phase transition in solution-grown VO₂ nanostructures," *Journal of the American Chemical Society*, vol. 131, no. 25, pp. 8884–8894, 2009.

[33] H. H. Yin, M. Luo, K. Yu et al., "Fabrication and temperature-dependent field-emission properties of bundlelike VO₂ nanostructures," *ACS Applied Materials & Interfaces*, vol. 3, no. 6, pp. 2057–2062, 2011.

[34] J. T. Zeng, Y. Wang, Y. X. Li, Q. B. Yang, and Q. R. Yin, "Ferroelectric and piezoelectric properties of tungsten doped $CaBi_4Ti_4O_{15}$ ceramics," *Journal of Electroceramics*, vol. 21, no. 1–4, pp. 305–308, 2008.

[35] C. Tang, P. Gergopoulos, M. E. Fine, and J. B. Cohen, "Local atomic and electronic arrangements in $W_xV_{1-x}O_2$," *Physical Review B*, vol. 31, no. 2, pp. 1000–1011, 1985.

[36] L. Whittaker, C. J. Patridge, and S. Banerjee, "Microscopic and nanoscale perspective of the metal−insulator phase transitions of VO₂: some new twists to an old tale," *The Journal of Physical Chemistry Letters*, vol. 2, no. 7, pp. 745–758, 2011.

Research Article

Enhancement of Photoluminescence Lifetime of ZnO Nanorods Making Use of Thiourea

Erdal Sönmez[1, 2] and Kadem Meral[2, 3]

[1] *Department of Physics, Faculty of Education, Atatürk University, 25240 Erzurum, Turkey*
[2] *Advanced Materials Research Laboratory, Department of Nanoscience & Nanoengineering, Graduate School of Natural and Applied Sciences, Atatürk University, 25240 Erzurum, Turkey*
[3] *Department of Chemistry, Faculty of Science, Atatürk University, 25240 Erzurum, Turkey*

Correspondence should be addressed to Erdal Sönmez, esonmez@atauni.edu.tr

We have investigated correlation of photoluminescence lifetime between zinc oxide (ZnO) nanorods and thiourea-doped ZnO nanorods (tu: CH_4N_2S). Aqueous solutions of ZnO nanorods were deposited on glass substrate by using pneumatic spray pyrolysis technique. The as-prepared specimens were characterized by X-ray diffraction (XRD), scanning electron microscopy (SEM), and time-resolved photoluminescence spectroscopy (TRPL). The photoluminescence lifetime of ZnO nanorods and ZnO nanorods containing thiourea was determined as $\tau = 1.56 \pm 0.05$ ns ($\chi^2 = 0.9$) and $\tau = 2.12 \pm 0.03$ ns ($\chi^2 = 1.0$), respectively. The calculated lifetime values of ZnO nanorods revealed that the presence of thiourea in ZnO nanorods resulted in increasing the exciton lifetime. In addition to the optical quality of ZnO nanorods, their exciton lifetime is comparable to the longest lifetimes reported for ZnO nanorods. The structural improvement of ZnO nanorods, containing thiourea, was also elucidated by taking their SEM images which show the thinner and longer ZnO nanorods compared to those without thiourea.

1. Introduction

Zinc oxide (ZnO) is a wide-band gap ($E_g \approx 3.37$ eV at 300 K) semiconductor with good carrier mobility and can be doped n-type or p-type. It has many applications in a very important area such as ultraviolet light-emitting diodes and nanolaser [1]. ZnO shows pronounced excitonic effects at high temperatures (>300 K) due to its large exciton binding energy (60 meV) [2]. Optically pumped lasing has been successfully demonstrated for the ZnO nanostructures, which have resulted in the intense attention to ZnO optical properties [3–21]. For example, the optical properties of ZnO nanostructures at different morphologies are reported at varying temperatures and the performance-structure relation for ZnO nanostructures are evaluated for some applications. Further improvement in the quality of ZnO is necessary to achieve the superior device performance [22]. In this regard, main progress has been made toward the growth of good-quality ZnO nanostructures for the fabrication of light-emitting diodes [8].

The material quality and optical properties of the nanostructures, such as ZnO, are commonly followed by using the photoluminescence (PL) and time-resolved photoluminescence (TRPL) measurements [23]. Especially, TRPL provides significant information in relation to the exciton lifetime which is an important indicator for the material quality and efficiency of the radiative recombination [6]. It is known that the lifetime is related to the radiative decay of the exciton and various nonradiative processes such as leak by deep-level traps, low-lying surface states and multiphonon scattering [24, 25]. In this regard, the separation of the radiative recombination and nonradiative processes is difficult [26]. However, the radiative excitation lifetime (k_r) is improved by decreasing the structural defect of ZnO nanostructures. Therefore, different morphologies of ZnO nanostructures exhibit very different lifetimes, with some showing very fast decay, while others have decay times as long as comparable to those of good-quality. As a result of these explanations, it is concluded that the morphologies and dimensions of

ZnO nanostructures affect the exciton lifetimes [15, 18]. For example, the high-quality ZnO single crystals have several nanoseconds exciton lifetime at room temperature [6]. Therefore, the exciton lifetime of ZnO nanostructures is changed by the controlling of their morphologies and dimensions. The structure of ZnO is controlled by precious parameters such as the starting zinc compound, chemical composition of solvent, nature of the precipitating agent, pH, temperature, and aging time [27]. In addition to growth conditions, deposition methods of ZnO onto solid surface play a key role for ZnO nanostructures. Therefore, different deposition methods have been developed to fabricate a variety of ZnO nanostructures such as well-known metal organic chemical vapor [28, 29], pulsed laser [30, 31], electrochemical deposition techniques [32, 33], vapor-liquid, solid [34, 35], and wet chemical methods [36–38]. In addition to those methods, the important one is chemical spray pyrolysis system which is one of the most elegant methods to the preparation of good-quality ZnO nanostructures. This method has several advantages over the other methods such as providing short time, being cost-effective and template-free [39]. Consequently, a variety of ZnO nanostructures are easily fabricated by tuning of material growth conditions. If the optimal conditions are determined, various ZnO nanostructures can be prepared such as nanowires, nanoribbons, tetrapods, and nanorods, which exhibit excellent optical properties [5].

In the present study, the smaller and longer ZnO nanorods were prepared by doping a little amount of thiourea (tu: CH_4N_2S) into zinc chloride ($ZnCl_2$) solution, ZnO nanorods with and without thiourea have been deposited on a glass substrates via chemical spray pyrolysis method at different temperatures. The optical and structural properties of ZnO nanorods have been examined by X-ray diffraction (XRD), scanning electron microscopy (SEM), and time-resolved photoluminescence (TRPL) techniques. The results showed that the exciton lifetime of ZnO nanorods was increased in the presence of thiourea.

2. Experimental

All chemicals were analytical grade and were used without further purification. ZnO was deposited using spray aqueous solutions by pneumatic spray pyrolysis technique. The solutions, used for the preparation of ZnO as thin films, were that the first contained $ZnCl_2$ while the second included $ZnCl_2$ and thiourea with molar ratios of 1 : 0.25. The starting solution was atomized at a frequency of 1.63 MHz by an ultrasonic nebulizer and by using dry air. The solution was mixed with magnetic mixer. Mixing process lasted for 20 min. The resultant amounts of each solution are 50 mL. The nozzle-substrate distance was maintained at 10 cm. The deposition temperature (temperature of substrate surface), in the range of 350–550°C, was varied by using electronic temperature controller (TET-612 temperature controller by product ColdfusionX Electronics) device on the hot plate metallic surface. The temperature of the metallic surface was totally stable throughout the process at 350, 450, and 550 ± 2°C, respectively. The substrates were not used at

temperature above 550°C because they were physically being an irreparable disrupted. The substrates are ordinary microscope slides. Before loading into the system, the substrates were washed with detergent and then completely rinsed in methanol, acetone, and deionized water, respectively, and dried in air. Before being sprayed on the substrates they were progressively heated up to the required temperature. The solution flow rate and gas pressure were kept constant at 1 mL/min. Air was used as the carrier gas supplied by a filtered oil-free compressor. The duration of the film deposition was about 50 min. The color of ZnO film was white and it had a very good adhesion to glass substrates.

The structural characterization of deposited films structures of ZnO was carried out by X-ray diffraction (XRD) measurements using a Rigaku D/Max-IIIC diffractometer with $CuK\alpha1$ radiation ($\lambda = 1.5418$ Å), at 30 kV, 10 mA. The 2θ range, used in the measurement, was from 100 to 700 in steps of $0.02\,s^{-1}$. Surface morphology was examined by a JEOL JSM5610 model scanning electron microscope operating at 25 kV. Photoluminescence decays, for the exciton lifetime measurements, were carried out with a Laser Strobe Model TM-3 lifetime fluorometer from Photon Technology International. The excitation source consists of a pulsed nitrogen laser/tunable dye laser combination. Pulse width is about 800 ps and has repetition rate up to 20 pulses per second. The samples were excited at 337 nm nitrogen laser and, then, photoluminescence decays were monitored. The photoluminescence decays were analyzed with the lifetime distribution analysis software (Felix32) from the instrument-supplying company. The quality of fits was assessed by chi-square (χ^2) values. Fitting with χ^2 not more than 1.5 was taken as acceptable.

3. Results and Discussion

Firstly, the morphology of spray-deposited ZnO nanostructures was investigated as a function of the growth temperature, which is one of the most important experimental factor for the elucidation of nanostructures [27]. For this purpose, ZnO nanostructures were deposited on the glass substrate—at different temperatures (350, 450, and 550°C). The results of those experiments showed that elongated hexagonal prisms shaped ZnO nanostructures have been formed at 550°C. Therefore, the deposition temperature was optimized as 550°C for all sample preparations. Figure 1 illustrates the SEM images of ZnO deposited onto the glass substrates by the spray pyrolysis process using only $ZnCl_2$ (Figures 1(a)–1(c)) and $ZnCl_2$ containing thiourea additive with a molar ratio of Zn : tu = 1 : 0.25 (Figure 1(d)). SEM images demonstrated that the nanorod structures of ZnO on the glass substrate were formed at 550°C. Additionally, it can be seen the SEM images (Figure 1) that this deposition temperature is suitable for the formation of ZnO nanorods without or with thiourea. The addition of thiourea into the $ZnCl_2$ solution drastically influenced the ZnO nanorods dimensions as seen by the careful investigation of SEM images. The diameter of the ZnO nanorods was decreased from 1000 nm to 500 nm, while their lengths increased to about 200 nm by thiourea doped in the solution. As a result,
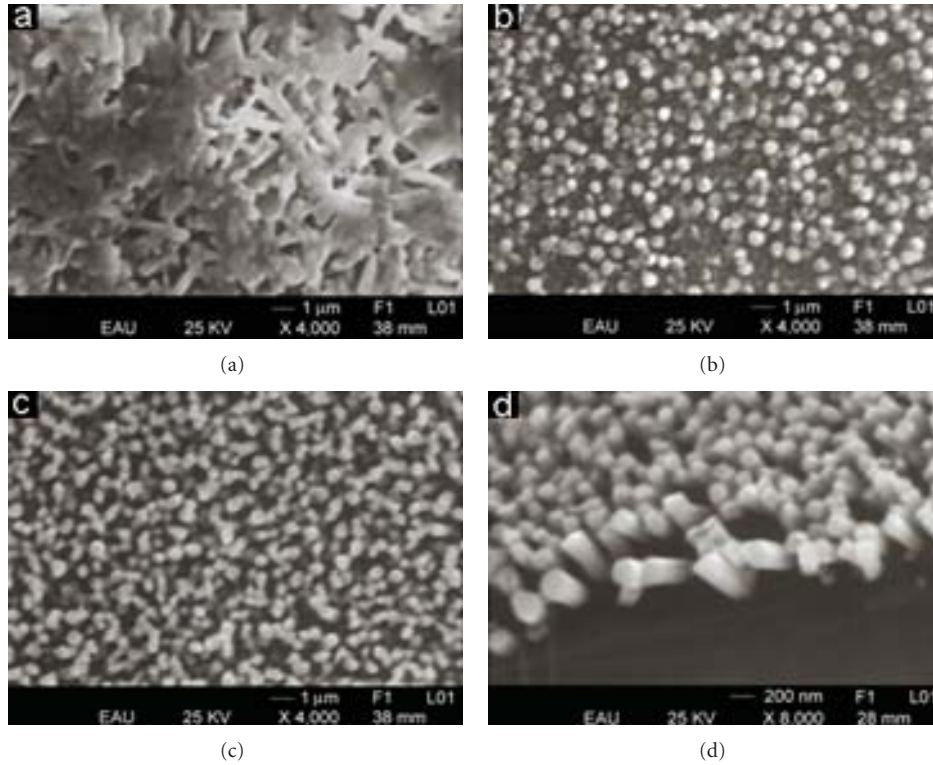
FIGURE 1: Typical SEM images of ZnO nanorods grown onto ordinary glass substrates at (a) 350°C (b) 450°C (c) 550°C and (d) 550°C with little amount of thiourea added.

the number of the nanorods and the width of the zinc oxide surface per unit area increased compared to those without thiourea. The molar ratio used for ZnO nanorods with thiourea is 1 : 0.25 (Zn : tu), since it is optimal condition for the growing of the nanorods at the highest aspect ratio. Besides, it is known that the amount of thiourea in solution is extremely important factor which determines the final rods dimensions and its addition, generally, leads to the formation of thinner rods [39, 40]. The possible mechanism in the morphological changes of the ZnO nanorods, which are produced from thiourea mixed $ZnCl_2$, solution is reported in the literature that in some crystallization processes. The growth rate of a crystal facet can be inhibited by an impurity adsorption during the front growth and incorporation of new molecules into that facet. For example, widening of the crystal is restricted by the adsorption of ZnS particles as the facet of the crystals is reported [40, 41]. As a result of this, longitudinal length in c-axis has increased that deteriorates optical properties of the crystals.

Figure 2 shows the XRD pattern of the ZnO nanorods prepared in the absence and presence of thiourea. As shown in the XRD pattern, the peak of (002) is dominant in ZnO nanorods grown in the absence of thiourea. In the ZnO nanorods grown in the presence of thiourea, in addition to ZnO structures, emerging of second phases, like ZnS, caused an increase in the peak count. Some of the reflections at 2θ = 27.20, 28.80, and 30.80° corresponding to Muller indices of 110, 111, and 200 detected in the XRD pattern can be attributed to the reflection of ZnS sphalerite phase
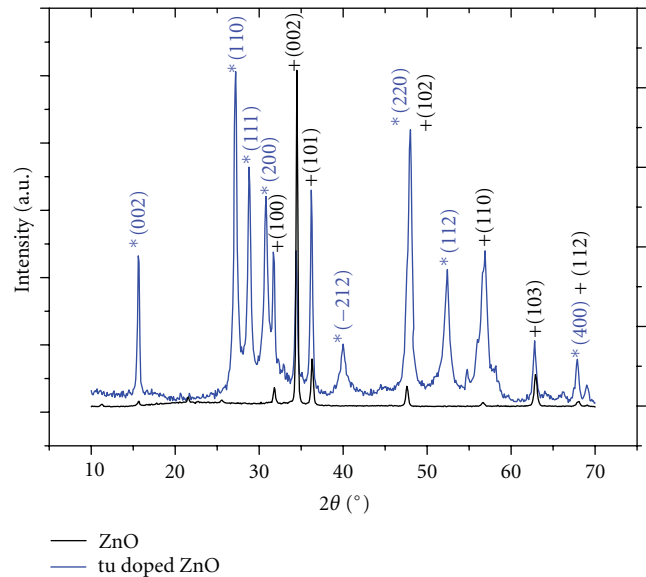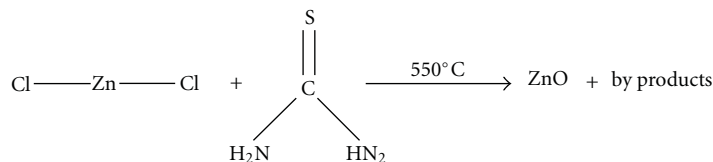

FIGURE 2: XRD patterns of ZnO nanorods.

in Figure 2, the $ZnCl_2$ and thiourea in aqueous solution yield a complex structure of thiourea zinc with molecular formula $Zn(tu)_2Cl_2$, which decomposes to the formation of zinc sulfide at temperatures above 300°C (as it has been reported in [40]). Besides, the possible growth mechanism

$$Cl \longrightarrow Zn \longrightarrow Cl \quad + \quad \underset{H_2N \qquad HN_2}{\overset{\overset{\displaystyle S}{\|}}{\underset{\displaystyle C}{|}}} \quad \xrightarrow{550^\circ C} \quad ZnO \quad + \quad \text{by products}$$
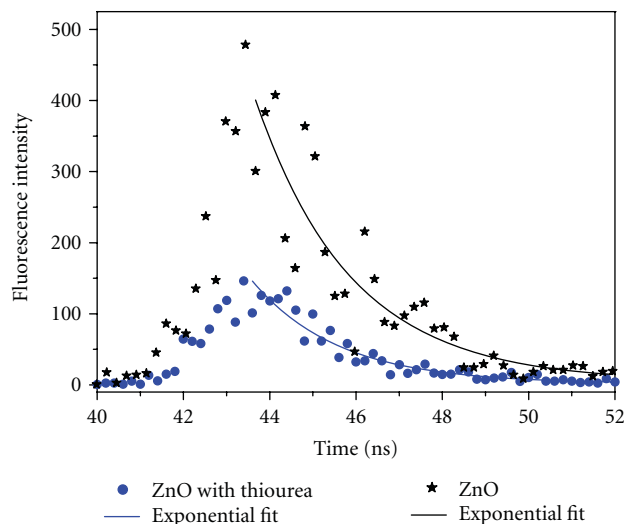
SCHEME 1

FIGURE 3: Fluorescence decay of ZnO nanorods with exponential fit.

for the formation of ZnO nanorods from the ZnCl$_2$ solution with thiourea at 550°C can be shown in Scheme 1.

The quality of ZnO is commonly examined using time-resolved photoluminescence (TRPL) measurement as well as steady-state photoluminescence (PL). TRPL measurement provides significant information about the exciton lifetime, which represents efficiency of the radiative recombination. In order to determine the exciton lifetime of ZnO nanorods, the photoluminescence decay spectra of the samples were recorded at 337 nm excitation wavelength at room temperature. Next, the lifetime of the samples was calculated by using specific fit software that belongs to PTI (Photon Technology International). The obtained photoluminescence decay of ZnO nanorods were analyzed to single-, bi-, and three-exponential fits according to (1)

$$I_{fl} = \sum_i \alpha_i \, \exp\left(\frac{-t}{\tau_i}\right), \tag{1}$$

where i is the number of exponentials, and τ_i and α_i are the lifetime and the preexponential factor, for each components. The photoluminescence decay spectra of the samples with exponential fits were given in Figure 3. As a result of the exponential analyses, it was determined that the photoluminescence decay of ZnO nanorods indicates single-exponential fits with the acceptable χ^2 values. Therefore, the single-exponential fit results for the evaluation of exciton lifetime of ZnO samples were used. The obtained single-exponential fit shows that ZnO nanorods also have

a homogeny distribution onto the glass surface. The exciton lifetime of ZnO nanorods was determined as $\tau = 1.56 \pm 0.05$ ns ($\chi^2 = 0.9$), when that of ZnO nanorods containing thiourea was calculated as $\tau = 2.12 \pm 0.03$ ns ($\chi^2 = 1.0$). The calculated lifetime values revealed that the presence of thiourea in ZnO nanorods resulted in increasing the exciton lifetime, suggesting an enhancement in radiative recombination. As considered by the experimental results, it is clear that the changing in the exciton lifetimes is resulted from the presence of the morphological difference between pure ZnO nanorods and ZnO nanorods containing thiourea, since it is known that the different morphologies of ZnO nanostructure act a significant role in the exciton lifetimes [22]. Additionally, it is inferred that ZnO nanostructures doped with thiourea bring about growing good-quality nanorods. Tuning of the exciton lifetime of ZnO nanostructure, depending on morphology, is desirable result in nanotechnological applications.

4. Conclusion

A little addition of thiourea into ZnCl$_2$ solution (ZnCl$_2$: tu = 1 : 0.25) provides thinner ZnO nanorods with the higher aspect ratio compared to that obtained from pure ZnCl$_2$ solution. The diameter of the ZnO nanorods was decreased from 1000 nm to 500 nm, while their lengths increased to about 200 nm by thiourea doping as seen by SEM images. At the same time, the number of the nanorods and the width of the zinc oxide surface per unit area increased. As a result of time-resolved photoluminescence studies, the lifetime of ZnO nanorods and ZnO nanorods containing thiourea was determined as $\tau = 1.56 \pm 0.05$ ns ($\chi^2 = 0.9$) and $\tau = 2.12 \pm 0.03$ ns ($\chi^2 = 1.0$), respectively. The results indicated that the exciton lifetime of ZnO nanorods containing thiourea increased through an increase in radiative recombination. It is clearly seen that the lifetime of ZnO nanorods is strongly dependant on the presence of the morphological differences between ZnO nanorods and ZnO nanorods containing thiourea. Summary, it is mentioned that the doping material prevents the nucleation of the sample and improves the exciton lifetime of synthesized ZnO nanorods. Discussion on the presented results in this study has a great potential for the application of ZnO in optoelectronic systems.

References

[1] M. Willander, O. Nur et al., "Zinc oxide nanorod based photonic devices: recent progress in growth, light emitting diodes and lasers," *Nanotechnology*, vol. 20, no. 33, Article ID 332001, pp. 1–40, 2009.

[2] D. G. Thomas, "The exciton spectrum of zinc oxide," *Journal of Physics and Chemistry of Solids*, vol. 15, no. 1-2, pp. 86–96, 1960.

[3] D. M. Bagnall, Y. F. Chen, Z. Zhu, T. Yao, M. Y. Shen, and T. Goto, "High temperature excitonic stimulated emission from ZnO epitaxial layers," *Applied Physics Letters*, vol. 73, no. 8, pp. 1038–1040, 1998.

[4] M. H. Huang, S. Mao, H. Feick et al., "Room-temperature ultraviolet nanowire nanolasers," *Science*, vol. 292, no. 5523, pp. 1897–1899, 2001.

[5] A. B. Djurišić and Y. H. Leung, "Optical properties of ZnO nanostructures," *Small*, vol. 2, no. 8-9, pp. 944–961, 2006.

[6] Ü. Özgür, Y. I. Alivov, C. Liu et al., "A comprehensive review of ZnO materials and devices," *Journal of Applied Physics*, vol. 98, no. 4, Article ID 041301, pp. 1–103, 2005.

[7] S. Chen, Y. Liu, C. Shao et al., "Structural and optical properties of uniform ZnO nanosheets," *Advanced Materials*, vol. 17, no. 5, pp. 586–590, 2005.

[8] A. Tsukazaki, A. Ohtomo, T. Onuma et al., "Repeated temperature modulation epitaxy for p-type doping and light-emitting diode based on ZnO," *Nature Materials*, vol. 4, no. 1, pp. 42–45, 2005.

[9] S. F. Chichibu, T. Onuma, M. Kubota et al., "Improvements in quantum efficiency of excitonic emissions in ZnO epilayers by the elimination of point defects," *Journal of Applied Physics*, vol. 99, no. 9, Article ID 093505, 2006.

[10] J. Koida, S. F. Chichibu, A. Uedono, T. Sota, A. Tsukazaki, and M. Kawasaki, "Radiative and nonradiative excitonic transitions in nonpolar (11$\bar{2}$0) and polar (000$\bar{1}$) and (0001) Zno epilayers," *Applied Physics Letters*, vol. 84, no. 7, pp. 1079–1081, 2004.

[11] T. Koida, A. Uedono, A. Tsukazaki, T. Sota, M. Kawasaki, and S. F. Chichibu, "Direct comparison of photoluminescence lifetime and defect densities in ZnO epilayers studied by time-resolved photoluminescence and slow positron annihilation techniques," *Physica Status Solidi A*, vol. 201, no. 12, pp. 2841–2845, 2004.

[12] A. Teke, Ü. Özgür, S. Doğan et al., "Excitonic fine structure and recombination dynamics in single-crystalline ZnO," *Physical Review B*, vol. 70, no. 19, Article ID 195207, pp. 1–10, 2004.

[13] X. H. Zhang, S. J. Chua, A. M. Yong et al., "Exciton radiative lifetime in ZnO nanorods fabricated by vapor phase transport method," *Applied Physics Letters*, vol. 90, no. 1, Article ID 013107, 2007.

[14] X. H. Zhang, S. J. Chua, A. M. Yong et al., "Exciton radiative lifetime in ZnO quantum dots embedded in SiOx matrix," *Applied Physics Letters*, vol. 88, no. 22, Article ID 221903, 2006.

[15] G. Xiong, U. Pal, and J. G. Serrano, "Correlations among size, defects, and photoluminescence in ZnO nanoparticles," *Journal of Applied Physics*, vol. 101, no. 2, Article ID 024317, 2007.

[16] N. C. Giles, C. Xu, M. J. Callahan, B. Wang, J. S. Neal, and L. A. Boatner, "Effects of phonon coupling and free carriers on band-edge emission at room temperature in n-type ZnO crystals," *Applied Physics Letters*, vol. 89, no. 25, Article ID 251906, 2006.

[17] A. B. Djurišić, Y. H. Leung, K. H. Tam et al., "Defect emissions in ZnO nanostructures," *Nanotechnology*, vol. 18, no. 9, Article ID 095702, 2007.

[18] W. M. Kwok, A. B. Djurišić, Y. H. Leung, W. K. Chan, and D. L. Phillips, "Time-resolved photoluminescence from ZnO nanostructures," *Applied Physics Letters*, vol. 87, no. 22, Article ID 223111, pp. 1–3, 2005.

[19] X. Zhou, Q. Kuang, Z. Y. Jiang et al., "The origin of green emission of ZnO microcrystallites: surface-dependent light emission studied by cathodoluminescence," *Journal of Physical Chemistry C*, vol. 111, no. 32, pp. 12091–12093, 2007.

[20] M. D. McCluskey and S. J. Jokela, "Sources of n-type conductivity in ZnO," *Physica B*, vol. 401-402, pp. 355–357, 2007.

[21] Z. Qiu, K. S. Wong, M. Wu, W. Lin, and H. Xu, "Microcavity lasing behavior of oriented hexagonal ZnO nanowhiskers grown by hydrothermal oxidation," *Applied Physics Letters*, vol. 84, no. 15, pp. 2739–2741, 2004.

[22] Y. Zhong, A. B. Djurišić, Y. F. Hsu et al., "Exceptionally long exciton photoluminescence lifetime in ZnO tetrapods," *Journal of Physical Chemistry C*, vol. 112, no. 42, pp. 16286–16295, 2008.

[23] J. Shi, J. Chen, Z. Feng et al., "Time-resolved photoluminescence characteristics of subnanometer ZnO clusters confined in the micropores of zeolites," *Journal of Physical Chemistry B*, vol. 110, no. 51, pp. 25612–25618, 2006.

[24] A. V. Kavokin, G. Malpuech, and W. Langbein, "Theory of propagation and scattering of exciton-polaritons in quantum wells," *Solid State Communications*, vol. 120, no. 7-8, pp. 259–263, 2001.

[25] B. Gil and A. V. Kavokin, "Giant exciton-light coupling in ZnO quantum dots," *Applied Physics Letters*, vol. 81, no. 4, pp. 748–750, 2002.

[26] S. Hong, T. Joo, W. Park, Y. H. Jun, and G. C. Yi, "Time-resolved photoluminescence of the size-controlled ZnO nanorods," *Applied Physics Letters*, vol. 83, no. 20, pp. 4157–4159, 2003.

[27] S. Musić, A. Šarić, and S. Popović, "Dependence of the microstructural properties of ZnO particles on their synthesis," *Journal of Alloys and Compounds*, vol. 448, no. 1-2, pp. 277–283, 2008.

[28] W. I. Park, D. H. Kim, S. W. Jung, and G. C. Yi, "Metalorganic vapor-phase epitaxial growth of vertically well-aligned ZnO nanorods," *Applied Physics Letters*, vol. 80, no. 22, pp. 4232–4234, 2002.

[29] J. Y. Park, D. J. Lee, Y. S. Yun, J. H. Moon, B. T. Lee, and S. S. Kim, "Temperature-induced morphological changes of ZnO grown by metalorganic chemical vapor deposition," *Journal of Crystal Growth*, vol. 276, no. 1-2, pp. 158–164, 2005.

[30] J.-H. Park, Y.-J. Choi, W.-J. Ko, I.-S. Whang, and J.-G. Park, "ZnO nanorods grown by a pulsed laser deposition process," *Materials Research Society Symposium Proceedings*, vol. 848, Article ID FF9.7, pp. 421–426, 2005.

[31] Z. W. Liu, C. K. Ong, T. Yu, and Z. X. Shen, "Catalyst-free pulsed-laser-deposited ZnO nanorods and their room-temperature photoluminescence properties," *Applied Physics Letters*, vol. 88, no. 5, Article ID 053110, pp. 1–3, 2006.

[32] Y. C. Wang, I. C. Leu, and M. H. Hon, "Preparation of nanosized ZnO arrays by electrophoretic deposition," *Electrochemical and Solid-State Letters*, vol. 5, no. 4, pp. C53–C55, 2002.

[33] M. J. Zheng, L. D. Zhang, G. H. Li, and W. Z. Shen, "Fabrication and optical properties of large-scale uniform zinc oxide nanowire arrays by one-step electrochemical deposition technique," *Chemical Physics Letters*, vol. 363, no. 1-2, pp. 123–128, 2002.

[34] M. H. Huang, Y. Wu, H. Feick, N. Tran, E. Weber, and P. Yang, "Catalytic growth of zinc oxide nanowires by vapor transport," *Advanced Materials*, vol. 13, no. 2, pp. 113–116, 2001.

[35] N. Pan, X. Wang, K. Zhang et al., "An approach to control the tip shapes and properties of ZnO nanorods," *Nanotechnology*, vol. 16, no. 8, pp. 1069–1072, 2005.

[36] H. Zhu, D. Yang, and H. Zhang, "A simple and novel low-temperature hydrothermal synthesis of ZnO nanorods," *Inorganic Materials*, vol. 42, no. 11, pp. 1210–1214, 2006.

[37] F. Li, Z. Li, and F. J. Jin, "Structural and luminescent properties of ZnO nanorods prepared from aqueous solution," *Materials Letters*, vol. 61, no. 8-9, pp. 1876–1880, 2007.

[38] L. Vayssieres, "Growth of arrayed nanorods and nanowires of ZnO from aqueous solutions," *Advanced Materials*, vol. 15, no. 5, pp. 464–466, 2003.

[39] E. Sonmez, T. Karacali, A. E. Ekinci, and M. Ertugrul, "Optical properties of ZnO nanorods on glass via spray deposition of solution containing zinc chloride and thiourea," *IEEE Transactions on Nanotechnology*, vol. 10, no. 3, pp. 532–536, 2011.

[40] T. Dedova, O. Volobujeva, J. Klauson, A. Mere, and M. Krunks, "ZnO nanorods via spray deposition of solutions containing zinc chloride and thiocarbamide," *Nanoscale Research Letters*, vol. 2, no. 8, pp. 391–396, 2007.

[41] T. Schilling and D. Frenkel, "Self-poisoning of crystal nuclei in hard-rod liquids," *Journal of Physics Condensed Matter*, vol. 16, no. 19, pp. S2029–S2036, 2004.

Research Article

Mixed Nanostructured Ti-W Oxides Films for Efficient Electrochromic Windows

Nguyen Nang Dinh,[1] Dang Hai Ninh,[1] Tran Thi Thao,[1] and Truong Vo-Van[2]

[1] *University of Engineering and Technology, Vietnam National University, Hanoi, 144 Xuan Thuy Street,*
   Cau Giay, Hanoi 10000, Vietnam
[2] *Department of Physics, Concordia University, 7141 Sherbrooke Street West, Montreal, QC, Canada H4B 1R6*

Correspondence should be addressed to Nguyen Nang Dinh, dinhnn@vnu.edu.vn

With the aim to enhance the electrochromic (EC) efficiency and electrochemical stability of electrochromic devices (ECD), mixed nanostructured TiO_2/WO_3 films were prepared by an electrochemical deposition method with the purpose of adding WO_3 nanoparticles to porous nanocrystalline doctor-blade TiO_2 (nc-TiO_2) films. The results of the characterization of electrochromic properties in 1 M $LiClO_4$ + propylene carbonate ($LiClO_4$ + PC) of both the nc-TiO2/F-doped tin oxide (FTO) and $WO_3/TiO_2/FTO$ configurations showed the reversible coloration and bleaching of the ECDs. The response time of the ECD coloration of $WO_3/TiO_2/FTO$ was found to be as small as 2 sec, and its coloration efficiency (CE) as high as 35.7 $cm^2 \times C^{-1}$. By inserting WO_3 nanoparticles into the porous TiO_2 structures, WO_3/TiO_2 heterojunctions were formed in the films, consequently enabling both the CE and electrochemical stability of the working electrodes to be considerably enhanced. Since a large-area WO_3/TiO_2 can be prepared by the doctor-blade technique followed by the electrochemical deposition process, mixed nanostructured Ti-W oxides electrodes constitute a good candidate for smart window applications, taking advantage of the excellent coloration and stability properties as well as the simple and economical fabrication process involved.

1. Introduction

Electrochromism is a topic that has attracted a great deal of interest from researchers because of its potential application in various areas (photonics, optics, electronics, architecture, etc.). Electrochromic (EC) properties can be found in almost all the transition-metal oxides, and their properties have been investigated extensively in the last decades [1]. These oxide films can be coloured anodically (Ir, Ni) or cathodically (W, Mo); however, WO_3 is clearly the preferred material for applications. This is principally due to the fact that WO_3-based electrochromic devices (ECDs) have normally a faster response time to a change in voltage and a larger coloration efficiency (CE) as compared to devices based on other electrochromic materials. Recently, Granqvist et al. [2] have made a comprehensive review of nanomaterials for benign indoor environments. In this paper, the authors show the characteristic data for a 5×5 cm^2 flexible EC foil incorporating WO_3, and NiO modified by the addition of a wide

bandgap oxide such as MgO or Al_2O_3, PMMA-based electrolyte, and ITO films. Durability of the EC devices was demonstrated in performing several tens of thousands of coloration/bleaching cycles, and the device optical properties were found to be unchanged for many hours. To improve further the electrochromic properties, Ti-doped WO_3 films were deposited by cosputtering metallic titanium and tungsten in an Ar/O_2 atmosphere [3]. Another way to improve electrochromic properties of thin films is to use nanostructured crystalline films. For instance, nanocrystalline WO_3 films were prepared by the organometallic chemical vapour deposition (OMCVD) method using tetra(allyl)tungsten. The size of grains found in these films was estimated by atomic force microscope (AFM) and scanning electron microscope (SEM) to be 20 ÷ 40 nm. The coloration of WO_3 deposited on indium tin oxides (ITO) substrates (WO_3/ITO) in 2 M HCl was less than 1 sec and the maximum coloration efficiency at 630 nm was 22 $cm^2 \times C^{-1}$ [4]. However, the HCl electrolyte is not suitable for practical use. The Au-doped WO_3 films were

made by a dip-coating technique [5]. With fabrication of nanostructured WO_3 films, Beydaghyan et al. [6] have shown that porous and thick WO_3 films can produce a high CE. The open structure, fast response, and high normal state transmission made them good candidates for use in practical applications. The nanocrystalline TiO_2 anatase thin films on ITO, prepared by sol-gel dipping method, exhibited a good reversible coloration and bleaching process [7], but the response time was slow and the electrochromic efficiency was not large. Recently [8], we have shown that by using the so-called "doctor-blade" method, nanoporous TiO_2 anatase films on F-doped tin oxide (FTO) substrates (nc-TiO_2/FTO) were prepared for the ECDs with much improved electrochromic response time and coloration efficiency (CE). However, with such porous films, for a long exposed performance time, the durability of the devices was limited, making the resulting ECD less satisfying for smart windows applications. In this work, with the aim to enhance the stability of the EC devices on one hand by making more tightly knitted films, and on the other hand, to improve the CE of the ECD performance with the help of nanostructured heterojunctions of TiO_2/WO_3, we combined a doctor-blade technique for preparing large-area films with an electrochemical process for depositing WO_3 films into the nanoporous TiO_2 structures.

2. Experimental

To prepare nanostructured TiO_2 films for ECD, a doctor-blade technique was used following the process reported in [8]. A glass slide, overcoated with a $0.2 \mu m$ thick FTO film having a sheet resistance of 15Ω and a transmittance of 90%, was used as a substrate; the useful area that constitutes the sample studied was of $1 cm^2$. A colloidal solution of 15 wt% nanoparticles (15 nm in size) of titanium oxide (Nyacol Products) in water was used. For producing thinner films, we added more distilled water to get ca. 5 wt% TiO_2 and a few drops of the liquid surfactant were added. Then the diluted solution was filled in the slot on the FTO electrode and spread along the tapes. The samples were left for drying during 15 min, then put to a furnace maintained at $450°C$ for 1 hour to recrystallize the nc-TiO_2 films.

To deposit WO_3 into nc-TiO_2/FTO, the peroxy-tungsten acid solution ($H_2W_2O_{11}$) was prepared. For this 4.6 g of high-purity metallic tungsten powder was dissolved in 25 ml H_2O_2 (30%). The excess H_2O_2 was decomposed by putting a large-area Pt sheet into the solution until gas evolution was stopped. After that, the solution was diluted to 50 mM by addition of water to form 500 mL of the solution and kept in cool air to avoid decomposition of peroxy tungstate to trioxide and polytungstate [9]. A standard three-electrode cell has been used: the working electrode was F-doped-SnO_2 coated glass (FTO) with a sheet resistance of 15Ω the reference electrode was saturated calomel electrode (SCE); a Pt grille was used as counter electrode. By using potentiostat "Auto lab. PGS-30," a potentiostatic method was chosen for film deposition. After their deposition, the films were dried in nitrogen gas. Electrochromic properties of the films were
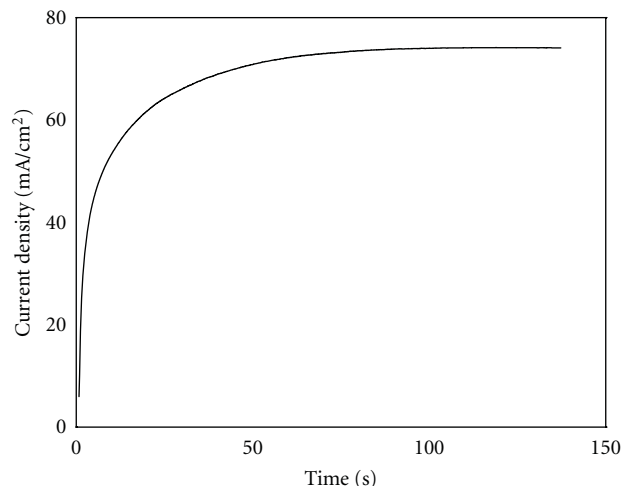

Figure 1: The time dependence of the current density during electrochemical deposition of WO_3 under a negatively polarized potential of -1.5 V/SCE.

determined by cyclic voltametry in electrolytic solutions of 1 M $LiClO_4$ + Propylene carbonate (PC).

The film thickness was measured by an Alpha-step profiler and its surface morphology examined with the help of a field-emission scanning electron microscope (FE-SEM). X-ray diffraction analysis (XRD) was done on a Brucker "Advance-8D" X-ray diffractometer with X-ray Cu wavelength $\lambda = 0.154$ nm. Electrochemical processes were carried-out on the same potentiostat. All measurements were executed at room temperature.

By using a JASCO "V-570" photospectrometer, *in situ* transmittance spectra of nc-TiO_2 in $LiClO_4$ + PC versus bias potential were recorded on the films of the working electrode mounted in a modified electrochemical cell which was placed under the pathway of the laser beam, and the three cell electrodes were connected to a potentiostat.

3. Results and Discussion

3.1. Electrochemical Deposition. Under an application of the potential of -1.5 V/SCE, the fact that the current density was increased with the increase in time would prove that W^{6+} was inserted into the working electrode with a compensation of negative charges (e^-). Due to the bonding of W^{6+} with O^{2-} ions, WO_3 was formed. This further was confirmed by XRD analysis (see the next section). From all the deposition experiments, it was seen that the current density increased fast and reached a saturate value in 40 sec (Figure 1).

With this interval, the WO_3 volume almost filled up the pores in the porous TiO_2 film, and then stopped increasing at the saturate current density. However, the total time of 130 sec for the deposition was chosen. The thickness of as-deposited WO_3/TiO_2 films, checked on the Alpha-Step Pro-filer, was of ~570 nm. These films were slightly thicker than the initial doctor-blade nc-TiO_2 films (namely 550 nm).
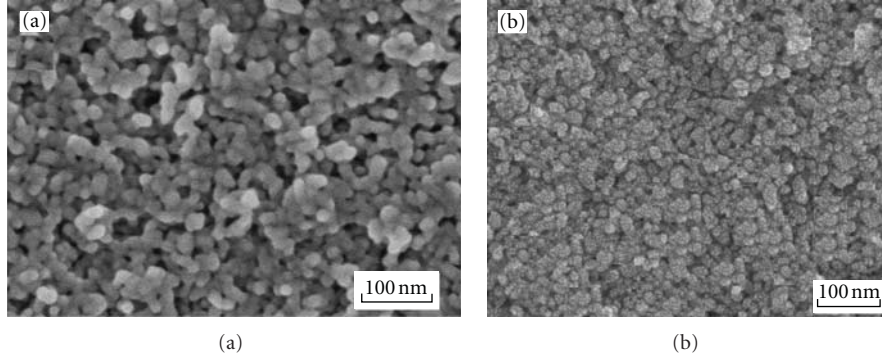
(a)

(b)

Figure 2: FE-SEM micrographs of as-prepared nc-TiO$_2$ films (a) and after the electrochemical deposition process in a H$_2$W$_2$O$_{11}$ electrolyte (b).

3.2. Morphology and Crystalline Structure.

In the doctor-blade deposition, the thickness of the films was found to be depending on preparation conditions such as the concentration of solutions and the spread speed. The samples used for further investigation were taken from films chosen with a concentration of 5 wt% TiO$_2$ in water and a spread speed of 8 mm/s. A bright-field micrograph of the film surface is shown in Figure 2(a). The film is quite uniform, but some crystallized nanoparticles are a little larger than the initial TiO$_2$ particles dispersed in water (namely 20 nm in size). The thickness of the films was of ca. 550 nm. In comparison with the nanostructured films prepared by sol-gel method [7], these films are thicker and much more porous. Thus, between the nc-TiO$_2$ particles, there are numerous nanoscale pores which would favour the insertion of ions like Li$^+$, Na$^+$, and/or W^{6+} into the films, when a polarized potential is applied on the working electrode (nc-TiO$_2$/FTO). With the insertion of the Li$^+$, one can obtain the ECD coloration, whereas the insertion of W^{6+} during the electrochemical deposition would result in the insertion of WO$_3$ nanoparticles into the pores of the nanostructured TiO$_2$ film. Figure 2(b) shows the FE-SEM of the surface of the TiO$_2$ electrode after the electrochemical process in the H$_2$W$_2$O$_{11}$ solution. During the deposition, we observed that the TiO$_2$/FTO electrode was coloured and became deep-blue with the increase in the deposition time. This coloration can be attributed to the insertion of W^{6+} (the ions from the H$_2$W$_2$O$_{11}$ electrolyte) into the TiO$_2$ films according to the following equation:

$$\text{TiO}_2\,(\text{transparent}) + x\text{W}^{3+} + xe^- \longrightarrow \text{W}_x\text{TiO}_2(\text{blue}), \tag{1}$$
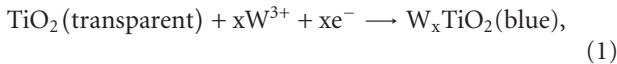
where W^{6+} plays the role of Li$^+$ in the well-known equation [10]:

$$\text{TiO}_2\,(\text{transparent}) + x(\text{Li}^+ + e^-) \longrightarrow \text{Li}_x\text{TiO}_2(\text{blue}). \tag{2}$$
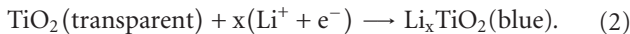
From our previous work [11], it was shown that an electrochromic WO$_3$ film was deposited onto the FTO electrode by the electrochemical technique. Hereby, simultaneously with the EC coloration, one can deposit WO$_3$ particles into

TiO$_2$/FTO to form a film with heterojunctions of WO$_3$/TiO$_2$ created from a mixture of WO$_3$ and TiO$_2$ nanoparticles. This would lead to the different features observed in the FE-SEM picture of the WO$_3$/TiO$_2$ film (Figure 2(b)) as compared to the FE-SEM picture for a nc-TiO$_2$ film (Figure 2(a)).

The crystalline structure of the films was confirmed by using an accessory for films with a small angle of the X-ray incident beam. For such a thick film of nc-TiO$_2$, all XRD patterns of the FTO substrate do not appear (Figure 3(a)). XRD patterns show all the diffraction peaks corresponding to titanium oxide. Indeed, for the doctor-blade film, in the XRD patterns, there are the most intense peak of the (101) direction corresponding to $d = 0.352$ nm and three smaller peaks corresponding to 0.238, 0.190, and 0.149 nm. These diffraction peaks are quite consistent with the peaks for a single crystal of TiO$_2$ anatase.

The fact that the peak width is rather small shows that the TiO$_2$ anatase film was crystallized into large grains. To obtain the grain size τ, we used the Scherrer formula:

$$\tau = \frac{0.9\,\lambda}{\beta \cdots \cos\theta}, \tag{3}$$

where λ is wavelength of the X-ray used ($\lambda = 0.154$ nm), β the peak width of half height in radians and θ the Bragg angle of the considered diffraction peak [12]. From the XRD patterns, the half-height peak width of the (101) direction was found to be $\beta = 0.005$, consequently, the size of (101) grain was determined as $\tau \approx 20$ nm. Similarly, the size for the other grains was found to be from 25 to 30 nm. This is in good agreement with data obtained by FE-SEM for the average size of particles where the crystalline grains were not identified by the Miller indexes (see Figure 2(a)).

The XRD patterns of the WO$_3$/TiO$_2$ (Figure 3(b)) possess both the peaks of TiO$_2$ and WO$_3$, where one peak of (004) direction of TiO$_2$ was not revealed and relative intensity of the peaks changed a little bit. This is due to the presence of WO$_3$ particles, whose average size, estimated by formula (1), is the same as the size of pores. This result, together with the observation of the FE-SEM pictures (Figure 1), demonstrates that WO$_3$ particles were indeed filling-up the nanopores of the porous nc-TiO$_2$ film.

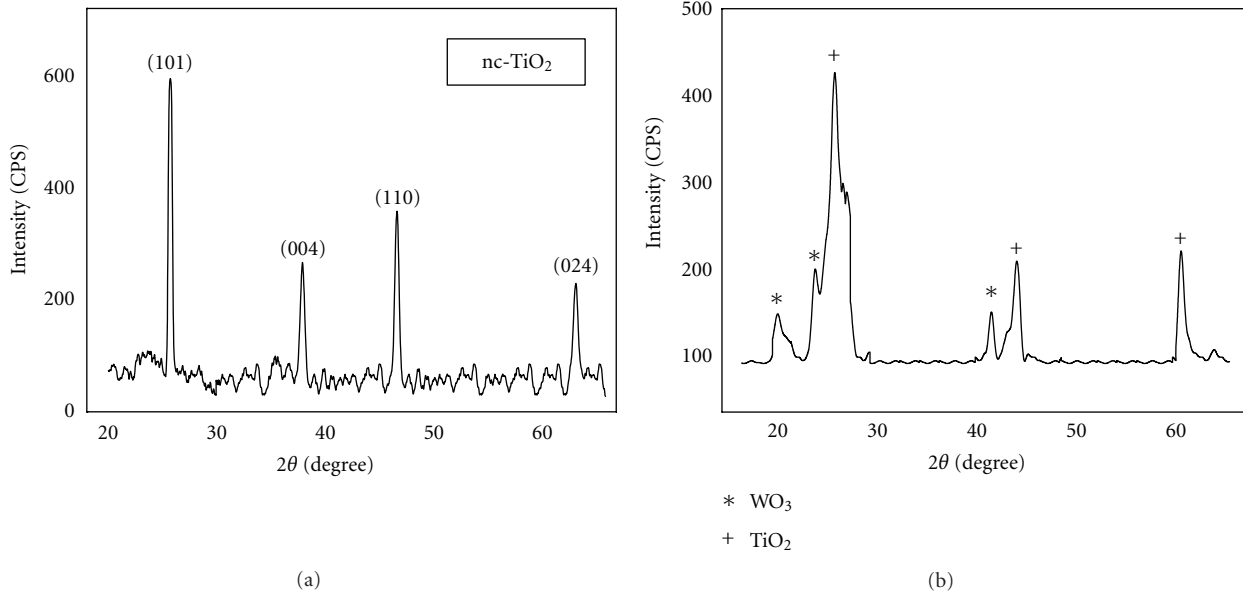(a)

*   WO₃

+   TiO₂

(b)

FIGURE 3: XRD of a nc-TiO₂ doctor-blade film (a) and of a WO₃/TiO₂ film coated by electrochemical deposition.

3.3. Electrochemical Property.

Figure 4 presents a chronoamperometric plot obtained by setting up five lapses of 5 sec for the coloration and bleaching, corresponding to −1.50 V/SCE and to +1.50 V/SCE, respectively. To calculate the inserted charge (Q) for the coloration state, we use the formula for integrating between the starting and ending times of each lapse of time as follows:

$$Q = \int_{t_1}^{t_2} J(t)dt. \tag{4}$$

The insertion charge was found to be Q_{in} = 21 mC × cm⁻², whereas for the extraction process the charge was Q_{ex} = 19 mC × cm⁻², that is slightly different from the insertion charge. The fact that the insertion and extraction charges are similar proves the reversibility of the electrochromic coloration/bleaching process—a desired characteristic for the electrochromic performance of the WO₃/TiO₂-based electrochromic devices.

Figure 5 shows the cyclic voltammetry (CV) spectra of a WO₃/TiO₂/FTO electrode cycled in 1 M LiClO₄ + PC. In the positive scanning direction (PSD) there are two peaks of the current density at potentials of −1.0 V/SCE and at −0.32 V/SCE. In the negative scanning direction (NSD) there are also two similar peaks. This proves the reversibility of the insertion/extraction of Li⁺ into/out of the WO₃/TiO₂/FTO electrode. Moreover, the CV spectra of the WO₃/TiO₂/FTO electrode possess a different characteristic from the one of each compound for either WO₃/FTO or TiO₂/FTO. These CV spectra can be seen as just the CV of a mixture of WO₃ and TiO₂ electrodes cycled simultaneously in LiClO₄ + PC electrolyte.

Therefore the electrochromic performance of the WO₃/TiO₂/FTO electrode in LiClO₃ + PC can be described by two
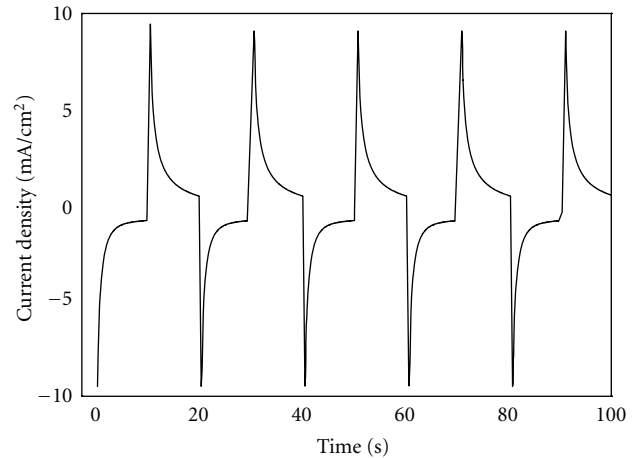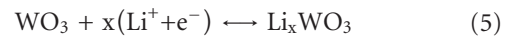

FIGURE 4: Insertion and extraction of Li⁺ ions into/out of the WO₂/TiO₂/FTO electrode. The inserted charge (a bottom half cycle) of the saturated coloration state and the completely bleaching state (a top half cycle), respectively, are Q_{in} = 21 mC × cm⁻² and Q_{ex} = 19 mC × cm⁻².

cathodic reactions; one is [13, 14]:

$$WO_3 + x(Li^+ + e^-) \longleftrightarrow Li_x WO_3 \tag{5}$$

and the other one is reaction (2).

3.4. Electrochromic Performance.

For a sample with a 570 nm thick WO₃/TiO₂ film, the *in situ* transmission spectra, obtained during coloration at a polarized potential of −1.2 V/SCE are given in Figure 6.

Figure 6 shows the transmittance of a 570 nm thick WO₃/TiO₂ film in 1 M LiClO₄ + PC at different polarizing bias potentials (from −0.5 V/SCE to + 0.3 V/SCE). From this

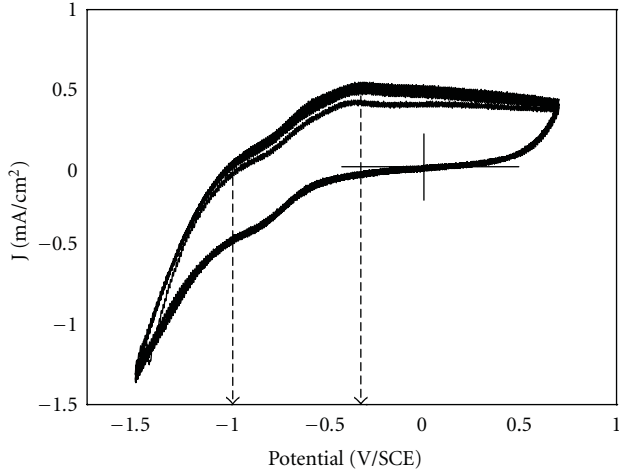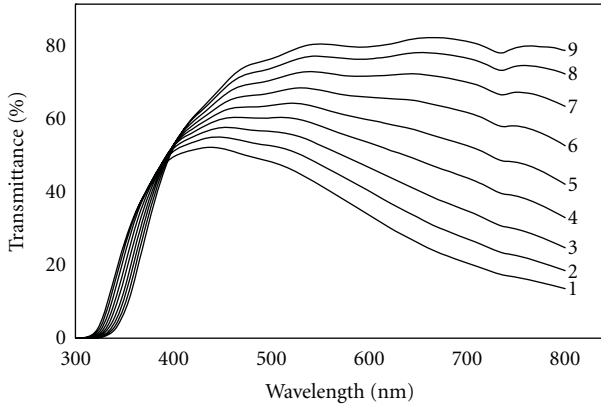FIGURE 5: Cyclic voltammetry spectra of WO$_3$/TiO$_2$/FTO cycled in LiClO$_4$ + PC (scanning rate v = 100 mV/s).

FIGURE 6: Transmittance spectra of the WO$_3$ film filled in 1 M LiClO$_4$ + PC solution with polarized potential ranging from −0.5 V/SCE to +0.3 V. Curves 1, 2, 3, 4, 5, 6, 7, 8, and 9 correspond, respectively, to −0.5, −0.4, −0.3, −0.2, −0.1, 0, +0.1, +0.2, and +0.3 V/SCE.

figure, one can see a large difference in transmittance spectra in the visible range of the film between the colored (curve 1) and bleached (curve 9) states. The transmittance at λ = 550 nm (the sensitivity peak of human eye) from ∼85% with the bleached state decreased to 40% with the colored state, corresponding respectively to bias potential from +0.3 V/SCE to −0.5 V/SCE. This result indicates that the electrochemically deposited WO$_3$/TiO$_2$ films exhibited an excellent EC performance that can be comparable to the one of the cosputtered Ti-doped WO$_3$ films, as reported in [3]. The transmittance decreases with the increasing of the bias potential in NSD interval.

The bleaching and coloration processes were measured under the application of negatively and positively polarized voltage to the working electrode, respectively. These processes were clearly associated with the Li$^+$ insertion (extraction) from the LiClO$_4$ + PC electrolyte into (out of) the WO$_3$/TiO$_2$/FTO electrode. In comparison with results
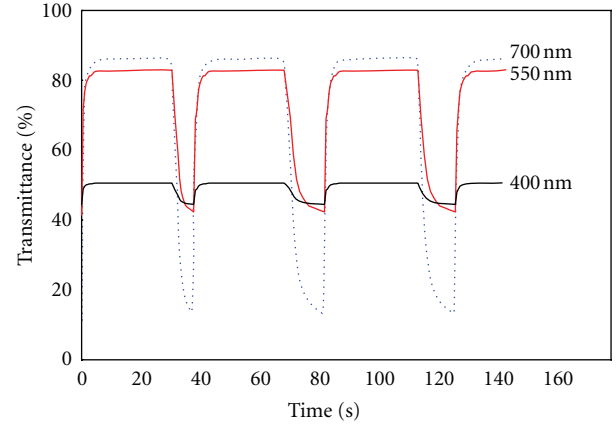

FIGURE 7: Time-dependence transmittance of the WO$_3$/TiO$_2$/FTO during electrochromic performance for three different wavelengths: 400, 550, and 700 nm.

reported previously [8], the optical modulation at the visible range for WO$_3$/TiO$_2$/FTO at longer wavelengths is improved. Herein, we attained a transmittance at λ = 550 nm (T$_{550}$) equal to 84% upon bleaching and to 42% after a coloration period of 30 s. The largest optical modulation in the visible range was observed for red light (T$_{700}$) as seen in Figure 7: the gap between the transmittances of bleaching and coloration states was of 70%. For blue light (T$_{400}$), the optical modulation at wavelength 400 nm was negligible, that is about 5%. This would result from the strong absorption by both WO$_3$ and TiO$_2$ at shorter wavelengths.

From the above-mentioned results for the ECDs with heterojunctions of WO$_3$/nc-TiO$_2$, it is seen that the efficient coloration can be achieved due to a double-coloration process, such as shown in (2) and (5). To evaluate the electrochromic coloration efficiency (η) we used a well-known expression relating the efficiency with the optical density (ΔOD), consequently the transmittances of coloration (T_c) and bleaching states (T_b), and the insertion charge (Q), as follows [15]:

$$\eta = \frac{\Delta \text{OD}}{Q} = \frac{1}{Q}\ln\left(\frac{T_b}{T_c}\right). \qquad (6)$$

At a wavelength of 550 nm, Q_{in} = 21 mC × cm^{-2}, T_b = 85% and T_c = 40%, the coloration efficiency was determined to be 35.7 cm^2× C^{-1}. The larger the wavelength is, the higher the coloration efficiency is. In the visible range of wavelengths, all the found values of η are comparable to those for WO$_3$ films [16] and much higher than those for TiO$_2$ films [7] prepared by sol-gel techniques and titanium-lanthanide oxides deposited by magnetron sputtering and coloured in a LiClO$_4$ + PC solution [17].

To investigate the ageing process of two types of electrochromic devices, the first one is made from nc-TiO$_2$ and the second one from WO$_3$/nc-TiO$_2$ electrode, we measured the optical density versus bias potential after cycling these electrodes in 1 M LiClO$_4$ + PC for 10^3 cycles. At a fixed wavelength, the larger is the difference between $T_c(\lambda)$ of the colored state and $T_b(\lambda)$ of the bleached state, the higher is
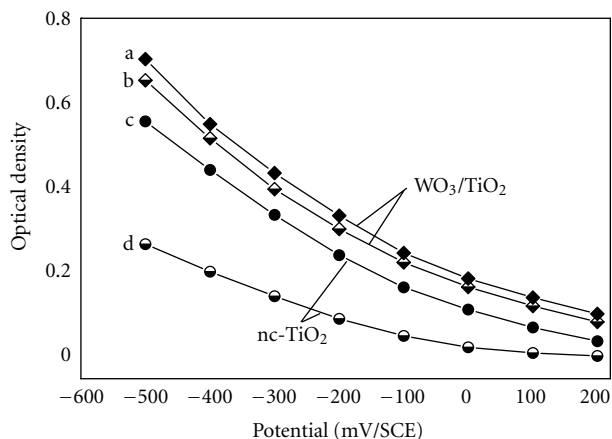
Figure 8: The potential dependence of the optical density of nc-TiO$_2$/FTO (two bottom curves) and WO$_3$/TiO$_2$/FTO (two top curves) electrodes during electrochromic performance in 1 M LiClO$_4$ + PC for as-prepared (a; c) and after cycling for 10^3 cycles (b; d).

the value of ΔOD. The potential dependence of ΔOD at λ = 550 nm for two above-mentioned electrodes is shown in Figure 8. From this figure, we can see that for both the mentioned electrodes, the best optical density has been found for the bias potential of -0.5 V/SCE. At this potential, the largest number of Li$^+$ cations would be inserted into the electrodes making the TiO$_2$ and WO$_3$ structures change to Li$_x$TiO$_2$ to Li$_x$WO$_3$, respectively. The number of colour centers (namely Li$_x$TiO$_2$ and Li$_x$WO$_3$) is dependent on the number of Li$^+$ cations and electrons injected into the electrodes. In general, this number increases proportionally to the bias potential applied on the working electrode. The reason why the ΔOD of the nc-TiO$_2$ based ECD decreased faster than that of WO$_3$/TiO$_2$ is revealed by the monitoring of the film thickness of the electrodes during the electrochromic performance. After 10^3 cycles of the ECD performance, the thickness of both electrodes was checked with the Alpha step profiler, and it was found that a part of the nc-TiO$_2$ film was removed while the WO$_3$/nc-TiO$_2$ was maintained almost unchanged. This demonstrates that WO$_3$ attached to TiO$_2$ particles enables the structure of WO$_3$/nc-TiO$_2$ film to be much more strengthened. Thus the devices with WO$_3$/TiO$_2$ nano-heterojunctions would possess a larger ECD lifetime.

4. Conclusion

Mixed nanostructured Ti-W oxides films were prepared by electrochemical deposition of WO$_3$ onto doctor-blade nc-TiO$_2$/FTO films. Electrochromic performance studies of both the nc-TiO$_2$/FTO and WO$_3$/TiO$_2$/FTO configurations were carried out in 1 M LiClO$_4$ + propylene carbonate. The reversible coloration and bleaching process of WO$_3$/TiO$_2$-based electrochromic devices was demonstrated. The response time of the ECD coloration of WO$_3$/TiO$_2$/FTO was found to be as small as 2 s and the coloration efficiency could be as high as 35.7 cm$^2 \times$ C^{-1}. *In situ* transmittance spectra of the WO$_3$/TiO$_2$/FTO working electrode showed the

insertion/extraction of Li$^+$ ions into/out of the electrode. By incorporating WO$_3$ inserted between TiO$_2$ nanoparticles, WO$_3$/TiO$_2$ heterojunctions were formed in the films. The resulting nanostructured film enables both the coloration efficiency and electrochemical stability of the working electrodes to be considerably improved.

Since a large-area WO$_3$/TiO$_2$ electrode can be prepared by the doctor-blade method, followed by an electrochemical deposition, this type of electrode constitutes a good candidate for smart window applications, taking advantage of its excellent properties in terms of EC efficiency and electrochemical stability, as well as the simplicity of the fabrication process.

References

[1] C. G. Granqvist, *Handbook of Inorganic Electrochromic Materials*, Elsevier, Amsterdam, The Netherlands, 1995.

[2] C. G. Granqvist, A. Azens, P. Heszler, L. B. Kish, and L. Österlund, "Nanomaterials for benign indoor environments: electrochromics for "smart windows", sensors for air quality, and photo-catalysts for air cleaning," *Solar Energy Materials and Solar Cells*, vol. 91, no. 4, pp. 355–365, 2007.

[3] A. Karuppasamy and A. Subrahmanyam, "Studies on electrochromic smart windows based on titanium doped WO$_3$ thin films," *Thin Solid Films*, vol. 516, no. 2–4, pp. 175–178, 2007.

[4] L. Meda, R. C. Breitkopf, T. E. Haas, and R. U. Kirss, "Investigation of electrochromic properties of nanocrystalline tungsten oxide thin film," *Thin Solid Films*, vol. 402, no. 1-2, pp. 126–130, 2002.

[5] N. Naseri, R. Azimirad, O. Akhavan, and A. Z. Moshfegh, "Improved electrochromical properties of sol-gel WO$_3$ thin films by doping gold nanocrystals," *Thin Solid Films*, vol. 518, no. 8, pp. 2250–2257, 2010.

[6] G. Beydaghyan, G. Bader, and P. V. Ashrit, "Electrochromic and morphological investigation of dry-lithiated nanostructured tungsten trioxide thin films," *Thin Solid Films*, vol. 516, no. 8, pp. 1646–1650, 2008.

[7] N. N. Dinh, N. T. T. Oanh, P. D. Long, M. C. Bernard, and A. H. L. Goff, "Electrochromic properties of TiO$_2$ anatase thin films prepared by a dipping sol-gel method," *Thin Solid Films*, vol. 423, no. 1, pp. 70–76, 2003.

[8] N. Nang Dinh, N. Minh Quyen, D. N. Chung, M. Zikova, and V. V. Truong, "Highly-efficient electrochromic performance of nanostructured TiO$_2$ films made by doctor blade technique," *Solar Energy Materials and Solar Cells*, vol. 95, no. 2, pp. 618–623, 2011.

[9] E. A. Meulenkamp, "Mechanism of WO$_3$ electrodeposition from peroxy-tungstate solution," *Journal of the Electrochemical Society*, vol. 144, no. 5, pp. 1664–1671, 1997.

[10] G. Campet, J. Portier, S. J. Wen, B. Morel, M. Bourrel, and J. M. Chabagno, "Electrochromism and electrochromic windows," *Active and Passive Electronic Components*, vol. 14, pp. 225–231, 1992.

[11] P. D. Long, N. N. Dinh, M. C. Bernard, and A. H. Le Goff, "Preparation and study of electrochromic properties of tunsten oxides films made by electrochemical method," *Vietnam Communications in Physics*, vol. 10, no. 3, pp. 164–170, 2000.

[12] B. D. Cullity, *Elements of X-Ray Diffraction*, Addison-Wesley, Reading, Mass, USA, 2nd edition, 1978.

[13] Y. Shigesato, "Photochromic properties of amorphous WO_3 films," *Japanese Journal of Applied Physics*, vol. 30, no. 7, pp. 1457–1462, 1991.

[14] S. I. C. de Torresi, A. Gorenstein, R. M. Torresi, and M. V. Vázquez, "Electrochromism of WO_3 in acid solutions: an electrochemical, optical and electrogravimetric study," *Journal of Electroanalytical Chemistry*, vol. 318, no. 1-2, pp. 131–144, 1991.

[15] P. M. S. Monk, R. J. Mortimer, and D. R. Rosseinsky, *Electrochromism: Fundamentals and Applications*, Wiley-VCH, Weinheim, Germany, 1995.

[16] P. Delichère, P. Falaras, and A. Hugot-Le Goff, "WO_3 anodic films in organic medium for electrochromic display devices," *Solar Energy Materials*, vol. 19, no. 3–5, pp. 323–333, 1989.

[17] L. Kullman, A. Azens, and C. Granqvist, "Decreased electrochromism in Li-intercalated Ti oxide films containing La, Ce, and Pr," *Journal of Applied Physics*, vol. 81, no. 12, pp. 8002–8010, 1997.

Research Article

Metal-Catalyst-Free Synthesis and Characterization of Single-Crystalline Silicon Oxynitride Nanowires

Shuang Xi,[1] Tielin Shi,[1] Liangliang Xu,[2] Zirong Tang,[2] Dan Liu,[1] Xiaoping Li,[2] and Shiyuan Liu[1]

[1] *State Key Laboratory of Digital Manufacturing Equipment and Technology, Huazhong University of Science and Technology, Wuhan 430074, China*
[2] *Wuhan National Laboratory for Optoelectronics, Huazhong University of Science and Technology, Wuhan 430074, China*

Correspondence should be addressed to Zirong Tang, zirong@mail.hust.edu.cn

Large quantities of single-crystal silicon oxynitride nanowires with high N concentration have been synthesized directly on silicon substrate at 1200°C without using any metal catalyst. The diameter of these ternary nanowires is ranging from 10 to 180 nm with log-normal distribution, and the length of these nanowires varies from a few hundreds of micrometers to several millimeters. A vapor-solid mechanism was proposed to explain the growth of the nanowires. These nanowires are grown to form a disordered mat with an ultrabright white nonspecular appearance. The mat demonstrates highly diffusive reflectivity with the optical reflectivity of around 80% over the whole visible wavelength, which is comparable to the most brilliant white beetle scales found in nature. The whiteness might be resulted from the strong multiscattering of a large fraction of incident light on the disordered nanowire mat. These ultra-bright white nanowires could form as reflecting surface to meet the stringent requirements of bright-white light-emitting-diode lighting for higher optical efficiency. They can also find applications in diverse fields such as sensors, cosmetics, paints, and tooth whitening.

1. Introduction

In recent years, silicon oxynitride (SiO_xN_y) has received considerable attention as an important dielectric material, due to its superior electrical and physical properties [1]. The fully compatibility of this material with conventional Si processing technology greatly accelerates its application in electronic and optoelectronic devices [2]. SiO_xN_y has a static dielectric constant that increases linearly with the nitrogen concentration from SiO_2 ($\varepsilon = 3.8$) to Si_3N_4 ($\varepsilon = 7.8$) [3], and a large refractive index ranging from 1.45 up to 2.0 [4, 5]. A high concentration of nitrogen in SiO_xN_y is generally desired: by increasing N/O ratio, a higher dielectric constant and refractive index can be obtained [6, 7]. However, most of the silicon oxynitride materials studied up to now have a nitrogen concentration less than 15 at.% [8, 9], and primarily are amorphous SiO_xN_y films. As a result, the properties of silicon oxynitride materials with high N concentration remain largely unexplored [10].

On the other hand, one-dimensional nanostructures have attracted steadily growing interests due to their peculiar properties and applications superior to their bulk counterparts [11, 12]. For example, it has been demonstrated that nanowires actually can be grown to form one of the most strongly scattering materials in a recent study [13]. Light scattering in nanowire materials has also been shown significant importance to optimize the external efficiency of nanowire-based photovoltaic devices [14, 15]. Furthermore, multielement alloy nanowires possess the characteristics of variety by adjusting their chemical composition and physical structure. Therefore, it is important to synthesize 1D SiO_xN_y nanostructures and explore their properties. However, ternary SiO_xN_y nanowires, especially N-rich single-crystal SiO_xN_y nanowires, have been seldom reported. Recently, Gu et al. [16] reported the successful fabrication of N-rich single crystalline SiO_xN_y nanowires using both $Fe(NO_3)_3 9H_2O$ and $Co(NO_3)_2 4H_2O$ as catalyst precursors, while little information is available regarding their optical

properties. It is desirable that nanowries could be synthesized without metal catalyst since catalyst contaminations might affect the characteristics of the nanowire, especially their optical properties.

In this work, we report the catalyst-free synthesis of bulk single-crystal SiO_xN_y nanowires with high N concentration. The chemical composition and structural characterization of these nanowires have been investigated, and the growth mechanism is discussed. The optical properties of the disordered SiO_xN_y nanowire mat have also been studied.

2. Experimental Details

In a typical synthesis procedure, the single-crystalline Si wafer [100] with a native oxidation layer (5 nm) was first dipped into acetone under ultrasonic agitation for 10 min to erase the surface contaminations. Then, the Si wafer was loaded to a quartz crucible boat and placed in the central region of an alumina tube furnace (GSL-1400X). Before the experiment, the furnace was evacuated to 10^{-3} Torr and then flushed with N_2 (99.999%) to eliminate the oxygen and moisture in the chamber. The crucible boat was heated to 1200°C at the heating rate of 15°C/min under a N_2 flow of 50 standard cubic centimeters per minute (sccm). When the temperature reached the preset value, the gas flux was switched to mixture gas flow of H_2 (5%)/N_2 (99.999%) at a rate of 100 sccm. The growth time can be varied to obtain nanowire mats with different thickness. During the cooling process, only N_2 (99.999%) was used as the feed gas. When the furnace was naturally cooled down to room temperature, ultrabright white products were observed on the wafer.

The structure, morphologies, and composition of the products were characterized with scanning electron microscope (SEM, JEOL JSM-5510LV), high-resolution transmission electron microscope (HRTEM, FEI-F20 with EDS attachment and JEOL 2010), and selected-area electron diffraction (SAED). X-ray photoelectron spectroscopy (XPS, Kratos Axis Ultra DLD) and Fourier transform-infrared Spectroscope (FT-IR, VERTEX 70) were also used to investigate their chemical composition. The optical reflectivity was measured under the wavelength from 400 to 780 nm using UV-Vis spectrophotometer (Lambda 35) with a 50 mm integrating sphere. Photoluminescence (PL) property was also studied using PL instrument (FP-6500) at room temperature with a xenon lamp line of 258 nm as the excitation source.

3. Result and Discussion

3.1. Morphologies and Structures. The SEM image see Figure 1(a) shows that the synthesized nanowires are up to several millimeters in length, with high density, and random directions to form a disordered thick mat. For each individual nanowire, the diameter is uniform along its entire length, and the surface of these nanowires is smooth and clear without any residues. To pursue detailed structural information on a single nanowire, TEM investigations were applied. Figure 1(b) shows a TEM image of SiO_xN_y nanowires, where different diameters are observed. Y-shaped

nanowires are also observed as marked in the figure. A histogram of the diameter distribution of 285 nanowires from TEM measurements is shown in Figure 1(c). It is shown that the diameter distribution follows a log-normal distribution function (solid line in the figure) with the peak distribution of around 42 nm.

A higher magnification TEM image of the Y-shaped SiO_xN_y nanowire is shown in Figure 2(a), which is obtained from one of the junctions between the stem and extended branch marked in Figure 1(b). From the picture, it appears that the diameter near the root of the Y-branch is almost the same with that of the stem, while close to the tip, its diameter gets smaller. To better understand the formation of the branch, a HRTEM image of the junction is obtained as shown in Figure 2(b). It is found that the SiO_xN_y nanowire consists of a single crystalline phase throughout the whole structure with a clean backbone-to-branch junction, indicating the possibly epitaxial growth of the branch from the stem. EDS analyses reveal that the chemical composition of the nanowire consists of three elements including Si, N, and O. Detailed composition result shows that the nanowire has the high concentration of N of around 54.27 at.% and the O concentration around 7.44 at.%. These N-rich nanowires may inherit the high refractive index of their bulk materials, which renders strong photonic property [15]. Figures 2(c) and 2(d) are the typical HRTEM images of the prepared nanowires, and the insets correspond to SAED patterns of the nanowires. HRTEM images show that the SiO_xN_y nanowires grew along two different directions with zone axes of $[2\bar{2}1]$ (Figure 2(c)) and $[1\bar{1}1]$ (Figure 2(d)), respectively, and the lattice spacings of the single crystal nanowire were measured to be 0.679 and 0.415 nm, respectively.

XPS has been employed to analyze the chemical bonding within the nanowires and to give insight into their composition, where monochromatic Al Kα X-ray source was operated at 150 W. Figure 3(a) shows the XPS spectra of the obtained nanowires with Si 2p, N 1s, and O 1s signals. Three strong XPS signals display direct evidence of the existence of Si, N, and O elements. The peak of N 1s, located at 397.5 eV, shifts to a higher binding energy compared with the 397.0 eV peak which is attributed to N combined with three Si atoms [17], due to the formation of N–O bond [18]. Deconvolution of the 2p Si spectrum yields three Gaussian-Lorentzian components centered at 101, 102, and 103.2 eV which are assigned to, respectively, Si–N and Si–O–N and Si–O bond configurations [19].

The chemical composition of these nanowires is further confirmed by FT-IR spectrometer. The broad FT-IR spectrum from 400 to 4000 cm^{-1} is shown in Figure 3(b). The absorption band at 492 originates from the vibrations of the Si–O–Si bonds. Peaks corresponding to the vibration modes of Si–N bonds appear at 846, 887, and 924 cm^{-1} [20]. The band of 1048 cm^{-1} indicates the asymmetrical stretching vibration of Si–O bonds. The 3440 cm^{-1} and 1632 cm^{-1} adsorption bands are attributed respectively to the stretching and bending vibrations of O–H bond for adsorbed water, which may come from its adsorption on the SiO_xN_y nanowire surface [21].
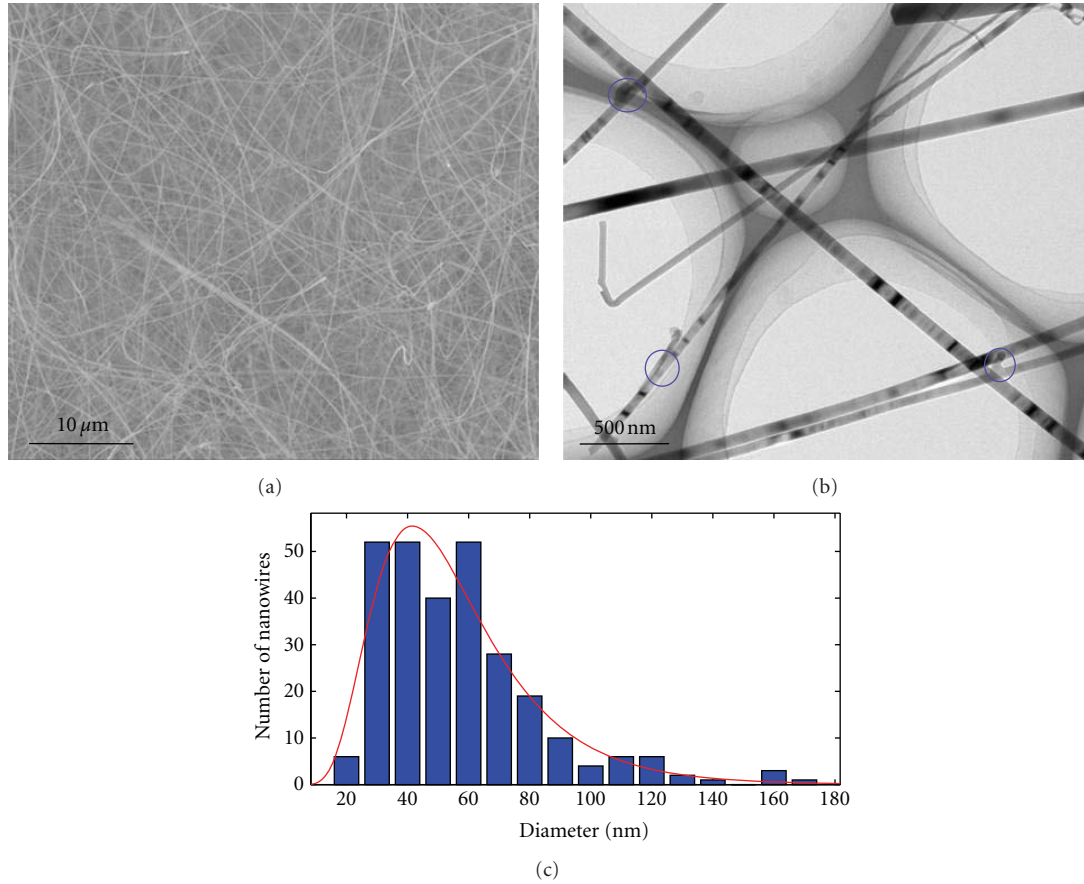
(a)

(b)

(c)

Figure 1: (a) SEM image of the as-grown SiO_xN_y nanowires. (b) TEM image of the as-grown SiO_xN_y nanowires. Circles mark the backbone-to-branch junctions of Y-shaped nanowire formation. (c) histogram of the nanowire diameter distribution with the solid line representing a log-normal fit.

3.2. Growth Mechanism.

Since the nanowires are synthesized without the aid of metal catalysis, vapor-solid (VS) growth mechanism is more plausible than the vapor-liquid-solid (VLS) growth model in this case. There was no other silicon species introduced into the system, so the silicon wafer was the only source of Si element. Sustained reaction of solid silicon or silicon dioxide (SiO_2) with N_2 is not allowed since solid silicon and SiO_2 are barriers for nitrogen diffusion [22]; therefore, gaseous SiO_x ($x \approx 1$) is the only source to directly supply Si element for Si-related nanowire growth [23]. In our experiment, hydrogen is introduced into the system as mixed gas, which can lead to the reaction of (1) and generate gaseous SiO_x. Meanwhile, the residual oxygen in the furnace due to the low vacuum condition and leakage can also lead to the generation of gaseous SiO_x through the reaction (2):

$$SiO_2(s) + (2 - x)H_2(g) \longrightarrow SiO_x(g) + (2 - x)H_2O(g), \tag{1}$$

$$2Si(s) + xO_2 \longrightarrow 2SiO_x(g). \tag{2}$$
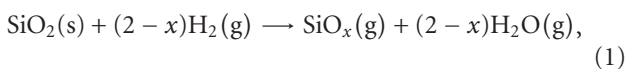
The reaction of SiO_x with introduced N_2 lead to the formation of SiO_xN_y, which is illustrated by (3):

$$2SiO_x(g) + yN_2(g) \longrightarrow 2SiO_xN_y. \tag{3}$$
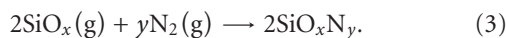
When we reduced the chamber temperature to $1100°C$, the growth of nanowire was not observed, while etched pits were found randomly distributed on the substrate shown in Figure 4(a), indicating that the temperature is critical to initiate the growth of nanowire. The EDS spectrum acquired from the pit showing only Si signal (Figure 4(b)) indicates that the silicon surface was etched, which also validate the reaction of (1) and (2). Thus, the formation process of the nanowires can be explained as follows: through the reactions (1) and (2), gaseous SiO_x was generated, and silicon oxide (SiO_x) nanoclusters were formed at the surface of the silicon substrates as illustrated in Figure 4(c). Then, SiO_x reacted with nitrogen to form SiO_xN_y nuclei according to the reaction indicated by (3) (Figure 4(d)). With continuous supply of Si, O, and N elements, the growth of SiO_xN_y, nanowire was initiated and maintained Figure 4(e).

A similar experiment has been reported by Ran et al. [24], in which crystalline Si_3N_4/amorphous SiO_2 nanocables were synthesized on silicon substrates under N_2 atmosphere at $1250°C$ without using catalyst and H_2. We believe that the difference is due to the different atmosphere and the temperature control curve. Another experiment reported by Farjas et al. [25] shows that oxygen partial pressure and the control
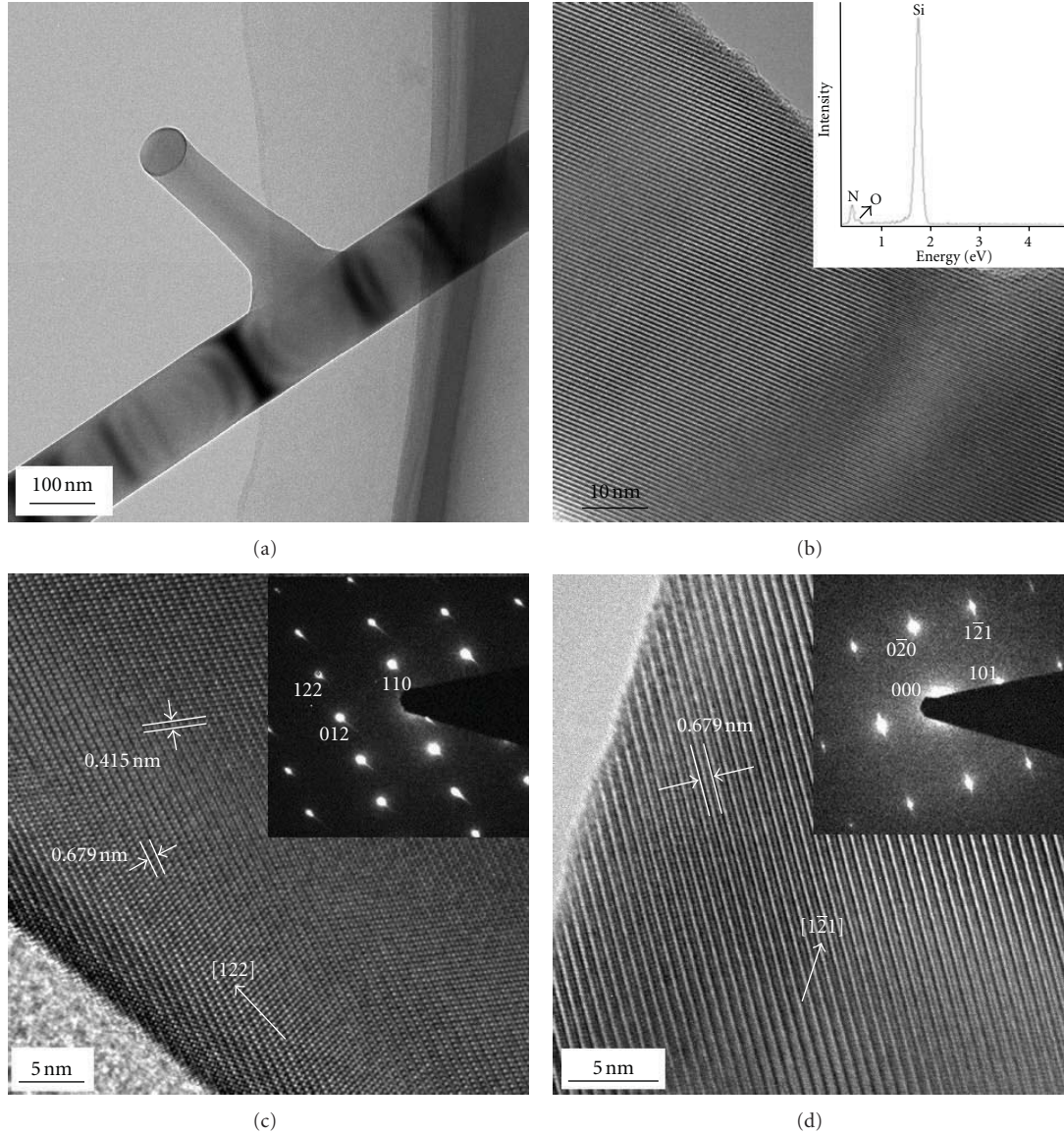
(a)

(b)

(c)

(d)

FIGURE 2: (a) and (b) are TEM image and HRTEM micrograph of Y-shaped SiO_xN_y nanowire obtained from one region marked in Figure 1(b), respectively, EDS spectrum as the inset in (b). (c) and (d) are typical HRTEM images of SiO_xN_y nanowires, each with the corresponding SAED pattern as an inset.

of temperature affect the formation of nanowires, in which Si_3N_4 nanowires were obtained through a CVD mechanism.

3.3. Optical Properties.

To show the brightness and whiteness of obtained nanowire mat, a thin carbon film has been patterned on Si wafer for comparison as shown in Figure 5(a), where black area is carbon film, and white rings are grown SiO_xN_y nanowires. Visual inspection of the samples shows no specular reflection and no obvious angular anisotropy. The optical properties of the nanowire mats were further characterized as shown in Figures 5(b) and 5(c).

The reflectivity was measured from 400 to 780 nm to quantitatively characterize the optical reflectance of SiO_xN_y nanowire mats. The reflectivity of two nanowire mats,

defined as thicker mat of sample A and thinner mat of sample B, is compared and shown in Figure 5(b). At the whole wavelength range, the reflectivity of sample A is maintained above 70%, and the highest point reaches out to 82%, while sample B has a lower reflectivity with an obvious similar appearance. The high optical reflectivity and its slight variations in whole visible-light wavelength result in ultrabright whiteness of the nanowire mat. The results are comparable to the optical performance of the most brilliant white beetle scales reported by Vukusic et al., in which around 60% of incident visible-light is reflected [26].

Strongly diffusive reflectivity of the disordered nanowire mat arises mainly from multiple scattering [27], unlike ordered vertical nanowire mat which has low reflectivity, and its optical interactions can be calculated by solving Maxwell's
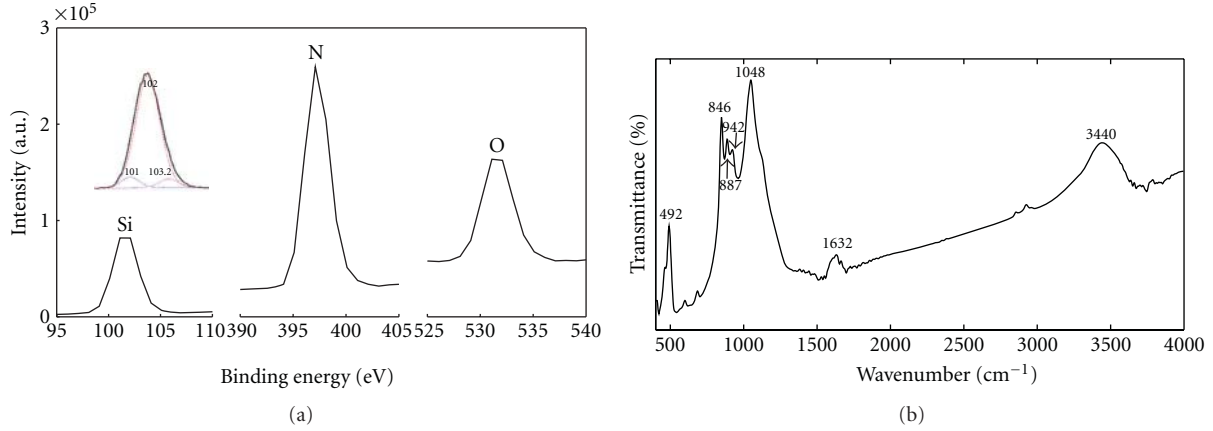
(a)

(b)

FIGURE 3: (a) XPS spectra of the SiO_xN_y nanowire around Si 2p, N 1s and O 1s binding energies; the inset shows the fitting to the original Si 2p peak. (b) FT-IR spectra of the SiO_xN_y nanowire.
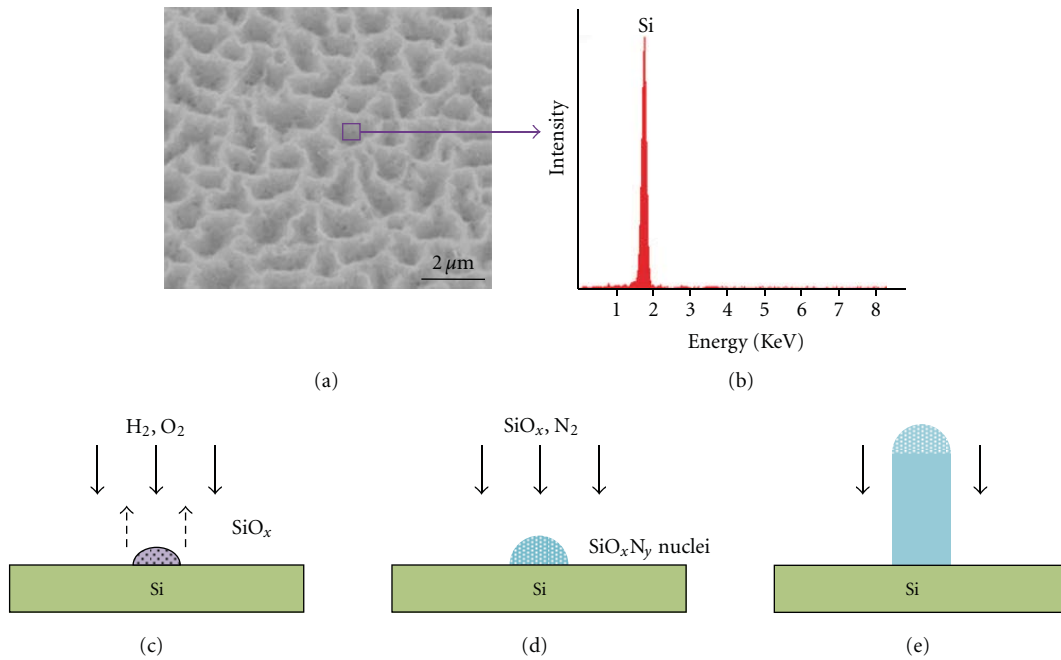

(a)

(b)

(c)

(d)

(e)

FIGURE 4: (a) SEM image of etched silicon wafer after the high-temperature handling at $1100°C$; (b) EDS spectrum acquired from the pit marked in (a); (c), (d), and (e) schematic growth process of the crystalline SiO_xN_y nanowires.

equations [28, 29]. Disordered SiO_xN_y nanowire mats have an ultrabright appearance due to the interaction between scattering and absorption in the nanowires. The small-scatterer (Rayleigh) limit is valid for diameters $d < \lambda/(\pi n)$ with $n = 3.5$, which sets the critical diameter well below $\lambda/10$, where λ is the optical wavelength. For nanowires with the thicker diameter than the critical diameter, light scattering strongly contributes to the nanowire optical reflectivity, which for a dense collection results in diffuse transport of light [15]. As characterized above, the diameter of the obtained nanowires follow a log-normalized distribution from 10–180 nm, showing the existence of large amount of nanowires thicker than $\lambda/10$ in the visible light range, which

keeps the diffuse reflectivity at a high level. Moreover, for a sufficiently thick nanowire mat, photons experience a finite number of scattering events before being reemitted from the surface, corresponding to a total path length for the photon. This length [30] is much less than the mat thickness ($\sim 20\,\mu m$ in sample A), allowing the neglect of significant absorption by the silicon substrate, and therefore contribute to the high reflectivity. Meanwhile, the strong photonic nanowires with high refractive index may enhance their overall scattering efficiency [15, 26].

In sample B, the reflectivity is lower than that of sample A probably because of stronger substrate absorption. Thus, the enhancement of the optical reflectivity could be further
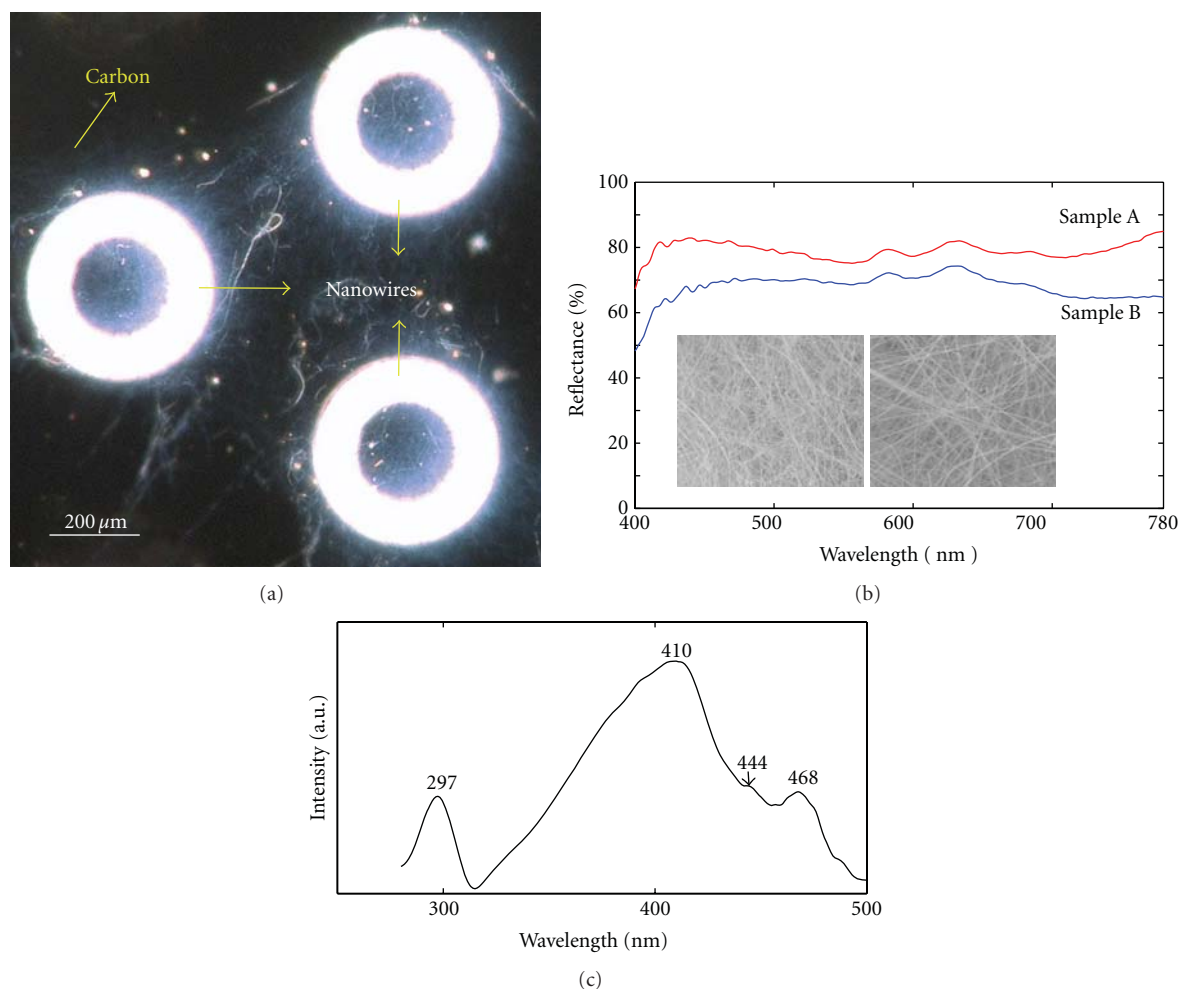
(a)

(b)

(c)

FIGURE 5: (a) photograph of SiO_xN_y nanowire mat on Si substrate with patterned carbon film. (b) reflectivity spectra from two samples of SiO_xN_y nanowire mats, and the inset shows SEM images of samples A and B from left to right. (c) room-temperature PL spectra of SiO_xN_y nanowires, using 258 nm line of a Xe lamp as the excitation.

expected through increasing the thickness of nanowire mat. The extraordinary optical diffusive reflection of these mass-produced nanowires indicates their inherent potential in optoelectronic applications. It has been proved that a diffuse reflector cup can reduce deterministic whispering-gallery modes, and thus enhance light extraction [31]. Considering the extraordinary diffuse reflectivity, the SiO_xN_y nanowires could be also used as coating material of reflector cup, aimed at greatly improving the efficiency of LED lamps.

The PL property of single-crystalline SiO_xN_y nanowires was further studied. The PL spectrum, taken under excitation with the 258 nm line of a Xe lamp at room temperature, is presented in Figure 5(c). Two broad emissions are observed one of which is centered at 297 nm, while the other one ranges from 380 to 500 nm with a maximum centered at 410 nm and two shoulders centered at 444 and 468 nm, respectively. The strong peak around 410 nm arises from recombination either from the conduction band to the N_2^0 level or from the valence band to the N_4^+ level [32]. The weak emission at 444 nm ($\sim$2.8 eV), has been experimentally suggested by Noma et al. [33], originates from Si–N bonds

in Si oxynitride. While the blue PL emission at 470 nm [34] and UVB PL emission at 297 nm [35] probably have an origin related to Si–O bonds.

4. Conclusion

We have successfully synthesized large amount of N-rich single-crystalline SiO_xN_y nanowires through vapor-solid mechanism avoiding metal catalyst contamination. Their morphologies and optical properties were investigated. In this work, these nanowires were grown to form an ultrabright white disordered mat, displaying high diffuse reflectivity over the whole visible-light range which is largely determined by multiscattering of incident light. The extraordinary optical diffusive reflection of these mass-produced nanowires is comparable to that of the most brilliant white beetle scales found in nature. The application of these nanowires in white reflector could improve overall light extracting efficiency for highbright white lighting. Their ultrabright white appearance could also find applications in many other fields, such as cosmetics, paints, and tooth whitening.

Acknowledgments

References

[1] M. L. Green, E. P. Gusev, R. Degraeve, and E. L. Garfunkel, "Ultrathin (<4 nm) SiO_2 and Si-O-N gate dielectric layers for silicon microelectronics: understanding the processing, structure, and physical and electrical limits," *Journal of Applied Physics*, vol. 90, pp. 2057–2121, 2001.

[2] J. Eng Jr., I. A. Hubner, J. Barriocanal, R. L. Opila, and D. J. Doren, "X-ray photoelectron spectroscopy of nitromethane adsorption products on Si(100): a model for N 1 s core-level shifts in silicon oxynitride films," *Journal of Applied Physics*, vol. 95, no. 4, pp. 1963–1968, 2004.

[3] X. T. Zhang, Z. Liu, Z. Zheng, S. K. Hark, Y. B. Fu, and G. B. Zhang, "Synthesis and photoluminescence properties of well-aligned Ga-doped N-rich SiO_xN_y nanowire bundles," *Applied Physics Letters*, vol. 90, no. 18, Article ID 183110, 3 pages, 2007.

[4] R. Germann, H. W. M. Salemink, R. Beyeler et al., "Silicon oxynitride layers for optical waveguide applications," *Journal of the Electrochemical Society*, vol. 147, no. 6, pp. 2237–2241, 2000.

[5] K. Wörhoff, L. T. H. Hilderink, A. Driessen, and P. V. Lambeck, "Selicon oxynitride. A versatile material for integrated optic applications," *Journal of the Electrochemical Society*, vol. 149, no. 8, pp. F85–F91, 2002.

[6] D. M. Brown, P. V. Gray, F. K. Heumann, H. R. Philipp, and E. A. Taft, "Properties of $Si_xO_yN_z$ films on Si," *Journal of The Electrochemical Society*, vol. 115, pp. 311–317, 1968.

[7] X. Guo and T. P. Ma, "Tunneling leakage current in oxynitride: dependence on oxygen/nitrogen content," *IEEE Electron Device Letters*, vol. 19, no. 6, pp. 207–209, 1998.

[8] C. Xu, M. Kim, J. Chun et al., "Gallium-doped silicon nitride nanowires sheathed with amorphous silicon oxynitride," *Scripta Materialia*, vol. 53, no. 8, pp. 949–954, 2005.

[9] M. I. Alayo, I. Pereyra, W. L. Scopel, and M. C. A. Fantini, "On the nitrogen and oxygen incorporation in plasma-enhanced chemical vapor deposition (PECVD) SiO_xN_y films," *Thin Solid Films*, vol. 402, no. 1-2, pp. 154–161, 2002.

[10] T. Qiu, X. L. Wu, G. J. Wan, Y. F. Mei, G. G. Siu, and P. K. Chu, "Self-assembled growth and enhanced blue emission of SiO_xN_y -capped silicon nanowire arrays," *Applied Physics Letters*, vol. 86, no. 19, Article ID 193111, pp. 1–3, 2005.

[11] Y. Xia, P. Yang, Y. Sun et al., "One-dimensional nanostructures: synthesis, characterization, and applications," *Advanced Materials*, vol. 15, no. 5, pp. 353–389, 2003.

[12] C. M. Lieber and Z. L. Wang, "Functional nanowires," *MRS Bulletin*, vol. 32, pp. 99–108, 2007.

[13] O. L. Muskens, S. L. Diedenhofen, B. C. Kaas et al., "large photonic strength of highly tunable resonant nanowire materials," *Nano Letters*, vol. 9, no. 3, pp. 930–934, 2009.

[14] J. G. Rivas, S. L. Diedenhofen, O. L. Muskens, and G. Grzela, "Tailoring light scattering of nanowires for photovoltaic applications," in *Solar & Alternative Energy*, Proceedings of SPIE, 2010.

[15] O. L. Muskens, J. G. Rivas, R. E. Algra, E. P. A. M. Bakkers, and A. Lagendijk, "Design of light scattering in nanowire materials for photovoltaic applications," *Nano Letters*, vol. 8, no. 9, pp. 2638–2642, 2008.

[16] L. Gu, Y. Yu, V. Penmatsa, C. Wang, J. Maier, and P. A. Van Aken, "Synthesis and characterization of N-rich single crystalline SiO_xN_y nanowires with three-dimensional branches," *Applied Physics Letters*, vol. 94, no. 23, Article ID 231903, 2009.

[17] Z. H. Lu, S. P. Tay, R. Cao, and P. Pianetta, "The effect of rapid thermal N_2O nitridation on the oxide/Si(100) interface structure," *Applied Physics Letters*, vol. 67, pp. 2836–2838, 1995.

[18] E. C. Carr and R. A. Buhrman, "Role of interfacial nitrogen in improving thin silicon oxides grown in N_2O," *Applied Physics Letters*, vol. 63, no. 1, pp. 54–56, 1993.

[19] O. Benkherourou and J. P. Deville, "X-ray Photoelectron Spectroscopy of silicon oxynitride layers obtained by low-energy ion implantation," *Applied Physics A Solids and Surfaces*, vol. 46, no. 2, pp. 87–90, 1988.

[20] J. Zheng, X. Song, X. Li, and Y. Pu, "Large-scale production of amorphous silicon oxynitride nanowires by nickel-catalyzed transformation of silicon wafers in NH_3 plasma," *Journal of Physical Chemistry C*, vol. 112, no. 1, pp. 27–34, 2008.

[21] L. Zheng, B. Huang, J. Wei, Y. Dai, and M. H. Whangbo, "Synthesis and optical properties of amorphous C-Si-O particles," *Journal of Luminescence*, vol. 131, no. 2, pp. 218–224, 2011.

[22] H. M. Jennings, "On reactions between silicon and nitrogen," *Journal of Materials Science*, vol. 18, no. 4, pp. 951–967, 1983.

[23] G. Z. Yang, H. Cui, Y. Sun et al., "Simple catalyst-free method to the synthesis of β-SiC nanowires and their field emission properties," *Journal of Physical Chemistry C*, vol. 113, no. 36, pp. 15969–15973, 2009.

[24] G. Z. Ran, L. P. You, L. Dai et al., "Catalystless synthesis of crystalline Si_3N_4/ amorphous SiO_2 nanocables from silicon substrates and N_2," *Chemical Physics Letters*, vol. 384, no. 1–3, pp. 94–97, 2004.

[25] J. Farjas, C. Rath, A. Pinyol, P. Roura, and E. Bertran, "Si_3N_4 single-crystal nanowires grown from silicon micro- and nanoparticles near the threshold of passive oxidation," *Applied Physics Letters*, vol. 87, no. 19, Article ID 192114, pp. 1–3, 2005.

[26] P. Vukusic, B. Hallam, and J. Noyes, "Brilliant whiteness in ultrathin beetle scales," *Science*, vol. 315, no. 5810, p. 348, 2007.

[27] R. A. Street, W. S. Wong, and C. Paulson, "Analytic model for diffuse reflectivity of silicon nanowire mats," *Nano Letters*, vol. 9, no. 10, pp. 3494–3497, 2009.

[28] J. Zhu, Z. Yu, G. F. Burkhart et al., "Optical absorption enhancement in amorphous silicon nanowire and nanocone arrays," *Nano Letters*, vol. 9, no. 1, pp. 279–282, 2009.

[29] L. Hu and G. Chen, "Analysis of optical absorption in silicon nanowire arrays for photovoltaic applications," *Nano Letters*, vol. 7, no. 11, pp. 3249–3252, 2007.

[30] R. A. Street, P. Qi, R. Lujan, and W. S. Wong, "Reflectivity of disordered silicon nanowires," *Applied Physics Letters*, vol. 93, pp. 163109–163111, 2008.

[31] H. Luo, J. K. Kim, Y. A. Xi et al., "Trapped whispering-gallery optical modes in white light-emitting diode lamps with remote phosphor," *Applied Physics Letters*, vol. 89, no. 4, Article ID 041125, 2006.

[32] W. Yang, L. Zhang, Z. Xie, J. Li, H. Miao, and L. An, "Growth and optical properties of ultra-long single-crystalline α-Si_3N_4 nanobelts," *Applied Physics A*, vol. 80, no. 7, pp. 1419–1423, 2005.

[33] T. Noma, K. S. Seol, H. Kato, M. Fujimaki, and Y. Ohki, "Origin of photoluminescence around 2.6–2.9 eV in silicon oxynitride," *Applied Physics Letters*, vol. 79, no. 13, pp. 1995–1997, 2001.

[34] Z. Yang, Y. Zhang, D. Liu et al., "Selective synthesis of SiO_2 NWs on Si substrate and their adjustable photoluminescence," *Journal of Non-Crystalline Solids*, vol. 356, no. 41-42, pp. 2207–2210, 2010.

[35] M. Cannas, "Luminescence properties of point defects in silica," GNSR 2001, State of Art and Future Development in Raman Spectroscopy and Related Techniques, 2002.

Research Article

Photocatalytic Degradation of Organic Dye by Sol-Gel-Derived Gallium-Doped Anatase Titanium Oxide Nanoparticles for Environmental Remediation

Arghya Narayan Banerjee,[1] Sang Woo Joo,[1] and Bong-Ki Min[2]

[1] *School of Mechanical Engineering, Yeungnam University, Gyeongsan 712-749, Republic of Korea*
[2] *Center for Research Facilities, Yeungnam University, Gyongsan 712-749, Republic of Korea*

Correspondence should be addressed to Arghya Narayan Banerjee, banerjee_arghya@hotmail.com and
Sang Woo Joo, swjoo@yu.ac.kr

Photocatalytic degradation of toxic organic chemicals is considered to be the most efficient green method for surface water treatment. We have reported the sol-gel synthesis of Gadoped anatase TiO_2 nanoparticles and the photocatalytic oxidation of organic dye into nontoxic inorganic products under UV irradiation. Photodegradation experiments show very good photocatalytic activity of Ga-doped TiO_2 nanoparticles with almost 90% degradation efficiency within 3 hrs of UV irradiation, which is faster than the undoped samples. Doping levels created within the bandgap of TiO_2 act as trapping centers to suppress the photogenerated electron-hole recombination for proper and timely utilization of charge carriers for the generation of strong oxidizing radicals to degrade the organic dye. Photocatalytic degradation is found to follow the pseudo-first-order kinetics with the apparent 1st-order rate constant around $1.3 \times 10^{-2}\,min^{-1}$. The cost-effective, sol-gel-derived $TiO_2 : Ga$ nanoparticles can be used efficiently for light-assisted oxidation of toxic organic molecules in the surface water for environmental remediation.

1. Introduction

Titanium dioxide (TiO_2) is one of the most important wide bandgap metal oxides which is having a vast range of applications from paint to sunscreen to food coloring to photocatalyst, hydrogen production, storage medium, sensors, solar cells, organic waste management, and various biological and health-related applications [1–13]. Because of its wide range of properties, TiO_2 bulk films as well as nanostructured materials become the subject of intense research within the global scientific community. In general, TiO_2 has two stable crystalline structures: anatase and rutile [14]. Rutile is preferred to anatase for optical applications because of its higher refractive index, whereas anatase is preferred for all the applications related to photocatalytic activity, gas sensing, and solar cells, due to its higher mobility and catalytic properties [15, 16].

Amongst various TiO_2 nanostructures, titania nanoparticles have specific advantages in the enhancement of light absorption due to the large fraction of surface atoms. Interband electron transition is the primary mechanism of light absorption in pure semiconductors. These transitions are direct as the momentum gain by the electron from light wave is small in comparison with $\pi h/a$ ("a" is the lattice constant). This absorption is small in direct-forbidden gap semiconductors, as in the case for TiO_2, for which the direct electron transitions between the band centers are prohibited by the crystal symmetry. However, momentum is not conserved if the absorption takes place at the boundary of the crystal, for example, at the surface or at the interface between two crystals, which leads to the indirect electron transitions that can result in the essential enhancement of light absorption. This means that considerable enhancement of the absorption can be observed in small nanocrystals where the surface-to-volume ratio is very high and the fraction of the surface atoms is sufficiently large. The particle size at which the interface enhancement of the absorption becomes significant is around 20 nm or less. An additional advantage obtained in nanoparticles in the few nanometer

size regimes is that the large surface-to-volume ratio makes possible the timely utilization of photogenerated carriers in interfacial processes [1, 17]. Additionally, the doping of TiO$_2$ nanoparticles is performed for improved photocatalytic activities by reducing the band gap of TiO$_2$ to utilize the wider fraction of solar radiation, especially the visible and near infrared (NIR) parts [4, 18–20]. Many efforts have been expended to narrow the TiO$_2$ band gap by substitutional doping. According to the crystal structure of TiO$_2$, it appears that replacement of Ti^{4+} with any cation is relatively easier than to substitute O^{2-} with any other anion due to the difference in the charge states and ionic radii. Cationic doping of TiO$_2$ with transition and rare earth metals has been extensively studied [18–24]. While several authors have reported that transition metal ion doping decreases the photothreshold energy of TiO$_2$, there is also an increase in thermal instability and a decrease in carrier lifetimes [25], which limits overall conversion efficiencies. Therefore, it is clear that there is always scope for improvement in the photoactivity of TiO$_2$ nanostructures either by applying various new dopants or (and) adopting different doping parameters through different deposition processes and conditions. Amongst various photocatalytic applications of TiO$_2$, photocatalytic degradation of toxic organic chemicals (especially organic dyes generated as industrial wastes and released in the surface water without proper treatment) is considered to be the most efficient green method for organic waste management in terms of photosensitized TiO$_2$-assisted oxidation of organic pollutants for surface water treatment, recovery of precious metals via TiO$_2$-assisted reduction, organic synthesis, photokilling activity, and self-cleaning activity among others [26–35].

As far as the syntheses of undoped and doped TiO$_2$ nanostructures are concerned, both solution-based chemical techniques as well as vacuum-based physical techniques [1, 7, 9] have been adopted. In the current study, we have reported the sol-gel syntheses and characterizations of Ga-doped anatase TiO$_2$ nanoparticles (TiO$_2$: Ga) and investigated the photocatalytic oxidation of organic dyes for environmental remediation. Apparently, sol-gel deposition process is preferred (at least in the research scale) over vacuum-based as well as hydrothermal syntheses, mainly because of its simplicity and cost-effectiveness in terms of materials, design, process, and implementation. As far as the reason behind the adoption of Ga as the doping material is concerned, previously few authors reported the improved photocatalytic activities of TiO$_2$: Ga (and TiO$_2$: Ga/I co-doped) nanomaterials in terms of solar hydrogen production and photodecomposition of various organic compounds used in disinfectants and pesticides [36–41]. The comparable ionic radii of Ta^{+4} (68 pm) and Ga^{+3} (62 pm) appears to be favorable for the substitutional doping of Ga atoms into the Ti matrix to improve the optical, electronic, and photocatalytic properties. To best of our knowledge, no report has been published on the photocatalytic oxidation of organic dyes by anatase TiO$_2$: Ga nanoparticles for organic waste treatments, which is one of the burning issues in the industrial waste management and, hence, needs much attention.

As far as the difference between our work against the previously reported sol-gel-derived Ga-doped (or Ga/I co-doped) TiO$_2$ nanomaterials is concerned [37, 38], both of these reports indicated the formation of phase impure TiO$_2$ nanopowders with a mixture of anatase and rutile (as well as a small fraction of brookite) phases under Ga (or Ga/I) (co-)doping, whereas we have been able to obtain phase pure anatase TiO$_2$ nanoparticles (as shown later) via our sol-gel route. It has been reported previously that phase pure anatase TiO$_2$ (along with commercially available Degussa P-25) has the highest hydroxyl radical ($^{\bullet}$OH) formation rate under photoirradiation, which is considered to be the main species responsible for the photooxidation of organic compounds [10]. Therefore, it is desirable to synthesize phase-pure anatase TiO$_2$ for efficient photodegradation of organic molecules, and, in that respect, our process to synthesize phase-pure Ga-doped anatase TiO$_2$ nanoparticles may become very important for efficient photocatalytic organic waste management. Also, for the application of waste water treatment via TiO$_2$: Ga-based photocatalytic degradation of organic molecules, photocatalytic oxidation of water soluble organic dyes (like Rhodamine B, as in our case) should be preferred as the testing agent against sparingly soluble organic substances (like 2-chlorophenol, 1,4-dichlorobenzene, and so forth, as used in [37, 38]), because the water soluble toxic dyes released from textile industries in the surface water as waste products pose considerable threats to the environment and, hence, warrants proper attention.
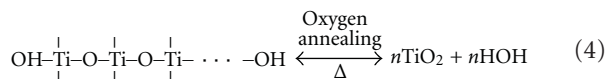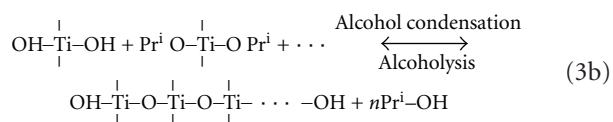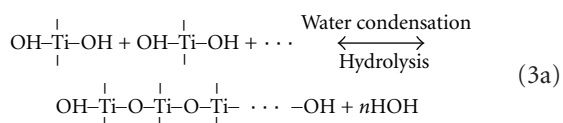
2. Experimental

2.1. Materials. Undoped and Ga-doped anatase TiO$_2$ nanopowders were synthesized by the sol-gel route using titanium isopropoxide [Ti{OCH(CH$_3$)$_2$}$_4$] and gallium(III) oxide (Ga$_2$O$_3$), (all from Sigma Aldrich, Korea, 99.9% pure) as Ti and Ga sources, respectively. Isopropanol, acetic acid (99.0%, Duksan Pure Chemicals, Republic of Korea), and deionized (DI) water is used for precursor solution preparation. For photocatalytic experiment, Rhodamine B (R^{h}B, Sigma Aldrich, Republic of Korea) is used as the organic dye in the aqueous solution.

2.2. Method. Firstly, 0.05 mol of titanium isopropoxide is dissolved into isopropanol with a 1 : 10 molar ratio, respectively. In order to stabilize the Ti solution, acetic acid is then added to the solution until the pH of the solution is in between 3.0 and 3.5. The resulting solution is stirred for 60 min at room temperature until a homogeneous sol is prepared. Then, the sol is aged for 24 hrs at ambient condition to get the gel. Thereafter, the gel is air-dried at 100°C to remove the solvents. The dried gels are then calcined in air ambient at 700°C (in a furnace, Thermo Fisher Scientific, Republic of Korea) for 2½ hours to get the nanocrystalline powder which is then grounded in an agate mortar to get TiO$_2$ nanoparticles. For the syntheses of Ga-doped TiO$_2$, 1.0 at.% Ga doping are performed in the nominal solution by dissolving stoichiometric amounts of Ga$_2$O$_3$

in 0.4 mol isopropanol and deionized water (with 10 : 1 molar ratio) and stirred for 30 min at room temperature. This doping solution is then added to the Ti sol prepared by above-mentioned msheethod and stirred for 60 min at room temperature followed by doped sol preparation and corresponding gelation as mentioned above. The layout of the deposition process is furnished in Figure 1.

The probable chemical reactions taking place at different stages of the sol-gel process are furnished as sources.

$$RO-Ti-OR + Pr^i-OH \underset{\text{Formation}}{\overset{\text{Alkoxide}}{\rightleftharpoons}} O\,Pr^i-Ti-O\,Pr^i + R-OH \quad (1)$$

$$O\,Pr^i-Ti-O\,Pr^i + HOH \underset{\text{Re-esterification}}{\overset{\text{Hydrolysis}}{\rightleftharpoons}} OH-Ti-OH + Pr^i-OH \quad (2)$$

$$OH-Ti-OH + OH-Ti-OH + \cdots \underset{\text{Hydrolysis}}{\overset{\text{Water condensation}}{\rightleftharpoons}}$$
$$OH-Ti-O-Ti-O-Ti- \cdots -OH + n\text{HOH} \quad (3a)$$

$$OH-Ti-OH + Pr^i\,O-Ti-O\,Pr^i + \cdots \underset{\text{Alcoholysis}}{\overset{\text{Alcohol condensation}}{\rightleftharpoons}}$$
$$OH-Ti-O-Ti-O-Ti- \cdots -OH + n\text{Pr}^i-OH \quad (3b)$$

$$OH-Ti-O-Ti-O-Ti- \cdots -OH \underset{\Delta}{\overset{\substack{\text{Oxygen}\\\text{annealing}}}{\rightleftharpoons}} n\text{TiO}_2 + n\text{HOH} \quad (4)$$
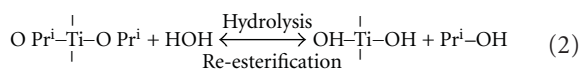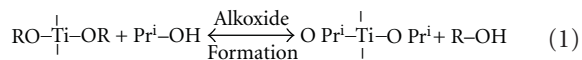
Titanium isopropoxide (Ti–OR) is reacted with isopropyl alcohol (Pr^i–OH) to form alkoxide which is then hydrolyzed to form Ti–OH, followed by condensation to get Ti–O–Ti group along with the by-products of water and alcohol. This produces the sol, which is then aged to get long chains of $\cdots$ Ti–O–Ti–O–Ti–O–$\cdots$, terminated by hydroxyl groups, resulting in the thickening of the sol to form the gel. Finally, the gel is dried and calcined in oxygen (or air) atmosphere to get TiO$_2$.

2.3. Characterizations. The structural properties of the as-synthesized undoped and Ga-doped TiO$_2$ nanoparticles are studied by X-ray diffractometer (XRD, Philips XPertPowder) and Raman spectroscopy (Confocal Raman Microscope, Model number alpha300R, WITec, Germany) with excitation of 532 nm. Microstructural analysis of the nanoparticles is performed by scanning transmission electron microscope (STEM, Tecnai G^2 F20). For high-resolution (HR) TEM characterizations, the nanoparticles are dispersed in alcohol, followed by stirring and drop casting onto the C-coated Cu grid and drying. Optical diffuse reflectance measurements are performed by using a UV-Vis-NIR spectrophotometer (Shimadzu UV-160A) in the spectral range of 300 to 2500 nm. X-ray photoelectron spectroscopic (XPS, K-Alpha, Thermo Fisher Scientific, Republic of Korea) measurements are done by using X-ray Al K$_\alpha$ source. The wide range survey spectra are carried out within the binding energy (B.E.) range of 0.0 to 1350.0 eV with a pass energy of 200.0 eV, whereas the high resolution spectra for O 1s, Ti 2p, Ga 3d electronic structures are measured with a 50.0 eV pass energy.

2.4. Photocatalytic Characterization. The photocatalytic activity of Ga-doped TiO$_2$ is performed by recording the degradation of R^{h}B in aqueous solution under UV radiation. The home-built photoreactor consists of two 16 W UV tube (Fisher Scientific, Republic of Korea) using 254 nm wavelength placed 8 cm away from the reaction vessel containing the dye solution. Before reaction, the dye solution (50 mL) is prepared by mixing R^{h}B and DI water in a molar ratio of 3.6×10^{-6} : 1 and stirred by a magnetic stirrer (Fisher Scientific, Republic of Korea) for 45 min in dark condition to ensure the proper adsorption-desorption equilibrium of dye molecules on the nanoparticle surfaces to act as efficient photocatalysts. The organic dye degradation experiment is performed at different times to observe the decrement in the dye concentration by taking digital photographs of the solution until the whole solution is decolored to ensure complete degradation of the dye molecules. To determine the dye concentration within the degraded solution, UV-Vis spectrophotometric measurements (Shimadzu UV-160A) of the dye solution oxidized at different times are performed within the spectral range of 300 to 800 nm. Before the optical measurements, the dye is separated from the nanoparticles by centrifuging the solution for 10 min (Model 1–14, Sigma, Germany).

3. Results and Discussion

3.1. XRD and HRTEM Analyses. XRD analyses of undoped and Ga-doped TiO$_2$ nanoparticles are shown in Figure 2(a). The peaks show the formation of anatase TiO$_2$ with $I4_1/amd$ space group (1999 JCPDS ICCD File Card nymber 83–2243). No peaks of initial constituents and any by-product have been observed for our samples to confirm the formation of phase pure anatase TiO$_2$ nanomaterials along with the proper doping within the Ga-doped sample. It has been observed that the peak intensities of both the patterns are almost similar, whereas the full width at half maxima (FWHM) of the peaks of undoped sample are slightly lesser than that of doped one. Especially, the broad peak between 36° to 40° is found to be fairly resolved in the undoped sample (as shown in Figure 2(b) through deconvolution) into three distinct peaks ((103), (004), and (112)), whereas the doped sample shows a broad hump around 37.8°. Similarly, the well-resolved (105)/(211) and (116)/(220) peaks in the undoped sample tend to merge in the doped sample. Also a relative comparison of the (101) peaks of as-synthesized undoped and metal-doped samples (cf. Figure 2(c)) reveals that the FWHM increases in the doped sample against undoped samples, with the peak positions remaining almost identical (and this trend is valid for all
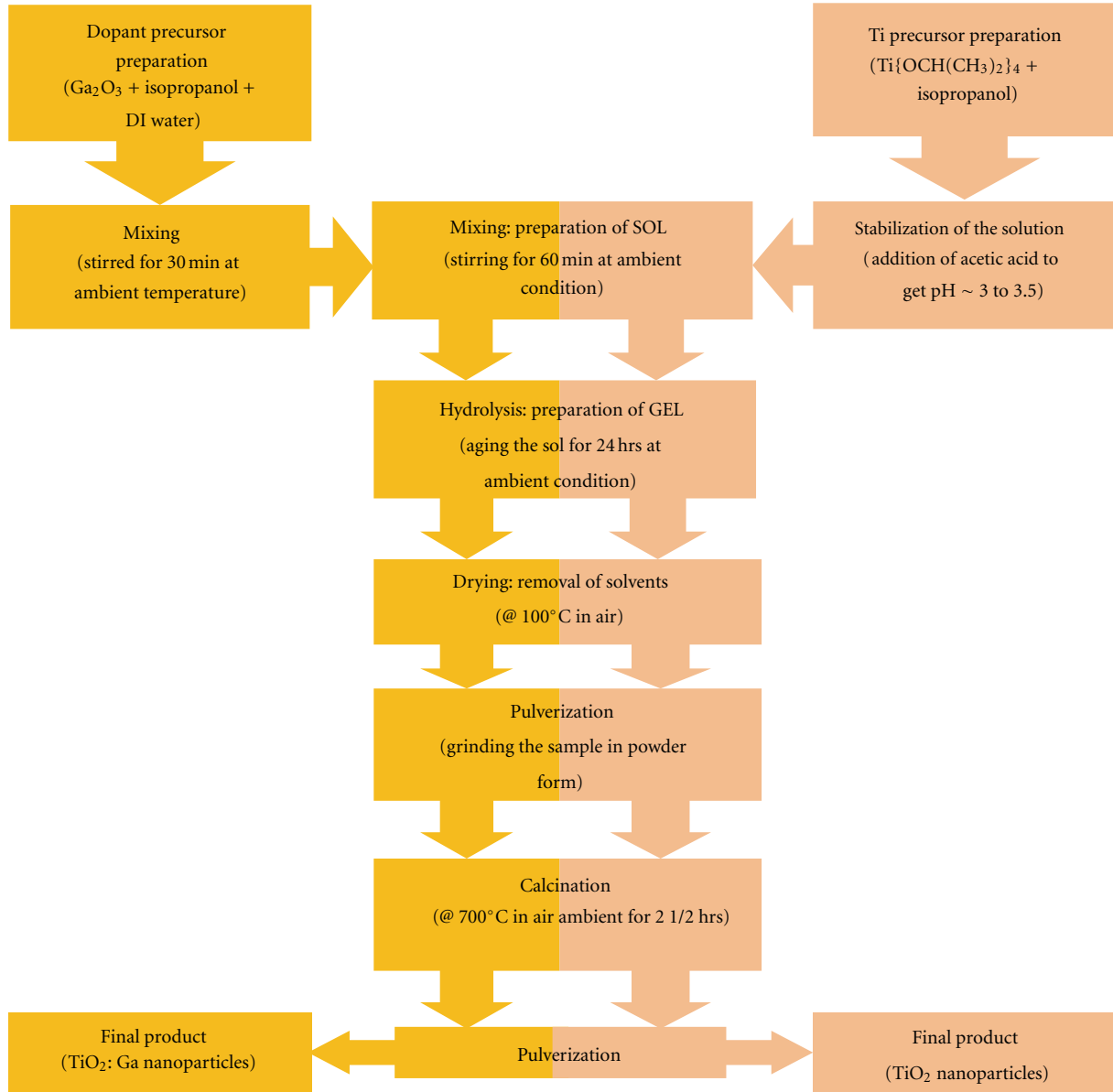
FIGURE 1: Flow chart of the sol-gel syntheses of undoped and Ga-doped TiO$_2$ nanoparticles. Two different colors are used to separate the doping processes from the nondoping case.

other peaks of the samples as well). It is well-known that "particle-broadening effect" generally increases the FWHMs of the diffraction peaks in nanoparticles [42]. But the HRTEM imaging reveals (shown later) that the particle sizes for both undoped and doped samples are almost similar, indicating negligible size effect within the samples. Therefore, it is speculated that "strain-broadening" is highly effective in the as-synthesized doped samples for the relative increment in the FHHMs of the XRD peaks. Generally, in a polycrystalline aggregate, the individual crystallites in a grain is not free to deform in the same way as an isolated crystal would, if subjected to the same deforming force. As a result of this restraint by its neighbors, a grain in a polycrystalline aggregate is usually in a state of tension or compression, which produces uniform or nonuniform strain within the sample and reflected either by a shift in the diffraction peaks (for uniform strain) or by a peak broadening (also called "strain-broadening" for nonuniform strain) without changing the peak position [42]. As mentioned earlier, the ionic radius of Ti^{+4} is 68 pm, whereas the same for Ga^{+3} is 62 pm. Apparently, the doping of Ga^{+3} into lattice Ti^{+4} sites (substitutional doping) as well as in the interstitial sites creates nonuniform strain within the doped samples which is reflected in the peak-broadening effect of the XRD peaks of TiO$_2$: Ga nanopowders. To quantitatively determine the effective crystallite size, L_{cryst}^{eff} and strain, ε^{eff} within

the undoped and metal-doped samples, the FWHMs (β, measured in radian) of the XRD peaks for different 2θ values are expressed as

$$\frac{\beta \cos \theta}{\lambda} = \frac{1}{L_{\text{cryst}}^{\text{eff}}} + \frac{\varepsilon^{\text{eff}} \sin \theta}{\lambda}, \qquad (5)$$

where λ is the incident X-ray wavelength (1.5406 Å). A plot of $\beta \cos \theta / \lambda$ versus $\sin \theta / \lambda$ will be a straight line, slope of which will give the estimation of the effective strain, whereas the intercept on $\beta \cos \theta / \lambda$ axis will carry the information of the effective crystallite size. Figure 2(d) shows the size-strain analysis plots of undoped and Ga-doped TiO_2 samples and reveal the average crystallite sizes around 10.0 to 12.0 nm, whereas the strain increases from 7.53×10^{-3} (for undoped samples) to a maximum of 2.71×10^{-2} (for Ga-doped samples), which is consistent with the above discussions regarding the increasing trend of FWHMs between undoped and doped samples. A comparison between size-strain values for two types of samples is furnished in Table 1.

Figures 3(a) to 3(d) show the HRTEM micrographs of undoped and Ga-doped TiO_2 nanoparticles for two different magnifications. High-mag images show the proper lattice spacing of TiO_2. The insets of Figures 3(a) and 3(c) represent the corresponding size distributions of as-synthesized nanoparticles. The sizes are calculated from the image analysis of the micrographs assuming the particle area to be the projection of spherical particles. The average particle sizes (L^{avg}) are obtained as 15.3 nm (undoped TiO_2) and 17.8 nm (TiO_2:Ga), respectively, and consistent with the crystallite size calculations from XRD data (Figure 2(d)) for polycrystalline nanoparticles. Also the insets of Figures 3(b) and 3(d) represent the selected area electron diffraction (SAED) patterns of the samples indicating the characteristics circles originating from the corresponding crystals planes of anatase TiO_2. Figure 4 shows the EDX data of undoped and metal-doped TiO_2 nanoparticles indicating the presence of elemental constituents within the as-synthesized samples. The atomic percentages of Ti, O, and Ga are furnished in Table 1.

3.2. XPS Analyses. The chemical and electronic structures of as-synthesized undoped and metal-doped samples are determined by XPS analysis and shown in Figure 5. Figure 5(a) shows the high-resolution XPS spectra of undoped and metal-doped TiO_2 nanoparticles of O 1s region, which, after deconvolution, can principally be assigned to lattice oxygen (Ti^x–O: $x = +3, +4$) and surface-adsorbed hydroxyl groups (Ti–OH). Table 2 lists the results of curve fitting of XPS spectra for undoped and metal-doped TiO_2. As seen in the table, the Ti–O peaks are formed at a binding energy (B.E.) around 530.5 eV for all the samples, which is slightly blue-shifted (+0.7 eV) from the standard value of ~529.8 eV [40]. Similar kinds of blue-shifts are reported by others [43, 44] as well and attributed to the presence of larger number of surface hydroxyl groups within the samples. In our case also, the comparatively higher percentage of Ti–OH concentration against previously reported values (8.0–25.0%) [40, 45] clearly depicts the higher OH$^-$-terminated surface in our

samples and may be attributed to the higher surface-to-volume ratio in our nanoparticles that created larger number of surface adsorption sites for hydroxyl ions. Also the relative concentrations of Ti–OH peaks are found to increase in the Ga-doped sample against undoped one, suggesting that the Ga-doped TiO_2 enhances the adsorption of OH$^-$ ions, which consequently increases the hydrophilicity of the nanoparticles [43]. As far as the photocatalytic activity is concerned, it has been reported that the so-called surface "titanol" groups (Ti–OH) in TiO_2 photocatalysts act as the hole scavenger to form the main oxidizing site to improve the photoactivity of TiO_2 [44]. Therefore, Ga-doped TiO_2 with higher Ti–OH concentration is expected to produce larger number of hydroxyl groups to enhance its photocatalytic activity during photolysis. Also, the substitution of a Ga^{+3} into Ti^{+4} sites will create oxygen vacancy, which serves as an electron trap and effectively enhances the lifetime of the hole, which, in turn, helps in the oxidative degradation of pollutants. As far as the presence of Ti^{+4} states in the as-synthesized samples is concerned, Figure 5(b) shows the typical high-resolution spectra of undoped and Ga-doped TiO_2 nanoparticles, indicating the spin-orbital splitting of Ti $2p_{3/2}$ and Ti $2p_{1/2}$ photoelectrons in anatase TiO_2 at B.E. values around 459.3 eV and 465 eV, respectively. The FWHMs of both the peaks are found to increase in the doped sample against the undoped one (cf. Table 2), which implies the presence of less-oxidized metals in the doped samples, indicating the existence of Ti^{+3} species within the TiO_2 matrix. A closer look into the Ti^{+4} $2p_{3/2}$ peaks of doped sample reveals the existence of a shoulder around 457.8 eV (cf. Figure 5(c) and Table 2), which originates from Ti^{+3} $2p_{3/2}$ state of photoelectrons [43]. The presence of this lesser oxidation states of Ti ions in the doped samples indicates the formation of higher percentage of loosely bound Ti^{+3}–O bonds against stronger Ti^{+4}–O bonds, which enhances the photoelectron transfer process between anions and cations and, thus improves the photocatalytic activities of the doped nanoparticles [44]. For Ga-doped samples, Ga 3d spectrum is shown in Figure 5(d), which after deconvolution, reveals the presence of two peaks, the lower B.E. peak (at 21.3 eV) originates from elemental Ga in Ga_2O_3 and the higher one (at 22.7 eV) is speculated to be due to Ga-Ti complex within the TiO_2:Ga nanoparticles. Similar unknown Ga 3d peak (at 22.8 eV B.E.) is observed by Ghita et al. [46] in their Ti-oxidized GaAs samples and speculated to be originated from Ga-Ti complex. The relative area of these two peaks (cf. Table 2) shows the lesser percentage of Ga_2O_3 formation against Ga-Ti complex and may be attributed to the greater fraction of interstitial doping with respect to substitutional doping in our highly doped TiO_2:Ga nanoparticles. This argument finds support from the EDX data (cf. Table 1), where it is found that the doped sample becomes more metal excess against the undoped sample. Ideally, the chemical formula for metal-doped TiO_2 would be $Ti_{1-x}O_2M_y$; (M is dopant ion, x is substitution of Ti by M ions, and y is doping concentration). For 100% substitutional doping of M ions in the Ti sites, x will assume the value of y. Else $x < y$, when interstitial doping is also present, which is thermodynamically more practical situation. Therefore,
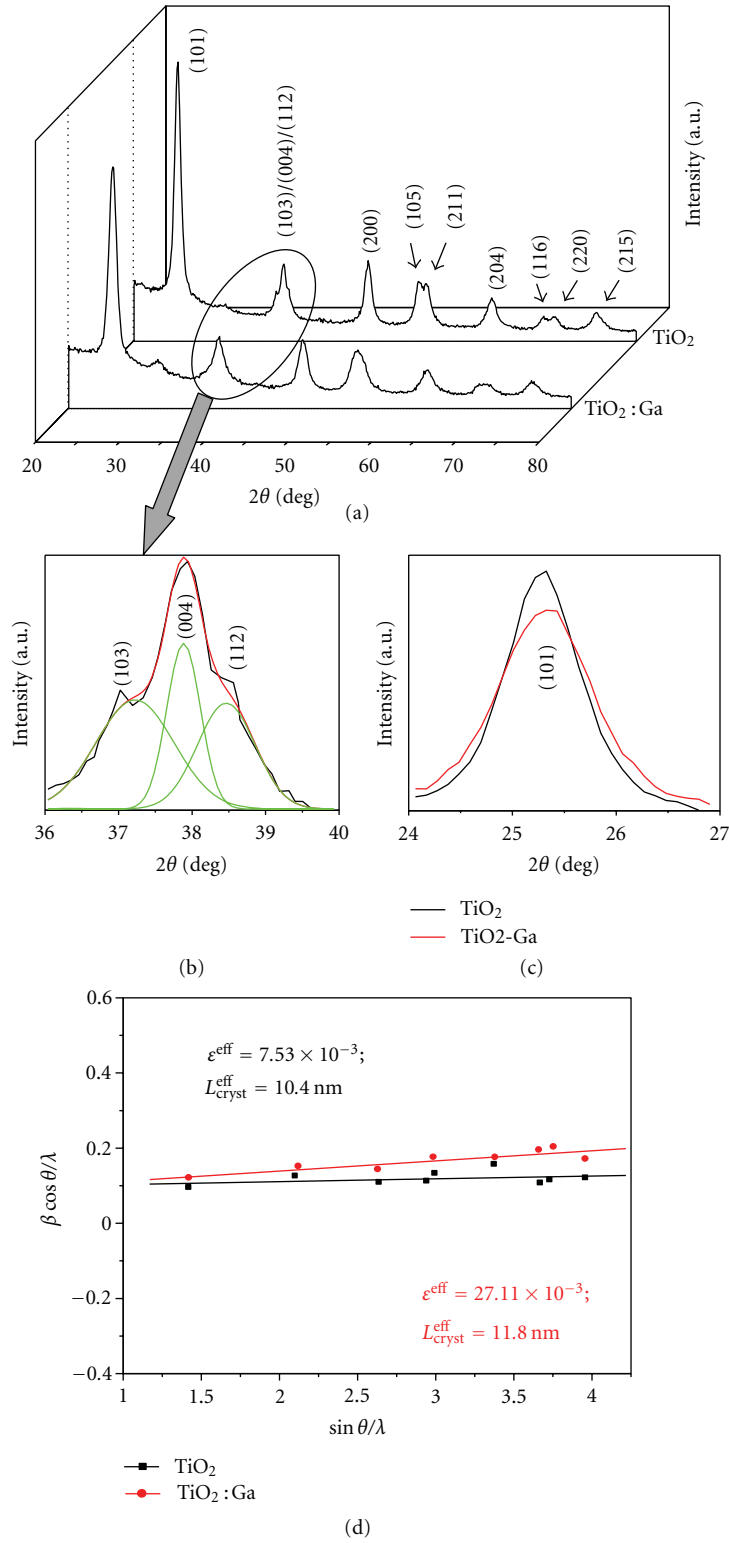
FIGURE 2: (a) XRD patterns of undoped and Ga-doped TiO_2 nanoparticles. (b) Magnified XRD graph of the undoped TiO_2 sample between $36°$ and $40°$ of 2θ values, showing the resolution of (103), (004), and (112) peaks after deconvolution. (c) Magnified (101) peaks of the undoped and Ga-doped TiO_2 nanoparticles showing the strain broadening effect within the doped samples. (d) Size-strain analyses of undoped and Ga-doped TiO_2 nanoparticles.

TABLE 1: Different structural parameters of undoped and metal-doped TiO_2.

Parameters	TiO_2	$TiO_2 : Ga$
Effective crystallite size (L_{cryst}^{eff}) (nm) (from XRD data)	10.4	11.8
Effective strain (ε^{eff}) (from XRD data)	7.53×10^{-3}	2.71×10^{-2}
Average particle size (L^{avg}) (nm) (from HRTEM micrographs)	15.3	17.8
Atomic ratio (Ti : O : Ga) (from EDX data)	$33.87 \pm 0.51 : 66.12 \pm 0.65$	$33.49 \pm 0.52 : 65.51 \pm 0.66 : 0.99 \pm 0.047$

TABLE 2: Various XPS data of O and Ti species within the undoped and metal-doped TiO_2 nanoparticles.

Electronic levels		Fitting parameters	TiO_2	$TiO_2 : Ga$
O 1s	Ti–O	B.E. (eV)	530.5	530.5
		FWHM (eV)	1.02	1.06
		Area[1] (%)	66.0	58.4
	Ti–OH	B.E. (eV)	531.7	531.9
		FWHM (eV)	2.77	3.34
		Area[1] (%)	34.0	41.6
Ti 2p	Ti^{+4} $2p_{3/2}$	B.E. (eV)	459.3	459.3
		FWHM (eV)	1.02	1.08
		Area[2] (%)	69.3	69.1
	Ti^{+4} $2p_{1/2}$	B.E. (eV)	465.0	465.0
		FWHM (eV)	1.68	1.75
		Area[2] (%)	30.7	30.9
	Ti^{+3} $2p_{3/2}$	B.E. (eV)	—	457.8
		FWHM (eV)	—	1.02
		Area[3] (%)	—	6.1
Ga 3d	Due to elemental Ga in Ga^{+3}–O	B.E. (eV)	—	21.3
		FWHM (eV)	—	5.27
		Area[4]	—	33.3
	Due to formation of Ga-Ti complex	B.E. (eV)	—	22.7
		FWHM (eV)	—	2.74
		Area[4]	—	66.7

[1] With respect to the entire area under the O 1s curve.
[2] With respect to the entire area under the Ti 2p curve.
[3] With respect to the area under the Ti $2p_{3/2}$ curve only.
[4] With respect to the entire area under the Ga 3d curve(s).

the presence of excess nonstoichiometric metal content in our Ga-doped samples indicates a larger fraction of interstitial doping within the TiO_2 matrix with respect to substitutional doping. It should also be mentioned in this connection that, in the XPS survey spectra of undoped and metal-doped samples (not shown here), presence of C 1s peaks is also observed, indicating the existence of small C contents within our samples, which may be attributed to the adventitious hydrocarbon from specimen handling and (or) pumping oil of the XPS system.

3.3. Optical Characterizations. Raman spectra of undoped and Ga-doped TiO_2 nanoparticles are shown in Figures 6(a) and 6(b), respectively. The peaks placed at 145, 398, 517, and 639 cm^{-1} (indexed as "A") for both the spectra are typical characteristics of the anatase phase of TiO_2, thus corroborating the XRD data [37]. A small peak at 318 cm^{-1}

is observed in the doped sample and speculated to be originating from vibrations of Ga_2O_3, as observed previously by others as well for β-Ga_2O_3 [47, 48], thus supporting the XPS data of our doped samples showing the presence of Ga_2O_3 within the TiO_2 matrix. The spectral variations of diffuse reflectance (R) of undoped and Ga-doped TiO_2 nanoparticles are shown in Figure 6(c). For undoped and doped samples, the strong absorption edge, which corresponds to the near-band-edge emission, is found to be less than 400 nm and typical of anatase TiO_2. But a relative comparison of the visible parts of the reflectance spectra of both the samples (cf. Inset-(i) of Figure 6(c)) depicts slight absorption into the visible region for the doped samples, owing to the charge-transfer between the Ga d electrons and the TiO_2 conduction band, as shown schematically in Figure 6(d). Apparently, metal doping creates a defect level within the bandgap of TiO_2 and electrons can be excited from the defect state to the TiO_2 conduction band by
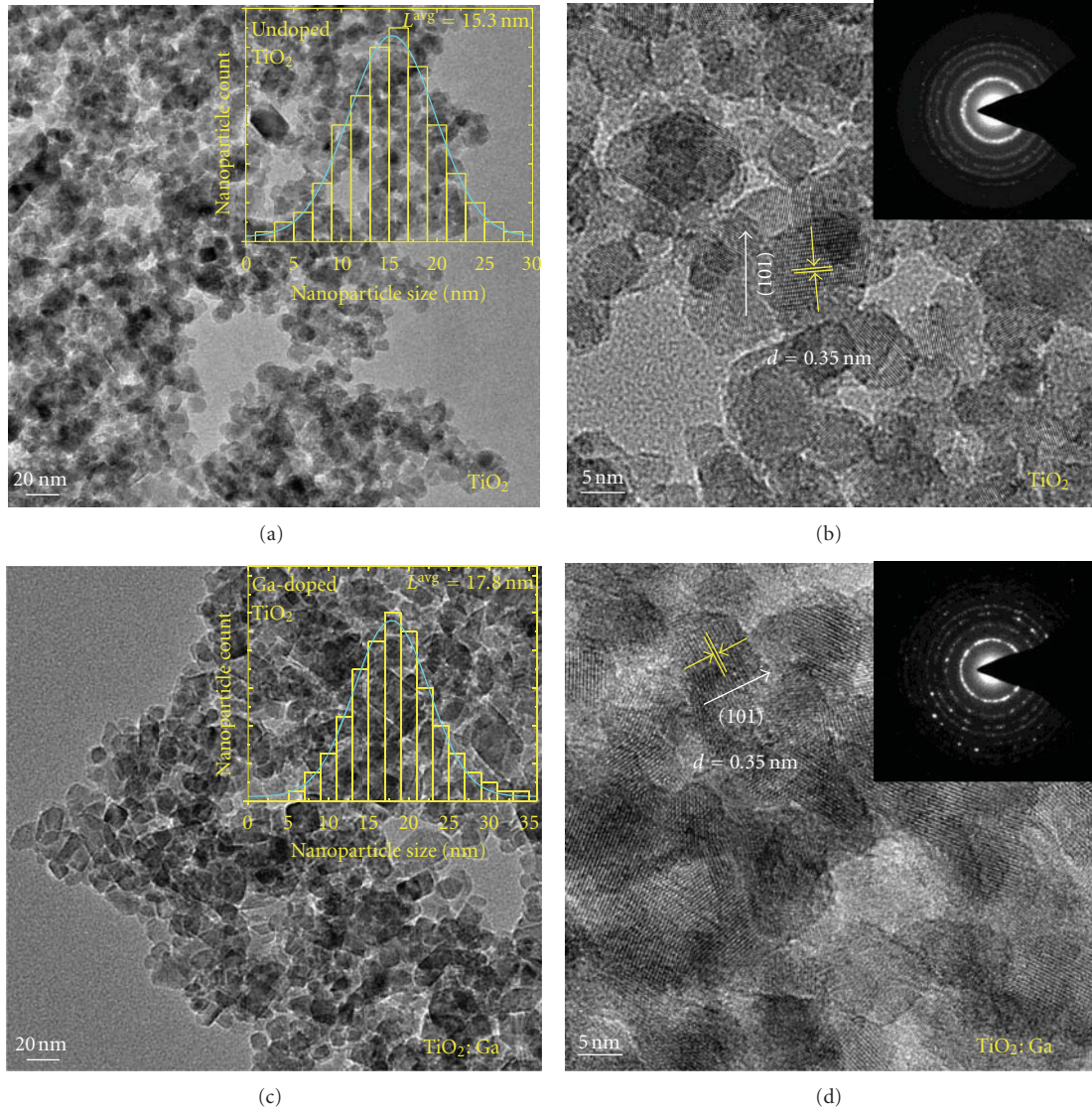
(a)

(b)

(c)

(d)

FIGURE 3: HRTEM micrographs of (a)/(b) undoped TiO_2 and (c)/(d) TiO_2 : Ga at two different magnifications. Insets of (a)/(c) are the corresponding size distributions of nanoparticles. Insets of (b)/(d) are the SAED patterns of undoped and Ga-doped TiO_2 nanoparticles, respectively.

photons with energy ($h\nu_D$) less than the bandgap energy ($h\nu_G$), thus expanding the active region of solar spectrum for photocatalytic activity of TiO_2 into the visible range. Additionally, the metal doping creates trapping centers for electrons to decrease the electron-hole recombination during irradiation to enhance the photoactivity [4]. To determine the exact bandgap values of two types of nanoparticles, an approximate relation between R, absorption coefficient (α), and scattering coefficient (s), based on Kubelka-Munk theory, is adopted, assuming no transmission within the powdered samples of few millimeters thickness [49],

$$\alpha = \frac{s}{2}\left(\frac{[1-R]^2}{R}\right). \tag{6}$$

Although both α and s are functions of the energy of incident radiation ($h\nu$), but at the region of strong absorption, s is far less wavelength dependent than α and, hence, can be considered as constant at the onset of absorption edge. To determine the bandgap values, a graph between $(\alpha h\nu)^2$ and $h\nu$ is plotted at and around the fundamental absorption region (cf. inset-(ii) of Figure 6(c)), which clearly shows that the fundamental bandgaps of both the samples are identical and fall at 3.32 eV. This indicates no size effect in our undoped and Ga-doped TiO_2 nanoparticles, as depicted from the HRTEM analysis.

3.4. Photocatalytic Activity. The role of Ga-doped TiO_2 nanoparticles as efficient photocatalyst is determined by the photocatalytic degradation of R[h]B under UV light at
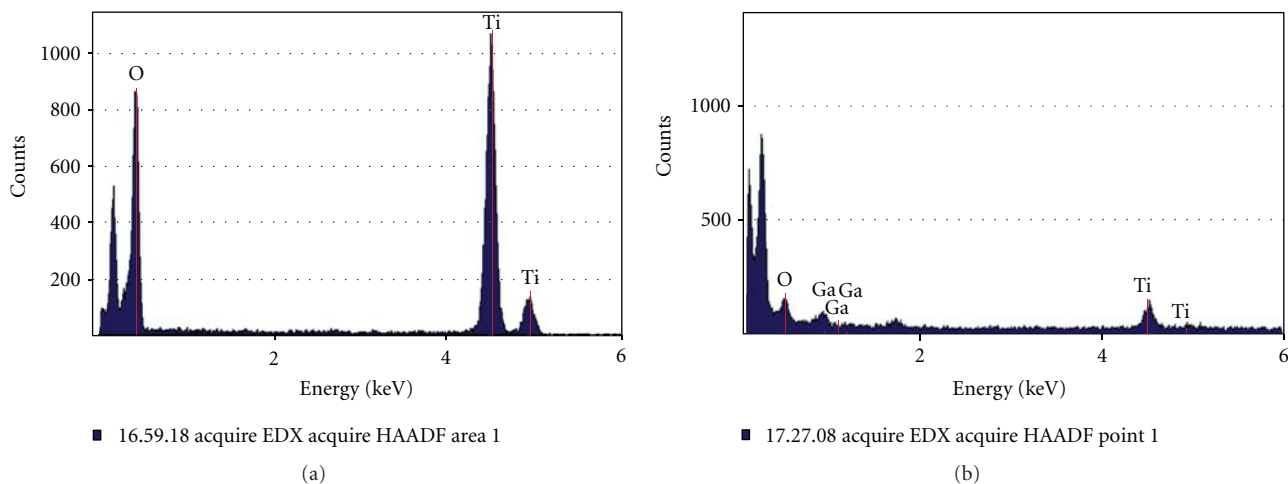
FIGURE 4: EDX analyses of (a) undoped and (b) Ga-doped TiO$_2$ nanoparticles, indicating the presence of elemental Ti, O, and Ga.
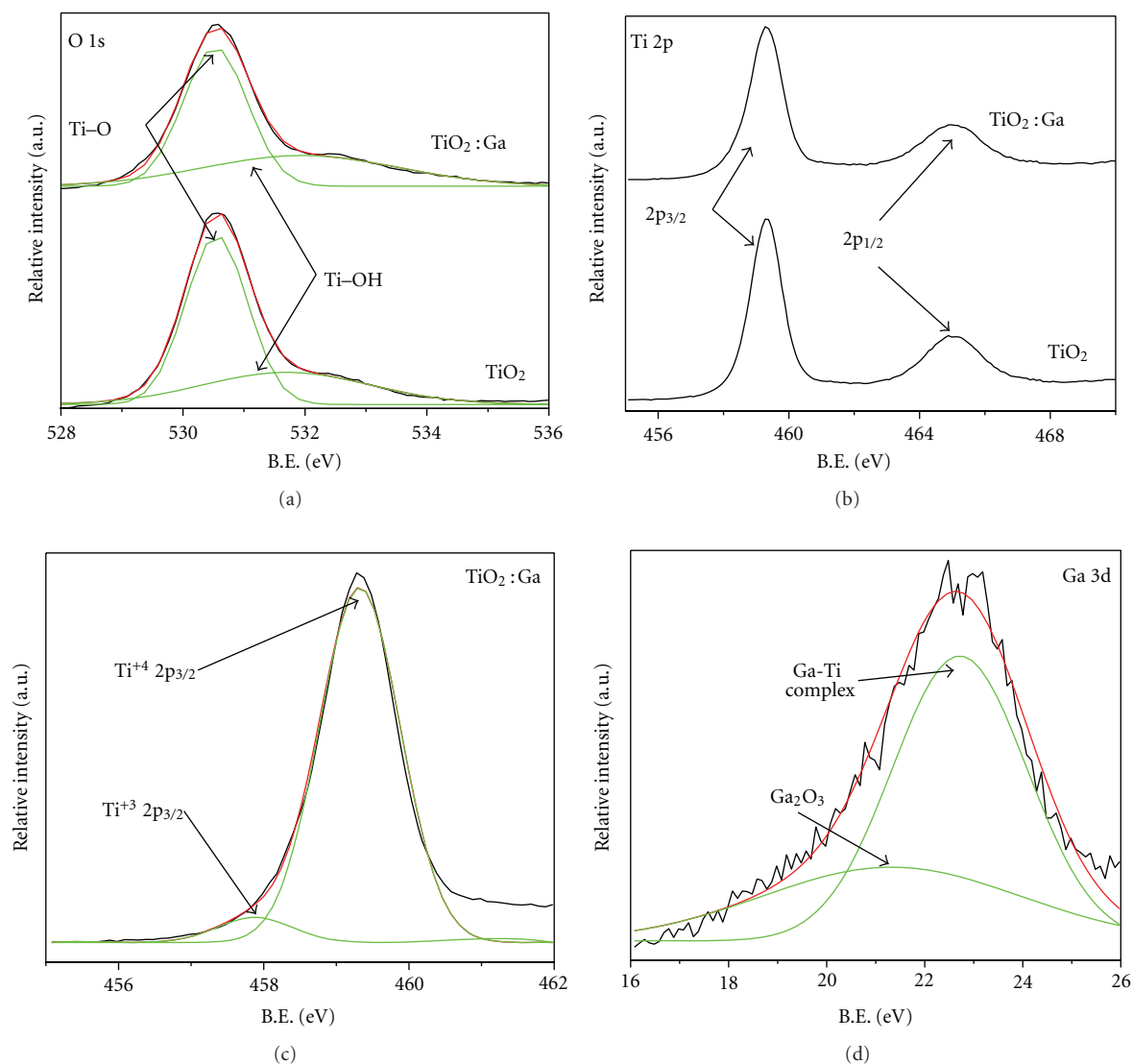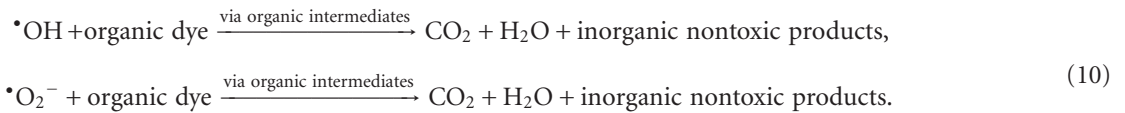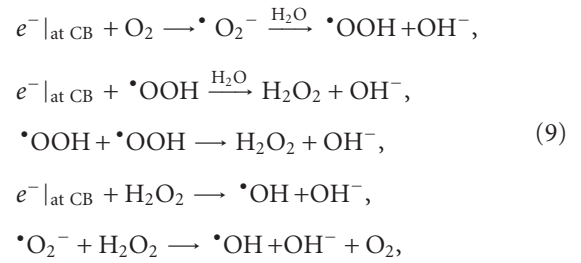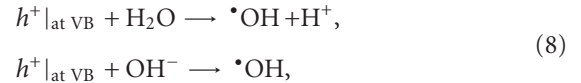

FIGURE 5: XPS spectra of (a) O 1s, (b) Ti 2p, (d) Ga 3d photoelectrons in undoped and Ga-doped TiO$_2$ nanoparticles. (c) Deconvolution of Ti 2p peaks of doped samples to show the existence of Ti^{+4} and Ti^{+3} ions.

different irradiation times, and corresponding time effluence of the absorption spectra of the degraded dye solution is shown in Figure 7(a). The characteristics absorption peak intensity of R^hB at 554.1 nm is shown to be significantly decreased within 2 hrs of irradiation, and the decoloration of the dye is completed within 3 hrs, as shown by the digital photographs of the dye solutions in the inset of Figure 7(a). The overall degradation time is lesser than that of previously reported degradation results of R^hB through TiO_2 photocatalyst [50], indicating higher efficiency of degradation of our Ga-doped TiO_2 nanoparticles. Also, a slight blue-shift of the absorption peak with an increase in time indicates the formation of some N-de-ethylated intermediates during photodegradation of R^hB, as reported by others as well [51]. The entire photocatalytic process for organic dye degradation is furnished as follows [3, 4].

$$TiO_2 : Ga \xrightarrow{h\nu_{in} > h\nu_D} e^-|_{at\ CB} + h^+|_{at\ VB}, \qquad (7)$$

$$h^+|_{at\ VB} + H_2O \longrightarrow {}^\bullet OH + H^+,$$

$$h^+|_{at\ VB} + OH^- \longrightarrow {}^\bullet OH, \qquad (8)$$

$$e^-|_{at\ CB} + O_2 \longrightarrow {}^\bullet O_2{}^- \xrightarrow{H_2O} {}^\bullet OOH + OH^-,$$

$$e^-|_{at\ CB} + {}^\bullet OOH \xrightarrow{H_2O} H_2O_2 + OH^-,$$

$${}^\bullet OOH + {}^\bullet OOH \longrightarrow H_2O_2 + OH^-, \qquad (9)$$

$$e^-|_{at\ CB} + H_2O_2 \longrightarrow {}^\bullet OH + OH^-,$$

$${}^\bullet O_2{}^- + H_2O_2 \longrightarrow {}^\bullet OH + OH^- + O_2,$$

$${}^\bullet OH + \text{organic dye} \xrightarrow{\text{via organic intermediates}} CO_2 + H_2O + \text{inorganic nontoxic products},$$

$${}^\bullet O_2{}^- + \text{organic dye} \xrightarrow{\text{via organic intermediates}} CO_2 + H_2O + \text{inorganic nontoxic products}. \qquad (10)$$

The incident photons, having energy ($h\nu_{in}$) greater than the threshold ($h\nu_D$), generate electron-hole pairs at the nanoparticle surface (7), a large part of which takes part in the photocatalytic process because of the suppression of e^--h^+ recombination by charge trapping of the defect levels generated by Ga doping. Depending upon the exact conditions, the holes at the valence band and electrons at the conduction band react with water and adsorbed oxygen to produce hydroxyl radicals (${}^\bullet OH$) and superoxide anion radicals (${}^\bullet O_2{}^-$), respectively, through some other products like OH^-, ${}^\bullet OOH$, H_2O_2, and O_2 (8), (9). Finally, these radicals with high redox oxidizing potential decompose the organic dye into CO_2, H_2O, and other inorganic nontoxic products (10). A schematic representation of the proposed mechanism is shown in Figure 6(d). Further, it has been reported previously [52, 53] that the ${}^\bullet OH$ radical, which is considered to be one of the main species with high redox oxidizing potential to decompose the organic dye, can be detected by photoluminescence (PL) technique and quantitatively scaled to compare the photocatalytic performance of various photocatalysts. According to this methodology, phase pure anatase TiO_2 (along with Degussa P-25) showed very high formation rate of ${}^\bullet OH$, so also better photoactivity [52]. Therefore, a detailed PL analysis of Ga-doped TiO_2 as a function of doping concentration is necessary to correlate the ${}^\bullet OH$ formation rate and the photocatalysis of our nanoparticles, which is further course of our research.

To quantitatively determine the performance of the photocatalyst, the percentage degradation (% d) is calculated by measuring relative decrease in the dye concentration against the initial value by estimating the peak absorbance of the absorption spectra of the dye solution at different irradiation times according to the following relation:

$$\% \ d = \left[1 - \frac{A_{dye}^\tau}{A_{dye}^0} \right] \times 100, \qquad (11)$$

where A_{dye}^0 and A_{dye}^τ are the peak absorbance of dye solution at initial concentration and after irradiation time τ, respectively. The degradation is found to be 50%, 80%, and 90% after irradiation times of 1 hr, 2 hr, and 3 hr, respectively. It is well known that the photocatalytic degradation kinetics follow the Langmuir-Hinshelwood model [54], which at low dye concentration can be approximated to an apparent 1st-order kinetic reaction according to the following relation [54]:

$$-\ln\left(\frac{C_{dye}^\tau}{C_{dye}^0} \right) = k^{app}\tau, \qquad (12)$$

where C_{dye}^0 and C_{dye}^τ are the dye concentrations at initial and at irradiation time τ and k^{app} is the apparent 1st-order rate constant. A plot of $\ln(C_{dye}^0/C_{dye}^\tau)$ versus τ will be a straight line, slope of which will carry the information of k^{app}. Figure 7(b) represents the $\ln(C_{dye}^0/C_{dye}^\tau)$ versus τ plot for our samples, and the value of k^{app} is obtained as 1.3×10^{-2} min^{-1}, which is found to be better than the previously reported values [50] of similar initial R^hB concentrations,
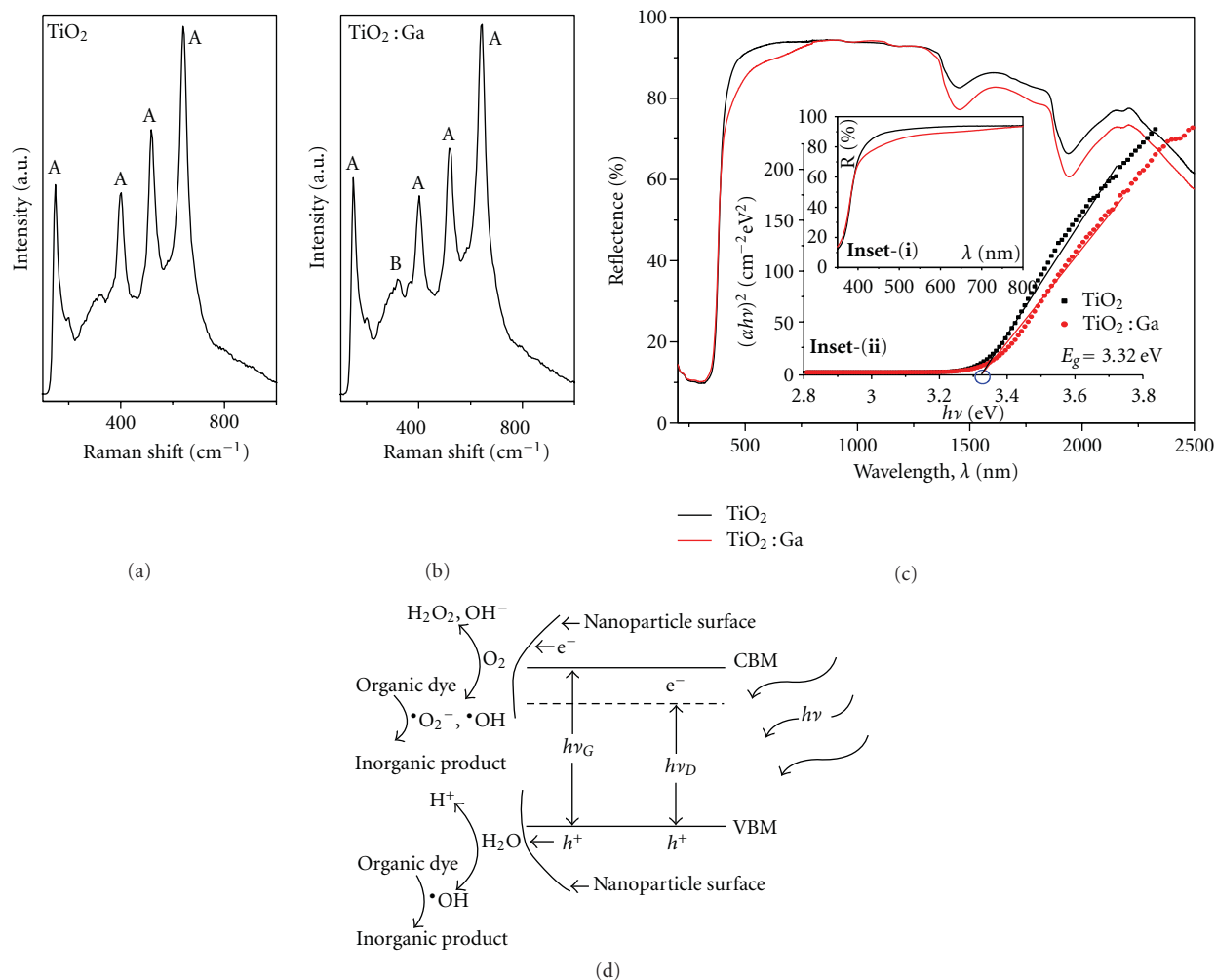
FIGURE 6: Raman spectra of (a) undoped, (b) Ga-doped TiO$_2$ nanoparticles. Peaks indexed as "A" are originating from vibrations associated with anatase TiO$_2$, whereas the peak indexed as "B" in the doped sample is from Ga$_2$O$_3$. (c) UV-Vis-NIR diffuse reflectance spectra of undoped and Ga-doped TiO$_2$ nanoparticles. **Inset (i)** represents the visible part of reflectance spectrum, and **inset (ii)** represents the direct bandgap calculations of undoped and Ga-doped TiO$_2$ nanoparticles, (d) approximate energy level diagram of doped TiO$_2$ showing the defect level generation for improved photoactivity and the photocatalytic degradation mechanism (the diagram is not to the scale).

photocatalyzed with TiO$_2$, indicating better photoactivity of our Ga-doped TiO$_2$ nanoparticles. Also, to compare the photocatalytic performance of our sample (1.0 at.% Ga-doped TiO$_2$ nanoparticles) with standard Degussa P-25 (as-received) samples, we have observed an 80% degradation of R^{h}B within 120 min of irradiation, which is better than the Degussa P-25 TiO$_2$ powders, where R^{h}B is found to be degraded upto 80–90% within 150 min [55]. Further, the results are found to be better for 2.0 at.% Ga-doped samples against Degussa P-25, where we have observed almost 90% degradation of R^{h}B within 90 min of irradiation.

As far as the effect of doping concentrations on the photocatalytic activity of the Ga-doped TiO$_2$ nanoparticles is concerned, we have observed a gradual increase in the photoactivity of the nanoparticles from 0.1 at.% to 2.0 at.% Ga-doped samples, beyond which the photoactivity started to decrease. It is speculated that, beyond the optimal doping concentration, the Ga^{+3} ions may not act favorably as the charge trapping centers to reduce the electron-hole recombination, rather become recombination centers through "quantum tunneling" to affect the photoactivity significantly, as observed previously for Fe^{+3}-doped TiO$_2$ nanomaterials [41, 56]. Similar effect is also observed for Ga-doped TiO$_2$ nanoparticles as well [36, 37], where the photoactivity is found to reach an optimum value for a certain dopant concentration (2 mol.% or 2–5 at%). In the current paper, we have reported all the data against 1.0 at% Ga doping, but a detailed study on the effect of doping concentration on the photocatalytic activity of Ga-TiO$_2$ for photodegradation of organic dye (such as R^{h}B, Methyl Orange, Orange-II, etc.) is underway and will be reported in due course.
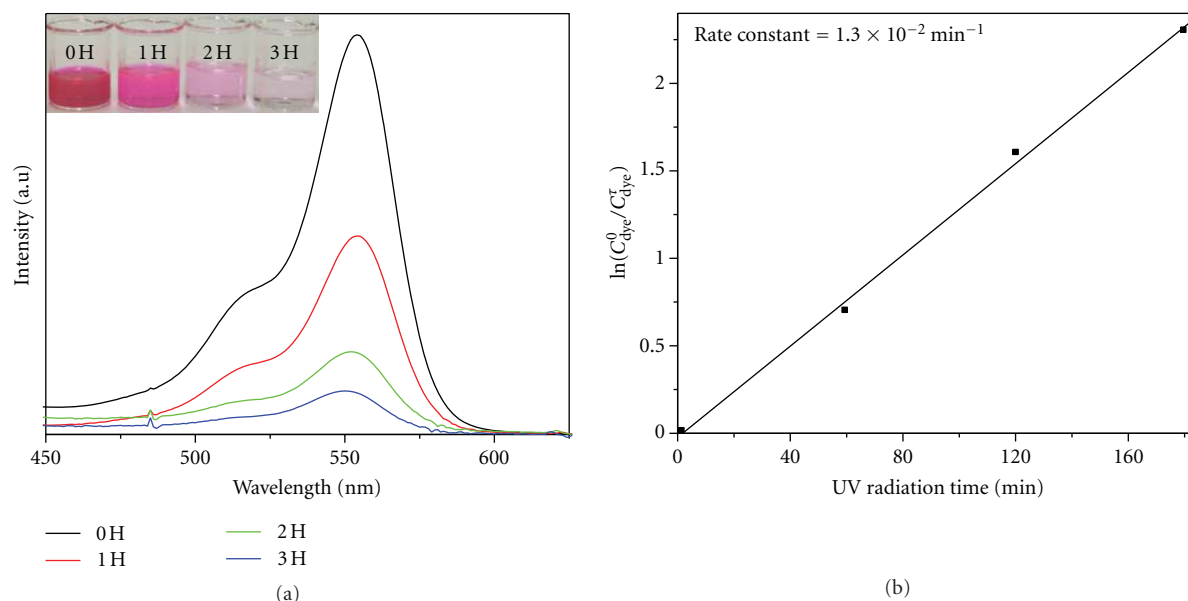
FIGURE 7: (a) Time effluence on photocatalytic degradation of Rhodamine B dye using TiO_2 : Ga nanoparticles as the photocatalyst under UV irradiation. Inset represents the digital photographs of dye solution at different irradiation times to show color change due to photocatalytic degradation of R^hB. (b) Pseudo-first-order kinetic plots and apparent rate constant of R^hB degradation.

4. Conclusions

Photocatalytic degradation of organic dye solution (Rhodamine B) is performed using Ga-doped TiO_2 nanoparticles as the photocatalyst. The nanoparticles are synthesized via sol-gel deposition process by using titanium isopropoxide and gallium oxide as the starting materials. XRD and Raman measurements confirm the pure anatase phase formation of the nanoparticles. Size-strain analysis shows that the doped samples are slightly strained due to the presence of Ga ions within TiO_2 matrix either as substitutional and (or) interstitial dopants. The nanoparticle size is found to be around 15 nm and confirmed via HRTEM imaging. XPS analysis shows the presence of Ti^{+3} and surface titanol groups, which enhance the photoactivity of the nanoparticles. Optical reflectance measurements showed a slight red-shift of the bandgap of the doped sample due to the formation of defect state within the bandgap of TiO_2 to improve the photocatalytic activity of TiO_2. Degradation of dye solution is done under UV irradiation and found to be highly efficient. The apparent 1st-order rate constant is found to be around 1.3×10^{-2} min^{-1}, which is relatively higher than the previously reported values of TiO_2-assisted photodegradation of R^hB with similar initial concentrations. The cost-effective, sol-gel-derived TiO_2 : Ga nanoparticles can be used efficiently for light-assisted oxidation of toxic organic molecules in the surface water for environmental remediation.

Acknowledgments

References

[1] A. N. Banerjee, "The design, fabrication, and photocatalytic utility of nanostructured semiconductors: focus on TiO_2-based nanostructures," *Nanotechnology, Science and Applications*, vol. 4, no. 1, pp. 35–65, 2011.

[2] A. Fujishima and K. Honda, "Electrochemical photolysis of water at a semiconductor electrode," *Nature*, vol. 238, no. 5358, pp. 37–38, 1972.

[3] A. L. Linsebigler, G. Lu, and J. T. Yates, "Photocatalysis on TiO_2 surfaces: principles, mechanisms, and selected results," *Chemical Reviews*, vol. 95, no. 3, pp. 735–758, 1995.

[4] A. Zaleska, "Doped-TiO_2: a review," *Recent Patents on Engineering*, vol. 2, no. 3, pp. 157–164, 2008.

[5] K. Shankar, J. I. Basham, N. K. Allam et al., "Recent advances In the use of TiO_2 nanotube and nanowire arrays for oxidative photoelectrochemistry," *Journal of Physical Chemistry C*, vol. 113, no. 16, pp. 6327–6359, 2009.

[6] K. Juodkazis, J. Juodkazyte, E. Jelmakas et al., "Photoelectrolysis of water: Solar hydrogen–achievements and perspectives," *Optic Express*, vol. 18, no. 102, pp. A147–A160, 2010.

[7] X. Chen and S. S. Mao, "Titanium dioxide nanomaterials: synthesis, properties, modifications and applications," *Chemical Reviews*, vol. 107, no. 7, pp. 2891–2959, 2007.

[8] A. Wold, "Photocatalytic properties of TiO_2," *Chemistry of Materials*, vol. 5, no. 3, pp. 280–283, 1993.

[9] U. Diebold, "The surface science of titanium dioxide," *Surface Science Reports*, vol. 48, no. 5–8, pp. 53–229, 2003.

[10] S. Liu, J. Yu, and M. Jaroniec, "Anatase TiO_2 with dominant high-energy 001 facets: synthesis, properties, and applications," *Chemistry of Materials*, vol. 23, pp. 4085–4093, 2011.

[11] Q. Xiang, J. Yu, and M. Jaroniec, "Graphene-based semiconductor photocatalysts," *Chemical Society Reviews*, vol. 41, pp. 782–796, 2012.

[12] J. G. Yu, H. G. Yu, B. Cheng, X. J. Zhao, J. C. Yu, and W. K. Ho, "The effect of calcination temperature on the surface microstructure and photocatalytic activity of TiO_2 thin films prepared by liquid phase deposition," *Journal of Physical Chemistry B*, vol. 107, no. 50, pp. 13871–13879, 2003.

[13] J. Yu, J. Xiong, B. Cheng, and S. Liu, "Fabrication and characterization of Ag-TiO_2 multiphase nanocomposite thin films with enhanced photocatalytic activity," *Applied Catalysis B: Environmental*, vol. 60, no. 3-4, pp. 211–221, 2005.

[14] L. Vegard, "Results of crystal analysis," *Philosophical Magazine*, vol. 32, pp. 505–515, 1916.

[15] B. O'Regan and M. Grätzel, "A low-cost, high-efficiency solar cell based on dye-sensitized colloidal TiO_2 films," *Nature*, vol. 353, no. 6346, pp. 737–740, 1991.

[16] H. Tang, K. Prasad, R. Sanjinés, and F. Lévy, "TiO_2 anatase thin films as gas sensors," *Sensors and Actuators B*, vol. 26, no. 1–3, pp. 71–75, 1995.

[17] M. A. Grela, M. A. Brusa, and A. J. Colussi, "Harnessing excess photon energy in photoinduced surface electron transfer between salicylate and illuminated titanium dioxide nanoparticles," *Journal of Physical Chemistry B*, vol. 101, no. 51, pp. 10986–10989, 1997.

[18] Y. Wang, Y. Hao, H. Cheng et al., "Photoelectrochemistry of transition metal-ion-doped TiO_2 nanocrystalline electrodes and higher solar cell conversion efficiency based on Zn^{2+}-doped TiO_2 electrode," *Journal of Materials Science*, vol. 34, no. 12, pp. 2773–2779, 1999.

[19] D. Dvoranová, V. Brezová, M. Mazúr, and M. A. Malati, "Investigations of metal-doped titanium dioxide photocatalysts," *Applied Catalysis B*, vol. 37, no. 2, pp. 91–105, 2002.

[20] A. Fuerte, M. D. Hernández-Alonso, A. J. Maira et al., "Visible light-activated nanosized doped-TiO_2 photocatalysts," *Chemical Communications*, no. 24, pp. 2718–2719, 2001.

[21] N. H. Hong, J. Sakai, W. Prellier, and A. Ruyter, "Room temperature ferromagnetism in laser ablated transition-metal-doped TiO_2 thin films on various types of substrates," *Journal of Physics D*, vol. 38, no. 6, pp. 816–821, 2005.

[22] A. W. Xu, Y. Gao, and H. Q. Liu, "The preparation, characterization, and their photocatalytic activities of rare-earth-doped TiO_2 nanoparticles," *Journal of Catalysis*, vol. 207, no. 2, pp. 151–157, 2002.

[23] J. Li and C. Z. Hua, "Hollowing Sn-doped TiO_2 nanospheres via Ostwald ripening," *Journal of the American Chemical Society*, vol. 129, no. 51, pp. 15839–15847, 2007.

[24] Y. Shen, T. Xiong, T. Li, and K. Yang, "Tungsten and nitrogen co-doped TiO_2 nano-powders with strong visible light response," *Applied Catalysis B: Environmental*, vol. 83, no. 3-4, pp. 177–185, 2008.

[25] K. Wilke and H. D. Breuer, "The influence of transition metal doping on the physical and photocatalytic properties of titania," *Journal of Photochemistry and Photobiology A*, vol. 121, no. 1, pp. 49–53, 1999.

[26] M. Melemeni, D. Stamatakis, N. P. Xekoukoulotakis, D. Mantzavinos, and N. Kalogerakis, "Disinfection of municipal wastewater by TiO_2 photocatalysis with UV-A, visible and solar irradiation and BDD electrolysis," *Global Nest Journal*, vol. 11, no. 3, pp. 357–363, 2009.

[27] D. F. Ollis, "Photocatalytic purification and remediation of contaminated air and water," *C R Academic Science of Paris, Chemical*, vol. 3, no. 6, pp. 405–411, 2000.

[28] A. Mills and S. Le Hunte, "An overview of semiconductor photocatalysis," *Journal of Photochemistry and Photobiology A*, vol. 108, no. 1, pp. 1–35, 1997.

[29] M. R. Hoffmann, S. T. Martin, W. Choi, and D. W. Bahnemann, "Environmental applications of semiconductor photocatalysis," *Chemical Reviews*, vol. 95, no. 1, pp. 69–96, 1995.

[30] K. Kabra, R. Chaudhury, and R. L. Sawney, "Treatment of hazardous organic and inorganic compounds through aqueous-phase photocatalysis: a review," *Indian Engineering Chemical Research*, vol. 43, no. 24, pp. 7683–7696, 2004.

[31] J. M. Herrmann, "Heterogeneous photocatalysis: state of the art and present applications," *Topics in Catalysis*, vol. 34, no. 1–4, pp. 49–65, 2005.

[32] G. Palmisano, V. Augugliaro, M. Pagliaro, and L. Palmisano, "Photocatalysis: a promising route for 21st century organic chemistry," *Chemical Communications*, no. 33, pp. 3425–3437, 2007.

[33] A. P. Zhang and Y. P. Sun, "Photocatalytic killing effect of TiO_2 nanoparticles on Ls-174-t human colon carcinoma cells," *World Journal of Gastroenterology*, vol. 10, no. 21, pp. 3191–3193, 2004.

[34] A. Fujishima, T. N. Rao, and D. A. Tryk, "Titanium dioxide photocatalysis," *Journal of Photochemistry and Photobiology C*, vol. 1, no. 1, pp. 1–21, 2000.

[35] C. Mccullagh, J. M. C. Robertson, D. W. Bahnemann, and P. K. J. Robertson, "The application of TiO_2 photocatalysis for disinfection of water contaminated with pathogenic microorganisms: a review," *Research on Chemical Intermediates*, vol. 33, no. 3–5, pp. 359–375, 2007.

[36] J. Chae, J. Lee, J. H. Jeong, and M. Kang, "Hydrogen production from photo splitting of water using the Ga-incorporated TiO_2s prepared by a solvothermal method and their characteristics," *Bulletin of Korean Chemical Society*, vol. 30, no. 2, pp. 302–308, 2009.

[37] C. M. Whang, J. G. Kim, E. Y. Kim, Y. H. Kim, and W. I. Lee, "Effect of Co, Ga, and Nd additions on the photocatalytic properties of TiO_2 nanopowders," *Glass Physics and Chemistry*, vol. 31, no. 3, pp. 390–395, 2005.

[38] S. Song, C. Wang, F. Hong, Z. He, Q. Cai, and J. Chen, "Gallium- and iodine-co-doped titanium dioxide for photocatalytic degradation of 2-chlorophenol in aqueous solution: Role of gallium," *Applied Surface Science*, vol. 257, no. 8, pp. 3427–3432, 2011.

[39] J. Zhou, Y. Zhang, X. S. Zhao, and A. K. Ray, "Photodegradation of benzoic acid over metal-doped TiO_2," *Industrial and Engineering Chemistry Research*, vol. 45, no. 10, pp. 3503–3511, 2006.

[40] T. Okajima, T. Yamamoto, M. Kunisu, S. Yoshioka, I. Tanaka, and N. Umesaki, "Dilute Ga dopant in TiO_2 by X-ray absorption near-edge structure," *Japanese Journal of Applied Physics Part 1*, vol. 45, no. 9, pp. 7028–7031, 2006.

[41] W. Choi, A. Termin, and M. R. Hoffmann, "The role of metal ion dopants in quantum-sized TiO_2: correlation between photoreactivity and charge carrier recombination dynamics," *Journal of Physical Chemistry*, vol. 98, no. 51, pp. 13669–13679, 1994.

[42] B. D. Cullity, *Elements of X-ray Diffraction*, Addison-Wesley, Reading, Mass, USA, 1978.

[43] R. Wang, N. Sakai, A. Fujishima, T. Watanabe, and K. Hashimoto, "Studies of surface wettability conversion on TiO_2 single-crystal surfaces," *Journal of Physical Chemistry B*, vol. 103, no. 12, pp. 2188–2194, 1999.

[44] N. L. Wu, M. S. Lee, Z. J. Pon, and J. Z. Hsu, "Effect of calcination atmosphere on TiO_2 photocatalysis in hydrogen production from methanol/water solution," *Journal of Photochemistry and Photobiology A*, vol. 163, no. 1-2, pp. 277–280, 2004.

[45] J. C. Yu, J. Yu, and J. Zhao, "Enhanced photocatalytic activity of mesoporous and ordinary TiO_2 thin films by sulfuric acid treatment," *Applied Catalysis B: Environmental*, vol. 36, no. 1, pp. 31–43, 2002.

[46] R. V. Ghita, C. Logofatu, C. Negrila et al., "XPS study of Ti/oxidized GaAs interface," *Journal of Optoelectronics and Advanced Materials*, vol. 8, no. 1, pp. 31–36, 2006.

[47] R. Rao, A. M. Rao, B. Xu, J. Dong, S. Sharma, and M. K. Sunkara, "Blueshifted Raman scattering and its correlation with the [110] growth direction in gallium oxide nanowires," *Journal of Applied Physics*, vol. 98, no. 9, Article ID 094312, 2005.

[48] P. W. Wang, Y. P. Song, X. Z. Zhang, J. Xu, and D. P. Yu, "Transformation from β-Ga_2O_3 to GaN nanowires via nitridation," *Chinese Physics Letters*, vol. 25, no. 3, pp. 1038–1041, 2008.

[49] J. D. Lindberg and D. G. Snyder, "Determination of the optical absorption coefficient of powdered materials whose particle size distribution and refractive indices are unknown," *Applied Optics*, vol. 12, no. 3, pp. 573–578, 1973.

[50] N. Barka, S. Qourzal, A. Assabbane, A. Nounah, and Y. Ait-Ichou, "Factors influencing the photocatalytic degradation of Rhodamine B by TiO_2-coated non-woven paper," *Journal of Photochemistry and Photobiology A*, vol. 195, no. 2-3, pp. 346–351, 2008.

[51] K. Yu, S. Yang, H. He, C. Sun, C. Gu, and Y. Ju, "Visible light-driven photocatalytic degradation of rhodamine B over $NaBiO_3$: pathways and mechanism," *Journal of Physical Chemistry A*, vol. 113, no. 37, pp. 10024–10032, 2009.

[52] Q. Xiang, J. Yu, and P. K. Wong, "Quantitative characterization of hydroxyl radicals produced by various photocatalysts," *Journal of Colloid and Interface Science*, vol. 357, no. 1, pp. 163–167, 2011.

[53] Q. Xiang, J. Yu, and M. Jaroniec, "Nitrogen and sulfur co-doped TiO_2 nanosheets with exposed {001} facets: synthesis, characterization and visible-light photocatalytic activity," *Physical Chemistry Chemical Physics*, vol. 13, no. 11, pp. 4853–4861, 2011.

[54] N. Guettaï and H. Ait Amar, "Photocatalytic oxidation of methyl orange in presence of titanium dioxide in aqueous suspension. Part II: kinetics study," *Desalination*, vol. 185, no. 1–3, pp. 439–448, 2005.

[55] X. Qin, L. Jing, G. Tian, Y. Qu, and Y. Feng, "Enhanced photocatalytic activity for degrading Rhodamine B solution of commercial Degussa P25 TiO_2 and its mechanisms," *Journal of Hazardous Materials*, vol. 172, no. 2-3, pp. 1168–1174, 2009.

[56] J. Yu, Q. Xiang, and M. Zhou, "Preparation, characterization and visible-light-driven photocatalytic activity of Fe-doped titania nanorods and first-principles study for electronic structures," *Applied Catalysis B*, vol. 90, no. 3-4, pp. 595–602, 2009.